Control of the emission properties of semiconducting nanowire quantum dots using plasmonic nanoantennas

Mathieu Emmanuel Jeannin

Communauté
UNIVERSITÉ Grenoble Alpes

THÈSE

Pour obtenir le grade de

DOCTEUR DE LA COMMUNAUTÉ UNIVERSITÉ GRENOBLE ALPES

Spécialité : **Physique**

Arrêté ministériel : 7 août 2006

Présentée par

Mathieu Emmanuel JEANNIN

Thèse dirigée par **Dr. Gilles NOGUES** et
codirigée par **Prof. Dr. Kuntheak KHENG**

préparée au sein de l'**Institut Néel, CNRS**
dans **l'Ecole Doctorale de Physique, Université Grenoble Alpes**

Control of the emission properties of semiconducting nanowire quantum dots using plasmonic nanoantennas

Thèse soutenue publiquement le **28 Octobre 2016**,
devant le jury composé de :

Dr. Serge HUANT
Directeur de recherches, Institut Néel, CNRS, Grenoble, Président du jury
Prof. Dr. Maria CHAMARRO
Professeur, Institut des Nanosciences de Paris, Université Pierre et Marie Curie, Paris, Rapporteuse
Dr. Jean-Jacques GREFFET
Directeur de recherches, Laboratoire Charles Fabry, Institut d'Optique, Palaiseau, Rapporteur
Prof. Dr. Jaime GÓMEZ-RIVAS
Professeur, Dutch Institute for Fundamental Energy Research, Examinateur
Dr. Nicolas CHAUVIN
Chargé de recherches, Institut des Nanotechnologies de Lyon, CNRS, Lyon, Examinateur
Dr. Gilles NOGUES
Chargé de recherches, Institut Néel, CNRS, Grenoble, Directeur de thèse
Prof. Dr. Kuntheak KHENG
Professeur, Institut Nanosciences et Cryogénie, CEA, Grenoble, co-Directeur de thèse

“ *You can’t always get what you want*
But if you try sometimes
You just might find
You get what you need”
The Rolling Stones - You can’t always get what you want

Remerciements

Il n'est de bonne thèse sans bons remerciements. Enfin, il me semble. N'étant pas particulièrement doué avec les mots, j'espère que ceux-ci ne gâcheront pas la lecture du travail présenté plus loin.

Je voudrais commencer par remercier chaleureusement mes encadrants, Gilles Nogues et Kuntheak Kheng, pour m'avoir donné l'opportunité d'étudier durant trois ans dans un environnement aussi exceptionnel. Je tiens à remercier tout particulièrement Gilles, avec qui j'ai travaillé quotidiennement, et qui a été une véritable source d'inspiration scientifique tout au long de ma thèse.

J'ai été immédiatement conquis par l'environnement de travail proposé au sein de l'équipe NPSC en visitant le laboratoire lors de ma recherche de thèse. Ces trois ans de recherche m'ont conforté dans l'idée qu'il s'agit d'un cadre privilégié. Je souhaite exprimer ma gratitude à tous les membres de l'équipe, et plus particulièrement David Ferrand, Joël Cibert, Jean-Philippe Poizat, Lucien Besombes, Jacek Kasprzak et Maxime Richard avec qui j'ai interagi de plus ou moins près durant ces trois ans. Ils m'ont tous beaucoup apporté, tant au point de vue scientifique que personnel. Ces remerciements ne sont pas confinés à l'équipe, et je voudrais également remercier sincèrement Guillaume Bachelier pour son aide dans la compréhension des phénomènes plasmoniques, et pour avoir toujours su poser les bonnes questions, conduisant à ce qui j'espère sera une collaboration réussie.

Mon travail de thèse m'a également amené à embêter de façon extrêmement répétitive un certain nombre d'ingénieurs de l'Institut Néel, parmi lesquels l'ensemble de l'équipe Nanofab. Ils m'ont apporté une aide exceptionnelle dans le développement de mes procédés technologiques, avec une grande patience et surtout en ayant toujours les bons conseils. Un énorme merci à Bruno Fernandez, Gwénaëlle Julie, Sébastien Dufresnes, Thierry Crozes, Jean-François Motte, et bien sûr Thierry Fournier. Je voudrais de plus remercier très chaleureusement Fabrice Donatini pour son aide sur les expériences de cathodoluminescence. Je remercie également Laurent Cagnon pour son aide avec l'ALD, Philippe David pour les dépôts au DP850 et David Jegouso pour avoir sauvé notre laser.

Le présent manuscrit aurait très certainement été ~~illisible~~ plus compliqué à lire sans la contribution inestimable de Joël Cibert et Guillaume Bachelier, qui ont fait un travail de relecture bénévole de grande qualité pour lequel je leur suis très reconnaissant. D'autre part, je remercie Régis André, Joël Cibert et Eva Monroy pour leurs nombreux et judicieux conseils lors de la

fin de ma thèse, tant au point de vue scientifique que pour la suite de mon parcours.

Je tiens également à mentionner ici mes collègues non-permanents au sein de l'équipe, notamment Gaston Hornecker et Cyril Elouard avec qui j'ai partagé un bureau durant ces trois dernières années, et auprès de qui j'ai pu me plaindre régulièrement à des heures diverses de la journée. Je remercie également Quentin Mermillod pour avoir été aussi agréablement désagréable avec moi durant ces deux ans et demie passés ensemble, une façon bien personnelle de montrer de l'affection mais qui a toujours contribué à l'excellent ambiance de travail dans notre bureau. Je plains, soutiens, et remercie son successeur, Valentin Delmonte, qui a du le supporter, et avec qui j'ai agréablement pris la plus grande part de mes pauses café sur la fin de ce travail. Je voudrais de plus remercier François Fras, qui malgré un séjour écourté dans notre équipe, a été une source de bonne humeur efficace, Tomasz Jakubczyk qui lui a parfaitement succédé sur ce plan, et Thomas Grange pour avoir été un compagnon de slow food constant et compréhensif. J'ai également une pensée pour mes collègues non-permanents du côté INAC de l'équipe, Akhil Ajay, Jonas Lähnemann, Luca Redaelli et David Browne, avec qui j'ai pu m'échapper le temps que quelques repas qui m'ont offert une bouffée d'air et quelques bonne discussions. Enfin et surtout, je tiens à remercier Alberto pour avoir partagé autant de frustration expérimentale avec moi, mais également pour les manips que l'on a pu faire ensemble et qui nous ont menés sur la piste haletante du trou léger (si, si, le terme est approprié), pour les déjeuner italiens, et pour avoir été une vraie soupape de décompression lors de ma deuxième année. *Era un casino.* Je te souhaite beaucoup de bonheur pour la suite, avec Natasha et Maïa.

Quoiqu'on en dise, la vie ne s'arrête pas à la sortie du laboratoire. J'ai pu compter sur beaucoup d'amis très proches, sans qui elle serait beaucoup plus grise. Certains la rendent même éclatante : merci infiniment à Willow, Adri, Jérémy, Cédric et Adrien. Vous m'avez tous apporté énormément.

L'aventure ne s'arrête pas là. Merci à Caroline, avec qui j'apprends tous les jours. Les mots pâlissent en s'assemblant dans ces phrases, et ne te font pas justice.

Enfin je voudrais remercier mes parents et ma sœur. J'espère qu'ils sont au moins aussi fiers de moi que je leur suis reconnaissant.

Contents

Introduction en Français

Ce travail de thèse s'inscrit dans le cadre des récents progrès faits dans le domaine des nanotechnologies visant à l'étude de l'interaction lumière-matière. Le développement de la science des matériaux et des techniques de fabrication a ouvert la possibilité de sonder et modifier les propriétés de la nature sur des échelles nanométriques, révélant ainsi un nouveau pan entier de la science moderne à l'interface de la biologie, de la chimie, de la physique et de la mécanique quantique. Les avancées faites en croissance des semiconducteurs, notamment par la technique d'épitaxie par jet moléculaire ont permis la fabrication et l'étude de structures de dimensionnalité réduite, allant des puits quantiques aux fils et boîtes quantiques [Kli12, ch. 8, 15]. Tout particulièrement, les boîtes quantiques, des structures de semiconducteur confinées dans les 3 directions de l'espace, sont rapidement apparues comme l'équivalent en matière condensée des atomes uniques étudiés jusqu'alors en physique atomique. Leurs propriétés de confinement électronique a permis rapidement de mettre en évidence la nature quantique des phénomènes mis en jeux dans les boîtes, en faisant un candidat idéal pour le développement de l'optique quantique en matière condensée [Mic00; Ima+00; San+01; Bes+04; Shi07; Urb+13; LMS15]. Une représentation schématique d'une boîte quantique est proposée en figure 1.

L'intérêt principal des boîtes quantiques est qu'il est possible de contrôler leurs propriétés électroniques en modifiant les matériaux utilisés pour leur fabrication. Le piège électronique créé par une boîte quantique permet le confinement d'un nombre discret de paires électron-trou, résultant en une discrétisation de la densité d'état électronique. La signature optique de ces boîtes réside donc dans la détection de recombinaisons discrètes entre ces paires de porteurs, caractérisées par l'émission de photons uniques [Mic00]. La problématique cruciale est alors de pouvoir manipuler l'émission spontanée de tels objets. Depuis la découverte par Purcell de l'exaltation de l'émission spontanée d'atomes placés dans une cavité résonnante [Pur46], il a été établi que l'émission spontanée d'un système peut être contrôlée en modifiant son couplage avec son environnement électromagnétique. De nombreuses stratégies expérimentales ont alors été développées selon deux idées complémentaires: maximiser le coupler couplage de l'émetteur à des modes électromagnétiques se propageant dans la direction souhaitée, et minimiser son couplage au autres modes, dits modes de fuite (voir figure 2).

Une stratégie originale et prometteuse émerge depuis quelques années, consistant à inclure ces boîtes quantiques dans des structures nanofils [Tri+08; Hei+13; Rue+14]. De par leur mécanisme de croissance, ces nanofils permettent l'obtention de structures avec une excellente qualité cristalline [Rue+14], et la fabrication d'hétérostructures radiales [Lau+02] et axiales [Rue+14] dopées sélectivement [Dua+01]. Ces hétérostructures permettent de contrôler le confinement et la contrainte mécanique dans les différentes parties du système. Notamment, contrôler le champ de contraintes subies par la boîte permet de modifier ses propriétés électroniques

[Tar+04; Huo+13; Zie13; FC14; Chr+15]. Enfin, la géométrie des nanofils les rend particulièrement simples à manipuler et isoler, facilitant la combinaison d'études sur un même objet et offrant une possibilité naturelle de contact électrique [Wan01; Des+13]. Un des type de boîte quantique insérée dans un nanofil à semiconducteur est présenté en figure 3.

La configuration particulière des boîtes insérées dans des nanofils permet un accès aisé au voisinage direct de la boîte. Cela implique que la densité d'états électromagnétiques dans le champ proche de la boîte peut être sondé ou modifié de façon extrêmement locale. Pour ce faire, il faut réussir à créer des éléments permettant de confiner et de modeler le champ électromagnétique proche de la boîte sur des dimensions sub-longueur d'onde, inférieures à la limite de diffraction. Les plasmons de surface supportés par des nanoparticules métalliques répondent à cette problématique, car ils fournissent un confinement du champ supérieur à la limite de diffraction, permettant l'interface entre un rayonnement propagatif en champ lointain et un champ local confiné aux alentours de la particule [Muh05; Mai07; BDN09]. Ces plasmons de surface sont des oscillations cohérentes et collectives des électrons de conduction du métal formant la particule. Elles produisent des résonances larges spectralement, dont l'énergie est accordable dans les gammes visible et infrarouge du spectre électromagnétique. Les particules supportant de telles résonances sont donc vues comme de potentielles antennes pour un rayonnement aux fréquences optiques.

Le but de ce travail de thèse est de coupler des nanoantennes plasmoniques à des boîtes quantiques insérées dans des nanofils à semiconducteur pour contrôler et exalter leurs propriétés d'émission, comme proposé en figure 5. Un tel couplage nécessite d'accorder spectralement et spatialement les modes de plasmons supportés par les antennes à l'émission spontanée de la boîte quantique. Il faudra donc caractériser précisément ces modes de plasmons, ainsi que l'émission de la boîte quantique, avant de proposer une géométrie de couplage.

Le premier chapitre de ce manuscrit apporte les fondements théoriques nécessaire à la compréhension du travail de plasmonique effectué dans cette thèse. Partant des équations de Maxwell, on détaille la réponse des matériaux métalliques à une excitation électronique aux fréquences visibles. Leurs propriété optique est introduite via le modèle de Drude, qui considère uniquement les électrons de conduction et les assimile à un gaz d'électrons libres. Le modèle est ensuite raffiné via l'exposition de la structure de bande des métaux utilisés ici (l'or et l'aluminium), et on discute notamment de l'impact des transitions électroniques interbandes. On démontre alors les conditions d'existence des plasmons polaritons de surface, qui sont des ondes transverses magnétiques à l'interface entre un milieu métallique et un diélectrique. On étend le cas d'étude à un système à plusieurs interfaces. Le rôle des paramètres physiques des matériaux est également discuté pour établir les propriétés plasmoniques de couches d'or et d'aluminium dans des milieux stratifiés. Enfin, on exposera les propriétés des plasmons de surface supportés par des nanoparticules métalliques, en s'attachant à discuter les effets de taille, de forme et l'impact des matériaux choisis.

Dans le chapitre 2, on détaille la caractérisation expérimentale de nanoantennes plasmoniques par cathodoluminescence (CL). On présente dans un premier temps quelques éléments théoriques concernant la CL, puis on expose les premiers résultats d'expériences sur des échantillons stratifiés continus composés de couches métalliques et diélectriques alternées. On montre l'intérêt d'un tel système pour fabriquer des antennes plasmoniques. On présente alors les expériences de CL sur des antennes patch plasmoniques basées sur ces films stratifiés. Les résultats de CL sont comparés à un modèle de densité d'états électromagnétiques. On démontre que les antennes

patchs en or peuvent opérer dans les gammes rouge et infrarouge du spectre électromagnétique, et qu'on peut contrôler leurs propriétés spectrales en agissant sur leur taille ou l'épaisseur de la couche d'oxyde séparant le patch du plan de masse. On compare alors des antennes patch en or, or-oxyde-aluminium et aluminium, et l'on montre qu'on peut étendre leur gamme d'opération à tout le spectre visible.

On se tourne ensuite dans le chapitre 3 sur l'étude des boîtes quantiques insérées dans des nanofils à semiconducteur. Ce travail de thèse s'appuie sur deux types de systèmes: des boîtes de CdMnTe dans des fils cœur/coquille ZnTe/ZnMgTe et des boîtes de CdSe dans des fils ZnSe/ZnMgSe. On commence par des rappels d'optique des semiconducteurs nécessaire à la compréhension des phénomènes mis en jeux dans l'émission des boîtes. On expose alors les expériences de microphotoluminescence et les résultats obtenus sur plusieurs fils de chaque système. On montre les mesures de microphotoluminescence, de temps de déclin et de microscopie de Fourier. Il apparaît que la compréhension des propriétés de ces nanoémetteurs nécessite de multiples caractérisations sur un même objet, afin d'extraire ses propriétés optiques et électroniques.

On propose alors dans le chapitre 4 une étude complète sur un nanofil basé Te, en combinant CL, microscopie de Fourier résolue en polarisation et spectroscopie magnéto-optique, accompagnée d'un modèle théorique décrivant l'émission de la boîte insérée dans le fil. A la lumière de ces résultats, on dégage également des conclusions plus générales sur les mesures statistiques effectuées sur plusieurs nanofils basés Tellure.

Pour conclure, le chapitre 5 est dédié à la fabrication et à la caractérisation de systèmes couplés nanofil-nanoantenne. On présente la méthode développée dans cette thèse, basée sur une lithographie en deux étapes utilisant la CL pour localiser la boîte quantique dans un repère de marques pré-lithographiées. On démontre la fabrication d'antennes dans le champ proche de boîtes quantiques, et on étudie le couplage entre les deux éléments. On montre une exaltation de la fluorescence en présence de l'antenne d'un facteur 2.5 dû au couplage radiatif entre la boîte et l'antenne.

Enfin, on apporte des pistes d'améliorations concernant les systèmes hybrides composés de boîtes quantiques insérées dans des nanofils et d'antennes plasmoniques. On montre également que le procédé de fabrication d'antennes a une portée plus générale et peut être utilisé dans d'autres domaines, notamment pour l'étude de nanostructure hybrides pour l'optique non linéaire.

Introduction

This thesis takes place in the frame of the recent advances in nanotechnologies for the study of light-matter interaction. The development of material sciences and fabrication techniques opened up the possibility to probe and modify nature on a nanometre scale, revealing a whole new area of science at the interface of biology, chemistry, physics and quantum mechanics. The progresses in semiconducting materials growth, especially in molecular beam epitaxy (MBE), lead to the possibility of studying structures of reduced dimensionality such as quantum wells, quantum wires and quantum dots [Kli12, ch. 8, 15]. By the same token, it allowed the rapid growth of the semiconductor optics field, driven by both the advances of optical physics as a spectroscopic tool for semiconductor physics [Koc+06; Sal+09; Kas+10], and semiconductor physics for optical applications ranging from light emitting diodes [BP66] to laser diodes [Hal+62] or quantum dot displays [Sun+07]. Semiconducting quantum dots (QDs), i.e. 3D-confined semiconducting materials, soon appeared as artificial, solid-state atoms that confine electronic carriers in dimensions small enough to evidence their quantum nature, and paved the way to solid-state based systems for quantum optics [Mic00; Ima+00; San+01; Bes+04; Shi07; Urb+13; LMS15]. A sketch of such a quantum dot structure is presented in figure 1.

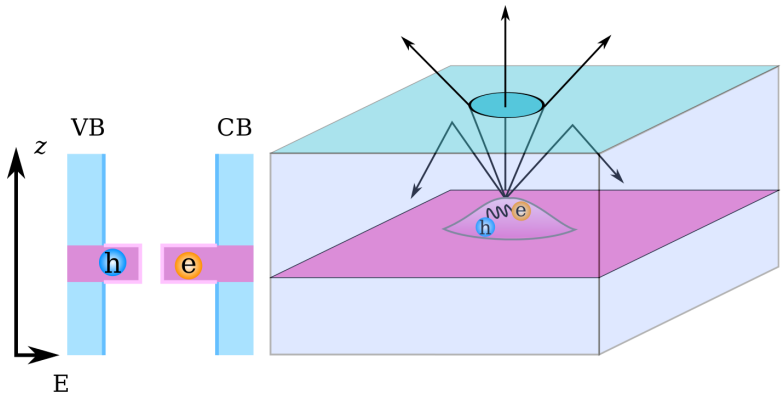

Figure 1 – A self-assembled quantum dot.
Left: Energy diagram of two semiconducting materials with a high (blue) and small (pink) bandgap arranged in an heterostructure configuration, showing the electronic confinement of the carriers along the growth axis z. The typical height of this heterostructure is of the order of a few nanometres.
Right: Sketch of a single self-assembled quantum dot (pink) in a homogeneous host matrix (blue). The in-plane size of the dot is around 10 nm, providing an electronic confinement in the three directions of space. A discrete number of electron-hole pairs, or excitons, can be trapped in the dot. Due to the high refractive index contrast with free space, direct extraction of the light emitted by the QD is limited to a few percent. Hence, most of the QD fluorescence is lost in the host material.

By physically limiting the size of a small gap semiconductor (pink), here embedded inside a semiconducting material of larger bandgap (blue), one can modify the electronic band structure inside the material to create spatially defined traps for the charges, engineering the electronic density of states. Upon excitation, electrons in the conduction band (CB) or holes in the valence band (VB) interact through the Coulomb interaction, forming an exciton that can be trapped inside the QD. The electron can then relax to the valence band by emitting a photon via spontaneous emission, or by non-radiative processes. However, unlike other semiconducting structures like simple heterojunctions or quantum wells, the confined nature of excitons in QDs is revealed by the discrete number of charges that can be trapped in the dot. Hence, single recombination events leading to the emission of single photons from the dot are the optical signature of these emitters [Mic00]. However, due to the large difference in refractive index n between the semiconducting host and free-space ($n \approx 3$), a large fraction of the emitted photons cannot be extracted in a convenient manner and are lost e.g. by total internal reflection, as demonstrated by the critical angle $\theta_c \approx 20°$ for $n = 3$.

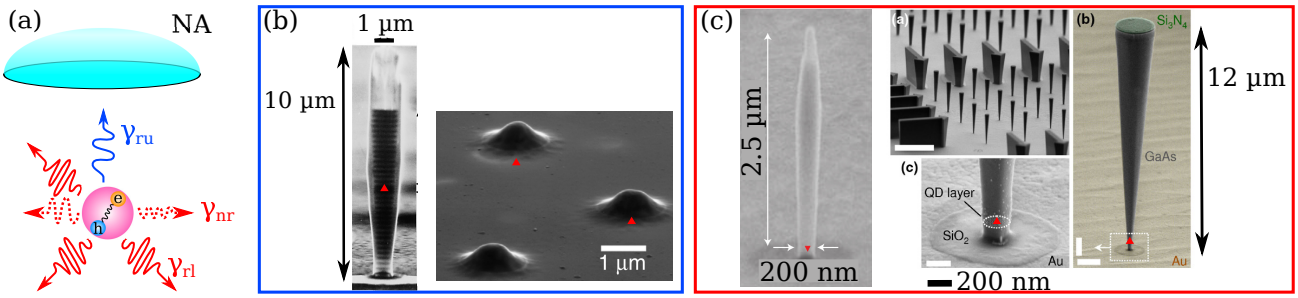

Figure 2 – Electromagnetic density of states engineering for quantum emitters. (a) A single quantum dot in a homogeneous medium and its different de-excitation channels: radiative and useful (γ_{ru}, blue) i.e. that can be collected in the experimental NA, radiative but lost (γ_{rl}, red) i.e. emitted in uncollected directions, and non-radiative (γ_{nr}, red dashes). (b) Enhancing contributions to γ_{ru} for quantum dots using vertical micropilar cavities with distributed Bragg reflectors [Gér+98] or deterministically positioned microlenses [Gsc+15]. (c) Suppressing radiative losses with the photonic needle [Cla+10], the photonic trumpet [Mun+13].

Controlling the spontaneous emission of single emitters is thus at the heart of quantum optics. Since the report by Purcell in 1946 of the enhancement of the spontaneous emission rate of atoms placed inside resonant cavities [Pur46] (the so-called Purcell effect), it is known that this spontaneous emission can be modified by acting on the coupling of the emitter with its electromagnetic environment. A huge effort has thus been made to answer to two fundamental points: how can one accelerate the spontaneous emission from a quantum dot, and how can this emission be beamed into a useful direction? In fact, semiconducting quantum dots are seen as extremely promising candidates to act as on-demand single photon emitters, which are necessary elements to implement light based quantum communication. Figure 2 (b),(c) shows a summary of some proposals that have been made to improve the performances of QDs. The QD is sketched in panel (a), and its position in each structure is marked by a red triangle. After excitation, the QD can decay radiatively into the useful numerical aperture (NA), or in detrimental direction with decay rates γ_{ru} (blue) and γ_{rl} (red) respectively. Non-radiative recombinations can also occur, with a rate γ_{nr} (red, dashed). As a first remark, one obviously wants to keep the non-radiative rate γ_{nr} as low as possible. Then two main strategies can be

employed: either enhancing as much as possible the coupling to electromagnetic modes directed towards the useful NA (figure 2 (b), [Gér+98; Gsc+15]) or suppressing as much as possible the coupling to unwanted radiative modes (figure 2 (c), [Cla+10; Mun+13]). The fundamental idea behind these two strategies is to engineer the electromagnetic density of states in the vicinity of the dot (referred to as the local density of states (LDOS) in this manuscript) to force the emission of the QD into the desired emission profile.

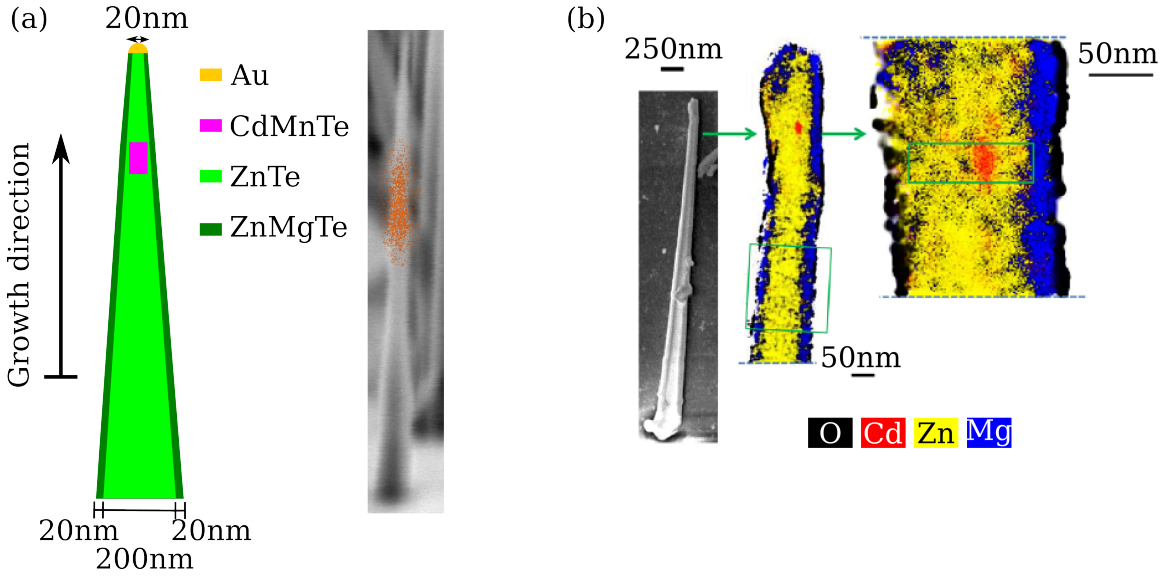

Figure 3 – Nanowire quantum dots.
(a) Sketch (left) and SEM image (right) of a NWQD structure studied in this thesis. It is grown by Au-catalysed molecular beam epitaxy, and consists in a CdMnTe QD inserted inside a ZnTe/ZnMgTe core/shell NW. The localised QD fluorescence is revealed by the monochromatic CL image superimposed on the SEM image. (b) SEM image and chemical reconstruction using energy dispersive X-ray spectrometry of a similar NWQD system from the same sample, adapted from [Rue+16]. It reveals the small QD size, its shape, and the spatial localisation of the different chemical species, confirming the composition of the heterostructure.

However, all the aforementioned strategies use self-assembled QDs which grow at random positions on the substrate, and require post-growth processing of the sample that can induce defects and generate non-radiative losses. The most common growth mechanism for such QDs is the Stranski-Krastanov (SK) growth, which is driven by strain. SK quantum dots thus experience a strain field imposed by their growth condition, over which one has very little control, limiting the possibilities of strain-mediated engineering of the dot properties. A promising alternative is to grow a semiconducting nanowire (NW) and to embed the QD inside this wire structure during the growth process [Tri+08; Hei+13; Rue+14]. It has the advantage of producing structures with a very high crystalline quality [Rue+14]. Furthermore, it allows the growth of both radial [Lau+02] and axial [Rue+14] heterostructures with additional selective doping [Dua+01]. The great control overt the morphological properties of these NWs renders possible to control the confinement and the strain experienced by the dot, which can be used to tune its electronic properties [Tar+04; Huo+13; Zie13; FC14; Chr+15]. Finally, their geometry makes the nanowire quantum dots (NWQDs) easier to isolate, facilitating multiple studies on a single

structure and electrical contacting [Wan01; Des+13]. Figure 3 (a) shows a sketch of one of the structures studied in this thesis, composed of a CdMnTe QD inside a ZnTe/ZnMgTe core/shell nanowire, and a scanning electron microscope (SEM) image of the wire with a superimposed monochromatic cathodoluminescence (CL) image revealing the localised QD emission. 3 (b) represents a chemical analysis performed on a NW from the same growth sample, revealing its chemical composition [Rue+16].

The practical NW geometry also opens an access to the close proximity of the embedded dot, which is hard to reach in other QD geometries. This means that the LDOS near the QD can be probed or modified by local, nanometre scale elements. Such elements are required to tailor electromagnetic field on a dimension smaller than the wavelength of light, breaking the so-called diffraction limit. Surface plasmons supported by metallic nanoparticles are known to provide sub-diffraction limited electric field confinement, allowing interfacing free-space radiation with localised fields [Muh05; Mai07; BDN09]. These surface plasmons are collective and coherent oscillations of the conduction electrons of the metal, generating intense electric fields in nanometre-sized regions. They provide broadband resonances that are tunable across the visible and infra-red (IR) spectral ranges as shown in figure 4 (a), allowing for an external control of the LDOS in the vicinity of close-by emitters [Tho+04; ABN06]. Hence, they can be used as very local optical antennas to enhance, control or probe the emission properties of semiconducting nanowire quantum dots. By carefully designing them, we can both accelerate the spontaneous emission rate from a QD via the Purcell effect, and modify the coupling of the emitted photons to free space radiation in the desired directions.

Some demonstrations of plasmonic modification of the properties of solid-state emitters are shown in figure 4 (b),(c) in the case of self-assembled QDs and bare NWs respectively, showing fluorescence enhancement through radiative coupling between the dot and the antenna mode [Pfe+14], and directional emission in a Yagi-Uda antenna configuration [Ram+15]. They provide proof-of-principle experiments for the purpose of this work, which is sketched in figure 5. We have developed a technique to couple plasmonic nanoantennas to semiconducting nanowire quantum dots, with the purpose of enhancing and obtaining an *external* control over their emission properties. The efficient coupling between the antenna and the emitter requires a prior thorough characterisation of both isolated systems properties. Hence, the goal of this thesis is many-fold: developing the relevant characterisation methods for both plasmonic antennas and semiconducting nanowire quantum dots, implementing a fabrication process allowing for the coupling between these two structures, and finally studying the effect of such coupling on the quantum dot emission properties.

In chapter 1, we provide a theoretical background for the study of plasmonic nanoantennas. We start from Maxwell's equations and detail the optical response of metals at visible frequencies. We introduce the description of their properties through the Drude model which accounts for the conduction electrons as a free electron gas, and discuss additional information revealed by their band structures, such as the role of interband transitions. We then derive the conditions for the existence of surface plasmon polaritons (SPPs) at a metallic interface, and extend the study to the case of stratified media. We show the role of materials parameters and set out the plasmonic properties of Au and Al layers in stratified media. We finally discuss the local surface plasmons supported by nanoparticles, with the influence of size, shape and materials.

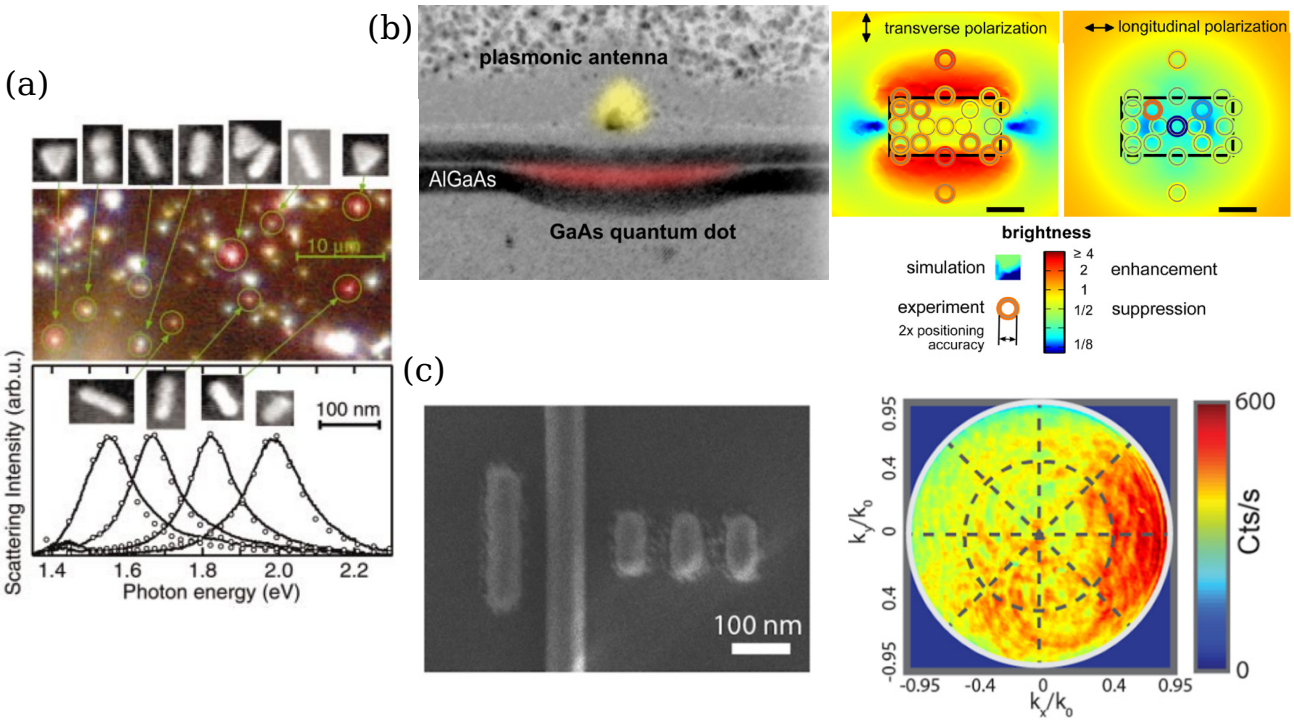

Figure 4 – Metallic nanoparticles as plasmonic antennas for light emission.
(a) Dark-field image and scattering spectra of colloidal Au nanoparticles deposited on a glass slide, with the corresponding SEM images, revealing that the localised surface plasmon resonance is tunable across the visible and near-IR spectral range with the antenna size and shape. Adapted from [Kuw+03]. (b) Au plasmonic dipole antenna for the fluorescence enhancement of a single GaAs QD, as shown in the transmission electron microscope image (left) and the comparison between simulations (colour-coded map) and experimental results (circles) of fluorescence enhancement up to a factor 2. Adapted from [Pfe+14]. (c) Hybrid semiconducting NW - Yagi-Uda plasmonic antenna system showing directional emission from the system. The left image is a SEM image of the system, and the right panel shows a directivity measurement using Fourier microscopy. Adapted from [Ram+15].

Chapter 2 concerns the experimental characterisation technique used during this thesis to study plasmonic antennas, namely cathodoluminescence. We set out the basic theory for CL and its application to plasmonics. We then detail our results on CL performed on stratified films composed of alternating metallic and oxide layers. We show that such systems can be used to fabricate plasmonic patch antennas, providing interesting field localisation properties. We then detail the CL experiment on Au patch antennas and link their CL response to a LDOS model. It reveals that the Au antennas can operate in the red and near-IR part of the spectrum. We show that we can control the spectral response of the antennas by tuning their size, and that we can control the dispersion of their eigenmodes by changing the coupling between the patch and the ground plane. Finally, we compare Au, Au-Al bi-metal and Al patch antennas to demonstrate that we can extend the range of operation of the patch antennas to the entire visible spectrum. We conclude on the interest of CL for the nanoscale study of plasmonic antennas, and discuss antennas configurations for our final goal.

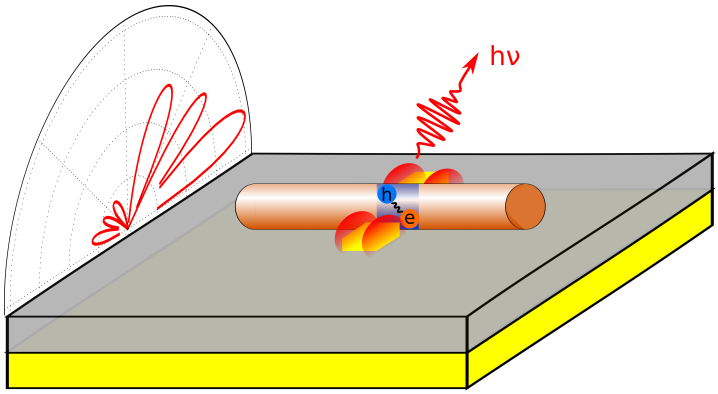

Figure 5 – Directional emission and Purcell enhancement of a NWQD coupled to plasmonic antennas.
Sketch of the target system of this thesis. Plasmonic antennas are placed in the vicinity of a single NWQD, enhancing its emission rate through the Purcell effect, and providing control over its radiation diagram by tailoring their scattering properties.

Having shown that we can fabricate and characterise plasmonic antennas, we turn to the investigation of the emission properties of semiconducting nanowire quantum dots in chapter 3. We characterised two types of NWQDs based on II-VI semiconducting materials: CdMnTe quantum dots inside ZnTe/ZnMgTe core/shell nanowires, and CdSe QDs inside ZnSe/ZnMgSe core/shell nanowires. We start by a brief reminder of semiconductor optics to set out the important physical ingredients necessary to understand the peculiar emission properties of NWQDs. We then perform microphotoluminescence on a statistical amount of NWQDs, and detail their spectral, temporal, polarisation and directional emission properties. We show that the understanding of the optical properties of these nanoemitters requires multiple characterisations on a single object to determine its electronic and optical properties.

Following the findings of chapter 3, we show in chapter 4 a single NWQD complete study on a Te-based NWQD, revealing for the first time a strain-induced light hole exciton ground state inside a NWQD, using Fourier microscopy combined with magneto-optical spectroscopy and cathodoluminescence. In light of these results, we conclude on the properties of the Te-based NWQDs and extract the relevant information to design the coupled NWQD-antenna structures.

Chapter 5 details the cathodoluminescence-based two step lithography procedure that allows us to deterministically fabricate plasmonic antennas in the near-field of a NWQD. We study the coupling between rectangular antennas supporting a dipolar resonance and Te-based NWQDs, evidencing a fluorescence enhancement factor up to 2.5 due to radiative coupling between the QD and the antenna.

Finally, we conclude on the coupling between plasmonic nanoantennas and NWQDs. We propose several improvements to the systems, and show that our fabrication process is not limited to fluorescence enhancement of NWQDs, as it has also been extended to the fabrication of hybrid structures for the study of non-linear optical processes at the single nanoparticle level.

Chapter 1

Plasmonics: Fundamentals

Résumé en Français

Ce chapitre sert d'introduction à la plasmonique. Prenant pour point de départ les équations de Maxwell (1.1a)-(1.1d)*, on met en lumière le rôle de la fonction de permittivité électrique d'un matériau pour décrire son interaction avec la lumière. On présente le modèle de Drude, dans lequel la réponse des métaux est assimilée à celle des électrons de conduction, modélisés comme un gaz d'électrons libres. On compare ce modèle à la réponse de métaux réels. Les désaccords sont traités dans un second temps, en introduisant la notion de structure de bande. Le point fondamental de cette partie est la description des transitions interbandes, qui limitent l'utilisation des métaux à certaines plages de fréquences.*

On décrit ensuite les conditions nécessaires à l'existence de plasmons polaritons de surface (SPPs), qui sont des ondes transverses magnétiques à l'interface entre un métal et un diélectrique. La plus fondamentale de leur caractéristique, leur relation de dispersion, est discutée dans le cadre d'un métal de Drude (figure 1.4) et de métaux réels (figure 1.5). On s'attache ensuite à décrire une procédure numérique pour calculer les modes de plasmons soutenus par des milieux multi-couches. Cette procédure est appliquée dans le cas de 3 interfaces, alternant isolant-métal-isolant-métal (IMIM) comme présenté en figure 1.6. Ils sont d'une grande importance pour la suite de ce manuscrit, car ils correspondent à la configuration expérimentale nécessaire à l'étude des émetteurs que nous voulons in fine coupler aux antennes plasmoniques. Dans le cas où la couche d'isolant entre les deux couches métallique est fine, le confinement du champ électromagnétique présente une structure intéressante qui sera utilisée dans le chapitre 2. Les résultats numériques sur les plasmons IMIM montrent l'existence de deux profils de champ, nommés symétrique et antisymétrique, localisés respectivement à l'intérieur de la couche isolante intermédiaire ou à la surface supérieure du métal (figure 1.8).

Enfin, on introduit les résonances de plasmons de surface supportées par des particules métalliques. A la différence des plasmons polaritons, ces plasmons de surfaces sont dit localisés (LSPs). Partant du cas de sphères métalliques dans l'approximation quasi-statique, on discute de l'influence du métal constituant la particule, de son milieu environnant et de sa taille. On présente ensuite le cas de particules sphéroïdales pour mettre en avant l'effet de la forme. Dans ce cas, la dégénérescence des modes de plasmons est levée et le facteur de forme d'une particule permet de modifier l'énergie des modes qu'elle supporte. On introduit enfin des corrections pour dépasser l'approximation quasi-statique et se rapprocher du cas de particules réelles.

Introduction

As semiconductor optics progresses, electronic carrier confinement appears as a fundamental requirement for solid-state light emission. Localised sources of light such as semiconducting quantum dots or nitrogen vacancy centers in diamond are emerging, urging the need for probing and controlling their electromagnetic environment on a sub-diffraction limited scale. Indeed, efficiently addressing such elements requires an interface between the far-field domain, on a macroscopic scale, and the nanoscopic scale. A possible answer to this challenge resides in the use of metals as optical materials. Through collective oscillation of their conduction electrons, they can confine light below the diffraction limit, providing a way to access optically access nanometric scales.

The starting point of this chapter is a thus description of the propagation of light and its interaction with metals. As conventional optics textbooks often deal with the propagation of electromagnetic fields in dielectric media only, we start be a brief introduction on the electromagnetic properties of metals at optical frequencies. We first present the Drude model which describes the interaction of free electrons in metals with an electromagnetic field, and serves as a simple model to discuss light-metal interactions. We then enter more into the details of the physical origin of metals properties by discussing their band structure, which governs the motion of their conduction electrons. We then show how the peculiar interaction between light and metals allows for the propagation of surface waves called SPPs, and how to predict their properties in stratified media corresponding to our experimental configurations. We finally describe the behaviour of these surface waves when occurring at the surface of metallic nanoparticles, resulting in the so-called localized surface plasmons (LSPs). We especially apply the physical concepts developed in this section to the main materials we used in this work: two metals, gold (Au) and aluminium (Al), and aluminium oxide (or alumina, Al_2O_3) when a dielectric medium is necessary.

1.1 Electromagnetic properties of metals

The aim of this first section is to set out the electromagnetic properties of metals at optical frequencies. It starts by a brief reminder of Maxwell's theory of electromagnetism, and provides a description for the interaction between light and metals. This interaction is governed by their electronic structure, and enclosed in their electric permittivity. Two contributions can be separated: the oscillations of free electrons, and interband transitions. We first derive the contribution of free electrons to this permittivity following the Drude model, which describes them as a free electron gas. Discrepancies between the experimentally measured permittivities and the Drude model arise as it does not take into account the full electronic structures of metals. We thus briefly introduce their energy band structure, and notably discuss the effect of electronic transitions from one band to an other (interband transitions). This section is greatly inspired from Stefan Maier's book [Mai07], which is an excellent introduction textbook to the field.

1.1.1 Maxwell's equations and basic relations

Most of the interaction between light and metals at optical frequencies is classically understood within the frame of Maxwell's electromagnetic theory. We thus start by recalling Maxwell's equations in a homogeneous medium:

$$\nabla \cdot \mathbf{D}(\mathbf{r},t) = \rho_{ext}(\mathbf{r},t) \tag{1.1a}$$
$$\nabla \cdot \mathbf{B}(\mathbf{r},t) = 0 \tag{1.1b}$$
$$\nabla \times \mathbf{E}(\mathbf{r},t) = -\frac{\partial \mathbf{B}(\mathbf{r},t)}{\partial t} \tag{1.1c}$$
$$\nabla \times \mathbf{H}(\mathbf{r},t) = \frac{\partial \mathbf{D}(\mathbf{r},t)}{\partial t} + \mathbf{J_{ext}}(\mathbf{r},t). \tag{1.1d}$$

where the four fields are linked by the constitutive relations:

$$\mathbf{D}(\mathbf{r},t) = \varepsilon_0 \mathbf{E}(\mathbf{r},t) + \mathbf{P}(\mathbf{r},t) \tag{1.2a}$$
$$\mathbf{H}(\mathbf{r},t) = \frac{1}{\mu_0}\mathbf{B}(\mathbf{r},t) - \mathbf{M}(\mathbf{r},t). \tag{1.2b}$$

$\mathbf{D}$, $\mathbf{B}$, $\mathbf{E}$ and $\mathbf{H}$ are respectively the electric displacement, magnetic induction, electric and magnetic fields. The total charges and current densities (ρ_{tot} and $\mathbf{J_{tot}}$ respectively) are decomposed into external (ρ_{ext}, $\mathbf{J_{ext}}$) and internal ($\rho_{int}, \mathbf{J_{int}}$) sets such that $\rho_{tot} = \rho_{int} + \rho_{ext}$ and $\mathbf{J_{tot}} = \mathbf{J_{int}} + \mathbf{J_{ext}}$. The external set corresponds to driving terms, or excitations, while the internal set encompasses the medium's response. The four macroscopic fields are linked to the medium response through the polarization $\mathbf{P}$ and the magnetization $\mathbf{M}$. The polarization $\mathbf{P}$ represents the medium's electric dipole moment per unit volume, and is thus related to the internal charges and current densities through:

$$\left.\begin{aligned} \nabla \cdot \mathbf{P} &= -\rho_{int} \\ \nabla \cdot \mathbf{J_{int}} &= -\frac{\partial \rho_{int}}{\partial t} \end{aligned}\right\} \Rightarrow \mathbf{J_{int}} = \frac{\partial \mathbf{P}}{\partial t}. \tag{1.3}$$

In the case of an instantaneous, linear response from an isotropic medium, e.g. in presence of small field intensities, we have:

$$\mathbf{D} = \varepsilon_0 \varepsilon \mathbf{E} \tag{1.4a}$$
$$\mathbf{B} = \mu_0 \mu \mathbf{H} \tag{1.4b}$$
$$\mathbf{J_{int}} = \sigma \mathbf{E} \tag{1.4c}$$

where ε_0 and ε are the vacuum and medium relative permittivity respectively, μ_0 and μ the magnetic vacuum and medium relative permeability and σ the material conductivity. As we do not consider magnetic excitation of metals we will neglect their magnetic response for the rest of this manuscript, setting $\mu = 1$. We are thus especially interested in a description of the *metal permittivity ε, which directly encompasses its response to an electromagnetic excitation.*

Derivation of the complex electric permittivity

In a medium free of external excitation ($\rho_{ext} = \mathbf{J_{ext}} = 0$), using the Fourier transform with respect to $\int dt\mathbf{dr}e^{i(\mathbf{k}\,\cdot\,\mathbf{r}-\omega t)}$ and combining equations (1.1a)-(1.1d) and the constitutive relations (1.4a)-(1.4c) yields the wave equation in time and momentum-frequency space:

$$\nabla \times \nabla \times \mathbf{E} = -\mu_0 \frac{\partial^2 \mathbf{D}}{\partial t^2} \tag{1.5a}$$

$$\implies \mathbf{k}\,(\mathbf{k}\,\cdot\,\mathbf{E}) - k^2\mathbf{E} = -\varepsilon\,(\mathbf{k},\omega)\,.\frac{\omega^2}{c^2}\mathbf{E} \tag{1.5b}$$

where the fields are decomposed into plane waves of wave vectors $\mathbf{k}$ and angular frequency ω. Using equation (1.3) we have identified the total electric permittivity to:

$$\varepsilon\,(\mathbf{k},\omega) = 1 + \frac{i\sigma\,(\mathbf{k},\omega)}{\varepsilon_0\omega} \tag{1.6}$$

At visible frequencies, the wavelength of light is longer than the metallic unit cell (4.08 Å for Au) and the electron mean free path (≈ 10 nm). This leads to a further simplification of the permittivity function, where we assume a spatially local response of the material in which the conductivity is taken as $\sigma\,(\mathbf{k},\omega) = \sigma\,(\mathbf{k}=0,\omega) = \sigma\,(\omega)$. Consequently, the wave vector dependence in ε is also omitted.

This expression of the permittivity gathers two opposite sides of the electromagnetic theory, as ε is usually used to describe the polarization response of a medium to an excitation, i.e. the effect of a driving field on bound electrons through the polarisation $\mathbf{P}$, while σ usually describes the motion of free electrons in a current $\mathbf{J_{int}}$. A first important point to notice is that, for non-zero conductivity, the electric permittivity of the material is a *complex quantity*. In order to evaluate the behaviour of this complex permittivity function with respect to frequency, one needs to find a description for σ. The Drude model presented thereafter is commonly used, as it describes well the response of the conduction electrons in metals, which governs most of their interaction with light.

1.1.2 The electric permittivity of a free electron gas

The metal is modelled as a free electron plasma moving inside a fixed cation frame. Assuming that we can describe the electrons oscillations in response to an electric field $\mathbf{E}$ as damped mechanical oscillators of mass m and charge $-\bar{e}$, where the damping coefficient γ represents the frequency at which free electrons experience collisions to the immobile cores, other electrons and phonons, the one-dimensional law of motion reads:

$$m\ddot{x} + m\gamma\dot{x} = -\bar{e}\mathbf{E}. \tag{1.7}$$

Assuming an harmonic response yields:

$$x\,(t) = \frac{\bar{e}/m}{\omega^2 + i\gamma\omega}\mathbf{E}\,(t)\,. \tag{1.8}$$

Introducing the macroscopic polarization $\mathbf{P} = -n\bar{e}x$ from equation (1.3), where n is the electron density, and inserting this back into (1.4a), we arrive at the final result of this section, the complex electric permittivity function of Drude metals:

$$\boxed{\varepsilon(\omega) = 1 - \frac{\omega_p^2}{\omega^2 + i\gamma\omega}} \tag{1.9}$$

where we define the plasma frequency of the metal $\omega_p = \frac{n\bar{e}^2}{\varepsilon_0 m}$. ω_p is the frequency of the collective oscillations of the free electrons in the medium [see further, figure 1.4 (b)]. This oscillation is thus a polarisation wave inside the medium.

Two main frequency regimes have to be distinguished, whether one considers optical frequencies ω above or below the plasma frequency ω_p of the metal. Below the plasma frequency, metals retain their metallic character: they reflect electromagnetic radiation, and no propagating wave exists inside the metal. Above this frequency, they can support propagating electromagnetic waves. We restrict our analysis to frequencies *below* the plasma frequency of each material, i.e. in a regime where metals do not support 3D propagating waves.

The Drude model and real metals: two examples

The real (ε_1) and imaginary (ε_2) parts of the electric permittivity of gold (Au) and aluminium (Al) have been experimentally measured. The results are presented in figure 1.1, and fitted using a Drude model. The main feature of these materials permittivity is that *the real part is negative* over a large spectral range, from the IR to the middle of the visible spectrum for Au, and to the ultra-violet (UV) for Al. This property is of fundamental importance, and strikingly differs from the case of semiconductors for which the dielectric function has a positive real part. Its implication will be discussed in section 1.2.1. The second important feature is the high value of ε_2, which is related to losses in the medium. As a comparison, ε_2 in semiconductors is commonly below 10 outside of the absorption resonant frequencies. Metals are thus intrinsically lossy optical materials. These losses come from two main contributions: intraband phenomena within the conduction band like electron-electron and electron-phonon interaction, and interband phenomena when an electron is promoted from the conduction band to a higher energy band in the material.

As it describes only free electrons, the Drude model does not account for these interband transitions. Thus, discrepancies can be seen between the experimental data and Drude fits in figure 1.1 below 500 nm (above 2.6 eV) for Au, and around 800 nm (around 1.2 eV) for Al. The contribution of interband transitions to ε_2 is very broad in the case of Au, while it is much narrower for aluminium.

To account for interband transitions, corrections to this model were first implemented as bound oscillators with one resonant frequency per transition, adding restoring forces terms to equation (1.7). This leads to Lorentz oscillator-like behaviour of the permittivity function ([BH83; Via+05]). More refined methods like the critical points model are now used in numerical procedures [Via07], better describing asymmetric lineshapes of some interband transitions. These transitions are well understood in the frame of the theory of band structure which is presented in the next section.

It is important to stress that, as demonstrated by the Drude mode, the treatment of *free* charges is mandatory to account for the observed values of ε for conducting materials. Solely

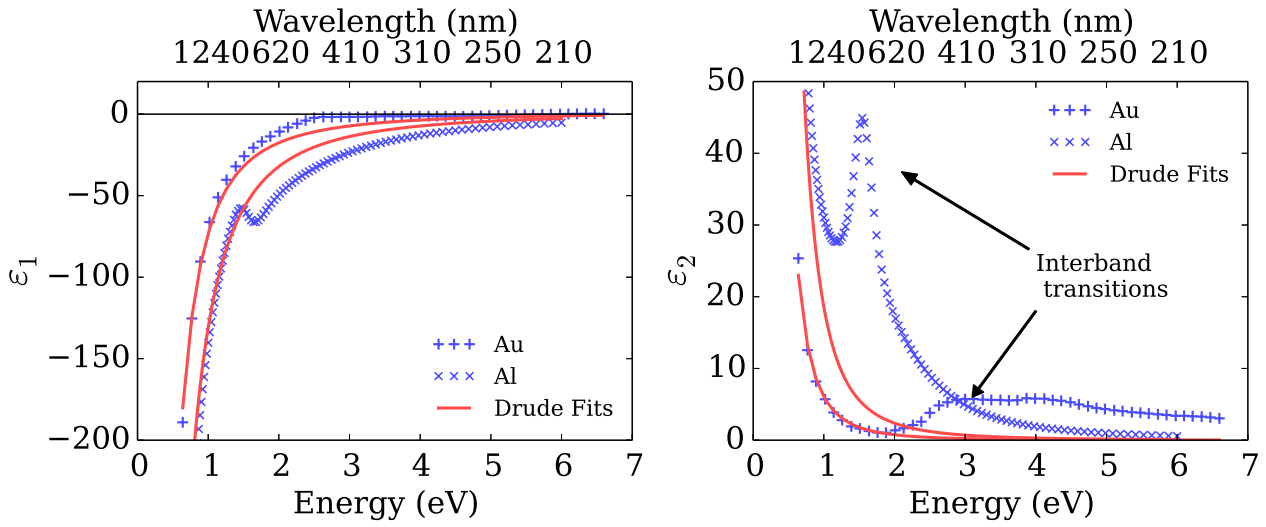

Figure 1.1 – Au and Al electric permittivities.
Real (right panel) and imaginary (left panel) parts of the electric permittivity of Au (blue "+" signs) and Al (blue "×" signs), with Drude fits (red solid lines). Au data are taken from [JC72], and Al data from [Rak95].

modelling the medium response by elastically bound electrons, as is commonly made in semiconductor optics textbooks only leads to a Lorentzian profile of the permittivity function. Despite the efficiency of all the aforementioned models, *the simulations in this work have been carried out by interpolating the experimental data ([JC72; Rak95]).*

Finally, the complex refractive index $\tilde{n} = n + i\kappa$ of the material is often a preferred quantity to the permittivity, and is defined as $\tilde{n} = \sqrt{\varepsilon}$:

$$n^2 = \frac{\varepsilon_1}{2} + \frac{1}{2}\sqrt{\varepsilon_1^2 + \varepsilon_2^2} \tag{1.10a}$$

$$\kappa^2 = \frac{\varepsilon_2^2}{2} + \frac{4}{n^2} \tag{1.10b}$$

$$\varepsilon_1 = n^2 - \kappa^2 \tag{1.10c}$$

$$\varepsilon_2 = 2n\kappa. \tag{1.10d}$$

As commonly used in semiconductor optics, n is linked to the refractive behaviour of the material, while κ is related to its absorption.

1.1.3 The band structure of metals

The electronic properties of metals and their interaction with light can be described in a more refined approach by considering the band structure of the materials. This theory was initially developed to describe the motion of electrons in periodic crystals, and a short introduction in the case of semiconductors can be found in section 3.1.1. The scope of this theory is to derive the states available to the metal electrons from the atomic orbitals of the atoms constituting

the material by an explicit calculation of the spatial dispersion and energy of these states. Due to the large number of atoms, these states form continuums of energy levels with well defined spatial properties, called bands, that govern the motion of the electrons. The band spatial dispersion is linked to the electron effective mass through:

$$\frac{1}{m^*} = \hbar^{-2}\frac{\partial^2 E}{\partial \mathbf{q}^2} \tag{1.11}$$

where $\mathbf{q}$ is the electron wave vector, E its energy and m^* its effective mass, assuming an isotropic material. This effective mass should be used instead of the electron rest mass to calculate the plasma frequency in the Drude model. Its dependence in electronic wave vector is crucial to understand the interband phenomena in metals.

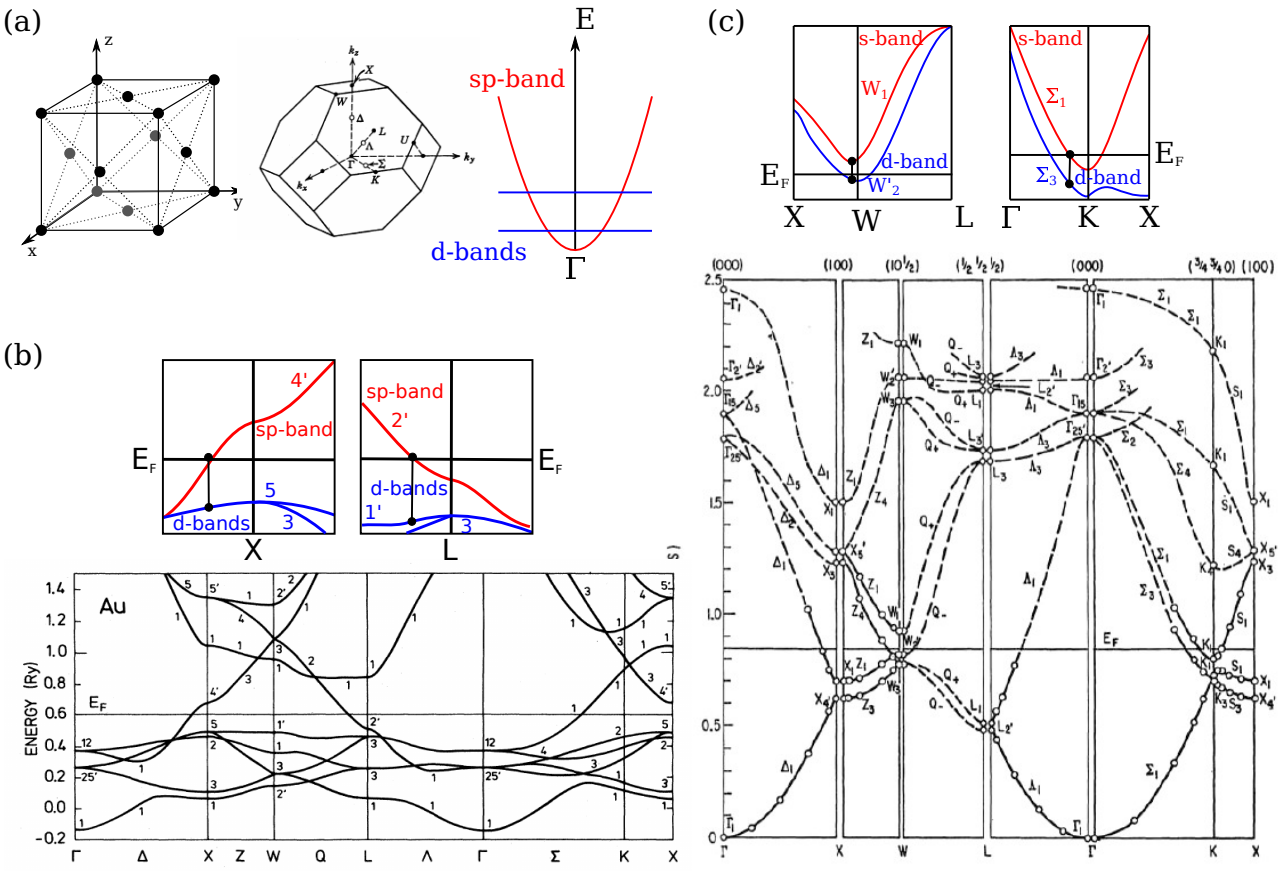

Figure 1.2 – Au and Al band structure.
(a) Face-centred cubic system and its first Brillouin zone, and a schematic of the core electrons d-band and the conduction electrons sp-band around the Γ point. (b),(c) Band structure of Au and Al, adapted from [JGM81] and [EPS63] respectively. The insets show zooms on the regions of interest in the band diagrams, where interband transitions occur. The red bands indicate partially occupied (valence) bands, and blue bands indicate fully occupied (conduction) bands.

Like most metals, Au and Al crystallise in a face-centered-cubic system ([PSL65; FQ33]). The cubic system, its first Brillouin zone and Au and Al band structures are presented in figure

1.2 (from [JGM81] and [EPS63] for Au and Al respectively). The energy of the last occupied state is indicated by the Fermi energy E_f. By analogy with semiconductors, the *last fully occupied* band will be referred to as the valence band, while the *first non-fully occupied* band will be referred to as the conduction band.

In the case of noble metals like Au, the valence band results mainly from d atomic orbitals and has a rather flat dispersion, while the conduction band results from the $s-p$ hybridised orbitals and has a characteristic parabolic dispersion. The d-bands and the sp-band dispersion around the center of the Brillouin zone are sketched in figure 1.2 (a). Further hybridisation between the d and $s-p$ orbitals has to be taken into account in the band calculation, but the valence and conduction bands are often still referred to as d and sp bands respectively [JGM81]. The result of a rigorous band structure calculation accounting for sp-d hybridisation in the case of Au is presented in figure 1.2 (b). Interbands transitions are more likely to occur when the energy gap between two bands on each side of the Fermi level is minimal. A zoom on such points, X and L, is presented in figure 1.2 (b) for the Au band structure. Because the d band dispersion is so small, possible interband transition are spread in energy, resulting in broad interband transitions responsible for the visible photoemission from Au (from 500 nm (2.6 eV), $5 \rightarrow 4'$ and $1' \rightarrow 2'$). Other phenomena also contribute to emission from gold through intraband transitions, which are usually forbidden [BBN03].

On the contrary, energy bands near the Fermi level in Al result from d-like (occupied) and s-like (vacant) bands. A zoom on the W and K points is provided in figure 1.2 (c). Near these points the energy bands exhibit a highly regular behaviour with an almost parabolic dispersion. Interband transitions can occur between the W_2' and the W_1 bands or between the Σ_3 and Σ_1 parallel bands. As the bands are parallel and with a quasi-parabolic dispersion this interband transition is much sharper than in the case of Au, and occurs around 800 nm (1.5 eV) as stated previously [GG14].

A last difference between Al and Au lies in the number of free electrons per atom, Al having 3 conduction electrons per atom as opposite to one for Au. Added to the higher value of ω_p for Al than for Au, this makes aluminium a better "Drude-like" metal in the visible spectral range.

1.2 Surface Plasmon Polaritons

1.2.1 A surface wave

With the optical properties of metals in mind, we can now start to consider the response of a bulk metallic material to an electromagnetic excitation. The wave equation for the electric field in an isotropic homogeneous medium reads:

$$\mathbf{k}\left(\mathbf{k}\cdot\mathbf{E}\right)-k^2\mathbf{E}=-\varepsilon\left(\mathbf{k},\omega\right)\frac{\omega^2}{c^2}\mathbf{E}. \tag{1.5b}$$

Two sets of waves can arise from this equation.

Longitudinal waves are characterised by:

$$\mathbf{k}\cdot\mathbf{E}=kE \tag{1.12}$$

so the left-hand side of equation (1.5b) is zero and the non trivial solution requires:

$$\varepsilon\left(\mathbf{k},\omega\right)=0 \tag{1.13}$$

which means that they can only occur at frequencies where the electric permittivity becomes null. Their dispersion relation thus reads:

$$\omega^2 = \omega_p^2 + k^2 c^2. \tag{1.14}$$

As the right-hand side of (1.14) is always greater than ω_p, such oscillations can only occur in a spectral range that will no be covered in this manuscript. They are referred to as *bulk plasmons*, and consist of collective in-phase oscillation of the whole conduction electron cloud of the material.

On the contrary, transverse waves follow:

$$\mathbf{k} \cdot \mathbf{E} = 0 \tag{1.15}$$

leading to the classical dispersion relation:

$$k^2 = \varepsilon(\mathbf{k}, \omega) \frac{\omega^2}{c^2}. \tag{1.16}$$

As $\mathrm{Im}\{\varepsilon\} \neq 0$, transverse waves in metals are subject to an exponential decay. Considering that we are interested only in the interaction of such transverse electromagnetic waves and metals, with frequencies lower than the metal plasma frequency, interfacing propagating photons and metals necessarily involves a metallic interface. Let us consider the geometry depicted in figure 1.3 of a semi-infinite dielectric medium of permittivity ε_d in the upper half-space and a metal of refractive index ε_m in the lower half-space.

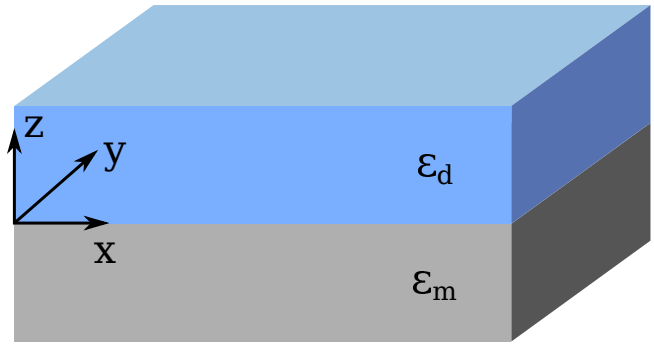

Figure 1.3 – Coordinate system for SPP derivation.
Sketch of the two infinite half-spaces used for the derivation of surface plasmon polaritons.

Starting from the wave equation in time domain:

$$\nabla \times \nabla \times \mathbf{E} = -\mu_0 \frac{\partial^2 \mathbf{D}}{\partial t^2} \tag{1.5a}$$

and assuming a harmonic dependence, invariance along the y axis and transverse plane wave propagation along the x axis, we can insert the ansatz solution $\mathbf{E}(\mathbf{r}, t) = \mathbf{E}(z)\, \mathrm{e}^{i(k_x x - \omega t)}$ into equation (1.5a) to solve into each semi-infinite medium, yielding:

$$\frac{\partial^2 \mathbf{E}(z)}{\partial z^2} + \left({k_0}^2 \varepsilon - k_x^2\right) \mathbf{E} = 0 \tag{1.17}$$

where k_0 is the free-space wave vector, and we now omit the possible explicit frequency dependence of ε.

Inserting the ansatz into the curl equations (1.1c)-(1.1d) and differentiating between TE ($\mathbf{E} = (0, E_y, 0)$) and TM ($\mathbf{H} = (0, H_y, 0)$) modes in each medium gives:

TM polarisation mode:

$$E_x = \frac{-i}{\omega\varepsilon_0\varepsilon}\frac{\partial H_y}{\partial z} \tag{1.18a}$$

$$E_z = -\frac{k_x}{\omega\varepsilon_0\varepsilon}H_y \tag{1.18b}$$

$$\frac{\partial^2 H_y}{\partial z^2} + \left(k_0^2\varepsilon - k_x^2\right)H_y = 0 \tag{1.18c}$$

TE polarisation mode:

$$H_x = \frac{i}{\omega\mu_0}\frac{\partial E_y}{\partial z} \tag{1.19a}$$

$$E_z = \frac{k_x}{\omega\mu_0}E_y \tag{1.19b}$$

$$\frac{\partial^2 E_y}{\partial z^2} + \left(k_0^2\varepsilon - k_x^2\right)E_y = 0. \tag{1.19c}$$

These sets of equations can be solved in each half-space, with field amplitudes $A_{i=m,d}$ and wave vectors

$$k_{i=m,d}^2 = k_0^2\varepsilon_{i=m,d} = k_{x,i}^2 + k_{z,i}^2. \tag{1.20}$$

Here it is important to remember that in the case of metals, $\varepsilon_1 < 0$. If we consider ideal lossless materials ($\varepsilon_2 = 0$), this implies that $k_m^2 < 0$. Restricting the analysis to waves confined to the surface and propagating along the positive x direction imposes that k_x is real and positive, and thus k_z is purely imaginary, leading to the expression $A_i e^{ik_{x,i}x} e^{\pm \mathrm{Im}\{k_{z,i}\}z}$, where the sign in front of the $\mathrm{Im}\{k_{z,i}\}$ term ensures an exponential decay along the z direction.

Continuity of the tangential components of $\mathbf{H}, \mathbf{E}$ and of the normal component of $\mathbf{D}$ at the $z = 0$ plane have to be ensured. Simple but careful manipulation yields:

TM polarisation mode:

$$\frac{\mathrm{Im}\{k_{z,d}\}}{\varepsilon_d} = -\frac{\mathrm{Im}\{k_{z,m}\}}{\varepsilon_m} \tag{1.21}$$

TE polarisation mode:

$$A_m\left(\mathrm{Im}\{k_{z,d}\} + \mathrm{Im}\{k_{z,m}\}\right) = 0 \tag{1.22}$$

With our choice of conventions, confinement to the surface thus requires $\mathrm{Im}\{k_{z,i}\} > 0$. In this case, the condition for TM modes is easily fulfilled: $\mathrm{Re}\{\varepsilon_d > 0\}$, and $\mathrm{Re}\{\varepsilon_m\} < 0$ over a broad range of frequencies for conductors as demonstrated in the previous section. However, the TE continuity condition subsequently requires $A_m = 0$, meaning that no surface mode is supported for TE polarization. The supported surface waves are called surface plasmon polaritons, they are *TM polarised electromagnetic waves caused by the collective and coherent oscillation of conduction electrons at a metal/dielectric interface.* Gathering equations (1.20) and (1.21) gives:

$$k_{x,m}^2 = k_0^2\varepsilon_m - \mathrm{Im}\{k_{z,m}\}^2 \tag{1.23a}$$

$$k_{x,d}^2 = k_0^2\varepsilon_d - \mathrm{Im}\{k_{z,d}\}^2 \tag{1.23b}$$

$$\frac{\mathrm{Im}\{k_{z,m}\}}{\mathrm{Im}\{k_{z,d}\}} = \frac{\varepsilon_d}{\varepsilon_m}. \tag{1.23c}$$

As the continuity of the field across the interface requires $k_{x,m} = k_{x,d}$ we can derive the main

and final result of this section, the surface plasmon polariton dispersion relation:

$$\boxed{k_{spp} = k_{x,m} = k_{x,d} = k_0\sqrt{\frac{\varepsilon_d\varepsilon_m}{\varepsilon_d + \varepsilon_m}}} \tag{1.24}$$

where k_{spp} is the surface plasmon in-plane wave vector.

1.2.2 A closer look on the dispersion relation

The case of a Drude metal

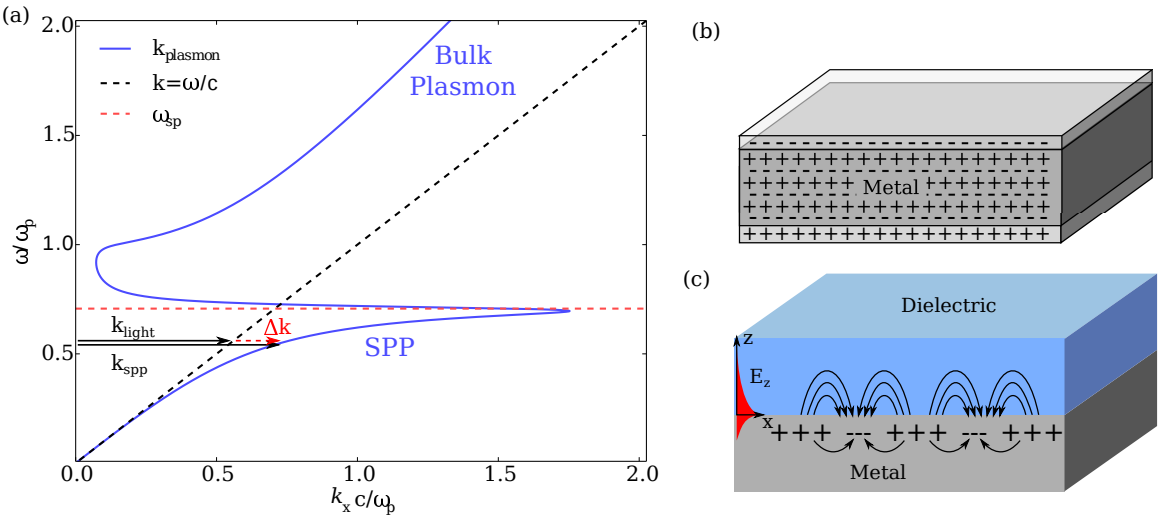

Figure 1.4 – Dispersion relation of a Drude metal: bulk and surface plasmons.
(a) Dispersion relation at the interface of a Drude metal and air (blue solid line), with the photonic dispersion relation in air $k = \omega/c$ (black dashed line) and the surface plasmon frequency ω_{sp} (red dashed line), normalised by the metal plasma frequency ω_p. (b) and (c) representation of a bulk plasmon travelling along the z axis, and a surface plasmon polariton travelling along the x axis, respectively.

We now investigate the surface plasmon polaritons properties through their dispersion relation (1.24). To illustrate the different regimes, we report in figure 1.4 (a) the classical dispersion relation for photons in air $k = \omega/c$ (black dashed lines), as well as the dispersion relation (1.24) at the interface between a Drude metal (blue solid line) and air, with all quantities normalised to the metal plasma frequency ω_p. k_s designates the in-plane wave vector at the interface.

The photonic dispersion relation defines two half-spaces. To the right of the light line, no photon can propagate in the medium as it would require an in-plane wave vector larger than the largest allowed wave vector k, leading to the so-called forbidden light space. On the contrary, photons can propagate with an arbitrary wave vector to the left of this light line, often referred to as the light cone.

For low energies the blue solid line asymptotically follows the light line, but then quickly deviates towards larger wave vectors and then asymptotically follows a horizontal line at the

surface plasmon frequency (red dashed line). This occurs when:

$$\varepsilon_m(\omega) + \varepsilon_d = 0 \tag{1.25}$$

which is known as the surface plasmon resonance (SPR) condition, and results in a surface plasmon frequency:

$$\omega_{sp} = \frac{\omega_p}{\sqrt{1+\varepsilon_d}} \tag{1.26}$$

in the case of a Drude metal. Below this frequency, the wave is a surface plasmon polariton, i.e. a mixed state of light and matter. At the surface plasmon frequency it consists in a pure surface charge density wave: the surface plasmon. The fact that k_{spp} is greater than the photon wave vector in the dielectric means that SPPs cannot be excited by direct irradiation of a metallic surface. An additional momentum kick Δk is required, as shown by the arrows in the graph. The red dashed arrow represents this additional momentum, and we will see a bit later how it can be obtained.

Between ω_{sp} and ω_p the wave is a leaky surface wave that is poorly bound to the surface and partly radiates into the media as the imaginary part of ε_m leads to a non-zero real part of the wave vector. Finally, above ω_p we retrieve the fact that the metal can support propagating electromagnetic waves, the bulk plasmons.

Figure 1.4 (b)-(c) illustrates the difference between bulk plasmons and SPPs respectively. As detailed previously, bulk plasmons are collective oscillations of the whole conduction electron cloud of the medium, while SPPs are coherent oscillation of surface conduction electrons. They are bound to the surface and decay exponentially along the z direction.

The case of real metal

We now show the implication of the dispersion relation for real metals and dielectric host media, as they will be used later on in this work. As ε_m is a complex quantity, so is k_{spp}, implying that SPPs are inherently lossy waves that decay exponentially along their propagation direction. Their characteristic propagation length is defined as:

$$L_{spp} = \frac{1}{2\,\mathrm{Im}\{k_{spp}\}} \tag{1.27}$$

and typically ranges from 10 nm to a few microns. Consequently, surface plasmons can be laterally confined in plasmonic cavities if the metal geometry is engineered such as its in-plane size is of the order of L_{spp}. In addition, the z-component of the total wave vector $\mathbf{k_i}$ is purely imaginary. The surface plasmon field intensity thus decays exponentially in the direction perpendicular to the dielectric-metal interface over a characteristic length $L_{z,i}$ in each medium $i = m, d$:

$$L_{z,i} = \frac{1}{2\,\mathrm{Im}\{k_{z,i}\}}. \tag{1.28}$$

This provides us with an idea of the vertical confinement of the field, i.e. the distance away from the interface over which a significant amount of the field is localised. This distance is naturally small in the metal, but can range between a few nanometers to a few microns inside the dielectric medium. Note that these two definitions explicitly show the trade-off between

field localisation and losses: reducing any of these length inherently requires to increase the imaginary part of the wave vector in the corresponding direction, increasing by the same token the attenuation of the field.

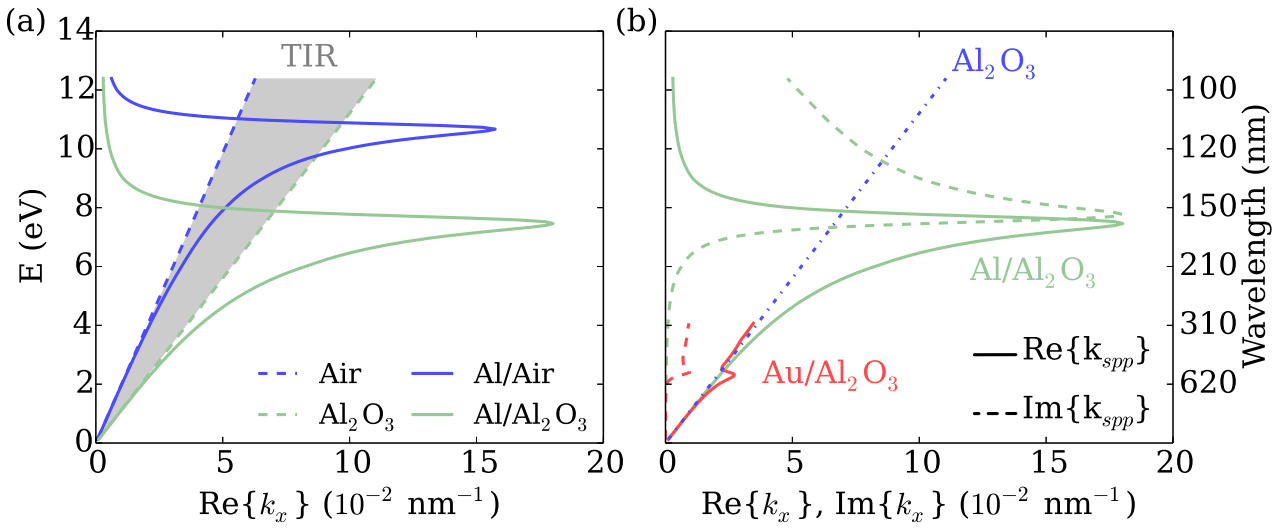

Figure 1.5 – Photonic and plasmonic dispersion relations of different materials. (a) Blue: Photonic dispersion relation in air (dashed line), and SPP dispersion relations at an Al/Air interface using experimental data (solid line). Green: same as blue for Al_2O_3 and Al/Al_2O_3 interface. (b) Blue: photonic dispersion relation in Al_2O_3. Green: real (solid line) and imaginary part (dashed line) of k_{spp} for an Al/Al_2O_3 interface. Red: same as green for a Au/Al_2O_3 interface. The refractive index of Al_2O_3 is taken to be constant ($n = 1.76$) for simplicity. Au data are taken from [JC72] while Al data are from [Rak95]

Several dispersion relations are represented in figure 1.5 (a), where k_x represents the in-plane wave vector. The straight dashed lines represent the photonic dispersion relation $k = \omega n/c$ in air ($n = 1$, blue) and alumina (Al_2O_3, n=1.76, green), each of them defining two light cones. Photons in the grey shaded area have a momentum between the alumina and the air light line, they can thus propagate in alumina but not in air. Such photons propagating in alumina *below* the air light cone experience the well known total internal reflection (TIR) at the alumina/air interface.

The real part of the SPP dispersion relations for an Al/Air interface is plotted in blue solid line in figure 1.5 (a). The finite value of ε_2 from the metal electric permittivity imposes a finite k_{spp} at the surface plasmon frequency, and thus an upper bound on the achievable field localization. Moreover, changing the dielectric environment also modifies the SPP properties. As an example, the relation dispersion at an Al/Al_2O_3 interface is also plotted in figure 1.5 (a) (green solid line). It shows that the surface plasmon red-shifts with increasing dielectric medium permittivity, as the resonant frequency is lower in the Al/Al_2O_3 interface case than in the Al/Air interface case. This demonstrates a simple way to tune the SPP properties, as we see that it is possible to tune the resonant frequency by tuning the dielectric environment around the metal. It can be intuited from the surface plasmon resonance condition (1.25) and the regularity of the real part of the Drude electric permittivity, which monotonically increases with energy, or

equivalently from the surface plasmon frequency for a Drude metal (1.26).

As already pointed out, SPPs cannot be excited by direct irradiation of a metallic surface. However, looking at the dispersion relation for an Al/Air SPP we can see that part of this dispersion relation lies *above* the alumina light line. Thus, the additional momentum kick can be provided to the exciting wave by using total internal reflection from the high refractive index medium. This is used in various usual coupling geometries such as the Kretschmann [KR68] or Otto [Ott68] configurations. Grating [Dev+03] or near-field [Hec+96] coupling are also used regularly. Looking at this dispersion relation, one can also deduce that sub diffraction-limited confinement of the light is possible near this surface plasmon frequency.

The metals parameters also bear great importance in the surface plasmon characteristics. For comparison, figure 1.5 (b) represents real (solid lines) and imaginary (dashed lines) parts of k_{spp} for an Al/Al_2O_3 interface (green) and a Au/Al_2O_3 interface (red). The photon dispersion in alumina is also represented in blue dashed line. It shows that the surface plasmon resonance occurs at a lower energy at the Au interface than for the Al interface. This observation has several origins. It first comes naturally in the model of a Drude metal as $\omega_{p,Au} < \omega_{p,Al}$, and $\omega_{sp,Drude}$ scales with the plasma frequency. The remaining discrepancy comes from the dramatically different imaginary parts of the metals permittivities. The broad interband contribution to ε_2 in the case of Au above 2 eV further shifts the surface plasmon frequency. It is also responsible for the different behaviour of the dispersion relation above the surface plasmon frequency. In the case of Al, the energy gap between ω_{sp} and ω_p is clearly, visible, as ω_p lies higher in energy and no propagating wave is supported in the displayed energy range, while we see that for Au the dispersion relation is rapidly clamped to the photonic dispersion relation in alumina above the surface plasmon energy.

Moreover, at the resonance, $\mathrm{Im}\{k_{spp}\}$ is much smaller for Au than for Al, indicating a less damped propagation of the SPP. This shows the metal used in SPP experiments has to be chosen with respect to the aimed spectral range. We favoured gold for most of our experiments, as it shows very good properties in the wavelength range of the light emission by our semiconducting structures. However, Al bear a great interest for UV plasmonics as it clearly appears in figure 1.5 (b) that it can be used for higher energy excitations than Au.

It also shows that propagation losses of the SPP characterised by $\mathrm{Im}\{k_{spp}\}$ increase extremely rapidly around the SPP frequency, illustrating the permanent trade-off between field localization (high $\mathrm{Re}\{k_{spp}\}$) and propagation losses. This issue can be partly addressed by using excitation energy well below the SPP resonance, as it is clear from figure 1.5 (b) that for decreasing energy, the imaginary part of the SPP wave vector declines more rapidly than its real part.

To get a better grasp on the length scales over which such waves exist, we can calculate the propagation length L_{spp} of a SPP at an Al/Al_2O_3 interface near and away from the SPP resonance. Around $E_{sp} = 7.4$ eV, $\lambda_0 = 167$ nm one finds a propagation length of 6 nm, while away from the resonance, e.g. for $E = 3.3$ eV, $\lambda_0 = 380$ nm the propagation length increases to 950 nm. It is clear that around the plasmon resonance a huge confinement is achievable, but at the expense of reducing the SPP propagation length by orders of magnitude.

1.2.3 Multilayer Systems

In practical geometries, one often has to deal with multiple layers of materials, and not only two semi-infinite subspaces. The 3 layers system is widely known and has been thoroughly studied (see [Mai07] and references therein, e.g. [Sar81; BST86; PVM91]) with metal-insulator-metal (MIM) and insulator-metal-insulator (IMI) geometries. An analytical set of solutions exists in these cases, even for non-symmetrical structures, leading to a splitting of the SPP dispersion relation into the so-called "long range" and "short range" SPPs. Long range SPPs are poorly confined and leak into the upper dielectric medium in the case of the IMI structure, while on the other hand short range SPPs are extremely confined inside the sandwiched material, but experience greater ohmic losses. These modes are further discriminated by their transverse (vertical) symmetry, and will help us understand the results found in more complex media.

Most of the plasmonics-related work in this thesis will concern Insulator-Metal-Insulator-Metal (IMIM) geometry, as depicted in figure 1.6. The top insulating layer is air, while the middle dielectric spacer is aluminium oxide. The metals can be either aluminium or gold. Unlike the aforementioned IMI and MIM, such complicated structures require a numerical evaluation of the dispersion relation and fields. We first introduce the theoretical elements allowing the derivation of the supported SPP modes in arbitrary stratified media, and then discuss its numerical implementation and the results introducing further work on the IMIM structure.

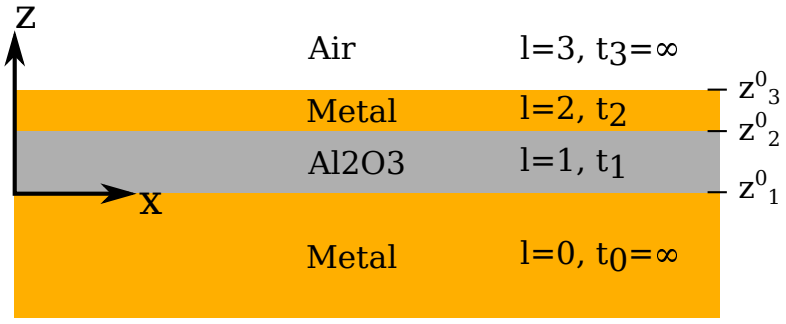

Figure 1.6 – IMIM multilayer system.
Geometrical conventions for the derivation of SPP modes in a IMIM multi-layer system.

SPP in stratified media

The theoretical work used in the computation of multi-layer SPP modes has been taken from [Dav09]. It relies on a matrix formulation for multi-layer media, using the upward and downward field amplitudes as a basis [BW99]. We aim at decomposing the fields into eigenmodes of the multi-layer system. A typical geometry for the derivation is pictured in figure 1.6, where layers are numbered from $l = 0$ (substrate) to $l = 3$ (air), and have a thickness t_i. We assume again a harmonic time dependence $e^{-i\omega t}$, and since we are interested in positive x-direction travelling waves, a spatial $e^{i\alpha_n x}$ dependence. Here, α_n is the propagation wave vector of the n-th eigenmode. We can thus rewrite the curl equations (1.1c)-(1.1d):

$$\nabla \times \mathbf{E}(\mathbf{r},\omega) - ik_0 \mathbf{H}(\mathbf{r},\omega) = 0 \tag{1.29a}$$

$$\nabla \times \mathbf{H}(\mathbf{r},\omega) + ik_0 \varepsilon \mathbf{E}(\mathbf{r},\omega) = 0 \tag{1.29b}$$

where $\varepsilon = \varepsilon(z,\omega)$ is a piecewise continuous function in the z direction.

Keeping in mind that SPPs are TM-polarised waves, we set the non-zero field components to be E_x, E_z and H_y. As boundary conditions require continuity of the tangential component of the field between layers l and $l+1$, the eigenfunctions are derived for the magnetic field. The electric field components are then retrieved using the curl equations. Combining (1.29a)-(1.29b) yields:

$$\varepsilon(z)\frac{\mathrm{d}}{\mathrm{d}z}\left(\frac{1}{\varepsilon(z)}\frac{\mathrm{d}u_n(z)}{\mathrm{d}z}\right) + \varepsilon(z)\,k_0^2 u_n(z) = \alpha_n^2 u_n(z) \tag{1.30}$$

where u_n is the n-th magnetic field eigenfunction with the associated eigenvalue α_n^2.

u_n is piecewise homogeneous in each layer, and retrieved through the sum over the layers:

$$u_n(z) = \sum_l H_{n,l}^+ \exp\left(i\gamma_{n,l}(z - z_l^0)\right) + H_{n,l}^- \exp\left(-i\gamma_{n,l}\left(z - z_l^0\right)\right) \tag{1.31}$$

where z_l^0 is the location of the lower boundary of layer l. The field is decomposed into upward (amplitude H^+) and downward (amplitude H^-) propagating waves. $\gamma_{n,l}$ is the z-component of the eigenmode total wave vector $\gamma_{n,l}^2 = \varepsilon_l k_0^2 - \alpha_n^2$ in each layer l. Accordingly, the fields are explicitly given by:

$$\mathbf{H}(\mathbf{r},\omega) = \sum_l \left[H_{n,l}^+ \exp\left(i\gamma_{n,l}(z - z_l^0)\right) + H_{n,l}^- \exp\left(-i\gamma_{n,l}(z - z_l^0)\right)\right] \exp(i\alpha_n x)\,\mathbf{y} \tag{1.32a}$$

$$= u_n(z)\exp(i\alpha_n x)\,\mathbf{y} \tag{1.32b}$$

and

$$\mathbf{E}(\mathbf{r},\omega) = \nabla \times \mathbf{H}(\mathbf{r},\omega) \tag{1.33a}$$

$$\begin{aligned} = \quad & \exp(i\alpha_n x)\sum_l \frac{1}{k_0\varepsilon_l} H_{n,l}^+ (i\gamma_{n,l}\mathbf{x} - \alpha_n \mathbf{z}) \exp\left(i\gamma_{n,l}(z - z_l^0)\right) \\ & - \exp(i\alpha_n x)\sum_l \frac{1}{k_0\varepsilon_l} H_{n,l}^- (i\gamma_{n,l}\mathbf{x} + \alpha_n \mathbf{z}) \exp\left(-i\gamma_{n,l}(z - z_l^0)\right). \end{aligned} \tag{1.33b}$$

Continuity condition imposes the matrix equation:

$$\begin{aligned} \begin{pmatrix} H_{n,l+1}^+ \\ H_{n,l+1}^- \end{pmatrix} \quad = \quad & \frac{1}{2}\begin{pmatrix} 1 & \varepsilon_{l+1}/\gamma_{n,l+1} \\ 1 & -\varepsilon_{l+1}/\gamma_{n,l+1} \end{pmatrix} \begin{pmatrix} 1 & 1 \\ \gamma_{n,l}/\varepsilon_l & -\gamma_{n,l}/\varepsilon_l \end{pmatrix} \\ & \times \begin{pmatrix} \exp(i\gamma_{n,l}t_l) & 0 \\ 0 & \exp(-i\gamma_{n,l}t_l) \end{pmatrix} \begin{pmatrix} H_{n,l}^+ \\ H_{n,l}^- \end{pmatrix} \end{aligned} \tag{1.34}$$

and the field in the upper-half space can be deduced from the field in the zeroth medium through recursive application of equation (1.34):

$$\begin{pmatrix} H_{n,3}^+ \\ H_{n,3}^- \end{pmatrix} = \begin{pmatrix} M_{11} & M_{12} \\ M_{21} & M_{22} \end{pmatrix} \begin{pmatrix} H_{n,0}^+ \\ H_{n,0}^- \end{pmatrix} \tag{1.35}$$

It is important to stop here and take a look at equation (1.35). As detailed in section 1.2.2, SPPs have a wave vector that lies outside the light cone, and cannot be accessed by direct

illumination of the structure. Surface plasmon modes are thus the supported modes for which there is no incident field, i.e. $H^+_{n,0} = H^-_{n,3} = 0$. Inserting this back into equation (1.35) gives the relation between the outward propagating fields $H^+_{n,3} = M_{12}H^-_{n,0}$ and the constraint:

$$\boxed{M_{22}H^-_{n,0} = 0 \implies H^-_{n,0} \neq 0, M_{22} = 0,} \tag{1.36}$$

for non-trivial solutions to exist. Equation (1.36) allows to calculate the eigenvalue α_n^2 and thus the set of plasmon modes supported by the structure. One can verify that this condition reduces to the SPP dispersion relation (1.24) in the case of a single interface. More complex systems require numerical evaluation of this condition, which we implemented to derive the surface plasmon modes of our multi-layer structure. The results are discussed in the next section.

IMIM numerical results

Let us consider an example structure where the metal is gold, the top Au layer being 35 nm thick and the alumina spacer being 57 nm thick, as this set of parameters will be greatly investigated later on.

Our approach now differs from the method used in [Dav09], as we are interested in the spectral response of the multilayer system instead of its modal properties at a given energy. We thus need to be able to track a given spatial mode through a broad spectral range. In order to do so, we numerically solve equation (1.36) for each wavelength using a readily python-implemented simplex algorithm [NM65] by minimizing the value of the $M_{22}(\alpha)$ coefficient. The algorithm thus requires an good initial guess, and will then propagate the determined eigenvalue at a given wavelength as the initial guess for the next step. The first set of parameters can be found by plotting the absolute value $|M_{22}(\tilde{n})|$ in the $(n-\kappa) \equiv \frac{1}{k_0}(\mathrm{Re}\{\alpha\} - \mathrm{Im}\{\alpha\})$ plane, i.e. as a function of the real and imaginary parts of the refractive index.

This map is presented in figure 1.7 (a) at a free-space wavelength $\lambda_0 = 525$ nm. One can see two local extrema around $n = 1, \kappa = 0.25$ and $n = 3.5, \kappa = 1.2$ respectively. They correspond to two propagating modes supported by the IMIM structure at this wavelength, and can be used to set an initial value to track their position as a function of energy. Their respective trajectories is represented by the green solid line and red "+" symbols respectively. We will refer to them as *antisymmetric* and *symmetric* modes.

Their corresponding dispersion relation is reported in figure 1.7 (b), where the light line in air and alumina are also plotted for reference. They both present a characteristic SPP dispersion relation, with a resonant frequency $E_{spp} \approx 2.25$ eV. The symmetric mode appears highly confined, displaying a much greater in-plane wave vector than photons in alumina. The antisymmetric mode is almost index-matched to air and closely follows the photonic line in air. In other words, the symmetric mode exhibits a strong polaritonic character, while the antisymmetric mode shows an almost photonic character. The large deviation between the symmetric mode and the alumina light line comes from the high value of the imaginary part of the mode's propagation constant. Conversely, the imaginary part of the propagation constant of the antisymmetric mode and its proximity to the light line make this mode a quasibound mode that will quickly dissipate by evanescent coupling into free-space, or by diffraction due to surface roughness at the top interface.

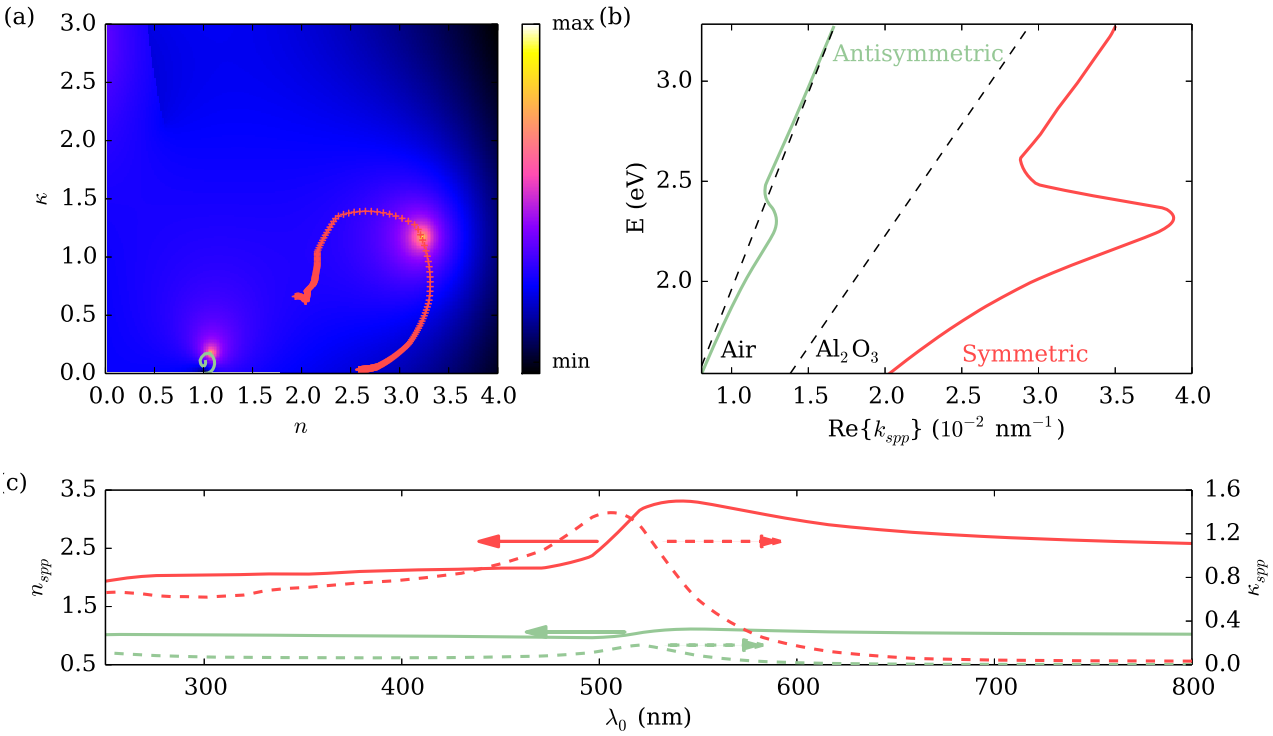

Figure 1.7 – Dispersion of the plasmonic modes of a Au-Al_2O_3-Au-Air system.
(a) Color map of $|M_{22}|/k_0$ in the complex $\tilde{n} = n + i\kappa$ plane at a free space wavelength of 525 nm. The green solid line indicates the dispersion of the antisymmetric mode with frequency, while the red "+" signs show the dispersion of the symmetric mode. (b) Real part of the dispersion relation of the symmetric (red) and antisymmetric modes along with the light line in air and alumina (black). (c) Real (solid lines) and imaginary (dashed lines) parts of the effective refractive indices of the symmetric and antisymmetric modes. Note the different vertical scales. The experimental data are taken from [JC72] (Au), [Rak95] (Al) and [HGK75; Dod86] (Al_2O_3).

Additional information is given in figure 1.7 (c) where the real (solid line) and imaginary (dashed line) parts of the SPP refractive indices are plotted. It shows that below the SPP resonance (i.e. for $\lambda < 505$ nm) both modes experience a rather constant attenuation κ and refractive index n. As already detailed in section 1.2.2, both κ and n then rapidly increase around the SPP resonance, leading to high confinement and losses of the supported mode. Finally, above the surface plasmon resonance wavelength, κ rapidly decreases for both modes while n shows less variations. This demonstrates again that employing energies well below the surface plasmon resonance improves the trade-off between confinement and losses.

Finally, equations (1.32a)-(1.33b) allow us to compute the field profiles for the different modes. The E_z component of the symmetric and antisymmetric modes are represented in figure 1.8 (a) and (b) respectively. Each spatial profile is normalised to unity. The calculation has been made at a free-space wavelength of 700 nm to avoid the high losses from SPP resonance, and better demonstrate the propagation properties of the modes.

The symmetric modes appears highly confined inside the alumina layer whilst the antisym-

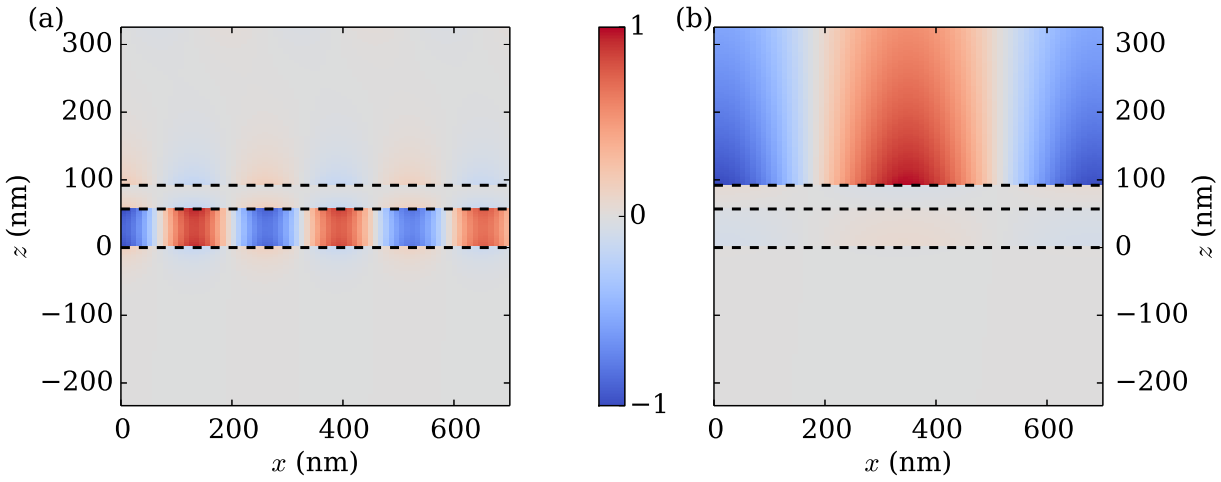

Figure 1.8 – Spatial profile of SPPs in the IMIM system.
(a) $z - x$ slice of the z-component of the symmetric mode electric field (normalised to unitary amplitude). (b) same as (a) for the antisymmetric mode. The field confinement of the symmetric mode inside the alumina layer is clearly visible, while the antisymmetric modes shows a leaky character into the upper half-space.

metric mode lies completely outside of the IMIM structure, explaining its low effective refractive index. The names of these two modes is derived from the well-known three-layer geometry. The symmetric mode appears to have a symmetric (i.e. even) profile across the alumina spacer, while the antisymmetric mode is of more odd, antisymmetric character. Similar graphs could be extracted for H_y and E_x, confirming e.g. that the z-component of the electric field and the y-component of the magnetic field propagate out of phase as a consequence of the large imaginary term κ [Dav09].

Having derived the properties of surface plasmon polaritons as confined surface waves, detailed their dispersion relation and demonstrated the basic treatment of surface plasmon modes in stratified media, we move on to explore the effect of lateral confinement of these waves when supported by nanometric particles.

1.3 Localised Surface Plasmons

Up to now we have considered waves supported by infinite metallic surfaces. Let us now consider what happens when we laterally confine the SPPs within lengths of the order of the SPP propagation length, L_{spp}. This is typically the case of metallic nanoparticles. Unlike in the case of SPPs, these particles support non-propagating surface waves called localised surface plasmons. Localised resonances of small spherical particles were initially studied by Mie in 1908 [Mie08] to describe their electromagnetic scattering properties. A more detailed introduction on the matter can be found in several textbooks, including [Jac75; Mai07; NH12]. We start by a brief introduction on the theory of scattering by small particles in the quasi-static limit, and

then show how it can be extended to larger particles. We will however not enter too much into the details of the Mie theory, as no analytical calculation has been carried out in this work. This section thus serves as a rather simple introduction on the matter of particles plasmons.

1.3.1 Light scattering by small particles

Let us consider a small sphere of radius a and permittivity ε_m in a homogeneous medium of permittivity ε_d, as depicted in figure 1.9. Assuming that the sphere is "small" enough, its response upon monochromatic electromagnetic excitation can be first understood in the frame of electrostatics. Here, "small" means that $a \ll \lambda$, where λ is the wavelength of the exciting field, so that retardation effects can be neglected. In the presence of an electrostatic field $\mathbf{E} = E_0\mathbf{z}$, the electrostatic response of the sphere is found by solving the Laplace equation $\nabla^2\Phi = 0$ for the electric potential Φ, from which we find the electric field through $\mathbf{E} = -\nabla\Phi$.

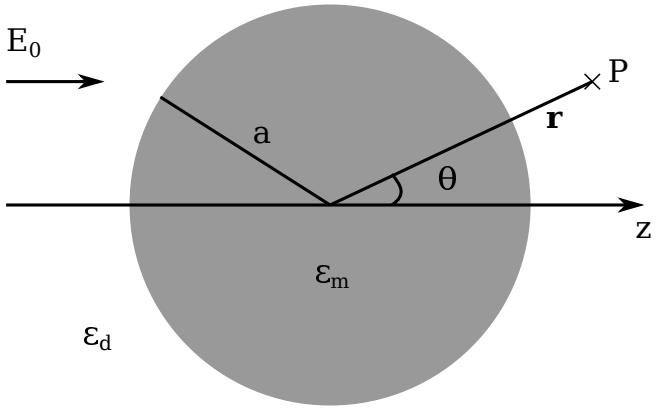

Figure 1.9 – Geometrical conventions for LSPR derivation.
The geometry considered for LSPR derivation. A small sphere of permittivity ε_m and radius a is embedded in a homogeneous medium of permittivity ε_d and excited by a static field E_0 along the z axis.

As the system is of spherical symmetry, a decomposition into Legendre polynomials $P_l(\cos\theta)$ gives:

$$\Phi(r,\theta) = \sum_{l=0}^{\infty} \left(A_l r^l + B_l r^{-(l+1)}\right) P_l(\cos\theta) \tag{1.37}$$

where θ is the angle between the position vector $\mathbf{r}$ of a point P and the z-axis.

Dividing the field inside and outside the sphere and applying boundary conditions yields:

$$\Phi_{in} = -\frac{3\varepsilon_d}{\varepsilon_m + 2\varepsilon_d} r E_0 \cos(\theta) \tag{1.38a}$$

$$\Phi_{out} = \left(-r + \frac{\varepsilon_m - \varepsilon_d}{\varepsilon_m + 2\varepsilon_d}\frac{a^3}{r^2}\right) E_0 \cos(\theta) \tag{1.38b}$$

where the analysis is restricted to the particle's *near field*.

One can note that while the potential inside the sphere simply resembles the applied static potential screened by the permittivity mismatch between the surrounding medium and the

sphere material, the potential outside the sphere is the superposition of the applied static potential and a dipolar-type potential produced by the scattering from the sphere. Rewriting equation (1.38b) in term of dipole moment $\mathbf{p}$:

$$\Phi_{out} = -E_0 r\cos(\theta) + \frac{\mathbf{p}\cdot\mathbf{r}}{4\pi\varepsilon_0\varepsilon_d r^3} \tag{1.39a}$$

$$\mathbf{p} = 4\pi\varepsilon_0\varepsilon_d a^3 \frac{\varepsilon_m - \varepsilon_d}{\varepsilon_m + 2\varepsilon_d}\mathbf{E_0} \tag{1.39b}$$

we can define the particle's polarisability α as $\mathbf{p} = \varepsilon_0\varepsilon_d\alpha\mathbf{E_0}$ and identify its expression with (1.39b):

$$\boxed{\alpha = 4\pi a^3 \frac{\varepsilon_m - \varepsilon_d}{\varepsilon_m + 2\varepsilon_d}} \tag{1.40}$$

It can be readily seen from equations (1.38a) and (1.40) that for $\varepsilon_m = -2\varepsilon_d$ the field inside and outside the particle experiences a resonant condition, known as the Frölich condition. Note that we have not inferred any metallic character of ε_m yet, and that the spectral position of the resonance is only dependant on the surrounding medium and sphere refractive indices.

We now waive the electrostatic condition and move on to an electrodynamic response, conserving the $a \ll \lambda$ condition in the so-called quasi-static approximation (QSA). The impinging field induces an oscillating dipole moment $\mathbf{p}(\mathbf{r},\mathbf{t})$ from the particle, with the polarisability defined by equation (1.40). The interaction between the field and the particle is often described in term of *extinction* cross-section (C_{ext}), which is the sum of the *absorption* (C_{abs}) and *scattering* (C_{sca}) cross-sections of the particle. They can be expressed as:

$$C_{abs} = k\,\mathrm{Im}\{\alpha\} \tag{1.41a}$$

$$C_{sca} = \frac{k^4}{6\pi}|\alpha|^2. \tag{1.41b}$$

They are often normalised to the particle's physical cross section and expressed as absorption and scattering efficiencies Q_{abs}, Q_{sca}.

All these quantities (α, Q_{abs} and Q_{sca}) are represented in figure 1.10, for Au and Al spheres in air and alumina. Panel (a) represents the polarisability of a Au sphere of radius 1 nm in Al_2O_3, normalised by the sphere volume (amplitude and phase in solid and dashed lines respectively). As shown in figure 1.1, the permittivity of Au is negative over a broad spectral range, easily fulfilling the Frölisch condition at the localized surface plasmon resonance (LSPR) wavelength λ_{lsp}. At resonance, the particle's polarisability shows a huge increase. Its finite value and width are due to the non-vanishing imaginary part of the metal permittivity function. It is also interesting to realize that the field scattered by the particle experiences a phase-shift while scanning the resonance, as shown on panel (a) on the right axis. On first approximation, α shows a damped harmonic oscillator-like behaviour. Note that due to the proximity of the interband transitions we do not retrieve the full expected π phase shift across the resonance.

Figure 1.10 (b) shows the absorption (solid lines) and scattering (dahsed lines) cross-sections of a Au sphere of radius 1 nm (blue) and 20 nm (red) in alumina, normalised to their physical cross-section. Two main informations are to be taken from this graph. First, it clearly shows the different scaling of $C_{abs} \propto a^3$ and $C_{sca} \propto a^6$. For very small particles (here $a \leq 20$ nm)

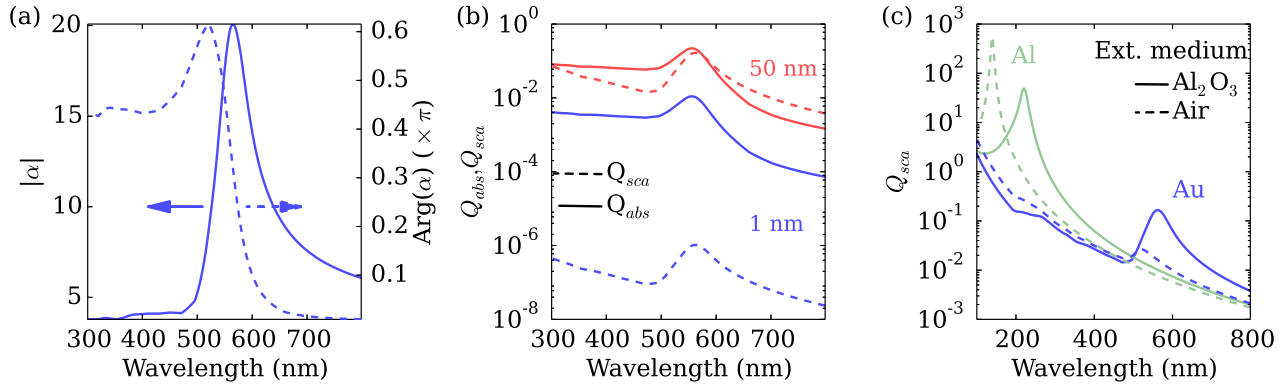

Figure 1.10 – LSPR in the quasi-static approximation.
(a) Amplitude and phase of the polarisability α of a Au sphere of radius 1 nm in Al_2O_3 (solid and dashed lines respectively). The LSPR is obtained when the Frölisch condition is met, its amplitude and width are governed by the finite imaginary part of the sphere's permittivity. A large phase shift in the scattered field occurs while sweeping through the resonance. (b) Absorption (solid lines) and scattering (dashed lines) cross-sections of 1 nm (blue) and 20 nm (red) radius Au spheres in Al_2O_3, illustrating the different scaling of C_{abs} and C_{sca}, and their frequency shift. (c) Scattering cross-sections of 20 nm radii Al (green) and Au (blue) spheres in air (dashed lines) and Al_2O_3 (solid lines). The LSPR wavelength increases with increasing surrounding medium permittivity, and is strongly material dependent.

the extinction is dominated by the absorption term, while it is the opposite for larger particles. Furthermore, the absorption resonance appears slightly blue-shifted from the scattering cross-section, leading to a small broadening of the total extinction cross-section.

As expected from equation (1.40), the predicted resonant wavelength does not depend on the particle's size, but only on the materials permittivities. Figure 1.10 (c) shows the scattering cross-section of Al (green) and Au (blue) particles of radius $a = 50$ nm in air (dashed lines) and alumina (solid lines). As for the SPP, the presence of a higher index material results in a red-shift of the LSPR, as can be understood by the decreasing value of $\mathrm{Re}\{\varepsilon_m\}$ with increasing wavelength in the Drude model [see fig. 1.1 (a)]. We can also see that the Al LSPR condition lies in the UV part of the spectrum, and that the resonance is sharper than in the case of Au. This is due to a lower value of ε_2 for Al, as shown previously in figure 1.1 (b).

1.4 Corrections to the polarisability, real-life particles and retardation effects

The previous results only work under the assumption of very small spherical particles, in what is called the quasi-static approximation. Several approaches have been developed to treat non-spherical or larger particles. We just give a brief introduction on these cases here, as they contain informations that we will have to keep in mind during the experimental study of plasmonic antennas in section 2.3.4.

As presented in equation (1.40), the polarisability does not take into account the effect of the scattered field on the particle itself, breaking the optical theorem. A correction can be added in the form of an effective polarisability α_{eff} [NH12]:

$$\alpha_{eff} = \frac{\alpha}{1 - i\,(k^3/(6\pi))\,\alpha} \tag{1.42}$$

This correction does not change the scattering and absorption cross-section results presented before, but re-establishes the optical theorem in the dipole limit. It introduces an additional phase-lag between the exciting and scattered fields.

We can then relax the spherical particle approximation by considering elliptical particles of semiaxes a_1, a_2 and a_3. It can be shown that [BH83]:

$$\alpha_i = \frac{4}{3}\pi \cdot a_1 \cdot a_2 \cdot a_3 \frac{\varepsilon_m - \varepsilon_d}{\varepsilon_d + L_i(\varepsilon_m - \varepsilon_d)} \tag{1.43}$$

where α_i is the polarisability along one of the principal axis ($x, y, z, \frac{x^2}{a_1^2} + \frac{y^2}{a_2^2} + \frac{z^2}{a_3^2} = 1$) and L_i is a geometrical factor given by:

$$L_i = \frac{a_1 a_2 a_3}{2} \int_0^\infty \frac{\mathrm{d}q}{(a_i^2 + q) f\,(q)}, \quad f\,(q) = \sqrt{\prod_{i=1}^{3}(q + a_i^2)}. \tag{1.44}$$

The sum of the three geometrical factors is always unity, and for a sphere $L_{i=1,2,3} = 1/3$.

Finally, dealing with larger particles (i.e. $a > 100$ nm) means that the electromagnetic field cannot be considered uniform over the particle any more, and that retardation effects have to be taken into account. This requires exact electrodynamics calculations as developed by Mie in 1908 [Mie08], by expanding the fields in normal modes, and not only considering the dipole limit. For illustration purpose, the latter can be retrieved by truncating a power series expansion of the Mie theory to the first order. The corrections to the first order (i.e. dipolar term) yield the polarisability of a sphere of volume V and size parameter $x = \pi a/\lambda_0$ as derived in the work of Kuwata et al. [Kuw+03]:

$$\alpha_{sphere} = \frac{1 - (\frac{1}{10})(\varepsilon_m + \varepsilon_d)x^2 + O\,(x^4)}{\left(\frac{1}{3} + \frac{\varepsilon_d}{\varepsilon_m - \varepsilon_d}\right) - \frac{1}{30}(\varepsilon_m + 10\varepsilon_d)x^2 - i\frac{4\pi^2\varepsilon_d^{3/2}}{3}\frac{V}{\lambda_0^3}} \tag{1.45}$$

and of a spheroid:

$$\alpha_{spheroid} = \frac{V}{\left(L + \frac{\varepsilon_d}{\varepsilon_m - \varepsilon_d}\right) + A\varepsilon_d x^2 + B\varepsilon_d^2 x^4 - i\frac{4\pi^2\varepsilon_d^{3/2}}{3}\frac{V}{\lambda_0^3}} \tag{1.46}$$

where a is the axis along which the incident light is polarised, and A and B are polynomials given by:

$$A\,(L) = -0.4865L - 1.046L^2 + 0.8481L^3 \tag{1.47a}$$

$$B\,(L) = 0.01909L + 0.1999L^2 \tag{1.47b}$$

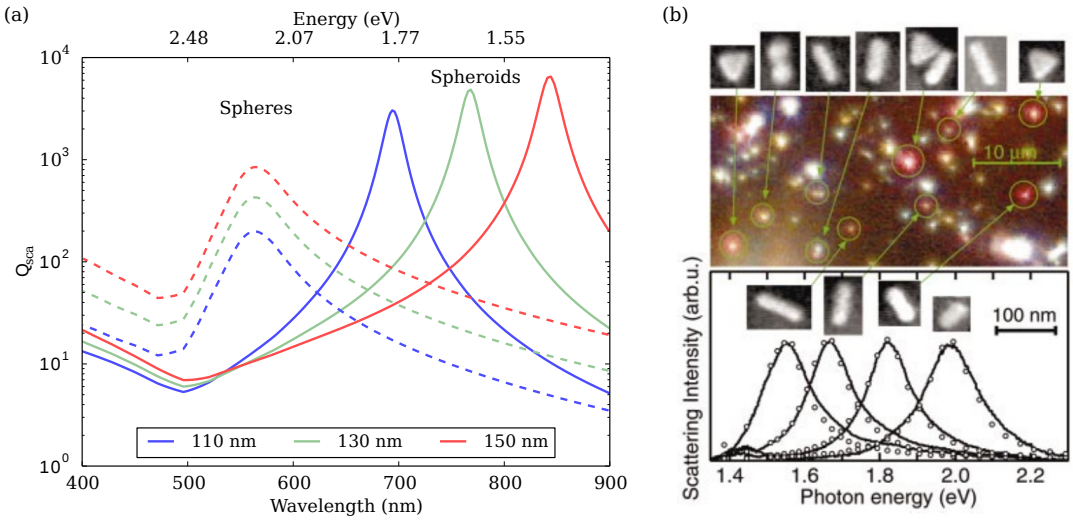

Figure 1.11 – Relaxing the QSA and real-life particle plasmons.
(a) Scattering cross-sections of Au spheres of different radii (dashed lines), and of oblate spheroids of the corresponding long axis length (solid lines), with a short axis length of 100 nm (blue: 110 nm, green: 130 nm and red: 150 nm). (b) SEM, dark-field image and scattering spectra of selected Au nanoparticles, reprinted from [Kuw+03]

This set of results is best exemplified in figures 1.11 and 1.12. Dashed lines in figure 1.11 (a) represent the scattering cross-sections of spheres of diameters 110, 130 and 150 nm computed using equation (1.45). While C_{sca} still shows a magnitude increase with particle size, retardation effects contained in the quadratic terms lead to a slight red shift of the resonant wavelength with increasing particle dimension. Solid lines in the same figure represent the scattering cross-sections of oblate spheroids excited along their long axis (lengths 110, 130 and 150 nm, the short axis is 100 nm long), computed from equation (1.46). Spherical symmetry breaking induces the appearance of two distinct resonances corresponding to the two axis of the particle. Here we only show the mode corresponding to the long axis resonance, which is stronger than for a sphere of the same dimension. Its position red-shifts with increasing axis length, or more precisely with increasing aspect ratio. This implies that, aside from changing the surrounding medium of a particle, *another way to tune the LSPR is to engineer the particle's shape.* An example of this is given in figure 1.11, presenting a dark-field image of dispersed gold nanoparticles along with SEM images and scattering spectra. The frequency change in LSPR is clearly visible from all the different colors scattered by the particles [Kuw+03] and the different spectra.

Finally, all these equations only describe dipolar-type modes supported by the particles. While this approach allows to describe small particles in the non-retarded or retarded regime, larger particles will support higher-order modes that have to be treated by a more rigorous calculation based on the full Mie theory. Such results are shown in figure 1.12 where not only the dipolar, but also higher order modes have been calculated. As a first consequence, the contributions of higher order modes lead to a more pronounced red shift of the dipolar mode. Near-field maps of the successive modes are presented in panels B-H. These modes have to be taken into account to properly describe the optical response of such particles as they all influence the field distribution around the particle. This is best demonstrated in panel E where

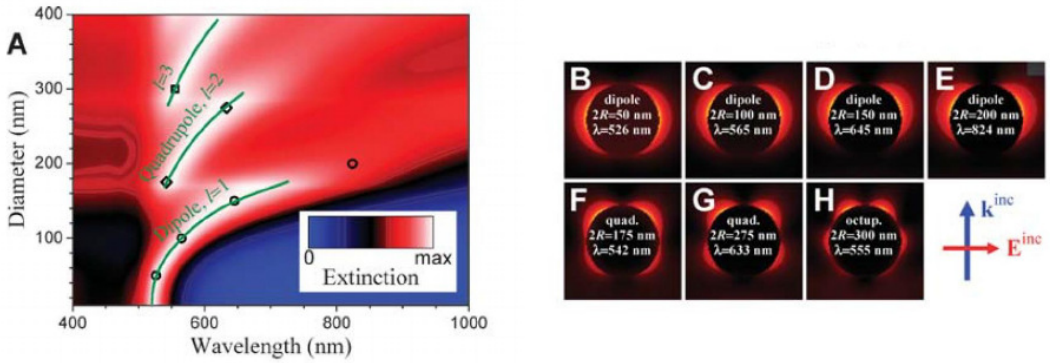

Figure 1.12 – Multipolar contributions to LSPRs.
A Calculated extinction spectrum for Au spheres of varying diameter. **B-H** selected near-field enhancement maps. The contribution of non-dipolar mode has to be taken into account for large particles. Reprinted from [Myr+08].

the effect of the quadrupolar mode on the dipolar one is visible by the apparent distortion of the two lobes around the particle. Their effect is of fundamental importance when trying to couple real particles to close-by emitters, and also play a role in the particles non-linear properties [But+10]. A fundamental point is that while all the successive plasmonic modes present a strong extinction, the relative weight of absorption and scattering terms in the mode depends on the mode order. As the final aim of this work is to enhance the optical properties of nanoemitters adjacent to the particle, it is important to differentiate the radiative behaviour of a mode to its absorption properties. Especially, we must ensure to use plasmon mode with a high dipolar character.

1.5 Conclusion

In this chapter, we have introduced the fundamentals of surface plasmons necessary to understand the work presented in the next sections. From the Maxwell equations, we showed that the description between light and metals required a precise knowledge of the electric permittivity ε of metals. In a first, oversimplified step, this quantity can be considered to originate from the response of the conduction electrons of the metal. Above the plasma frequency, the electromagnetic field vanishes inside the metal, making this permittivity mainly a surface property. Hence, the Drude model describing the interaction of a free electron gas and light has been introduced as a first description of ε. A further step was taken to explain the discrepancies between the experimental value of the metals permittivity and the Drude model, relying on the metal band structure. Notably, we showed the importance of interband transitions in Au and Al.

Having established these physical properties, we showed that an interface between a metal and a dielectric material could support a surface wave called surface plasmon polariton, which can confine electromagnetic radiation on a subwavelength scale in the direction orthogonal to the interface. We discussed the SPPs properties using first Drude model and then experimental values of the permittivity, showing the lossy character of SPPs and their relation to the materials parameters. Extending the discussion to stratified media, we demonstrated ways to tailor the

spectral and spatial properties of SPPs, especially evidencing the vertical confinement properties of IMIM media.

Finally, we discussed the case of surface plasmon resonances supported by nanometre-scale particles. We showed that these LSPs provide electromagnetic fields confined in the near field of the particle. In simple cases such as spheroidal particles, we showed how these resonances can be tunes by changing the particle material, its environment or its shape. We extended briefly the discussion to the case of large particles supporting high order LSP modes and their implication on the particles scattering and absorption properties.

By providing a way to concentrate electromagnetic energy in small volumes, metallic surfaces or particles thus bear a great interest as very local probes, field enhancing structures or waveguides. However, SPPs are not easily accessible by far-field illumination techniques, and experimental characterisation of LSPs requires sub-diffraction limited imaging. The next chapter will be dedicated to experimental spectroscopy and characterisation of plasmonic structures in order to better understand their properties, and determine a strategy to use plasmonic particles to enhance the optical properties of close-by emitters.

Chapter 2

Characterisation of plasmonic antennas by cathodoluminescence

Résumé en Français

Ce chapitre traite de l'utilisation de la cathodoluminescence (CL) pour déterminer les propriétés optiques d'antennes plasmoniques. Il s'agit d'une technique de microscopie optique par excitation électronique. Un faisceau d'électron est utilisé pour générer une excitation optique du matériaux. La lumière émise est collectée par un miroir parabolique et analysée dans un spectromètre (figure 2.2). La CL est donc une technique de spectroscopie d'excitation qui permet de caractériser des échantillons avec la résolution latérale du faisceau électronique, soit quelques dizaines de nanomètres, ce qui est inférieur à la limite de diffraction limitant les caractérisations optiques.

On s'attachera d'abord à décrire le champ généré par un électron se déplaçant en espace libre, avant de discuter des sources de rayonnement à considérer lors d'une expérience de CL.

Dans un second temps, on présente les propriétés de CL de films isolant-métal-isolant-métal (IMIM), et un modèle de densité d'états électromagnétiques décrivant les modes de plasmons soutenus par ces systèmes stratifiés. On montre notamment que la densité d'état seule ne décrit pas les observations de CL, qui nécessitent de prendre en compte la façon dont les modes de plasmons sont diffractés.

On discute ensuite des propriétés de CL d'antennes patchs (voir figures 2.11 et 2.14). Un modèle analytique pour la densité d'états locale (LDOS) des modes supportés par le patch introduit par les références [Fil+12] et [Moh+14] est exposé, se basant sur la procédure numérique décrite en section 1.2.3 et ne prenant en compte que le profile de champ vertical symétrique du système multicouche. Ce modèle décrit les modes propres du systèmes par des modes de Bessel. On établit alors que :

- *Expérimentalement, on observe des séries de résonances dans le spectre du signal de CL. Une imagerie filtrée en longueur d'onde corrélant l'intensité du signal de CL et la position du faisceau électronique image la LDOS radiative de l'antenne (figure 2.18).*

- *Le modèle permet de décrire qualitativement la structure des modes supportés par l'antenne. Notamment, le fait qu'une résonance peut correspondre à la superposition de plusieurs modes de l'antenne d'ordre radiaux et azimutaux différents apparaît clairement.*

- *Ce modèle ne décrit pas correctement la dispersion des modes de plasmons, ce qui lui retire son caractère prédictif. Une correction est introduite, mais reste peu satisfaisante car elle nécessite de surévaluer le vecteur d'onde du mode de plasmon. (figure 2.19).*

- *Le modèle ne décrit que la densité d'états, et non leur couplage au champ rayonné. Il ne reproduit donc pas les amplitudes relatives des résonances observées en CL.*

- *Le signal de CL comporte des contributions non liées aux modes de patchs de profil vertical symétrique. Notamment, une résonance fixe en énergie est présente pour toutes les antennes et n'est pas prédite par le modèle.*

Afin d'approfondir la compréhension du système, on étudie alors l'effet de deux paramètres sur la réponse de CL: l'épaisseur de la couche diélectrique séparant l'antenne du plan métallique, et le métal constituant le plan infini ou l'antenne. On montre que l'épaisseur du diélectrique permet de contrôler la dispersion en énergie des modes supportés par les antennes. L'étude de la résonance fixe en énergie en fonction de l'épaisseur du diélectrique et des matériaux constituant le système nous pousse à proposer que cette dernière est dûe aux plasmons supportés par le film métallique diffractés aux bords de l'antenne. Cette interprétation est encore ouverte, et n'est pas la seule possible. Des travaux de simulations numériques sont encore en cours pour affiner notre compréhension du système et de son étude en CL. Enfin, la caractérisation d'antennes en aluminium montre qu'on peut étendre l'opération de ces antennes patchs dans la gamme bleue du spectre électromagnétique.

Introduction

The previous chapter provided all the required fundamentals to understand the concept of surface plasmon polaritons and localised surface plasmons supported by small metallic particles. We demonstrated that surface plasmon polaritons can not be excited by free space radiation, and that the very nature of the particle plasmons makes them sub-diffraction limited electromagnetic excitations. This means that in-depth study of plasmonic resonances requires original techniques to excite and characterise the plasmonic properties of metallic films and small metallic antennas. Optical methods relying on near-field scanning techniques are amongst the most widely used, as exemplified in ref. [HK01; Hil+03; Est+08], while non-linear far field techniques are rapidly developing [Via+13; Eth+16], even leading to non-linear near-field techniques [Kra+16]. In this chapter we show how CL, i.e. the use of electrons as an exciting source for optical microscopy, allows us to study metallic nanoparticles and surface plasmons with a sub-diffraction limited resolution. The main advantages as compared to optical techniques is that the electronic excitation provides a broad source spectrum and is non-invasive, as opposed to near-field optical methods. A typical cathodoluminescence experiment consists in bombarding a sample with energetic electrons and collecting the light emitted by the sample in response to this excitation. This light can have several origins, such as recombination of carriers directly injected by the electron beam, Cherenkov radiation or scattering of the field created by the electrons. In a CL experiment for plasmonics, one is only interested in this last source of radiation to study the structures of interest.

The first part of this chapter is dedicated to a description of the cathodoluminescence experiment, first from a theoretical and then from an experimental point of view. We especially focus on multi-layered structures introduced in the previous chapter. They correspond to a realistic experimental configuration for the final purpose of this thesis, which is to study the coupling between plasmonic structures with quantum dots and requires the use of metallic substrates. Furthermore, they bear strong vertical field confinement ability which is appealing in the perspective of fabricating novel plasmonic antennas. We then show in detail the results of CL spectroscopy and imaging on plasmonic patch antennas fabricated using IMIM substrates. We propose a discussion on the CL experiment interpretation and the role of the substrate in the experiment, and conclude on the high interest of CL for plasmonic studies.

2.1 Cathodoluminescence: a tool for plasmonics

The optical response of plasmonic antennas is highly dependant of their shape, and because of their small size, probing their local properties implies obtaining nanometric scale spatial resolution. Because the diffraction limit can not be overcome in optical techniques, hybrid characterization tools based on electron imaging has been developed. Among these, electron energy loss spectroscopy (EELS) and cathodoluminescence are the most wildly used. Comprehensive theoretical work has already been reviewed on the subject [Gar10], along with extensive practical discussions [KS14]. The latter gives a clear link between optical properties and electronically probed quantities when studying metallic nanoparticles, namely relating EELS probability to the absorption and CL to optically bright modes supported by the particles.

In order to characterize both spectrally and spatially the plasmonic nanoantennas, we used

the CL setup developed in our lab from a scanning electron microscope (SEM). The first part of this chapter gives the theoretical basis to understand our CL experiments. In the second part, we present the custom CL set-up used during this thesis. We then move to the study of isolated plasmonic antennas.

2.1.1 Electrons as local electromagnetic excitations

In this section, we develop the necessary theoretical basis to understand the cathodoluminescence experiments. We start by treating the radiation created by moving particles, and then apply our findings to plamonic antennas investigation.

Let us first derive the field created by an electron moving in a straight line in a homogeneous medium with a velocity $\mathbf{v}$ and transferring to the field a wave-vector $\tilde{\mathbf{q}}$. Restricting the velocity to experimentally achievable values in our SEM with acceleration voltage of 30 keV, the derivation can be done in a non-relativistic approximation. Following [Gar10], the electron charge density in the medium in $\tilde{\mathbf{q}} - \omega$ space is:

$$\rho_{ext}\left(\omega, \tilde{\mathbf{q}}\right) = -2\pi\bar{e}\delta\left(\omega - \tilde{\mathbf{q}} \cdot \mathbf{v}\right). \tag{2.1}$$

The field created by the moving charge can be calculated from Maxwell's equations (1.1a)-(1.1d). Combining the curl equations yields:

$$\nabla \times \nabla \times \mathbf{E} = \nabla \times \left(-\frac{\partial \mathbf{B}}{\partial t}\right) = \nabla\left(\nabla \cdot \mathbf{E}\right) - \nabla^2\mathbf{E}. \tag{2.2}$$

This equation is equally valid in position-time or frequency-wave vectors conjugate spaces, but becomes especially easy to manipulate when assuming harmonic decompositions. We then have the following Fourier transforms:

$$\mathbf{E}\left(\mathbf{r}, t\right) = \frac{1}{2\pi}\int \mathbf{E}\left(\mathbf{r}, \omega\right) \mathrm{e}^{-i\omega t}\mathrm{d}\omega \tag{2.3}$$

$$\mathbf{E}\left(\mathbf{r}, t\right) = \frac{1}{\left(2\pi\right)^3}\int \mathbf{E}\left(\tilde{\mathbf{q}}, t\right) \mathrm{e}^{i\tilde{\mathbf{q}} \cdot \mathbf{r}}\mathrm{d}^3\tilde{\mathbf{q}} \tag{2.4}$$

and relations:

$$\frac{\partial}{\partial t} = -i\omega \qquad \nabla \cdot \; = i\tilde{\mathbf{q}} \cdot \qquad \nabla\times = i\tilde{\mathbf{q}} \times \qquad \nabla^2 = -\tilde{q}^2 \tag{2.5}$$

The field created by the moving charge is obtained by solving equation (2.2) in conjugate space, assuming an isotropic medium of permittivity ε:

$$\begin{aligned}
\nabla\left(\nabla \cdot \mathbf{E}\right) - \nabla^2\mathbf{E} =& \nabla \times \left(-\frac{\partial \mathbf{B}}{\partial t}\right) \\
\nabla\left(\frac{\rho_{ext}}{\varepsilon\varepsilon_0}\right) + \tilde{q}^2\mathbf{E} =& i\omega\nabla \times \mathbf{B} \\
i\frac{\boldsymbol{\rho_{ext}}}{\varepsilon\varepsilon_0}\tilde{\mathbf{q}} + \tilde{q}^2\mathbf{E} =& i\omega\mu_0\left(\mathbf{J} - i\varepsilon\varepsilon_0\omega\mathbf{E}\right) \\
i\frac{\boldsymbol{\rho_{ext}}}{\varepsilon\varepsilon_0}\tilde{\mathbf{q}} + \tilde{q}^2\mathbf{E} =& \frac{i\omega}{\varepsilon_0 c^2}\left(\rho_{ext}\mathbf{v} - i\varepsilon\varepsilon_0\omega\mathbf{E}\right) \\
\left(\tilde{q}^2 - \frac{\omega^2\varepsilon}{c^2}\right)\mathbf{E} =& i\left(\frac{\omega\mathbf{v}}{\varepsilon_0 c^2} - \frac{\tilde{\mathbf{q}}}{\varepsilon_0\varepsilon}\right)\rho_{ext}
\end{aligned}$$

which yields the electric field in frequency-wave vector space:

$$\begin{aligned}\mathbf{E}\left(\tilde{\mathbf{q}},\omega\right) &= -i\frac{\tilde{\mathbf{q}}/\varepsilon-\omega\mathbf{v}/c^2}{\tilde{q}^2-\omega^2\varepsilon/c^2}\frac{\rho_{ext}}{\varepsilon_0}\\ &= -i\frac{\tilde{\mathbf{q}}/\varepsilon-k_0\mathbf{v}/c}{\tilde{q}^2-k_0^2\varepsilon}\frac{\rho_{ext}}{\varepsilon_0}\end{aligned} \tag{2.6}$$

where $k_0=\omega/c$ is the light wave number in vacuum.

In order to understand the physical properties of such a moving charge, the field is better expressed in space-frequency coordinates using the Fourier transforms and substituting equation (2.1) into (2.6):

$$\boxed{\mathbf{E}\left(\mathbf{r},\omega\right)=\frac{i\bar{e}}{\varepsilon_0(2\pi)^2}\int\frac{\tilde{\mathbf{q}}\varepsilon-k_0\mathbf{v}/c}{\tilde{q}^2-k_0^2\varepsilon}\mathrm{e}^{i\tilde{\mathbf{q}}\,\cdot\,\mathbf{r}}\delta\left(\omega-\tilde{\mathbf{q}}.\mathbf{v}\right)\mathrm{d}^3\tilde{\mathbf{q}}}} \tag{2.7}$$

Equation (2.7) contains several important informations. First, the Dirac function in the integrals indicates energy conservation in the momentum transfer from the electron to the electromagnetic field. In the non-relativistic approximation, this condition simply reduces to $\omega=\tilde{\mathbf{q}}\cdot\mathbf{v}$. Energy transfers are allowed for any orientation between $\mathbf{v}$ and $\tilde{\mathbf{q}}$, with $\omega=\tilde{q}v$ as upper limit. The poles of the integrand in equation (2.7) follow the dispersion relation of light in the medium, indicating momentum transfer with the same wave vectors as photons in the medium $\tilde{q}=k=k_0\sqrt{\varepsilon}$.

Two regimes have then to be distinguished according to the electron velocity, as a function of the sign of $v^2\varepsilon-c^2$. If $v^2\varepsilon<c^2$ then the transferred wave vector is always larger than the one of the light propagating in the medium:

$$\begin{aligned}\omega=\tilde{q}v &< \tilde{q}\frac{c}{\sqrt{\varepsilon}}\\ k=\omega\frac{\sqrt{\varepsilon}}{c} &< \tilde{q}\end{aligned}$$

and the electron cannot couple to propagating electromagnetic waves in the medium. Conversely, if $v^2\varepsilon>c^2$ then it is possible to find wave vectors that are smaller than the ones of light in the medium. Consequently, the propagating electrons is a source of propagating radiation in the medium. The threshold $v^2\varepsilon=c^2$ is called the Cherenkov radiation limit. With the electron velocities and material permittivities considered in this manuscript, we are ensured to remain below this threshold. For such frequencies, the field determined from equation (2.7) is explicitely given by [Jac75]:

$$\mathbf{E}\left(\mathbf{r},\omega\right)=\frac{2\bar{e}\omega}{v^2\gamma_e\varepsilon}\mathrm{e}^{i\omega z/v}\left[\frac{i}{\gamma_e}K_0\left(\zeta\right)\mathbf{z}-K_1\left(\zeta\right)\boldsymbol{\rho}\right] \tag{2.8}$$

using $\mathbf{r}=(\boldsymbol{\rho},z)$, $\zeta=\frac{\omega\rho}{v\gamma_e}$ is the reduced radius away from the electron trajectory and $\gamma_e=1/\sqrt{1-\varepsilon v^2/c^2}$ is the Lorentz contraction factor. K_0 and K_1 are the first modified Bessel functions. Similarly, the magnetic field reads:

$$\mathbf{H}\left(\boldsymbol{\rho},\omega\right)=-\frac{2\bar{e}\omega}{vc\gamma_e\varepsilon}\mathrm{e}^{i\omega z/v}K_1\left(\zeta\right)\boldsymbol{\varphi} \tag{2.9}$$

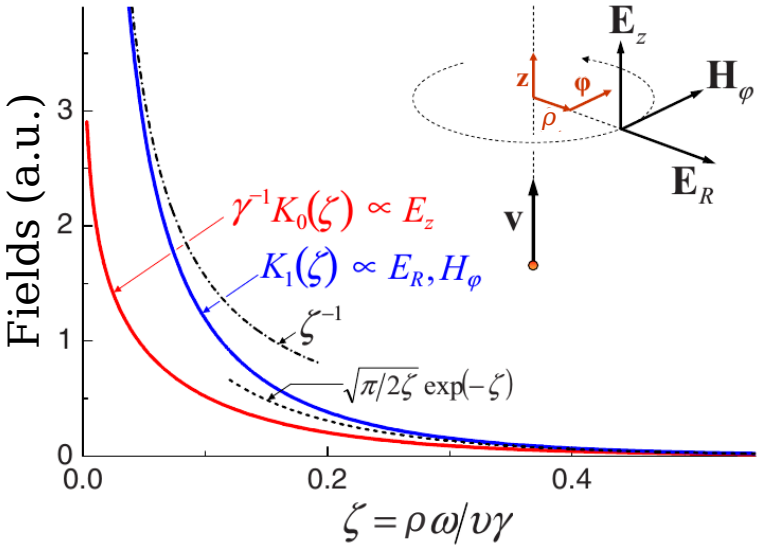

Figure 2.1 – Field created by a swift electron.
Different components of the field created by a moving electron in free space as a function of the reduced radius ζ. The calculation was made for an electron moving with $v = 0.7c$ in vacuum, which is way larger that the achievable velocities in our SEM setup ($\sim 0.3c$). It clearly evidences the exponentially decaying character of the field components. Reproduced from [Gar10].

where $\boldsymbol{\varphi}$ is the azimuthal unit vector.

For each frequency of the field, both **E** and **H** decay exponentially away from the electron up to distances of the order of $v\gamma_e/\omega$. ζ becomes imaginary above the limit $v = c/\sqrt{\varepsilon}$ and the fields decay exponentially with oscillatory behaviour. *An electron in uniform motion as used in SEMs can thus be regarded as extremely localized, broadband pulsed sources of electromagnetic radiation.* Direct evaluation in the case of 30 keV energetic electrons in our CL setup leads to a characteristic interaction distance of $20 - 30$ nm, which can be thought as the typical spatial extension of our exciting source and hence represents a limitation of our spatial resolution.

In real experimental configurations, the electron beam of a SEM does not propagate in a homogeneous medium, but is impinging on a material surface. When crossing the surface, the field created by the electron has to reorganise itself to account for the abrupt change in surrounding refractive index. This leads to the emission of transition radiation (TR). This radiation depends on the material and the electron velocity. Its spatial and polarisation distributions resemble the emission from a vertically oriented dipole placed at the impact point of the electron, and having an extremely broad spectrum. Furthermore, as the field created by the electron is evanescent, it bears electromagnetic excitations with larger wave vectors than the one of the light in the medium. As discussed in section 1.2.2 this allows excitation of SPPs at the dielectric/metal interface. These two mechanisms of light emission are coherent, and lead to interferences when detected in the far-field, as demonstrated for example when measuring SPP diffraction from a single step [YS08]. Finally as the electronic excitation can be thought as a pulsed, broadband excitation, fluorescence properties of the material can also be probed locally in the experiment, with a spatial resolution corresponding to the carriers diffusion length in the material. The

fluorescence process results in photons that are not coherent with the generated TR and SPPs.

The ability to induce electromagnetic excitation with electron beams in a spatially selective manner has recently resulted a huge gain of interest around hybrid electronic-optical microscopy and spectroscopy techniques such as CL and EELS. A great conceptual effort has thus been realised to relate the measured properties of samples and materials to electromagnetic quantities. We leave aside fluorescent properties that simply result in electron-hole pairs creations and recombination. The detection of a CL signal necessarily implies momentum transfer from the electron to the electromagnetic field at some point along its trajectory, and in a electromagnetic mode that can be converted to free-space radiation. As greatly discussed in several articles and reviews [GK08; Gar10; KS14; Koc+14], this exchange of momentum is related to a vectorial quantity called (electromagnetic) LDOS, which quantifies the number of available electromagnetic mode at every point in space and field orientation, for a given energy. While no exact formal link exists yet between CL and LDOS in the general case, it has been proposed that CL probes the integration over the whole electron beam path of the radiative LDOS projected along the electron beam direction [LK15]. CL images are thus excitation images, which means that they allow measurement *of the probability of excitation at the electron beam position.*

2.1.2 Experimental cathodoluminescence setup

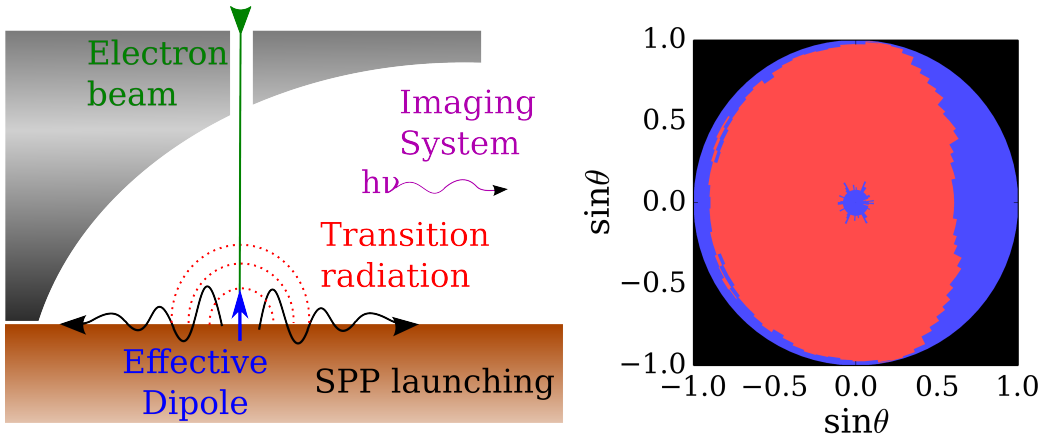

Figure 2.2 – **Cathodoluminescence experiment**.
Left: Excitation and collection scheme. The electron beam passes through the hole in the parabolic mirror and impacts the surface of the substrates. Upon impact, TR, SPPs and LSPs (not shown) are generated. The radiation coupling to the far-field is collected by the parabolic mirror and sent to an imaging system. Right: Collection range of the parabolic mirror (in red) in polar coordinates, in units of numerical aperture. It can be seen as a top view projection of the left panel, in which the rightmost direction indicates the direction of light collection. It is obtained from ray tracing simulations (Zemax). The numerical artefacts come from numerical interpolation on a spherical coordinates grid after calculation.

To perform a CL experiment one needs to be able to excite a sample with an electron beam and collect the light emitted upon electron impacts. A SEM (FEI quanta 200 [FEI]) is thus fitted with a drilled parabolic mirror, allowing electrons to pass through a hole to excite the sample,

and collecting light from the sample after reflection on the mirror, as sketched in figure 2.2. The mirror collects photons emitted up to very large angles as represented in the right part of the figure (Zemax ray tracing simulation by David Jegouso). The central hole is ~ 500 µm wide. As the probability for electron-mediated SPP excitation increases with the electron acceleration voltage [Gar10], we always use the maximum available acceleration voltage of our SEM of 30 kV. We can see that the collection is asymmetric due to the shape of the mirror: light emitted at large angles towards the detection side is not collected. Small features in the image come from numerical errors in the evaluation of the collection from the mirror.

A spherical mirror focuses the collected light on the entrance slit of a spectrometer (Horiba Jobin-Yvon IHR550 [Job]) equipped with a 150gr/mm grating blazed at 550 nm, to be spectrally filtered. The small dispersion provided by this grating is well suitable for plasmonics, as we expect to study broad resonances ($\sim$ 100 nm bandwidth) over a large spectral range in the visible spectrum. It is projected on a charge-coupled device (CCD) camera (Andor Newton [New]) to be spectrally resolved, or filtered through the exit slit of the spectrometer and sent to a single photon counting module to obtain energy-selective CL images.

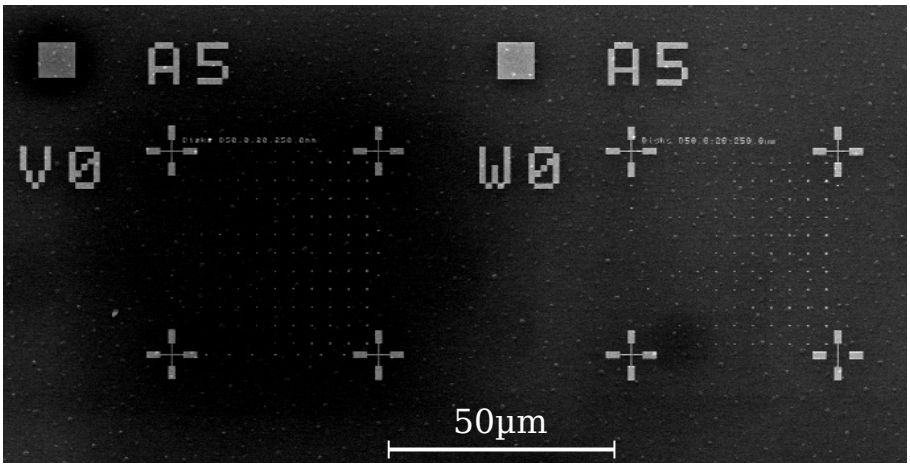

Figure 2.3 – **Electron-beam induced contamination**.
Wide-field SEM image of a patch antenna sample after a CL experiment. The left array and the bottom left part of the right array have been exposed to the electron beam. The black haze around all the observed antennas is due to electron-beam induced deposition of impurities (mainly carbon) which limits the number of acquisitions one can take on a single object before degrading its properties.

The CL efficiency of a gold plasmonic antenna is typically of the order of a few tens of photons/10^6 electrons. Hence, the collected intensity ranges in the few tens of photons per second and per pixel on the detector. Due to the low yield of the process, one needs to integrate the signal for a long time, which causes several problems. First, an electrostatic drift can appear, degrading the spatial resolution over time. Second, backscattered electrons can generate excitations at locations different from the electron beam position, also degrading the spatial resolution of the technique. Finally, electron-beam induced deposition of the residual impurities in the SEM chamber degrade the antenna optical properties in time, limiting the number of images and spectra one can acquire from a single structure (see figure 2.3). Some of these drawbacks can be avoided or minimised by changing the experimental configuration and do not interfere in the study of IMIM films presented thereafter, but are unavoidable in the case of

antenna LDOS imaging (see section 2.3.4). The e-beam induced deposition of impurities can be reduced by using an in-situ O_2 plasma cleaning in the SEM chamber (not yet available in our experiment), or taken care of after the experiment by an acetone batch and an O_2 plasma cleaning.

2.2 The optical properties of IMIM films

2.2.1 Cathodoluminescence of IMIM films

As shown in section 1.2.3, insulator-metal-insulator-metal (IMIM) layered structures show interesting properties in terms of supported SPP modes, and allow strong field confinement in the vertical direction. In order to understand what happens in a cathodoluminescence experiment, it is interesting to try and link the derived optical properties in section 1.2.3 with their observed CL response. The following sections on IMIM films are also intended to serve as an introduction for the study of the optical properties of plasmonic antennas made from IMIM stacks.

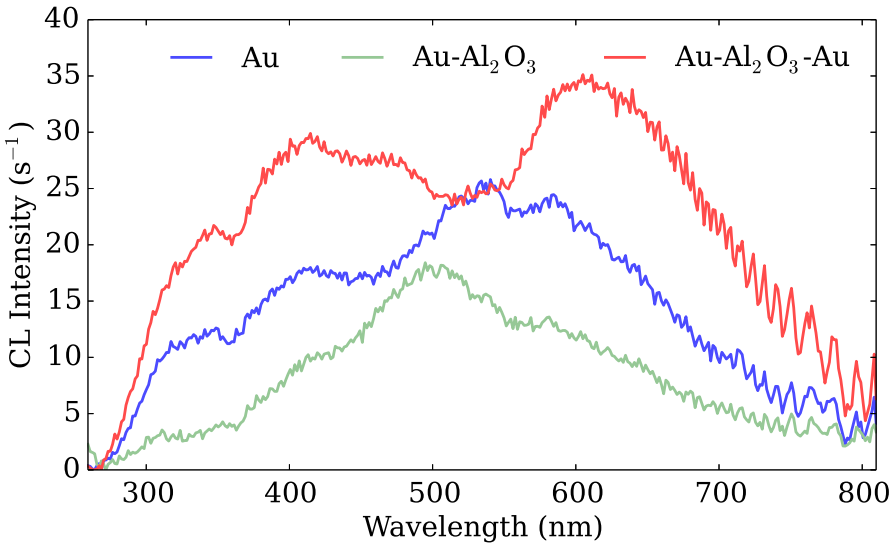

Figure 2.4 – Cathodoluminescence spectra of multilayer structures.
Cathodoluminescence spectra of a single Au interface (blue), a Au-Al_2O_3(26 nm) interface (green) and a Au-Al_2O_3(26 nm)-Au(35 nm) stack (red).

As a first example, figure 2.4 shows the CL spectrum of three different film structures: a simple Au layer (blue), a Au-Al_2O_3 layer with an oxide thickness of 26 nm (green) and a uniform Au-Al_2O_3-Au structure for which the top Au layer is 35 nm thick and the Al_2O_3 spacer is 26 nm thick (red). The Au layers are deposited by electron gun evaporation under vacuum, and are thus a bit rough. SEM images reveal grains of $\sim$ 10 nm in size. The alumina layer is deposited using atomic layer deposition (ALD) and is thus conformal to the Au surface. The CL spectrum from the Au film presents a broad peak centred at 550 nm which decays rapidly towards larger wavelengths, but presents some broad features at higher energy. Note that the decay in CL intensity at high energy is due to the detection cut-off from the CCD camera. The one of the Au-Al_2O_3 film resembles the one of the Au film with a slight blue shift of the maximum intensity

position down to 500 nm. It also exhibits a slightly lower CL intensity. The CL spectrum from the IMIM structure clearly differs from the others. While the CL emission around 550 nm is roughly the same as for the Au film, a more pronounced emission is observed at longer and smaller wavelengths.

As explained in section 2.1.1, three main mechanisms are at play in the CL experiment: transition radiation, surface plasmon polariton launching and fluorescence. Figure 2.5 shows the emission probability of TR and SPP for 30 keV electrons impinging on a smooth Au surface [Gar10; Gar]. It is readily visible that SPP is dominating at this accelerating voltage: a generation peak is predicted around the Au SPR wavelength, with a rapid decay of emission probability towards longer wavelengths. However, it poorly resembles the measured Au CL spectrum of figure 2.4. This is a hint that more phenomena are involved in the CL process. Incoherent luminescence from Au partly explains the higher energy contributions to the spectrum, due to interband transitions as detailed in section 1.1.3 [BYS86; BBN03] . Moreover, the calculation only reflects SPP excitation probability, assuming a smooth surface. Studies on the photoluminescence of rough Au surfaces show that surface roughness increases photoluminescence from Au films through surface plasmon mediated phenomena [BYS86; BBN03].

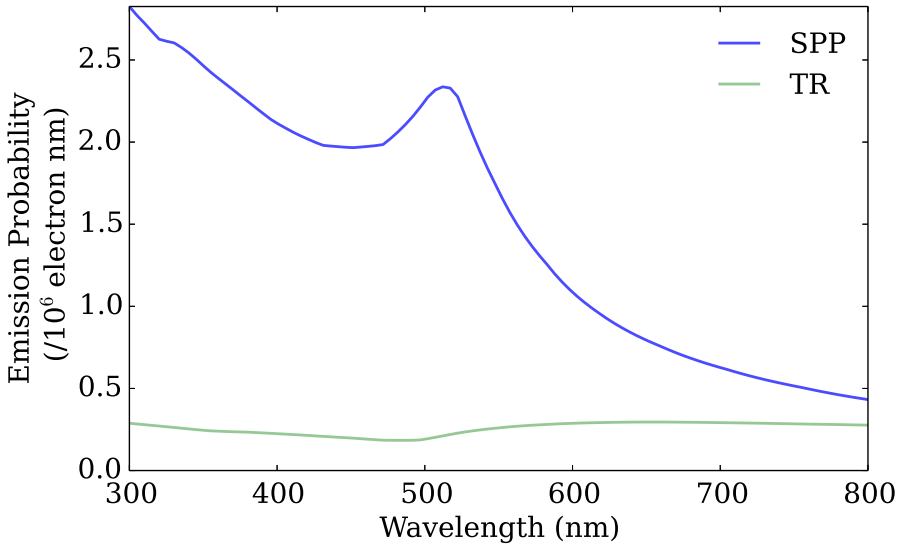

Figure 2.5 – SPP and TR emission probabilities.
SPP (blue) and TR (green) emission probabilities from a single smooth Au surface with 30 keV electrons impinging normal to the surface, computed from [Gar10; Gar]

2.2.2 Plasmonic LDOS for IMIM films

The crucial role of SPPs in CL experiments on films supporting SPP modes has to be linked with the LDOS introduced in the conclusion of section 2.1.1. We thus propose to use the calculation of the surface plasmon mode supported by the metallic films to derive *the plasmonic density of states (DOS)* Γ_{sp} at the electron impact point. Note that the "local" term has been dropped here since this quantity is invariant with $\boldsymbol{\rho}$ for a planar film, and has already been integrated along z, making it a scalar quantity. As the DOS is related to the amount of local

electromagnetic energy, we write:

$$\Gamma_{\mathrm{sp}}(\omega) \propto \int |\mathbf{E}(\boldsymbol{r},\omega)|^2 \,\mathrm{d}z = \iint |\mathbf{E}(\boldsymbol{r},\omega')|^2 \,\delta(\omega-\omega')\,\mathrm{d}\omega'\mathrm{d}z. \tag{2.10}$$

z being the axis of electron propagation, we only probe the DOS related to the z-component of the electric field. The latter can be written as:

$$E_z(\mathbf{r},\omega) = a(z,\omega)\, E_{\mathrm{sp}}(\boldsymbol{\rho},\omega) \tag{2.11}$$

for a given frequency ω, where $a(z)$ is the vertical envelope profile of the SPP mode which decays exponentially away from the metallic surface, and E_{sp} is the normalised in-plane electric field profile with in-plane radius coordinate $\boldsymbol{\rho}$. Each SPP mode has to be normalised in energy. The in-plane field profile can be decomposed into plane SPP waves with wave vectors k_{SPP} in the form $\exp(ik_{\mathrm{SPP}}\rho)$, yielding an in-plane exponential decay of the field following $\exp(-\operatorname{Im}\{k_{\mathrm{SPP}}\}\rho)$. The normalisation constant is then:

$$I(\omega) = \int |a(z)|^2 \,\mathrm{d}z \times (2\operatorname{Im}\{k_{\mathrm{SPP}}\})^{-1} \tag{2.12}$$

In the case of a single metallic interface, the vertical envelope profile would simply yield a $\exp(-\operatorname{Im}\{k_{z,i}\}|z|)$ exponential decay in each medium i, resulting in a final normalisation term $(2\operatorname{Im}\{k_z\})^{-1}$. For more complex geometries, the numerical procedure described in section 1.2.3 is used. The 2D DOS can thus be obtained with respect to energy following:

$$\Gamma_{\mathrm{sp}}(\omega) \propto \int 2\pi \operatorname{Re}\{k_{\mathrm{SPP}}\} I(\omega)^{-1} \frac{\mathrm{d}k_{\mathrm{SPP}}}{\mathrm{d}\omega} \delta(\omega-\omega')\,\mathrm{d}\omega' \tag{2.13}$$

where the $2\pi \operatorname{Re}\{k_{SPP}\}$ accounts for the number of SPP modes in the 2D reciprocal space and the normalisation term $I(\omega)$ accounts for their spatial (vertical and in-plane) extension.

Following the work of refs [Fil+12; Moh+14], we further take into account the lossy nature of SPP modes by a frequency broadening in the form of a Lorentzian function of unitary integral $\mathcal{L}(\omega,\omega',\gamma)$ centred at the frequency ω' and with full width at half maximum $\gamma/\omega = (2\operatorname{Im}\{k_{\mathrm{SPP}}\})^2 + \gamma_0(1+\omega_{\mathrm{norm}}^b)^{-1}$, where $\gamma_0 = 0.1$ and $b = 1.7$ are empirical parameters and we set $\omega_{\mathrm{norm}} = \omega/(1800\ \mathrm{THz})$. These parameters are set to obtain a realistic scaling of the SPP mode bandwidth with frequency, according to [Fil+12; Moh+14]. Our final expression thus reads:

$$\boxed{\Gamma_{\mathrm{sp}}(\omega) \propto \frac{2\pi \operatorname{Re}\{k_{\mathrm{SPP}}\}\beta_{\mathrm{SPP}}}{I(\omega)} \int \mathcal{L}(\omega,\omega',\gamma)\,\mathrm{d}\omega'.} \tag{2.14}$$

where $\beta_{\mathrm{SPP}} = \frac{\mathrm{d}k_{\mathrm{SPP}}}{\mathrm{d}\omega}$ is the inverse of the SPP dispersion relation.

This expression is evaluated numerically using the procedure presented in section 1.2.3 which readily yields the vertical mode profile $a(z)$ as well as the SPP propagation wave vector k_{SPP} and dispersion relation β_{SPP}. In the case of multilayered structures, we have seen that several vertical mode profiles exist, two examples of which being the symmetric and antisymmetric modes presented in section 1.2.3. It is thus required to compute the LDOS for each vertical mode profile separately.

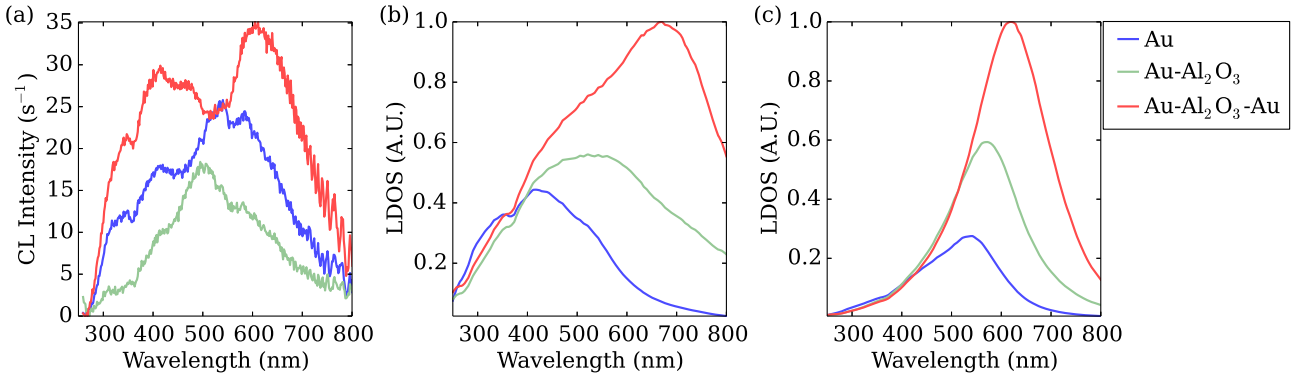

Figure 2.6 – CL spectra of multilayer structures and corresponding DOS calculations. (a) CL spectra of the same structures presented in figure 2.4 (see legend). (b) DOS calculations for the same structures using equation (2.14) and corrected by the system detection efficiency. Only the symmetric IMIM vertical mode profile is shown. (c) Same DOS calculation modulated by the diffraction efficiency of the surface (see text). The DOS model alone does not take into account the outcoupling efficiency for the SPPs but shows that the increase in CL signal for the IMIM mode comes from an increase in plasmonic DOS between 600 and 800 nm. The surface diffraction model shows how the outcoupling efficiency modifies the spectral profile of the measured DOS.

Figures 2.6 (a) and (b) shows the comparison between the experimental spectra and the DOS evaluation for the same structures studied in figure 2.4, corrected for the experimental detection efficiencies of the grating and CCD camera. We only show the symmetric IMIM mode from the calculation, as it presents a DOS one to two orders of magnitude greater than the antisymmetric mode. Moreover, it is commonly accepted that it is the most easily excited mode in CL experiments on such multilayer structures, as its symmetry matches the polarisation of the exciting CL field [KGP10; Moh+14].

The blue curve corresponding to a bare Au interface slightly resembles the one from figure 2.5 where the instruments response function is responsible for the decrease in amplitude towards the U.V. range, but the broadening due to the Lorentzian term smeared out the local maximum near the surface plasmon resonance wavelength. We find an increase of DOS at higher energy, which is due to the presence of interband transitions leading to an increase in losses, and thus a decrease in $I(\omega)$. The green curve shows an increase in DOS around the SPR wavelength (575 nm), which is red shifted by the presence of the thin oxide layer. Finally, the red curve shows a great increase in DOS at longer wavelengths, which corresponds to the excitation of the symmetric mode of the IMIM structure. However, these calculation do not strictly match the experimental CL curves, because they only take into account *excitation* of SPP. To couple out to the far field, they have to be diffracted e.g. by surface roughness, which results in the modulation of the DOS curve by the diffraction efficiency of the rough surface. The spectral dependence of this diffraction efficiency is unknown, and the calculation of SPP scattering by a randomly rough surface is an extremely complex problem that lies beyond the scope of this thesis. It is well treated in refs [ZSM05; Bau+11] for example, but requires a computationally intensive work. Moreover, these references only show results for monochromatic calculations, leaving us with no estimation of the spectral lineshape of the surface scattering properties. For a qualitative evaluation of this scattering efficiency, we can consider that the surface scattering is

produced by weakly prolate spheroids of radius between 0.1 and 10 nm immersed in an medium with permittivity given by the SPP refractive index $n_{\mathrm{SPP}} = k_{\mathrm{SPP}}/k_0$, which corresponds to an effective refractive index between the ones of the substrate and of the surrounding material, as is often assumed in empirical calculations [Kuw+03]. This very strong approximation comes from the similar properties between the polarisability of truncated spheres and lying spheroids on a substrate [Win+88]. Further assuming that the scattering efficiency has a Lorentzian lineshape centred at the resonant frequency evaluated from equation (1.46), with a full width at half maximum of 200 nm, the measured DOS can be evaluated as shown in figure 2.6 (c).

The modulation by the spheroid scattering efficiency shows that Γ_{sp} is not enough to describe the observed CL signal from rough metallic surfaces. In the present case, it qualitatively shows how the measured CL signal can present a peak wavelength or spectral variations different from the DOS calculation alone. This model is of course far from being quantitative, but nevertheless gives an insight on the origin of some contributions to the CL signal, and notably shows that the enhancement around 600 nm in the case of the IMIM structure comes from the larger density of surface plasmon modes that are confined in the oxide layer.

2.2.3 IMIM structures with various capping materials

Having detailed the case of a single IMIM structure, we can try to confirm our approach by applying the same modelling to other kinds of stacked films. Additional information can be determined by using different materials, to link the CL response to the materials properties. We thus use Al instead of Au as a thick metallic layer, and study the properties of uncapped, Al-capped and Au capped IMIM structures. Figure 2.7 (a) shows the measured CL signal from infinite structures composed of:

- Au(35 nm)-Al_2O_3(57 nm)-Al(substrate) (blue),
- Al(35 nm)-Al_2O_3(57 nm)-Al(substrate) (green),
- Al_2O_3(57 nm)-Al(substrate) (red)

The corresponding SPP LDOS calculation is reported in panel (b), where we have again only represented the symmetric IMIM mode. The Al_2O_3-Al (red) curve shows the typical wavelength dependence of a SPP mode as expected from a single metallic interface, and retrieved in the CL measurement, with a SPR wavelength of 415 nm. The simulated IMIM LDOS for both Au (blue) and Al (green) top layer display the same increase in DOS around 650 nm, which corresponds to an enhanced coupling to the confined symmetric mode. This well reproduces the measured DOS from the Au-capped IMIM structure in panel (a). The comparison with the Al-capped structure is less favourable, as is the comparison between the relative intensities in the Au-capped and Al-capped systems.

We attribute this discrepancy to the difference in scattering efficiency from the three structures. While e-gun evaporated Au layers have a typical roughness of 0.1 to 10 nm, Al layers present a surface roughness of the order of 20 to 40 nm (see section 2.3.2). In order to evidence the effect of such difference in surface roughness, we use the same modelling procedure

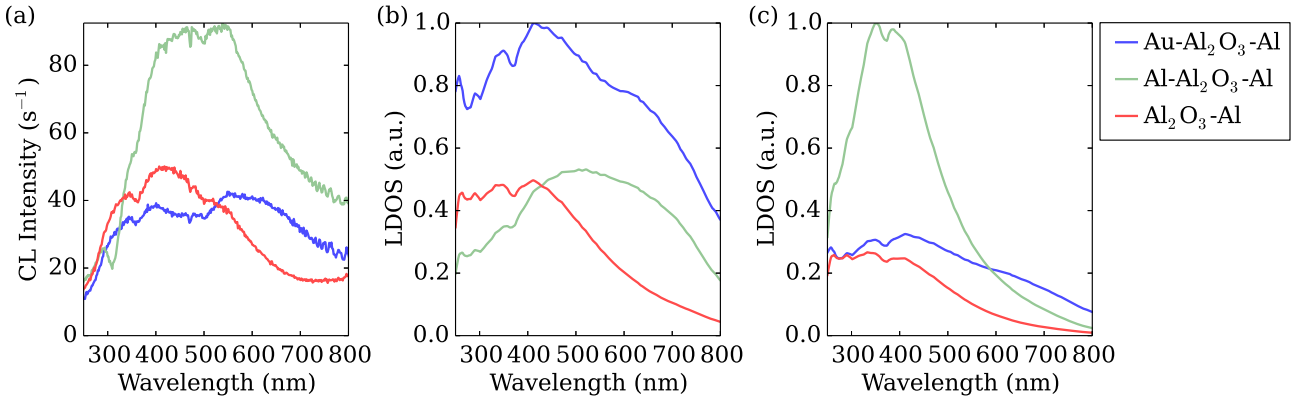

Figure 2.7 – CL spectra and DOS calculation for various capping materials.
(a) CL spectra of different XX-Al_2O_3-Al stacks where XX is Au, Al and Air (see legend). (b) DOS calculations following equation 2.14. Only the symmetric IMIM vertical mode profile is shown. (c) Same DOS modulated by the surface diffraction efficiency (see text). The DOS calculation shows the increase in plasmonic mode density above 600 nm for the IMIM mode, but fails to reproduce the intensity ratios and lineshapes of the measured CL signal. Some features are retrieved by the surface diffraction model, due to the geometrical difference between the Al and Au surfaces.

to describe the scattering by the surface as detailed in the previous paragraph: the scattering by surface particles is described by Lorentzian functions centred at the LSPR wavelength of the particles and with full width at half maximum adjusted to fit the calculated scattering amplitudes. The result of this calculation is presented in figure 2.7 (c). As larger particles have a larger scattering efficiency (see section 1.3.1), the outcoupled signal is stronger for a top Al layer than for a top Au layer, in agreement with the experimental results. Interestingly, this very basic model seems to reproduce the difference in lineshapes between the Au-capped and Al-capped layers DOS. This could maybe be ascribed to the fact that the LSPR of Al particles is blue shifted and sharper in comparison with the one of Au particles (see section 1.3.1), therefore acting differently on the fixed DOS reservoir provided by the symmetric mode around 600 nm. However, we want to strongly stress once more the fact that quantitative evaluation of such surface effects should be properly modelled before establishing further conclusions.

2.2.4 IMIM structures with different oxide spacer thickness

As a final example of the characteristic of IMIM films, we study the effects of the oxide spacer thickness on the IMIM optical properties.

We restrict the discussion on the plasmonic DOS *above* the SPR wavelength of the stacked system. This is due to the fact that for Au-based multilayers, the SPP propagation losses drastically increase below this wavelength. This is exemplified in figure 2.8 where we compare the plasmonic DOS and the SPP effective refractive index $\tilde{n}_{\mathrm{SPP}} = n_{\mathrm{SPP}} + i\kappa_{\mathrm{SPP}}$ for the uncapped and IMIM structures with a 20 nm oxide layer. As already detailed in section 1.2.3, we see that the imaginary part of the refractive index increases below the SPR wavelength due to interband transitions in Au. Hence, contributions to the DOS in this spectral region are only due to very lossy modes, which bear no interest when laterally confining the plasmon modes in plasmonic antennas. When studying the plasmonic DOS of an IMIM film, we are thus only interested in

local maxima at wavelengths above the SPR.

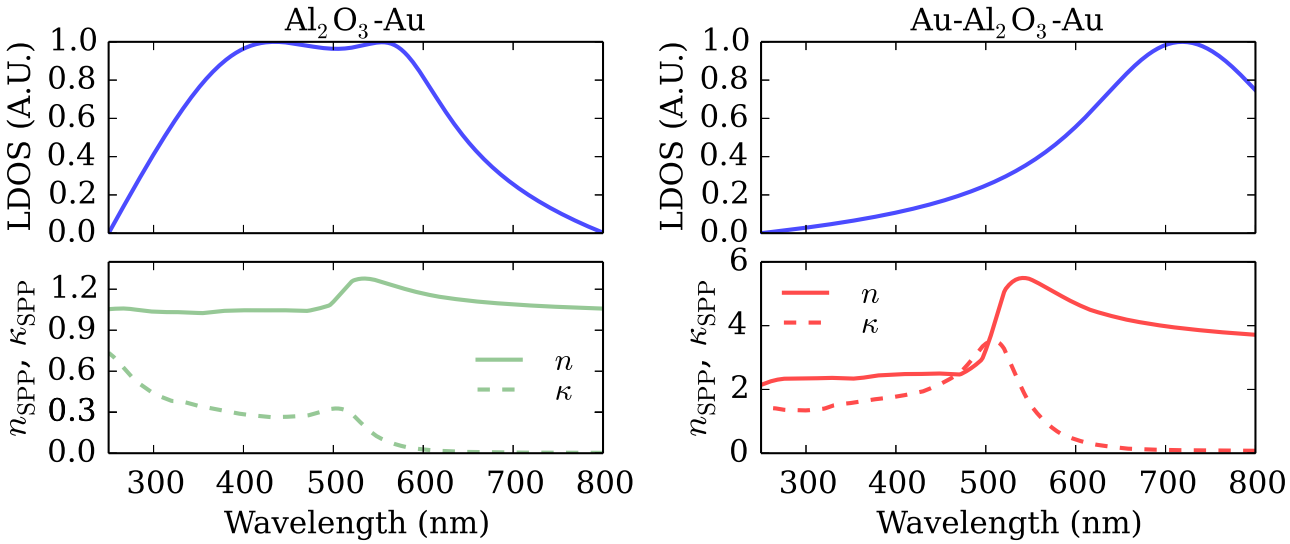

Figure 2.8 – Comparison between the plasmonic DOS and dispersion relation of the SPP modes.
Comparison between the plasmonic DOS and the real and imaginary parts of the SPP effective refractive index $\tilde{n}_{\mathrm{SPP}} = n_{\mathrm{SPP}} + i\kappa_{\mathrm{SPP}}$ for the Al_2O_3-Au and Au-Al_2O_3-Au structures with an oxide thickness of 20 nm. It reveals that modes locates below the SPR wavelength experience a huge increase in propagation losses through κ_{SPP} due to interband transitions in Au.

The results of CL spectroscopy on Al_2O_3-Au and Au(35 nm)-Al_2O_3-Au structures with varying oxide thickness are presented in figure 2.9 (a) and 2.10 (a) respectively, and the corresponding DOS calculations are presented in panel (b) of each figure. The oxide layer thickness is indicated in the legend. Relative amplitudes between the spectra are preserved, allowing to compare directly the amplitude of two spectra in the same panel.

These results show an increasing density of plasmonic modes with increasing oxide thickness, for both the structure without and with the top Au layer. We think that the large spectral structures in the CL signals for the 242 nm oxide layer thickness are due to interferences between the scattered plasmon fields and their reflections at the different surfaces, not taken into account in the simulations, or to luminescence from the alumina layer [Ort+99; Aar+05].

For each graph, we have reported in black solid line a guide for the eye to point out the increase in CL intensity or DOS *above the SPR wavelength* of the layered system. In the case of the IMIM symmetric mode DOS presented in figure 2.10 (b), it corresponds to a local maximum in CL signal, and a maximum of the 2D DOS. The dispersion of this position with respect to the Al_2O_3 thickness shows that we are able to tune the spectral position of this enhanced DOS. This ability to tune the wavelength of the maximum of plasmonic DOS above the SPR will later be employed to tune the dispersion relation of patch plasmonic antenna modes.

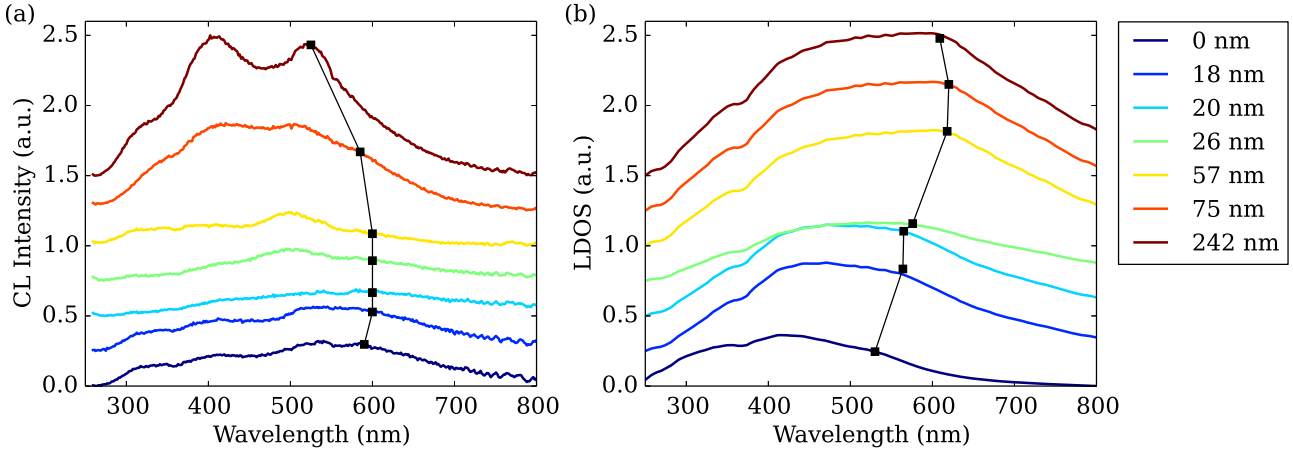

Figure 2.9 – CL and plasmonic DOS of Al_2O_3-Au structures.
(a) CL spectra and (b) DOS calculations for Al_2O_3-Au structures of varying oxide thickness (see legend). The black line is a guide for the eye following the dispersion of the local maximum of DOS above the SPR wavelength (see text).

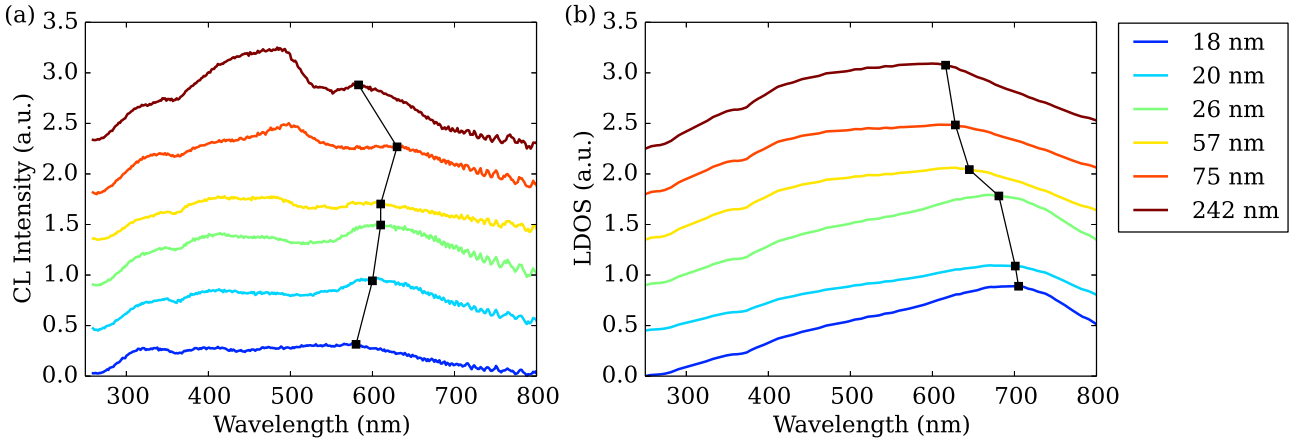

Figure 2.10 – CL and plasmonic LDOS of Au-Al_2O_3-Au structures.
(a) CL spectra and (b) LDOS calculations for Au-Al_2O_3-Au structures of varying oxide thickness (see legend). The black line is a guide for the eye following the dispersion of the local maximum of LDOS above the SPR wavelength (see text).

2.2.5 Conclusion on the optical properties of IMIM films

In the last section, we have demonstrated how CL spectroscopy can be used to study the optical properties of IMIM structures. Electrons impinging on the multilayer structure surface can efficiently generate surface plasmons, and especially probe the symmetric IMIM mode. We have shown that it is possible to establish an expression for the plasmonic DOS of the system using the SPP dispersion relation and mode profile derived from the numerical procedure detailed in section 1.2.3. While this description does not renders directly the CL signal, it gives a lot of information on the density of plasmonic modes, through their spectral distribution and dependence on the geometrical characteristics of the system. A further modelling step would be required to properly account for the observed CL signal through the study of the SPP scattering properties of the rough surfaces in the structure. It has been here only roughly approximated, but still gives an idea of the expected results.

2.3 Plasmonic patch antennas

2.3.1 Introduction on patch antennas

The concept of patch antenna comes from radiofrequency (RF) antennas requiring a low vertical profile. Small flat metallic elements separated from a ground plane by an oxide layer emerged as very promising candidates, acting as planar cavity for electromagnetic radiation. Also known as microstrip antennas because they consist in a truncated microstrip transmission line, they are especially appreciated for their simple design, directivity and large operation bandwidth.

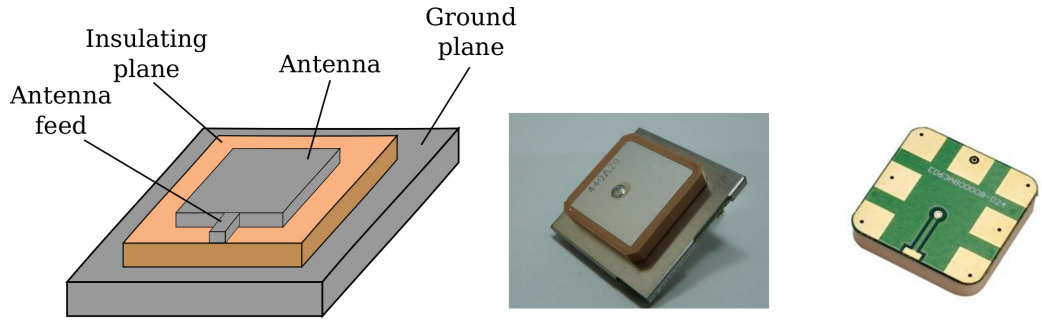

Figure 2.11 – Microstrip patch antenna.
Left: Schematic of a square RF patch antenna, composed of a metallic square separated from a metallic ground plane by an insulating spacer. The antenna excitation is provided by a RF transmission line (antenna feed). Middle and right: examples of commercial GPS patch antenna systems.

A schematic rectangular patch antenna is presented in figure 2.11, along with two examples of commercial GPS patch antennas. Their resonant frequencies is given by the lateral dimensions of the structure which forms a planar cavity for a vertically confined TM field inside the insulating layer.

By geometrical similarities, laterally confined IMIM nanostructures with plasmonic properties were then designated as *plasmonic patch antennas*. The symmetric vertical mode profile

for example is especially similar to the RF fields because of its strong localisation inside the oxide layer. The prediction of the properties of circular plasmonic antennas and their interesting properties in the fluorescence enhancement of QDs localised in the spacing layer in the work of Esteban, Teperik, and Greffet [ETG10] was then followed by theoretical developments [Fil+12; Big+14; UA15], cathodoluminescence spectroscopy and imaging [KGP10; Moh+14] and experimental realisations of the coupling scheme with colloidal quantum dots [Bel+13; HAM16].

As we will see when treating single nanowire quantum dot spectroscopy issues in the next chapter (section 3.2.2), the presence of a metallic substrate is an experimental constraint throughout the work presented here, as it allows a better luminescence collection from the semiconducting emitters. Hence, any relevant plasmonic antenna structure will have to be designed taking this into account. While for a sufficiently large oxide thickness the antenna mode is decoupled from the lower metallic film, studying plasmonic patch antennas appears as a promising route toward fluorescence enhancement, directivity and polarisation control of the emission from the quantum dot structures. We first detail the fabrication process, before demonstrating CL spectroscopy on circular plasmonic patch antennas.

2.3.2 Fabrication

The patch antenna fabrication is performed on Si substrates. A first, optically thick layer of metal (Au or Al) is evaporated on the substrate using e-beam evaporation. In order to get the best optical properties, we aimed at lowering as much as possible the surface roughness and granular structure of the films. Au evaporation is performed under $\sim 10^{-6}$ mbar at an evaporation rate of ~ 2 Å/s. Al has a tendency to oxidise a lot more easily than Au, and therefore smooth Al films are hard to obtain with the vacuums levels available in conventional e-beam evaporation machines. A possible way to improve the quality of the film is to use a higher evaporation rate, in our case 2 nm/s [McP+15]. The spacing oxide layer is then deposited using ALD, and its thickness is controlled using an interferometric measurement after deposition.

All the plasmonic structures studied in this thesis were fabricated by electron beam lithography, as sketched in figure 2.12. An electron-sensitive, positive resist is spin-coated on the sample and soft-baked on a hot plate. The sample is then inserted in the lithography system, and an electron beam patterns the surface of the sample, exposing the resist upon electron impact. The resist is then developed in a methy-isobutyl ketone:isopropanol (MIBK:IPA) (1:3) solution. 35 nm of metal is deposited using electron gun evaporation, and a final lift-off process is performed in N-methyl-2-pyrrolidone (NMP) heated at 80 °C to remove the remaining resist.

Two lithography systems were used during this work: initially, a Zeiss SEM (LEO, [Zei]) with a 30 kV acceleration voltage and a ∼10 pA current, then a NanoBeam nB5 [Nan] device offering much higher acceleration voltages (80 kV) and currents (1 to 10 nA).

When employing the LEO SEM, the Raith Elphy software suite was used to control the patterning [Rai], and we used a bi-layer resist formed with two layers of 2% poly(methyl methacrylate) (PMMA) with respective molecular weights of 50 and 950 kDa, using the electrosensitivity difference of each layer to create a mechanical mask. Both layers were ∼100 nm thick and baked at 180 °C for 5 minutes. This bi-layer resist, formed only by PMMA layers instead of the usual combination of PMMA and MAA copolymer, was developed by Jean-François Motte from the Nanofab team. It helped a lot during the various process steps, yielding more reproducible

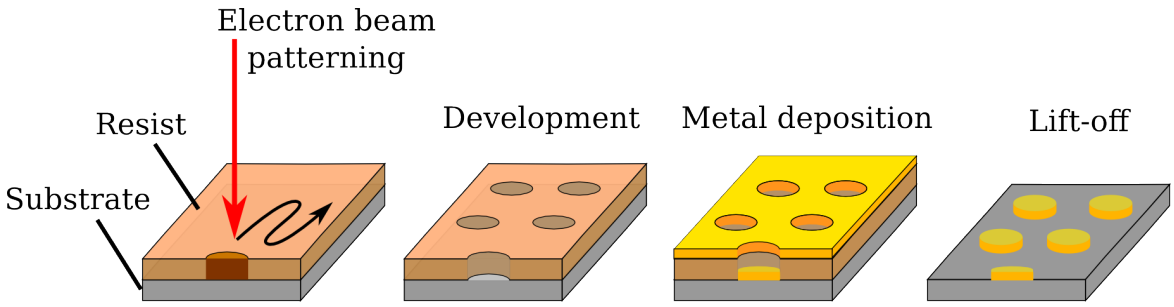

Figure 2.12 – Electron-beam lithography process.
Schematic of an e-beam lithography process. An electrosensitive resist spin-coated on the sample surface is exposed to an electron beam scanning its surface. In the case of a positive resist, a development step in a solvent removes the patterned areas. A metal layer is evaporated on the sample surface, and a lift-off step dissolves the unexposed resist, leaving the metal patterned shapes on the sample surface.

results, because the PMMA alone leaves a cleaner surface after development than the MAA layer, and appears less sensitive to small electron dose and development time variations. The bi-layer structure in the resist also improves the efficiency of the NMP lift-off process.

Lithography with the nB5 system was performed on a single 240 nm thick 3% PMMA layer, also baked at 180 °C for 5 minutes. The high current - high voltage properties of the nB5 systems allowed us to avoid some troubles encountered with the SEM setup, making the use of the bi-layer resist unnecessary. The remarkable precision of the nB5 system allowed fabrication of more controlled and well-defined structures and on a larger scale. It was however bought towards the end of the present thesis, so most of the processes developed here have been optimised for the LEO setup.

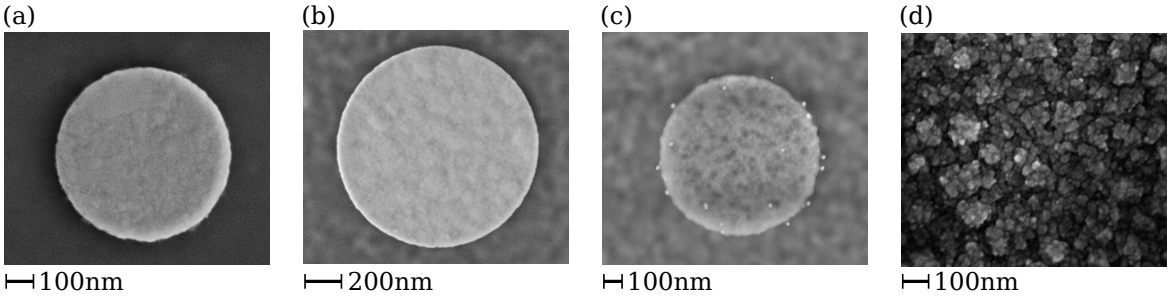

Figure 2.13 – Examples of patch antennas.
(a) to (c): SEM images of circular patch antennas with different materials, with an alumina layer thickness of 57 nm. (a) Au antenna on a Au-Al_2O_3 substrate. (b) Au antenna on a Al-Al_2O_3 substrate. (c) Al antenna on a Al-Al_2O_3 substrate.
(d) Image of a bare Al surface before oxide deposition.

Figure 2.13 shows SEM images of circular patchs antennas made of Au and Al on Au-Al_2O_3 and Al-Al_2O_3 substrates, as well as an image of a bare Al surface before antenna fabrication. Comparing the substrate around the antenna between panel (a) and (b),(c), we can see that the Au substrate presents a smaller roughness than the Al substrate. It is evidenced by panel

(d), which shows that the Al surface before the ALD step is extremely rough with grains of a few tens of nanometres in size. In comparison, a Au surface has a typical grain size of 10 nm and looks like the antenna surface on panel (a). We noticed that the surface quality of the Al layer degrades with increasing thickness. Hence, as visible from panel (c), the antenna surface appears of better quality because the antenna is only 35 nm thick, while the continuous Al film is 100 nm thick. As the ALD of alumina produces a conformal layer, the final antenna surface is also influenced by the poor quality of the Al layer, as visible from the greater roughness of the Au antenna in panel (b) with respect to its counterpart on a Au base layer.

2.3.3 A simple theoretical model for disk patch antennas

While plasmonic patch antennas can be made with arbitrary shapes, we focused on circular patch antennas as they appear very promising in their coupling properties to localised emitters [ETG10; Bel+13; Big+14]. They are particularly interesting as a starting point because of their high degree of symmetry, simplifying the theoretical analysis. It is worth mentioning that other geometries and fabrication techniques are investigated, such as dispersing chemically synthesised Au nanocubes [HAM16].

We detail the theoretical model describing the optical properties of the circular patch plasmonic antennas as proposed in ref. [Fil+12], and extensively used in a recent cathodoluminescence study on circular patch antennas [Moh+14]. Note that we did not implement the full theory proposed by Filter et al. [Fil+12] but its simplification presented in ref. [Moh+14]. The main consequence of this simplification is detailed later.

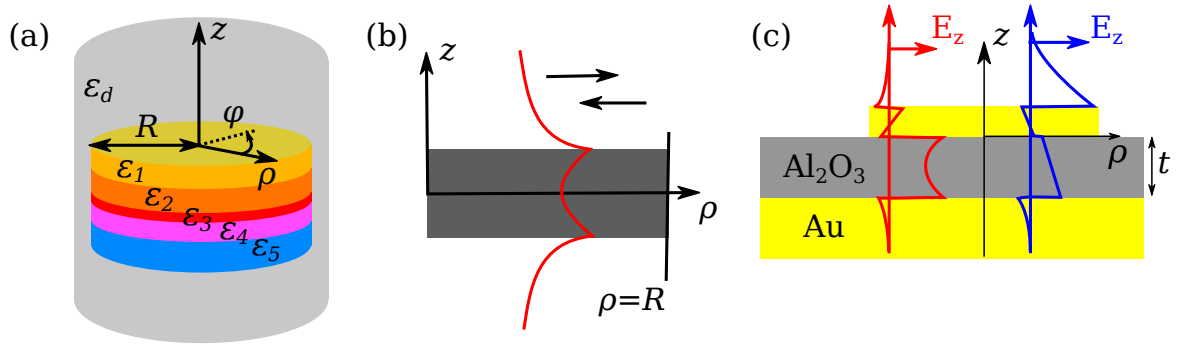

Figure 2.14 – Patch antenna model: theoretical configuration and definitions.
(a) Sktech of the general system under investigation: we consider a circularly symmetric stack of layers of permittivity ε_i embedded inside an infinite homogeneous medium of permittivity ε_d. The stack has a finite radius R. (b) The resonator model relies on the circular symmetry of the system and assumes that it supports outward Hankel-type SPPs that are reflected at the $\rho = R$ boundary of the system. (c) Sketch of the experimental geometry. Contrary to the theoretical case, only our antenna is of finite radius R. The other layers can be considered infinite. The system supports two main vertical profiles of SPP modes denoted as symmetric (red) and antisymmetric (blue) with respect to the symmetry of their E_z component.

The system under consideration is presented in figure 2.14 (a). It consists in an arbitrary number of circular layers *of the same radius* R with permittivities $\varepsilon_{i=1,2,...}$ embedded inside an homogeneous medium of permittivity ε_d. Because of the circular symmetry of the problem, the

field is decomposed into outward propagating Hankel-type SPPs that are reflected at the $\rho = R$ boundary into inward propagating SPPs, as depicted in figure 2.14 (b). This representation in terms of Hankel-type SPPs is necessary to define out and inward propagating waves, and allows the authors of ref [Fil+12] to evaluate the reflection coefficient at the $\rho = R$ interface. However, the Hankel functions are not finite at the origin. Hence, to describe the localised plasmon modes of the antennas, the model assumes that the field is decomposed into eigenmodes of the circularly symmetric geometry in which the z and ρ and φ dependences can be separated as:

$$E_z^m(\rho, z) = a(z)\, J_m(k_{\mathrm{SPP}}\rho)\, \mathrm{e}^{im\varphi} \tag{2.15}$$

where $a(z)$ is the vertical mode profile, J_m is the Bessel function of the first kind of azimuthal order m, and k_{SPP} is the surface plasmon polariton wave vector supported by the multilayer structure. The Hankel and Bessel functions are related through:

$$H_m^{\pm} = \frac{J_{-m} - e^{\mp m\pi i} J_m}{\pm i \sin m\pi}. \tag{2.16}$$

The eigenfunctions are further determined by the resonance condition:

$$\mathrm{Re}\{k_{\mathrm{SPP}}\}2R + \varphi_m = 2x_n(J_m). \tag{2.17}$$

The phase factor φ_m accounts for the phase accumulated upon reflection at the patch edge. x_n is the $n-th$ zero of the Bessel function J_m. While φ_m can be directly calculated according to ref. [Fil+12], we used the empirical formulas and method reported in ref. [Moh+14] instead. The main approximation is that φ_m is considered the same for all antenna modes (n, m) while ref. [Fil+12] shows that this coefficient can vary with the azimuthal order m. A detailed calculation of φ_m appeared however prohibitively complicated within the time frame of this work.

Equation 2.17 gives the resonant frequencies $\omega_{n,m}$ of the disk after inversion of the SPP dispersion relation. Similarly to the 2D case, the LDOS probed during the CL experiment can thus be expressed as:

$$\boxed{\Gamma(\omega, \rho) \propto \sum_{n,m} \left|E_z^{n,m}(\rho)\right|^2 \mathcal{L}(\omega, \omega_{n,m}, \gamma)} \tag{2.18}$$

where the mode profile $E_z^{n,m}(\rho)$ is normalised in energy, and $\mathcal{L}(\omega, \omega_{n,m}, \gamma)$ is a normalised Lorentzian function centred at frequency $\omega_{n,m}$ with a full width at half maximum γ given by $\gamma/\omega = (2\,\mathrm{Im}\{k_{\mathrm{SPP}}\})^2 + \gamma_0(1+\omega_{\mathrm{norm}}^b)^{-1}$, where γ_0 and b are adjustable parameters used to fit the resonance bandwidth of the antennas, and $\omega_{\mathrm{norm}} = \omega/(1800\ \mathrm{THz})$. The frequency broadening of the antennas resonances describes the loss-induced frequency broadening of the plasmonic patches. Note that as the LDOS is related to the square modulus of the electric field, one can only detect the radial dependence of the plasmon mode, and not its azimuthal dependence.

Both $a(z)$ and k_{SPP} are determined using the numerical procedure detailed in section 1.2.3. In our geometry two vertical mode profile coexist, the symmetric and antisymmetric modes, sketched in red and blue solid lines respectively in figure 2.14 (c). We note that contrary to other studies on milled structures [KGP10], our experimental configuration, depicted in figure 2.14 (c), *does not strictly correspond to the model* as only the top disk has a finite radius R (or equivalently diameter D). In ref. [Moh+14] the lower metallic film is also infinite, but both the

oxide layer and top metal layer are of radius R. In these last two configurations, the plasmon field is not strictly restricted to the region $\rho \leq R$, deviating from the theory as the latter is based on a "cavity" model. As pointed out in ref. [Fil+12], discrepancies between the model and experimental results might appear if the reflection coefficient at the antenna boundary strongly deviates from unity. In the case of ref. [Moh+14], the fact that the oxide layer is also limited in the $\rho \leq R$ region ensures a high reflection coefficient at the antenna boundary. In opposition, this is less true in our experiment, deteriorating the predictions of the model. A possible correction accounting for our experimental configuration is to consider an effective dispersion relation of the resonant wavevector k_{eff} describing the fact that the plasmon field can extend outside of the $\rho \leq R$ region, as will be discussed later. However, even if the model loses its *predictive* quality, it gives a good insight on the physics of such patch antennas and is thus still worth considering.

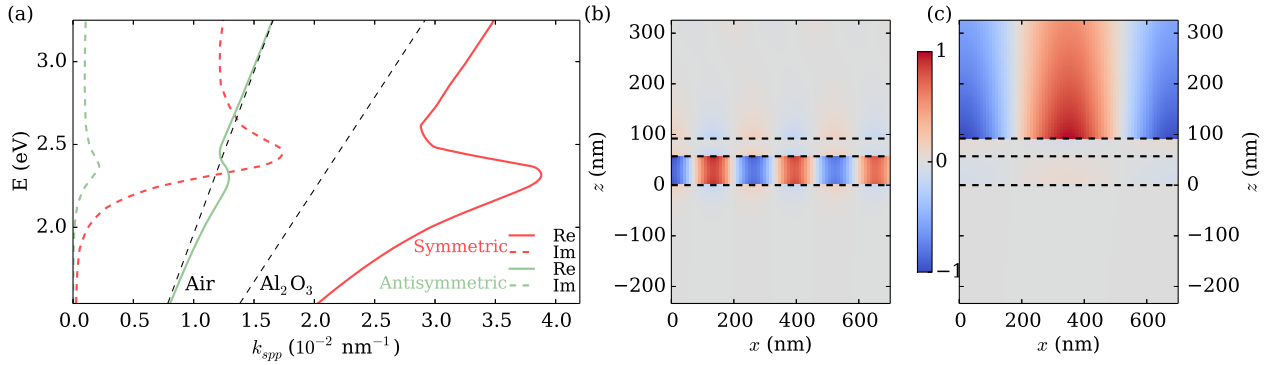

Figure 2.15 – Reminder of the IMIM surface plasmons properties.
(a) Real (solid lines) and imaginary (dashed lines) parts of the SPP dispersion relation of the symmetric (red) and antisymmetric (green) IMIM modes, compared with the light lines in air and alumina (black dashed lines). (b) and (c) Normalised amplitude of the z-component of the electric field corresponding to the symmetric (b) and antisymmetric (c) SPP modes.

As an example, let us consider the IMIM structure already discussed in details in section 1.2.3 composed of an optically thick Au layer ($\geq$ 100 nm), a 57 nm thick alumina spacer and a 35 nm thick Au top layer. Its properties are recalled in figure 2.15. The antisymmetric mode is almost index-matched to air and weakly confined at the upper Au-Air interface, while the symmetric mode exhibits a dispersion relation well below the light line in alumina, and is confined inside the Al_2O_3 spacer. It also suffers from greater propagation losses than the anstisymmetric mode. Because it presents a very strong electric field inside the alumina layer matching the polarisation of the exciting field, this mode plays a dominant role in the CL experiment, as discussed in the previous section. Hence, as in refs. [KGP10; Moh+14], we restrict the subsequent analysis to the symmetric vertical mode profile.

For a 300 nm diameter disk antenna, we invert the dispersion relation of the symmetric mode to find the resonant wavelengths of the patch antenna using equation (2.17), and compute the associated LDOS. The result of this calculation is presented in figure 2.16, using the parameters $\gamma_0 = 0.2$, $b = 1.7$ and $\varphi_m = 2.2$ rad. Panel (a) shows the antenna resonant spectrum (blue thick line) with two pronounced peaks. Panels (c) and (d) show the different modes of radial

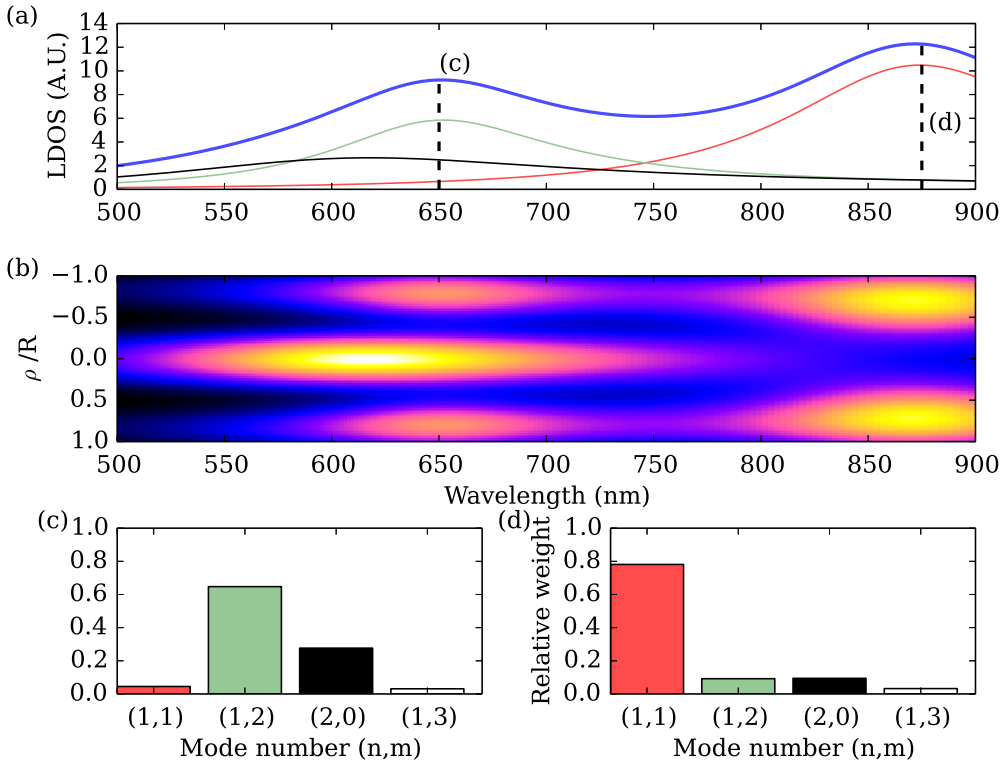

Figure 2.16 – **Calculated LDOS of a** 300 nm **diameter patch antenna**.
(a) LDOS spectrum of the antenna (blue thick solid line) and the three first antenna modes $(n, m) = (1, 1)$, $(1, 2)$ and $(2, 0)$ (thin red, green and black lines respectively). (b) Spatial map of the LDOS as a function of the wavelength and the antenna reduced radius ρ/R. (c) and (d) Histogram of the contributing Bessel modes. The colors of the first three rectangles correspond to the ones in the spectrum (a). The numbers below the chart indicate the (n, m) quantum numbers.

order n and azimuthal order m supported by the antenna, and their relative contribution on the spectrum at 650 nm and 875 nm respectively. They are shown in panel (a) in thin lines with their corresponding colour. The antenna LDOS in panel (b) reveals the spatial dependence of the electric field as a function of the reduced radius ρ/R. Notably, we see that in the long wavelength range (peak at 875 nm in the spectrum), the LDOS is located on a single ring of constant radius, and has a zero in the antenna center, corresponding to a $n = 1, m = 1$ mode [panel (d)]. On the contrary, the peak at 650 nm is composed of two Bessel modes, a ring-like mode (green line in the spectrum) $n = 1, m = 2$, and a mode located at the antenna center (black line) with $n = 2, m = 0$ [panel (c)]. The last mode is weakly contributing and is not represented.

As pointed out in ref. [Moh+14] it is important to realise that the spectrum of increasingly large antennas is not constituted only by Bessel modes of increasing radial quantum numbers, but is a superposition of modes of increasing radial and/or azimuthal number. Furthermore, due to the large bandwidth of each resonance, single mode operation is impossible for diameters larger than a few hundreds of nanometres. Here it is clear that for a 300 nm diameter antenna, only the first (red) resonance is composed of a single mode. This is a major difference with the

RF patch antenna case, for which only the $\lambda/2$ fundamental mode is used in most configurations.

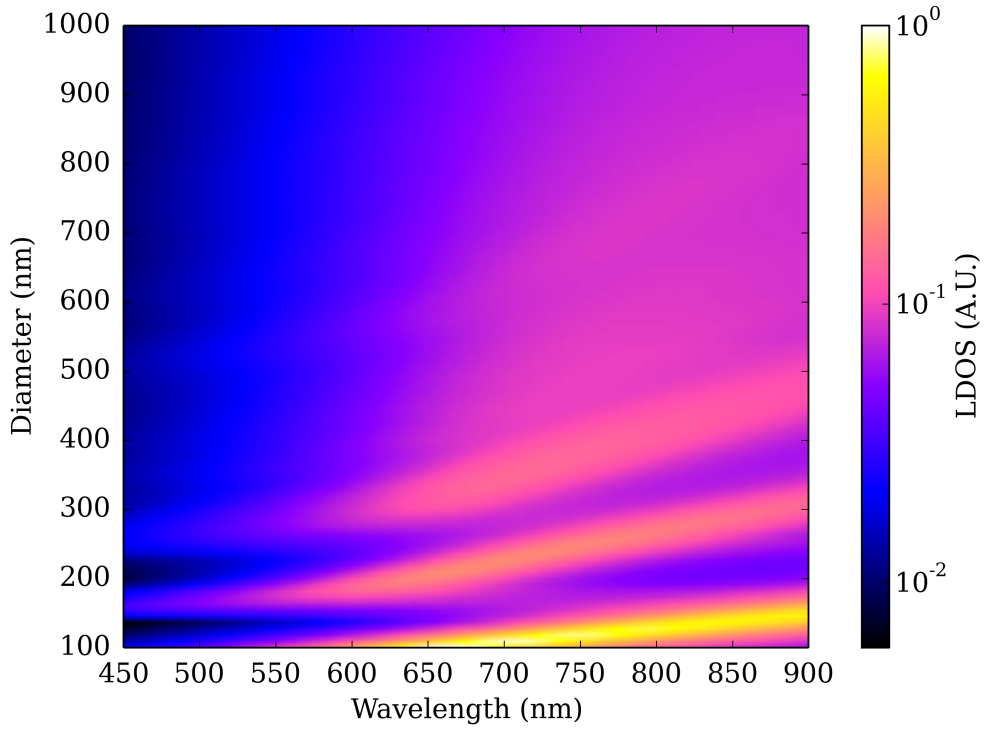

Figure 2.17 – Spectral map of the patch antenna resonances.
Calculated spectral map of the patch antennas resonances as a function of wavelength and antenna diameter. The colour encodes the LDOS amplitude (note the logarithmic colour scale). Successive mode branches appear, composed of one or more Bessel modes of the patch antenna (see e.g. figure 2.16). The parameters used in the calculation are $\gamma_0 = 0.1$, $b = 1.7$, $\varphi_m = 2.2$ rad.

Gathering the LDOS spectra for different antenna size yields the spectral map presented in figure 2.17 (normalised to the antenna area), using the same computation parameters. It shows clear successive mode branches revealing the dispersion relation of the successive Bessel modes with increasing antenna size. Here the particles are described as plasmonic cavities for SPPs, but this dispersion can also be thought of as induced by retardation effects due to the size of the particle if reasoning in terms of LSP modes, as presented in section 1.3. No LDOS is present below the SPR wavelength because of the strong losses due to interband transitions in Au, limiting the operating range of the antennas to above this resonant wavelength. To properly describe the antenna resonances, one finally has to match the position and dispersion of the mode branches with the experimental results presented thereafter.

2.3.4 Cathodoluminescence of circular patch antennas

To confront this model to our experimental data, we fabricated disk patch antennas of various diameters on a Au(thick)/Al_2O_3(57 nm) substrate, and characterised them using CL spectroscopy.

Spectral properties

For this experiment, the electron beam is raster scanned on the antenna surface in a square region exactly circumscribing the antenna, using the same magnification and scanning speed for all the antennas. The e-beam scanning time is set to be much smaller than the integration time (∼1 minute) so that every point on the antenna surface can be considered as equally excited. The CL signal is spectrally dispersed by the 150gr/mm grating and collected by the CCD camera. The rapid scanning of the electron beam ensures us that no or little spatial drift occurs, and that it can be corrected in real time during the acquisition if necessary. It also reduces the deposition of impurities in order not to interfere with the LDOS imaging experiment described in the next section. A background spectrum is taken by exciting the same area of the substrate without the top disk and subtracted from the antenna spectrum to remove eventual fluorescence from the substrate.

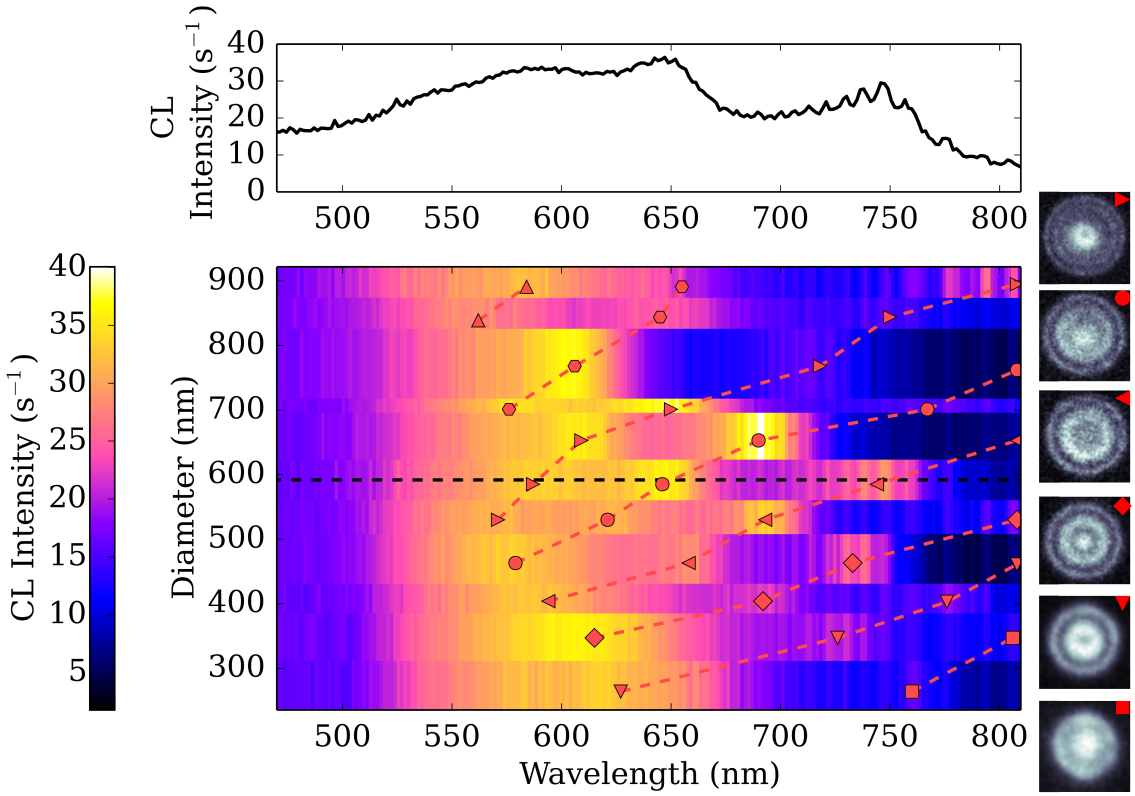

Figure 2.18 – Experimental CL spectral map of patch antennas.
Experimental CL spectral map of the plasmonic patch antennas, as a function of wavelength and antenna diameter. The colour encodes the CL signal intensity (linear scale). The top inset shows a typical antenna spectrum corresponding to the black dashed line cut in the 2D map. A broad resonance is visible at 590 nm, which remains at the same energy for all the antennas. Sharper resonances are visible at lower energy. They red-shift with increasing antenna diameter, showing the dispersion relation of the successive patch modes. Each patch mode branch is represented by a dashed red line with a symbol indicating the position of each resonance. The corresponding LDOS image reconstructed from the CL signal is shown in the insets on the right for the first six modes.

The results of this experiment are presented in figure 2.18. A typical antenna spectrum (top panel) is composed of a broad peak around 590 nm, and of one or several sharper peaks at lower energy. The rapid oscillations in the spectrum (less than 10 nm in bandwidth) are due to fringing. Gathering the spectra for all the antennas yields the corresponding spectral map, which reveals that the sharper peaks red shift with increasing antenna dimension, while the broad peak at 590 nm remains at a constant energy. It is present at the same energy for other antennas of different shapes and dimensions fabricated on the same substrate. This peak has a very complex origin, and is discussed in more details in sections 2.3.5 and 2.3.6. The red-shifting resonances align in successive branches as in the theoretical model (figure 2.17). At higher energy with respect to the fixed resonance, the remaining CL signal is not due to plasmons but to residual interband luminescence of Au (see section 2.3.6). The background signal subtraction from the substrate does not remove all the Au fluorescence from the spectrum because a larger Au volume is excited when scanning the antenna, leading to this additional contribution.

However, this spectral characterisation alone is not sufficient to determine the model fitting parameters, as it is necessary to identify the Bessel modes contributing to each resonance. We thus need to measure the CL intensity as a function of energy and position of the electron beam to image the plasmonic LDOS and unambiguously determine the antenna modes.

Spatial properties

We reconstruct the spatial profile of the LDOS for each resonance by slowly scanning the electron beam over the antenna surface, filtering the total CL emission in a 50 to 80 nm spectral bandwidth around the resonance. This filtered CL emission is then integrated on an avalanche photodiode (APD) and correlated to the electron beam position. The spectral integration bandwidth is selected to maximise the collected intensity, matching the resonance bandwidth but ensuring that we collect only light emitted from a single resonance. However, it is too broad to directly resolve all the distinct Bessel modes contributing to a given resonance. The APD output is connected to an electronic pulse generator. We ensure that the amplitude and time of the pulse are set so that we operate in a photon counting mode. Typically, the pulse duration is one third of the pause time of the electron beam on each position. The resulting image is thus composed of pixels of discrete intensity values. A digitalisation step is perform to convert these discrete intensity values into a number of counting events. To account for the spatial extension of the electron beam, a spatial Gaussian filter of 10 nm width is applied on the signal. In the rest of the manuscript, the LDOS image presented is the filtered image normalised in intensity. The typical emission probability is of the order of 10^{-6} photons per incident electrons. A more detailed description of the LDOS image processing is available in appendix A.

Because of the low yield of the process, one has to use a very slow scanning time for the electron beam, potentially leading to an electrostatic drift which can not be corrected in real time. This imposes an upper limit on the achievable integration time and hence signal to noise ratio of the experiment. Furthermore, as the beam remains at a fixed position for a long time, a lot of contamination by e-beam induced impurity deposition occur during the process, strongly degrading the measurement with time and imposing another limit on the experiment. To avoid at best these drawback while maintaining a good signal to noise ratio in our LDOS images, we used a pause time on each position of the order of a few seconds. This ensured almost no electrostatic drift, and a reasonable contamination allowing to record around 3 to 5 images per

antenna before significantly degrading its properties.

We performed this LDOS imaging on all the resonances in the spectral map. The fixed, broad resonance does not reveal any spatial dependence of the LDOS, and will be discussed in more details in the next sections. On the contrary, all the resonances belonging to a given branch show the same spatial structure, represented by the insets in figure 2.18 with the corresponding symbols indicating their mode branch. The LDOS patterns successively present a minimum or a maximum of CL intensity in the center of the antenna. Successive maxima in the antenna center indicate successive radial orders of the $m = 0$ mode. Concentric ring structures with a zero LDOS at the disk center correspond to different Bessel $m > 0$ modes of radial order n.

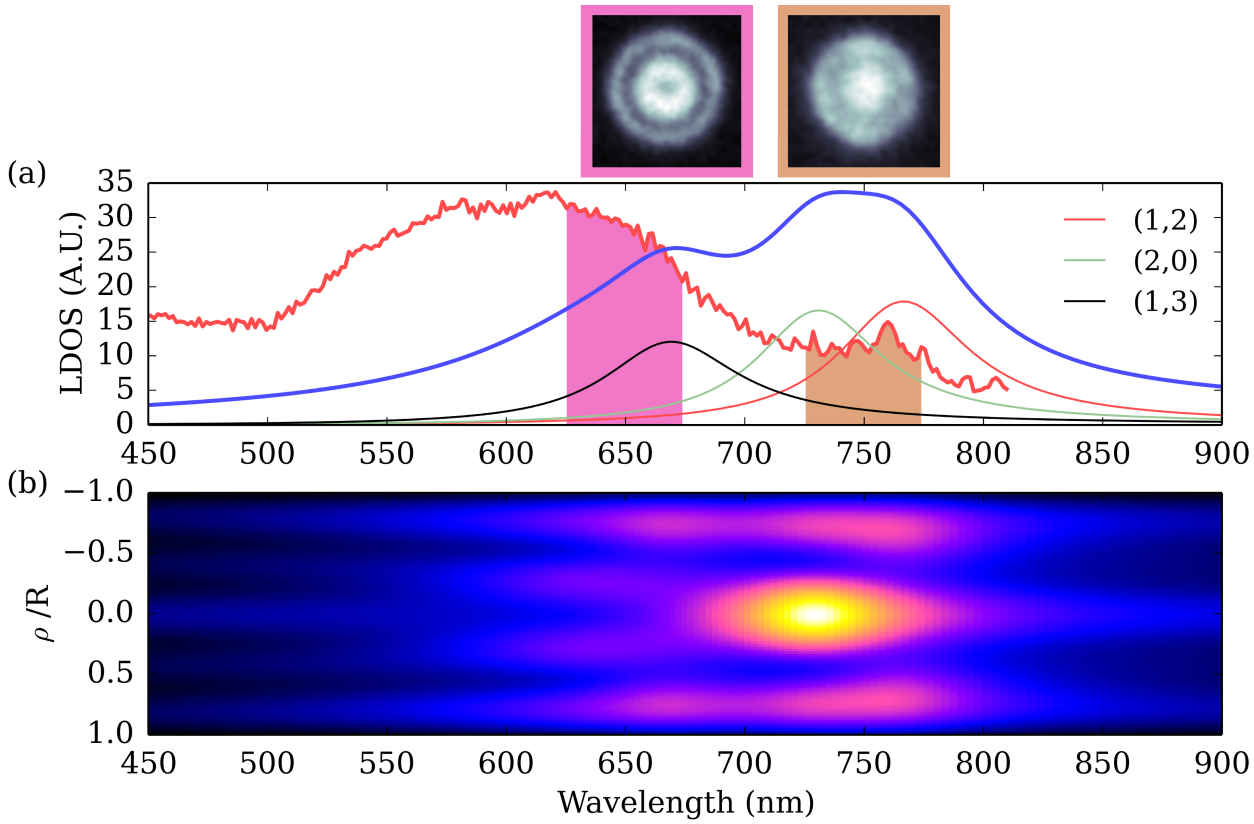

Figure 2.19 – Comparison between the LDOS model and the CL properties of a patch antenna.
(a) CL spectrum of a 272 nm diameter patch antenna (red thick solid line), to be compared with the simulated LDOS spectrum (thick blue solid line). The thin lines (red, green and black) show the calculated Bessel modes of order (n, m) (see legend) contributing to each resonance. It corresponds to the bottom line of the spectral map in figure 2.17. The insets show the experimentally reconstructed LDOS image from CL. The coloured regions under the experimental spectrum indicate the respective integration bandwidth for each experiment. (b) Simulated LDOS map as a function of wavelength and reduced diameter ρ/R, to be compared with the insets in (a). The lowest energy resonance is composed of the $(n = 1, m = 2)$ and $(n = 2, m = 0)$ modes, leading to the bright antenna center, while the highest energy one is mainly composed of the $(n = 1, m = 3)$ mode and thus has no LDOS at the center.

Having identified the n and m orders of the lowest resonance, we can deduce the fitting parameters for the resonator model $\gamma_0 = 0.1$ and $b = 1.7$. As mentioned previously, we have to introduce a correction to the dispersion relation for the antenna mode wavevector because of the low reflection coefficient at the antenna boundary. The effect of φ_m is simply to shift the resonant energies to larger or smaller diameters, and acts equally on all the modes. To properly describe the various modes branches dispersions, we need an additional modulation as a function of the wavelength. The effective wavevector k_{eff} was determined by fitting the dispersion relation of the second mode branch with the expected resonant diameters, using an empirical scaling similar to the one used for the resonance linewidth:

$$k_{eff} = k_{\mathrm{SPP}}(\alpha + \beta x^{-1}) \tag{2.19}$$

where $x = k_{\mathrm{spp}}/k_{norm}$, $k_{norm} = 2\pi/800$ nm. We found $\alpha = 1.1$, $\beta = 0.5$, and finally a phase factor φ_m of 0.8 rad (see the discussion below for the impact of these parameters on the value of k_{eff}).

For comparison, figure 2.19 (a) shows the simulation results for a 272 nm diameter antenna along with its measured CL spectrum (thick red line) and the measured LDOS at the two resonances positions. The coloured regions show the spectral integration bandwidths for the LDOS measurements. This spectrum corresponds to the first line of the spectral map in figure 2.18. The simulated spectrum is presented in blue solid lines, and the three mainly participating mode in thin lines. The numbers in the legend represent their respective (n,m) orders. The simulated spatial profile of the LDOS is shown in panel (b). We can see that the lower energy resonance is composed of two Bessel modes (thin red and green lines) while the higher energy resonance is mainly composed of the $(n = 1, m = 3)$ mode. The rest of the participating modes are not represented, but give a rather low and flat contribution. The simulated spatial profile of the LDOS agrees with the measurements, revealing that the low energy resonance is composed of a bright ring and a bright antenna center while the high energy one is composed of two concentric rings. Note that only the green resonance contributes to the LDOS signal in the center of the antenna, as it is the only mode that posses a $m = 0$ azimuthal number.

Discussion on the LDOS model

So far we have fitted the dispersion relation of the patch modes with the experimental data, and confirmed the general agreement between the simulated spatial LDOS profile and the measured LDOS. Let us now discuss the validity of this LDOS model.

Several discrepancies are to be considered:

- The broad resonance at 590 nm is not present in the LDOS model, showing that it does not originate from the discrete number of Bessel modes supported by the patch. Its origin is complex, and some hints are presented in sections 2.3.5 and 2.3.6.

- The amplitude ratios between different resonances is not always reproduced,

- It is worth pointing out that the correction to the dispersion relation of the patch modes reveals that the model underestimates the mode wavevector by a factor 1.5 to 2,

- In the initial model [Fil+12], the authors show that in fact, the reflection coefficient at the patch edge varies with the dimensionless number k_0R where k_0 is the free-space wavelength, but also with the mode order m. Following ref. [Moh+14], we have considered it constant for all structures and mode orders.

However, it contains two major physical elements:

- It clearly shows that modes of increasing n and m orders compete, and not only successive radial orders. This point is crucial in order to understand the mode structure of the antennas.

- The different modes evolve with different dispersion relations. While the IMIM model alone does not fully reproduce this dispersion, it is evidenced in figure 2.19 by the fact that the mode $(2, 0)$ with $m = 0$ (green thin line) appears at higher energy than the $(1, 2)$ mode (red thin line).

The first two discrepancies naturally arise because *this model only describes the LDOS of the patch antenna*. In contrast, CL does not only probe the LDOS of the antenna, but a quantity related to the *radiative* part of the LDOS at each electron beam position [LK15]. This means that the intensity of the collected CL signal depends on the radiative efficiency of each mode, that is not taken into account in the LDOS model. Especially, the LDOS tends to increase with the antenna size because it can support an increasing number of modes, as introduced in section 1.3. On the contrary, while high order plasmonic modes can present a strong extinction, their radiative efficiency can decrease with increasing mode order [LK15]. Furthermore, CL due to other phenomena such as fluorescence from interband transitions or excitations of surface plasmons at wavevectors different from k_{SPP} are not accounted for in this model.

The fact that we need to correct for the dispersion relation of the patch modes forbids any predictive use of this model in our case. However, calculating the reflection coefficient for each mode appears prohibitive, especially for highly multimode structures, and strongly reduces the interest of a semi-analytical model. In their work, Mohtashami et al. report that no one-to-one correspondence can be found between the model and their experimental data [Moh+14]. Here we clearly show that in the case of monomode or few mode structures, we do obtain at a one-to-one correspondence. Hence, we believe that this model mainly has a *descriptive* quality, as it allows a better understanding of the complex interplay between the different Bessel modes supported by a given structure.

To better emphasise this last point, we present in figure 2.20 the comparison of an experimental hyperspectral map of a patch antenna and its corresponding simulated LDOS. The patch antenna is a Au disk structure on a Al/Al_2O_3 substrate and has a diameter of 435 nm. The effect of the change in substrate is discussed in section 2.3.6 but does not alter the mode structure of the antenna. The experimental data were obtained using a commercial CL setup produced by Attolight [Att], with the help of Névine Rochat (CEA-Leti, PFNC). This setup allows for hyperspectral imaging which is not accessible in our own experiment. It thus provides a direct comparison with the simulated spatial LDOS maps, allowing us to resolve the different contributions of each mode. However, as the acceleration voltage of this setup is limited to 10 keV, it has a lower plasmon generation probability. Furthermore, light collection is possible in a narrower angle than our mirror, changing the relative contribution of each plasmon mode.

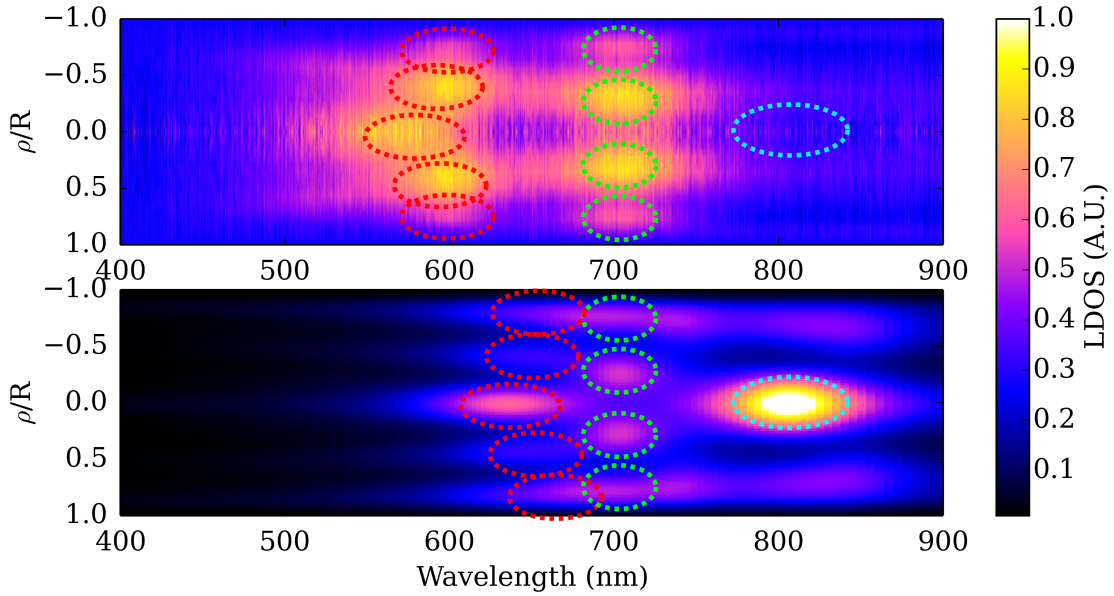

Figure 2.20 – Comparison between experimental and simulated hyperspectral maps. Comparison between an experimental CL hyperspectral map (upper panel) and the corresponding simulated LDOS map (lower panel) of a plasmonic patch antenna of 435 nm diameter. The two high energy resonances are well reproduced. Especially, the highest energy one clearly evidences the separation of the $m = 0$ mode (bright antenna center) from the $m \neq 0$ modes (ring-like structures), circled in red dashed line. The double ring structure is also well reproduced (green dashed line). We note that the lowest energy mode in the simulation is also expected to appear in the experiment (cyan dashed line). We could detect it very well for other antenna diameters, and extrapolation of its experimentally determined dispersion relation places it around 800 nm. We attribute its absence from all our experimental data to the interband absorption in Al (substrate) at this energy.

Because of its hyperspectral operation principle, performing CL characterisation with this setup is by far longer than in our experiment. Hence, we could not perform many experiment with this setup and restrict its use to the present result.

The comparison reveals fine details that could not be retrieved using our own CL experiment. Three resonances are present in the model. In the case of the highest energy mode (red dashed ellipses), it reveals that the $m = 0$ mode (producing a maximum at the antenna center) appears at a slightly higher energy than the $m \neq 0$ modes (ring-like contributions). The double ring structure of the central mode around 700 nm (green dashed ellipses) is also well reproduced. Furthermore, the spatial localisation of these rings while going from the 700 nm resonance to the high energy one is well described, as the inner ring seems to "open up" while the outer ring remains at a constant radius in both the experiment and the simulation. However, the spatial extension of these structures is much small in the simulation, probably because of the low spatial resolution of the 10 keV electron beam. We note that the lowest energy mode (cyan dashed ellipse) with a maximum at the antenna center was expected to appear at a wavelength of ∼800 nm in our experimental data, considering its dispersion measured on other antennas of smaller diameter. Its absence in this experiment is still not completely clear, but we think that

it is due to the strong absorption of Al in this region due to interband transitions (see section 1.1.3). In fact, the CL signal degrades at this wavelength for all the antennas on this substrate [see figure 2.24 (b)]. Finally, the dispersion relation of the simulated modes is not well describe near the SPR of the Au antenna as the high energy resonance appear red-shifted with respect to the experimental data.

As a conclusion, the LDOS model proposed in refs. [Fil+12] and [Moh+14] lacks several physical ingredients to properly describe the CL properties of plasmonic patch antennas. It appears to render well their mode structure, and has the extremely important advantage to clearly evidence that an antenna resonance can be composed of several competing Bessel modes. However, it fails at correctly predicting the dispersion of these modes. Neglecting the antisymmetric vertical mode profile appears as the first simplification to tackle, but taking this mode into account results in a lot of free parameters one would have to determine for this model. As we can not differentiate between the vertical mode profiles in the experimental data, simply superimposing the two profiles as has been done in ref. [Bar+11] for metallic stripes appears to be a dead-end.

To better understand all these CL results, we started a numerical simulation effort in collaboration with Guillaume Bachelier and Guillaume Laurent (Institut Néel, NOF team). The initial step is to use an electric point dipole as excitation [Bar+11; Moh+14]. However, simply scanning the dipole in the dielectric spacer as proposed in [Moh+14] does not readily reproduce the experimental results. Notably, it appears that it results in a coupling to the symmetric and antisymmetric mode different from the one we observe in CL. It is worth reminding here that in our configuration, CL probes the z-component of the LDOS *integrated along the electron trajectory*. Hence, coupling to the antisymmetric mode can be expected when the electron is above the antenna surface. However, an efficient excitation of this mode would require that the phase accumulated by the electron field flips by π over the whole antenna+spacer thickness [Kut09, ch. 8], which is not the case for a 30 keV electron beam. In opposition, the symmetric mode profile matches the electron beam polarisation and phase accumulation. Hence, finding a numerical description of the CL process in our configuration is still pending at the end of this work.

2.3.5 Effect of the spacer thickness

Having studied the effect of the spacer thickness on the properties of IMIM films in section 2.2.4, and the CL properties of the circular patch antennas, we now detail the effect of the spacer thickness on the patch antenna properties. Figure 2.21 (a),(b) shows the comparison of the spectral map obtained for (a), a 17 nm spacer thickness and (b), the reference 57 nm thickness. The analysis in section 2.3.4 showed that the lowest mode branch of the spectral map does not correspond to the fundamental $(n = 1, m = 1)$ antenna mode. We thus scaled down the antenna sizes for this new sample, down to a diameter of 100 nm. We performed LDOS imaging on all the antenna resonances, and reported the corresponding LDOS pattern on the spectral map. An example of each LDOS image is shown in panel (e), with the corresponding symbol.

First, we show that the lowest order resonance can be achieved, and is plotted in green triangles. The antenna mode is composed of the fundamental $\lambda/2$ resonance, as evidenced by the LDOS that displays a single ring pattern. Second, we see that the spacer thickness changes

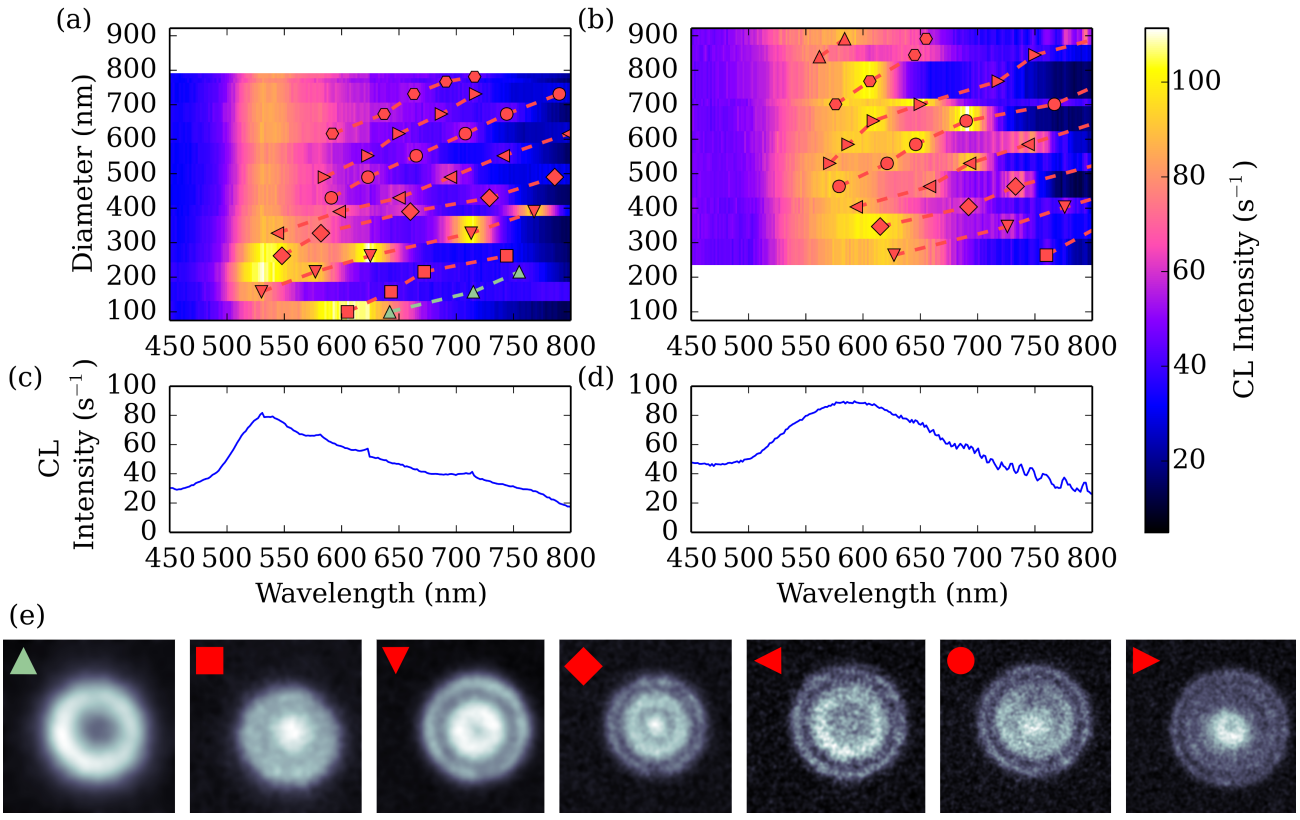

Figure 2.21 – Effect of the spacer thickness.
(a) and (b): Colour encoded CL intensity as a function of wavelength and antenna diameter for a 17 nm thick oxide spacer (a) and the reference 57 nm thick spacer (b). The successive mode branches are shown with their corresponding markers, in red dashed lines for already characterised ones, and in green dashed lines for the fundamental mode revealed by panel (a). (c) and (d): Average of the spectral map for all the antenna dimensions, clearly showing the effect of the fixed, broad resonance at a wavelength of 530 nm for the thin spacer (c) and 590 nm for the reference one (d). (e): LDOS of the different antenna modes with the corresponding mode branch symbol.

the dispersion relation of the antenna modes. As the symmetric mode of a MIM-type structure has no cut-off frequency, there is no theoretical limit to the vertical confinement of the field. The latter thus experiences a refractive index that can be tuned continuously from very high values for a small thickness (e.g. up to $n = 6$ for a 20 nm thick spacer) to the effective index sensed by the plasmon at a Au/Al_2O_3 interface (≈ 1.5 at the SPR). Hence, the spacer thickness allows one to tune the dispersion relation of the patch antenna modes by changing the effective refractive index of the mode, as proposed at the end of section 2.2.4.

We note that the spacer thickness also plays a role on the broad, fixed resonance. Panels (c) and (d) show the spectra averaged over the antenna diameters to better emphasise the position of the fixed energy peak (respectively (c), 530 nm and (d), 590 nm). As already mentioned, we observe this broad peak at the same energy for every structure fabricated on the same substrate (rectangles, squares, bow-tie antennas etc.). It does not reveal any spatial structure during LDOS imaging. We report in figure 2.22 the central position of this peak as a function of the spacer thickness, along with the position of the maximum of the plasmonic DOS computed

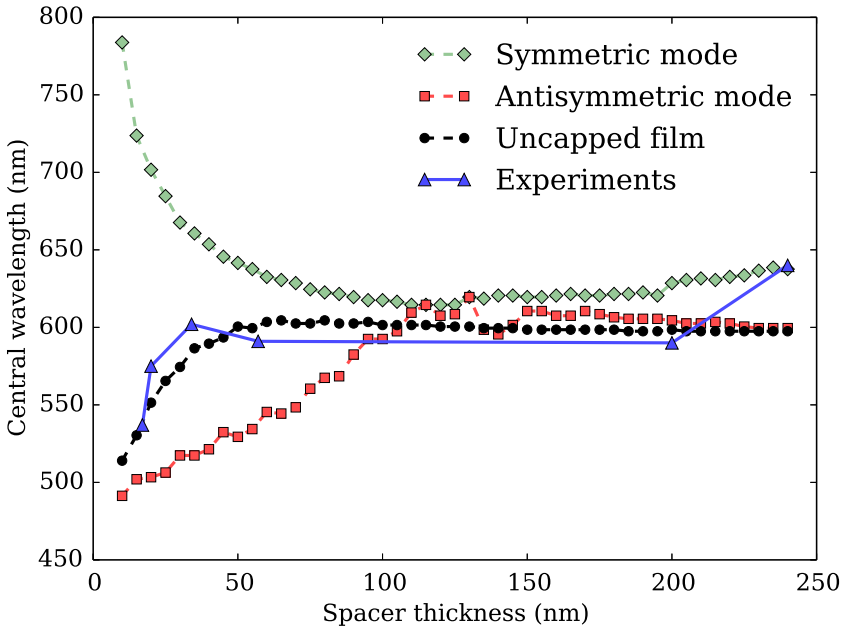

Figure 2.22 – Dispersion in energy of the fixed CL resonance and of the plasmonic DOS of the SPP modes supported by the infinite layered system.
Blue triangles: Position of the center of the fixed CL peak as a function of spacer thickness and wavelength. Green diamonds, red squares and black circles: Position of the maximum of plasmonic DOS of the symmetric, antisymmetric and uncapped system SPP modes calculated as described in section 2.2.4. The experimental curve follows the uncapped mode. It is present at a given frequency for all the structures fabricated on a given substrate, and follows the uncapped system SPP mode, so we attribute this resonance to the scattering of the uncapped SPP mode on the patch edge.

for the symmetric and antisymmetric modes of the IMIM film structure and of the uncapped structure. As expected, we see that the symmetric mode red-shifts with a decreasing spacer thickness, as it experiences a stronger vertical field confinement and hence a higher refractive index. The SPP mode of the uncapped system red-shifts with increasing oxide layer thickness as it is partly located inside the oxide layer. For thin oxide layer, the tail of the field is thus partly located in the vacuum above the structure, while for thick layers it is fully contained inside alumina. All the modes converge to the uncoupled Au/Al_2O_3 SPP mode for thick oxide layers. As the antisymmetric mode is very weakly confined, the determination of its dispersion relation, and especially of $\mathrm{Im}\{k_{\mathrm{SPP}}\}$ in the numerical procedure is difficult, leading to an apparent noise in the central position of its maximum of DOS. The same problem holds for the uncapped layer mode, but it is strongly confined at the Al_2O_3/au interface and hence yields more precise results. We see that the dispersion of the broad resonance is close to the one of the SPP mode of the uncapped system. Because of this reason, the fact that it is present for all antenna shapes and sizes, and the absence of characteristic LDOS pattern for this resonance, we think that it is at least partly due to the diffraction by the antennas of the surface plasmon polaritons supported by the Al_2O_3-Au(substrate). It could also be due to highly confined plasmonic modes at the antenna edge [Moh+14], or volume plasmons excited by the longitudinal components of the field created by the electron beam [AZ84]. We continue discussing its origin in the next section.

2.3.6 Towards blue and U.V. spectral range

Figure 2.23 – Different materials combinations used for the patch antennas.
Sketch of the three materials combinations used to demonstrate the effect of material on the patch antennas CL properties. The oxide layer is always 57 nm thick, while the antenna is 35 nm thick.

So far, we have presented a LDOS model for both the IMIM films and the plasmonic patch antennas, and detailed the CL properties of circular Au plasmonic patch antennas. We have shown that they support successive modes at wavelengths larger than the SPR wavelength of the IMIM film. We can tune a given mode energy by changing the antenna diameter, and we can tune their dispersion relation by varying the spacer thickness. The broad, fixed resonance peak is at least partly attributed to the SPPs supported by the multilayered structure. As a final experiment, we change the film and antenna material, and study Au patch antennas on an Al film, and Al antennas on an Al film. These structures are sketched in figure 2.23. The oxide layer thickness is 57 nm, and the antenna is 35 nm thick.

Spectral and spatial characterisations were performed on the bi-metal and Al patch antenna samples. The results are presented in figure 2.24. Panels (a), (b) and (c) show the colour encoded CL intensity as a function of wavelength and antenna diameter. The mode branches are represented by the dashed lines where the symbols refer to the LDOS images in figure 2.21. Panels (d), (e) and (f) show the CL signal averaged over all the antenna lengths.

Let us first discuss the additional information we gain by changing the material on the physical understanding of the CL experiment on patch antennas. Comparing panels (a),(d) and (b),(e), we see that changing the bottom mirror material from Au to Al results in a strong decrease of the signal below the Au-Al_2O_3 SPR wavelength ($\sim$ 550 nm). This is a good indication that this residual signal originates from Au luminescence not suppressed by the background subtraction procedure.

Additional information on the broad resonance are found by comparing all the panels.

- In the case of panel (a),(d) (reference), the broad resonance is symmetric and centred around 590 nm. We can see that changing the substrate from Au to Al [panels (b),(e)] results in a rapid decrease of this peak in intensity towards the blue spectral range, without any change in spectral position.

- Changing both the antenna and the substrate material to Al [panels (c),(f)] results in a blue shift of this peak to 500 nm.

- We also note that the CL intensity of this resonance presents a minimum for small antenna lengths, which evolves into a "dark branch" between the squares and triangle markers. This dark branch is also observed for other antenna shapes. It appears at the same position for panels (b) and (c) and is thus independent of the antenna material.

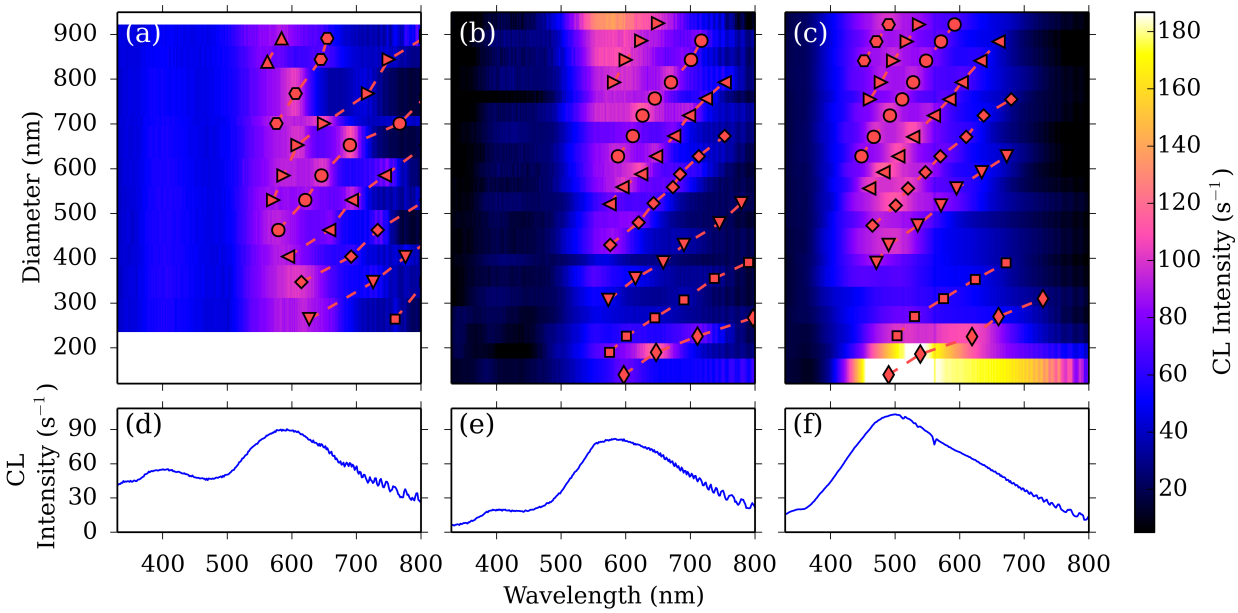

Figure 2.24 – CL spectral maps of the three patch antenna systems.
(a), (b) and (c): Colour coded CL intensity of the patch antennas as a function of wavelength and antenna diameter for the Au-Al_2O_3-Au (a), the Au-Al_2O_3-Al (b) and the Al-Al_2O_3-Al (c) systems. The mode branches are indicated in red dashed lines where the symbols correspond to the LDOS patterns presented in figure 2.21 (e). (d), (e) and (f): CL intensity averaged over all the antennas, showing the contribution of the residual luminescence and SPP diffraction in the fixed, broad resonance. Note that we made the lowest resonance of panel (c) saturate to get a better contrast on the different mode branches.

These features lead us to propose that this broad contribution arises from the diffraction of the uncapped layered system SPPs by the antenna:

- Changing only the antenna substrate from Au to Al leads to a change in the uncapped system DOS, as previously shown in figure 2.7. It blue shifts to $\sim$ 400 nm, constituting a reservoir of SPP modes that can be diffracted by the antenna.

- The position of the broad resonance also depends on the antenna material, as it modulates the diffraction efficiency of the SPPs. For Au antennas [panel (b)], little scattering can occur above the SPR energy as the patch then presents a strong absorption due to inter-band transitions. As a result, the continuum of SPPs from the uncapped system is only efficiently scattered around the SPR wavelength of the Au particles on the substrate, at 590 nm. For Al antennas [panel (c)], their scattering efficiency modulates the SPP DOS of the uncapped system, as proposed in section 2.2.3, resulting in the strong scattering around 500 nm.

- We think that the dark branch corresponds to destructive interferences of the uncapped system SPPs scattered by the antenna. Considering that the antenna diffracts SPPs supported by the uncapped layer system, we evaluated the condition for constructive or destructive interference of the scattered field with respect to k_{SPP} at the Al_2O_3/Al

interface. We could verify that the dispersion of the dark mode branch is in relative agreement with the condition of destructive interference for the scattering of the uncapped system SPPs by the two opposite edges of the antenna. Furthermore, a constructive interference is expected for smaller diameters, closely following the diamond markers. It is hardly visible in panel (b) because the Au absorption damps the signal below 590 nm and the Al interband transition around 800 nm, but we think it contributes to the increased signal of this branch in panel (c) as it reinforces the emission from the fundamental patch mode. This effects smears out for larger antenna diameters as we leave the regime of diffraction by the whole antenna and are only sensitive to the diffraction of one antenna edge.

However, we remind that we can not exclude other contributions to this CL signal, such as plasmon modes highly confined at the patch edge [Moh+14] or volume plasmons excited by the longitudinal components of the field created by the electron beam [AZ84].

Finally, aluminium is foreseen as a promising candidate for plasmonic systems operating at higher energies [Kni+12; GG14]. Panels (c) and (f) show that by changing all the metallic materials to aluminium, one can fabricate antenna operating in the blue spectral range. We note that on the red and near-IR part of the spectrum, the optical properties of Al structures degrade because of interband transitions, as already pointed out in chapter 1. We also have to mention that because of the roughness of metallic films, a lot of parasitic signal arises from SPP diffraction on the Al-Al_2O_3-Al system (see section 2.2.3). This contribution is partly suppressed by the background subtraction, allowing a clear evidence of the LSP modes in figure 2.24 (c). However, this represents losses channels when coupling the antenna to an external excitation, e.g. in fluorescence enhancement of localised emitters, as part of the excitation is not funnelled into the desired LSP antenna mode but simply diffracted by surface roughness. This also made LDOS imaging on the Al structures very difficult, because this scattering by surface roughness produces an homogeneous background degrading the signal to noise ratio on the measurement. Improving the material quality is thus one of the major challenges to allow the use of aluminium as an efficient plasmonic material.

2.4 Conclusion on the CL properties of plasmonic antennas

2.4.1 Plasmonic patch antennas

Throughout this chapter, we have demonstrated the use of cathodoluminescence in plasmonics to perform single plasmonic structure spectroscopy and LDOS imaging. As CL is an excitation spectroscopy technique, and because electronic excitation provides an intense and broadband local electromagnetic field, the interpretation of a CL experiment is not straightforward. We have emphasised this point by focussing the discussion on patch antennas, showing that the antenna modes are not the only contribution to the CL signal. In fact, because the electron beam probes a large depth in the sample, substrate effects are visible and have to be taken into account, in opposition to EELS experiments where the structures stand on a very thin membrane. A simplified LDOS model has been introduced and discussed. It appears to be

useful to understand the mode structure of the antennas, but does not bear a predictive quality because of our experimental configuration. However, it proved to provide a good description of the antenna LDOS. The plasmonic patch antennas appear as very promising candidates to be coupled with small, localised emitters placed at the center of the spacing layer, as shown in refs. [ETG10; Bel+13; Big+14; HAM16]. Circular patch antenna provide the possibility of a strong beaming [Moh+14] which adds directionality to fluorescence enhancement.

2.4.2 Cathodoluminescence as a tool for plasmonics

Due to their high degree of symmetry, we focused the plasmonics-related work of this thesis on the circular patch antennas. However, we also performed experiments on other kind of antennas to get a better insight on the role of their shape on their plasmonic properties. For comparison purposes, we briefly considered square patch antennas, which showed chessboard-like LDOS patterns (see e.g. [Kut09, ch. 7]), or equilateral triangles and rectangular antennas on Si-SiO_2 substrates, which are presented briefly in figure 2.25.

Figure 2.25 (a) shows the colour coded CL intensity from Au triangles as a function of their length L and wavelength, along with the LDOS of some resonances marked with the green symbols. They consist in very early measurements and we thus do not provide detailed interpretation of these results. However, they clearly evidence that we can use CL to perform spectroscopy on arbitrarily shaped nanoparticles from very different sizes, ranging from a few tens of nanometres to a micron. Moreover, we are able to image the LDOS of high order modes, previously reported in refs. [Nel+07; Gu+11; Maj+13; Via+13] for example, and recently simulated in ref. [Arb+14]. These preliminary results provide a high spatial resolution map of the LDOS of such prisms, which are of great interest as they can be easily fabricated with a high crystalline quality, and show that CL is a great tool to study complex plasmonic systems.

Figure 2.25 (b) shows the colour coded CL intensity from Au rectangles as a function of their length L and wavelength, along with the LDOS of the two fundamental modes (green symbols) and higher order modes (red symbols). The rectangles have a fixed width of ~ 100 nm, and only their length L varies. The spectral map reveals mode branches for the successive longitudinal modes, and a fixed resonance corresponding to the antenna transverse mode, as investigated in numerous references (see eg. [Ves+07; Dor+09; Ros+11; Kni+12; LK15]). LDOS at several positions reveal the presence of the fundamental longitudinal mode (horizontal green rectangle), the fundamental transverse mode (vertical green rectangle), the higher order longitudinal mode (horizontal red rectangle) and the overlap between this latter and the transverse mode (vertical red rectangle). It is interesting to note that the CL emission from the longitudinal mode is polarised along the rectangle long axis. This structure will be used in greater details in chapter 5 to enhance the emission properties of a localised emitter. Additional phenomena contribute to the fixed resonance. The transverse antenna mode has been isolated, but we cannot rule out the contribution of plasmon modes localised at the antenna edge, and interband transitions from the Au antennas [BBN03]. Contrary to the patch antenna configuration, here we cannot suppress any of this luminescence as the substrate is not made of Au.

In conclusion, we have showed that CL allows spectral and spatial characterisation on single plasmonic nanoantennas, providing a wealth of information on the origin of their plasmonic response. The very local probe of an electron beam allows to obtain a sub-diffraction limited

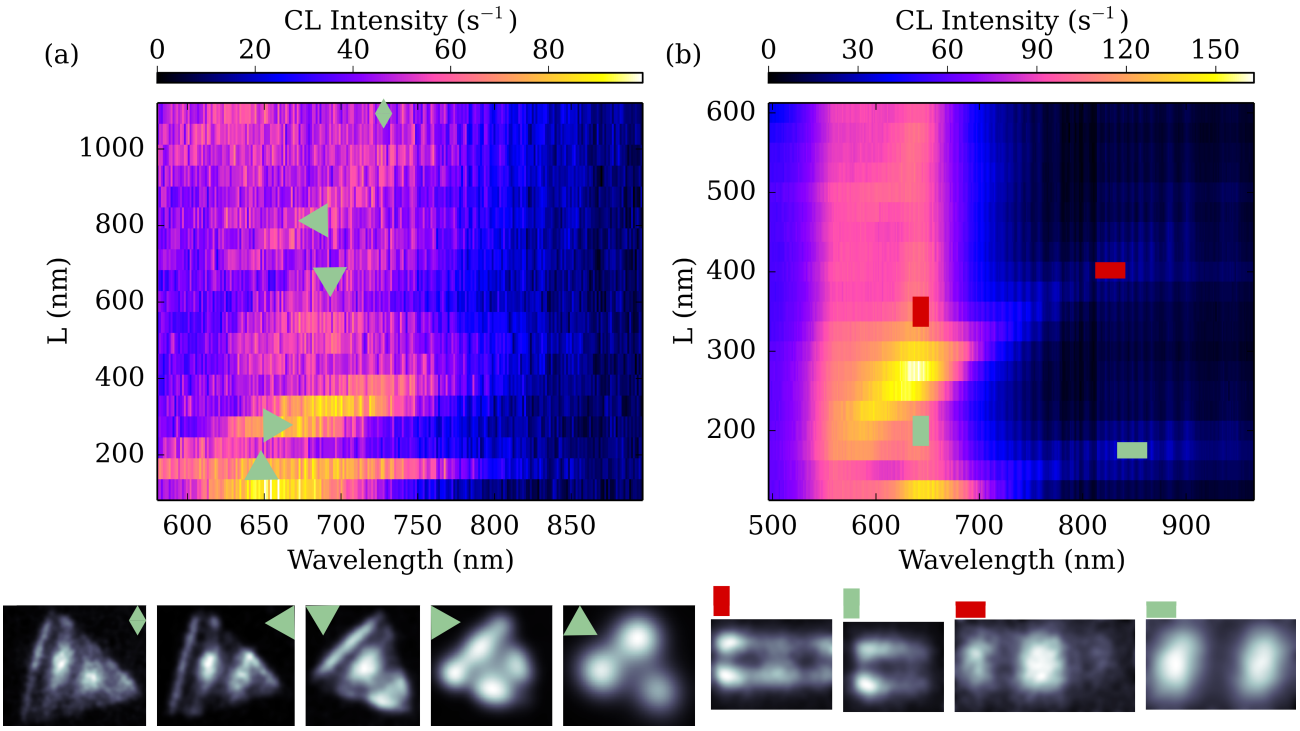

Figure 2.25 – CL spectral maps for triangular and rectangle antennas.
(a) Colour coded CL intensity of equilateral triangular antennas on a Si-SiO_2 substrate as a function of wavelength and triangle side length L. Several resonances are shown in green markers corresponding to the LDOS patterns presented in inset below the panel (a). Due to the complex nature of the mode structure for these antennas, the mode branches are hard to isolate. (b) Colour coded CL intensity of rectangular antennas on a Si-SiO_2 substrate as a function of wavelength and length L. The rectangles have a fixed width of ~ 100 nm. Two very distinct red-shifting mode branches are visible, evidencing the longitudinal dipolar and quadrupolar modes dispersion relations. The fixed resonance is attributed to the transverse plasmon mode of the antenna. The LDOS of several resonances are shown in inset with the corresponding symbols.

optical characterisation of nanoparticles without using invasive probes, such as in near-field microscopy. While we have mainly carried out experimental work, we hope that improvement in computational procedures will lead to easier and better interpretation of the CL experiments. A lot of work is currently done to link EELS and CL to electromagnetic quantities, as shown by refs. [GK08; Gar10; KS14; Koc+14; LK15]. However, they restrict to the case of extremely thin substrates, as required for EELS. We thus hope that an effort will also be made towards the description of CL in realistic experimental configurations involving substrate effects that have to be taken into account, and keep on working on this issue for the time being.

Chapter 3

Semiconducting Nanowires Quantum Dots

Résumé en Français

Ayant introduit les concepts fondamentaux, puis les expériences et les résultats principaux sur les systèmes plasmoniques, on s'intéresse maintenant au deuxième pan de ce travail de thèse, les boîtes quantiques insérées dans des nanofils à semiconducteur. Afin de proposer une stratégie de couplage avec des antennes plasmoniques, il est nécessaire de caractériser les propriétés d'émission de ces boîtes. Les semiconducteurs utilisés lors de cette thèse sont à base de matériaux II-VI. On étudie respectivement des boîtes de CdMnTe dans des fils cœur/coquille de ZnTe/ZnMgTe et des boîtes de CdSe dans des fils cœur/coquille de ZnSe/ZnMgSe.

On présente d'abord des rappels d'optique des semiconducteurs massifs, en introduisant la structure cristalline des matériaux utilisés (figure 3.1) et leur structure de bandes (figure 3.3 pour CdTe). On rappelle les propriétés de base d'une excitation optique d'un semiconducteur, menant à la création d'un exciton, et le couplage de cette excitation à la lumière dans le cadre de l'approximation dipolaire. On discute ensuite de l'effet du confinement électronique des porteurs dans une boîte quantique, et des diverses stratégies proposées jusqu'à présent pour contrôler les propriétés optiques et électroniques des boîtes. On introduit alors l'intérêt de la géométrie nanofil, qui permet d'obtenir des structures avec une grande qualité cristalline, tout en ayant un contrôle électronique et photonique sur les propriétés optiques des boîtes.

Dans une seconde partie, on présente les techniques expérimentales utilisées. Le montage optique est exposé en figure 3.9. Il s'agit d'un montage de microphotoluminescence (μPL) permettant de caractériser une boîte quantique unique dans un nanofil isolé, basé sur un montage de microscope confocal. Une opération résolue en temps est possible grâce à l'emploi d'un laser d'excitation pulsé (voir figure 3.10). Une particularité de ce montage est l'utilisation de la microscopie de Fourier, qui permet d'imager directement le diagramme de rayonnement d'un émetteur unique (figure 3.12). Enfin, on détaille la procédure de fabrication des substrats permettant les mesures de μPL sur des nanofils uniques.

On expose alors les résultats de μPL sur un grand échantillon de nanofils Te dispersés mécaniquement sur un substrat. Ayant initiallement très peu de données disponibles sur les boîtes de CdMnTe, nous avons mis au point une étape de sélection des fils étudiés par cathodoluminescence (CL) à température cryogénique. On vérifie la présence d'une émission localisée dans le

nanofil à une position correspondant aux prévisions de croissance, et à une énergie concordante (figure 3.17). On présente alors les mesures de μPL résolues en temps, en polarisation et les diagrammes de rayonnement. Les résultats sont résumés en figure 3.21. On constate que la raie d'émission excitonique à 4 K *est très large (largeur à mi-hauteur* 4.4 ± 0.9 nm*), ce qu'on attribue à de l'élargissement inhomogène par effet Zeeman dû à la présence des atomes de Mn dans la boîte. De plus, on constate une forte disparité tant pour l'énergie d'émission que pour la durée de vie excitonique. Un premier modèle décrivant simplement l'effet photonique du fil est proposé, basé sur des simulations d'éléments finis. Il ne décrit toutefois pas complètement les données de polarisation, et ne permet pas de rendre compte de la disparité des résultats.*

L'étude de fils basés Se est en deux étapes: une première étude sur des fils dispersés traite du temps de déclin de l'exciton et du biexciton en fonction de la température (figure 3.24). On observe des temps de déclins très longs (de l'ordre de quelques nanosecondes). Le temps de vie du biexciton reste stable avec la température dans les deux échantillons étudiés, mais celui de l'exciton varie. Dans un cas, il monte très rapidement entre 5 et 50 K *pour atteindre un plateau autour de* 4 ns*. Dans l'autre, il augmente progressivement entre 5 et* 175 K *et sature à* 6 ns*. Dans les deux cas, il chute ensuite fortement à partir de* 200 K*. Un modèle qualitatif est proposé, basé sur l'existence d'un exciton noir dû au premier état excité de trou dans la boîte (figure 3.26). On étudie dans un second temps l'effet de l'ajout d'une coquille d'alumine autour des nanofils sur l'intensité de μPL et sur le temps de déclin de l'exciton, lorsque le fil est debout sur son substrat de croissance (figure 3.28). On observe une importante variabilité dans les résultats, mais l'enveloppe montre que le temps de déclin de l'exciton augmente pour une coquille d'épaisseur nulle jusqu'à* 20 nm *pour atteindre* 6 ns*, avant de rechuter jusqu'à* 2 ns*. L'intensité totale émise par l'exciton augmente avec l'épaisseur de la coquille. Ces résultats sont comparés à des simulations numériques mettant en évidence le différent couplage des dipôle radiaux et longitudinaux dans la structure (figure 3.29), qui nous orientent vers l'existence d'une forte composante de dipôle radial dans la structure.*

Introduction

Semiconducting QDs are seen as extremely promising candidates for solid-state based quantum optics [Mic00; Zre+02; Shi07], as they can serve as source of single [San+01; Cla+10] or entangled photons [San+02; Ako+06; Dou+10]. However, one of the main challenge for their application is to efficiently couple them to freely propagating radiation. Recent progress in semiconductor growth research now allows for the fabrication of quantum dots embedded inside NW structures, which are of great interest for their high crystalline quality and practical geometry. A key step towards the realisation of nano-optical circuits and applications using NWQDs consists in interfacing them with other optical elements. In the previous chapters, we have discussed the optical response of plasmonic antennas. Coupling them to NWQDs is the final purpose of this work, and requires a precise understanding of both the antenna and the quantum dot properties.

This chapter treats the optical properties of semiconducting nanowire quantum dots. All the work done in this thesis has been carried out using semiconducting nanowires made of alloys of compounds from column II of the periodic table (Zn, Cd) and from column VI (Te, Se), consequently named II-VI materials. Therefore, we restrict the discussion on semiconductor properties to such II-VI compounds. Two types of nanowires are then to distinguish, whether they are Tellurium-based (Te) or Selenium-based (Se), and we will try to set out the relevant properties for both kinds according to the work carried out on each type of material.

Te-based quantum dots are of particular interest for spintronics and magneto-optical applications, as magnetic atoms can easily be inserted in the dot, creating confined and localised spins. Spin physics with single [Bes+04; KF11; Bes+15; Laf+16] or a moderate number [Fur88; Seu+01; Urb+13] of nuclear spins inserted in the dot (the field of diluted magnetic semiconductors (DMS) physics) is thus seen as promising for quantum information processing based on the manipulation of the confined spins.

On the other hand, Se-based NWQDs have been proven efficient single photon sources even at high temperature [Tri+08; Bou+12a], a desirable property for quantum optics applications. More generally, Se-based semiconductors are of great interest because of their high bandgap covering the blue and green spectral region.

We do not discuss in details the growth process by which these nanowires were fabricated, as it has been carried out outside this thesis. Te-based nanowires were grown by Pamela Rueda-Fonseca during her PhD thesis [Rue+14; Rue15; Rue+16] before this thesis started, while Se-based nanowires were fabricated by Thibault Cremel within the time of this work [Cre+14; Zan+15].

We start by a brief reminder on semiconductor optics. We introduce the optical properties of semiconducting materials, in relation with their electronic band structure, and we discuss the effect of carriers confinement. We especially discuss ways to engineer the optical and electronic properties of semiconducting quantum dots, and introduce the dot-in-a-nanowire configuration. Then, we present the optical spectroscopy experiments used in this thesis, namely time-resolved photoluminescence and Fourier imaging. We detail the preparation of the samples to allow multiple characterisations on well defined NW structures and optimise the light extraction from the QDs. We perform these experiment on a statistical set of both Te-based and Se-based NWQDs. The growth process leads to inhomogeneities in the structural characteristics of the

QDs, which in turns induce different optical properties. This statistical approach thus reveals a rich distribution of QD properties that requires careful analysis of correlated measurements on several emitters to be understood.

3.1 Optical properties of semiconducting nanowires

The aim of this section is to give a brief reminder of semiconductor optics, and detail the effects of confining and shaping semiconductors to the nano-scale.

3.1.1 Semiconductor Optics: A reminder

The crystal structures of II-VI semiconductors are illustrated in figure 3.1. II-VI NWs can grow in both zinc blende (ZB) or wurtzite (WZ) structure. However, during this work we have preferentially studied *thick Te-based nanowires* which crystallise in *ZB phase*, and *thin Se-based nanowires* which crystallise in *WZ phase*, as they exhibited the best optical properties [Art+13; Rue+14; Cre+14; Zan+15].

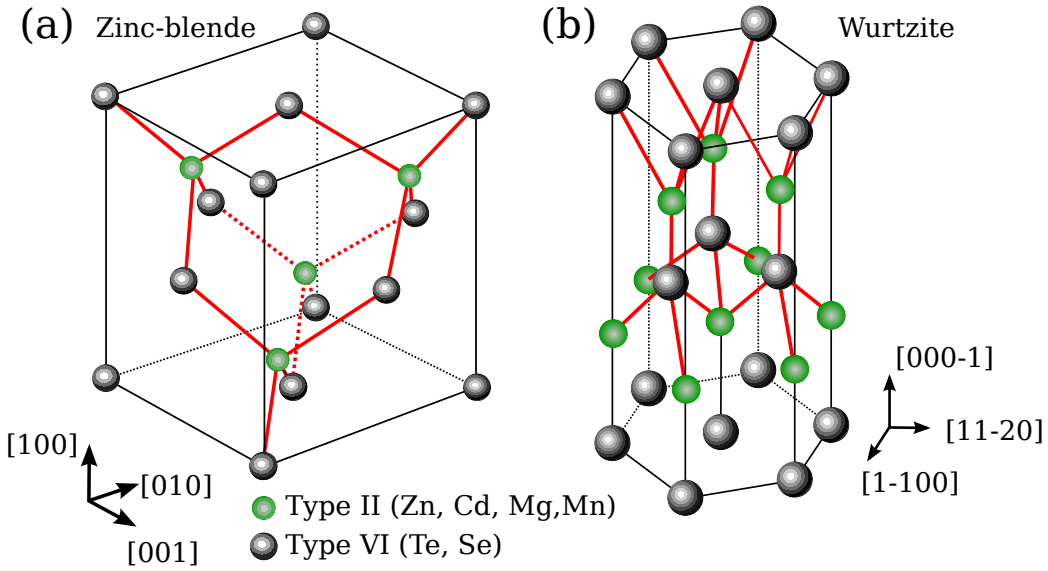

Figure 3.1 – Crystallographic structure of II-VI semiconductors.
(a) Zinc-blende and (b) Wurtzite crystal structures. The Te-based NWs studied have a ZB phase, while the Se-based NWs have a WZ phase.

The ZB structure consists in two face-centered-cubic (FCC) system shifted by a quarter of a unit cell, while the WZ phase is a hexagonal structure. It is summarised in the following table:

Structure	Lattice	Chemical compounds
ZB	FCC	Cd*Te*, Zn*Te* etc.
WZ	Hexagonal	Cd*Se*, Zn*Se* etc.

A (very) brief introduction to the k · p theory and band structures

The electronic properties of semiconducting materials are very well described within the theory of band structures. The available electronic states are described by energy bands in the reciprocal lattice, i.e. the momentum space. For semiconductors at 0 K, all the states below a certain energy (the Fermi Energy E_f) are occupied, the last occupied band being designated as the valence band, while above E_f the bands are empty, and the first non-occupied band is named the conduction band. A striking difference with the band structure of metals is that an *energy gap is opened around the Fermi energy, i.e. no electronic band crosses this level.* A thorough introduction to band theory and $\mathbf{k} \cdot \mathbf{p}$[1] calculations can be found in [Fis10], which has been used extensively to carry out the work on semiconductors presented in this thesis. We will shortly introduce how the band structure of semiconductors can be calculated and illustrate the method on our II-VI materials.

As a starting point, we consider the atomic orbitals playing a role in the atomic bonding within the crystal, namely the valence orbitals. The electrons wavefunctions Ψ are found by solving the Schrödinger equation in presence of the atomic potential V_{at}:

$$H_{at}\Psi = \left[\frac{\mathbf{p}^2}{2m_0} + V_{at}\right]\Psi = E\Psi \tag{3.1}$$

where $\mathbf{p} = -i\hbar\nabla$ is the momentum operator, m_0 is the electron rest mass and E the energy of the orbital. In our case the valence orbitals are of s and p type and are commonly described within the sp^3 hybridisation. This hybridisation allows each atom to have four bonding orbitals with tetrahedral symmetry, well suited to build the unit cell of figure 3.1. Using the approximation of the linear combination of atomic orbitals, one can calculate the molecular orbitals resulting of the bonding of two adjacent atoms. This leads to the formation of bonding and antibonding orbitals. Electrons shared by the atoms occupy the bonding orbitals, while the antibonding orbitals are empty. This theory is expanded to the crystal where adjacent atoms are placed in the crystal lattice. The potential created by the atoms is assumed to be periodic. Usually, a further and rather strong approximation is made by neglecting the overlap between the atomic orbitals of two adjacent atoms, and considering only the interaction between the nearest neighbours. For two adjacent atoms, $\Psi_{\rightarrow}$ and $\Psi'_{\leftarrow}$ being two orbital functions pointing towards each other, this leads to the following relations:

$$\langle \Psi_{\rightarrow} | \Psi'_{\leftarrow} \rangle = 0 \tag{3.2a}$$

$$\langle \Psi_{\rightarrow} | V_{at} | \Psi'_{\leftarrow} \rangle = \langle \Psi_{\rightarrow} | V'_{at} | \Psi'_{\leftarrow} \rangle = -\lambda \tag{3.2b}$$

where V_{at} and V'_{at} are the atomic potential centred at the location of the two atoms and λ is the interaction energy. In order to find the available electronic states in the crystal, one has then to solve the Schrödinger equation:

$$H_{\mathfrak{U}}\Psi^B_{n,\mathbf{q}}(\mathbf{r}) = E_{n,\mathbf{q}}\Psi^B_{n,\mathbf{q}}(\mathbf{r}) \tag{3.3a}$$

$$H_{\mathfrak{U}} = \frac{\mathbf{p}^2}{2m_0} + \mathfrak{U}(\mathbf{r}) \tag{3.3b}$$

[1] Electrons wave vectors are always designated by $\mathbf{q}$ in this manuscript, while $\mathbf{k}$ represent electromagnetic wave vectors, but we will not dare changing the usual name of this theory for the simple purpose of symbol consistency !

where $H_{\mathfrak{U}}$ is the Bloch Hamiltonian, $\mathfrak{U}(\mathbf{r})$ is the (periodic) crystal potential, $\Psi^B_{n,\mathbf{q}}$ is the n-th Bloch wavefunction for the electron with wave vector q and $E_{n,\mathbf{q}}$ is its energy. The Bloch theorem states that $\Psi^B_{n,\mathbf{q}}$ has the same periodicity as the crystal potential. Due to the large number of atoms in the crystal, the discrete atomic levels now form continuous energy bands in which the electrons can move. The symmetry of these energy band is governed by the atomic orbitals from which they are formed, and by the crystal symmetry. In the case of ZB structure, these bands have the symmetry of the tetrahedral group T_d. On the contrary to atomic orbitals which are commonly described by spherical harmonics, we use cubic functions which are other linear combinations of atomic orbitals [Fis10, sec: 1.7-1.8]. They provide a basis on which the electronic bands will be decomposed. Exploiting the periodicity condition, the Bloch functions are decomposed into:

$$\Psi^B_{n,\mathbf{q}}(\mathbf{r}) = \mathrm{e}^{i\mathbf{q}\,\cdot\,\mathbf{r}} U_{n,\mathbf{q}}(\mathbf{r}) \tag{3.4}$$

where $U_{n,\mathbf{q}}(\mathbf{r})$ also has the same periodicity as the crystal lattice. The $\mathbf{k}\cdot\mathbf{p}$ theory relies on the fact that equation (3.3a) can be rewritten as:

$$\left[H_{\mathfrak{U}} + \frac{\hbar}{m_0}\mathbf{q}\,\cdot\,\mathbf{p} + \frac{\hbar^2 q^2}{2m_0}\right] U_{n,\mathbf{q}}(\mathbf{r}) = E_{n,\mathbf{q}} U_{n,\mathbf{q}}(\mathbf{r})\,. \tag{3.5}$$

Assuming that we know the symmetries of the functions $U_{n,\mathbf{q}}$ at the center of the Brillouin zone (i.e. for $\mathbf{q}=0$) and their associated expectation value with respect to $H_{\mathfrak{U}}$ and $\mathbf{p}$, the solutions of:

$$\left[H_{\mathfrak{U}} + \frac{\hbar^2 q^2}{2m_0}\right] U_{n,\mathbf{q}=0}(\mathbf{r}) = \left(E_{n,\mathbf{q}=0} U_{n,\mathbf{q}=0} + \frac{\hbar^2 q^2}{2m_0}\right) U_{n,\mathbf{q}=0}(\mathbf{r})\,. \tag{3.6}$$

are known and we can then derive the solutions of equation (3.5). Numerical values for equation (3.6), i.e. gap energies and effective masses, can be determined by experiments such as cyclotron resonance. We recall that in the case of an isotropic dispersion relation for the electrons, the effective mass is given by:

$$\frac{1}{m^*} = \hbar^{-2}\frac{\partial^2 E}{\partial \mathbf{q}^2} \tag{1.11}$$

Until this point, the solutions of equation (3.5) are still *exact* solutions of the Schrödinger equations (3.3a), but depend on a given electron wave vector $\mathbf{q}$. The method then consists in projecting the Hamiltonian (3.5) on a subspace of the Hilbert space formed by the $U_{n,\mathbf{q}=0}$ functions (i.e. a finite number of $U_{n,\mathbf{q}=0}$ functions), which consists in a first approximation. Another one is made by treating the $\mathbf{q}\cdot\mathbf{p}$ term as a perturbation term in the equation (to first, second, etc. order).

We start by discussing the results while neglecting the spin of the electron. In the case of our II-VI semiconductors, for the T_d group, the last occupied band is the Γ_5 band, resulting from the bonding *sp* type functions. The first empty band is the Γ_1 band and results from the contribution of antibonding *s* type functions. It can be shown that projecting the Hamiltonian only on the Γ_5 and Γ_1 bands is not sufficient, and that the contribution from the antibonding *sp* type band Γ_{5C} has to be taken into account. A schematic representation of the results is shown in the left part of figure 3.2, with the indication of spin degeneracy. The valence and conduction bands are separated by an energy gap E_G, and are of opposite curvature.

Taking now the electron spin into account lifts the Γ_5 degeneracy because of spin-orbit coupling, as represented on the right of figure 3.2. The splitting energy is Δ_{SO}, and leads to

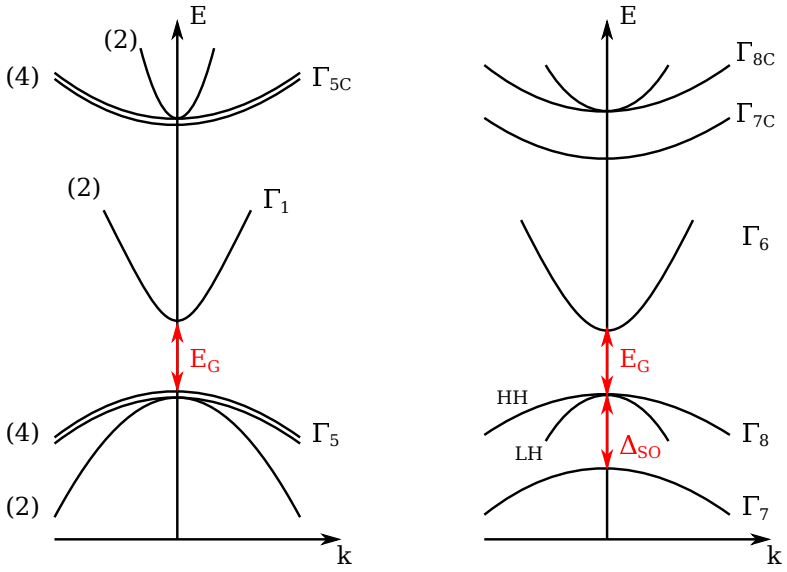

Figure 3.2 – **k · p calculation and band structure**.
The left panel shows the results of a **k** · **p** calculation neglecting the spin-orbit coupling, while the right-panel shows the same calculation when accounting for the spin-orbit coupling. The band symmetries are indicated, and the numbers in parenthesis represent the spin degeneracy. The gap energy E_G and the spin-orbit splitting Δ_{SO} are indicated.

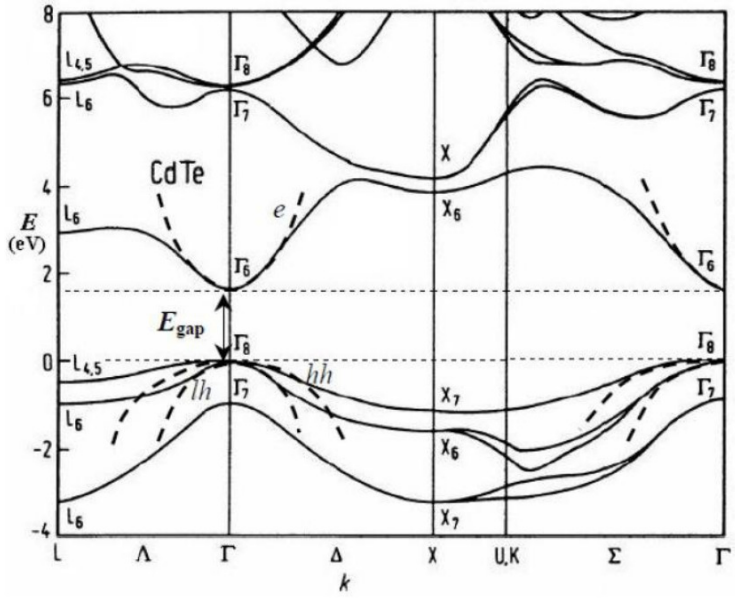

Figure 3.3 – **CdTe band structure.**
Result of a **k** · **p** calculation for the case of bulk CdTe [Fis88]. The origin of the energies is taken at the top of the valence band. The gap energy is explicitly shown, as well as the parabolic approximation of conduction, light and heavy hole bands Γ_6, Γ_7 and Γ_8.

the separation of the valence band into Γ_7 and Γ_8 bands, both of pseudo-orbital momentum $L = 1$. The Γ_7 band is of total pseudo-angular momentum $J = 1/2$, while Γ_8 is fourfold degenerate into $J = 3/2$ and $J = 1/2$ bands, known as heavy hole (HH) and light hole (LH) bands respectively. The conduction band is of Γ_6 symmetry with pseudo-orbital momentum $L = 0$, and total pseudo-angular momentum $J = 1/2$.

The result of $\mathbf{k} \cdot \mathbf{p}$ calculation in the case of bulk cadmium telluride (CdTe) is presented in figure 3.3, reprinted from [Fis88]. The origin of the energies is taken at the top of the valence band. All the previously mentioned energy bands are clearly visible around the center of the Brillouin zone. It is however important to note that, while near $\mathbf{q} = 0$ the bands can be easily approximated as parabolas, the effective masses of electrons and holes deviate from a quadratic dispersion at larger wave vectors. Due to the large energy splitting induced by the spin-orbit coupling and the high energy of the upper conduction bands Γ_{7C} and Γ_{8C}, we only focus on the LH, HH and Γ_6 bands for the rest of this thesis, as they are more easily accessed by optical methods.

Optical excitations of semiconductors

Like all the semiconductors studied in this thesis, CdTe has a direct bandgap in the center of the Brillouin zone, i.e. both the minimum of the conduction band and the maximum of the valence band are located at the Γ point, and its gap energy is 1.6 eV. We are interested in linear optical properties of the semiconductors, and will only consider electronic transition with no momentum transfer, which means vertical trajectories on the $E - k$ diagram. The optical properties of the material are thus controlled by the symmetry of the bands around the Γ point.

A photon impinging on this material with an energy higher than the gap energy can be absorbed, promoting an electron from the valence band to the conduction band. Due to the band curvature, and assuming that the photon energy is not too large, the excited electron will rapidly decay non-radiatively to the lowest energy point accessible, i.e. the Γ point of the Γ_6 band. While excited, the electron can interact with the vacancy left in the valence band through Coulomb interaction. This vacancy is designated as a "hole". The resulting electron-hole pair is called an exciton, and can be described by a two-body Schrödinger equation:

$$\left[\frac{\mathbf{p_e}^2}{2m_e^*} + \frac{\mathbf{p_h}^2}{2m_h^*} - \frac{\bar{e}^2}{4\pi\varepsilon\varepsilon_0 \left|\mathbf{r_e} - \mathbf{r_h}\right|}\right] \Psi\left(\mathbf{r_e}, \mathbf{r_h}\right) = E_{\mathrm{X}} \Psi\left(\mathbf{r_e}, \mathbf{r_h}\right) \tag{3.7}$$

where the subscript e is for the electron, and h for the hole. The momentum operator $\mathbf{p}$ is applied to both particles, m_i^* is the particle's effective mass which is proportional to the curvature of the parabolas presented in figure 3.3, $\bar{e}$ is the elementary charge, ε the dielectric constant of the semiconductor, and $\mathbf{r_i}$ the position of the particle. The solution of this equation resembles the one of the Hydrogen atom, and we define an excitonic Bohr radius:

$$a^* = a_0 \varepsilon m_0 / m_r \tag{3.8}$$

where a_0 is the Bohr radius of the Hydrogen atom, m_0 is the free electron mass and m_r the reduced mass of the two-particles system. This Bohr radius gives an idea of the spatial extension of the exciton wave function. Due to the usually large values of ε (of the order of 10 in most used semiconductors) and the low values of the effective masses, the exciton Bohr radius is usually

much larger than a crystalline unit cell. As an example, the Bohr radius in bulk CdTe is 6.9 nm [Mad87], and the lattice constant is 6.48 Å. The exciton can then recombine upon annihilation of the electron-hole pair. The electron will decay to the valence band by emitting a photon of energy E_{X}, different from the gap energy E_g.

The probability for a given transition to be optically active is given by the Fermi golden rule:

$$P_{i\to f} = \frac{2\pi}{\hbar} \left| \langle f|H_{\mathrm{opt}}|i\rangle \right|^2 \delta\left(E_f - E_i \pm \hbar\omega\right) \tag{3.9}$$

where i and f represent the initial and final states of energy E_i and E_f, and $\hbar\omega$ is the photon energy. H_{opt} is the optical interaction Hamiltonian:

$$H_{\mathrm{opt}} = \frac{1}{2m_0}\left(\mathbf{p} + \bar{e}\mathbf{A}\right)^2 \tag{3.10}$$

for a single electron, where $\mathbf{A}$ is the potential vector and $\mathbf{p}$ is the momentum operator [Fis10, chap. 8.2.2]. The $+\hbar\omega$ term in equation 3.9 describes the absorption of a photon and the creation of an electron-hole pair, while the $-\hbar\omega$ term describes the emission of a photon upon exciton annihilation. Equation 3.9 introduces selection rules in the optical transitions according to the electron and hole wavefunction and spin properties. In an optical spectroscopy framework, the large wavelength approximation allows us to neglect the field variations on the length scale of the exciton radius. The Hamiltonian can then be expressed in terms of a power series of $\mathbf{r}$, and we make the *dipolar approximation* by truncating the series to the first order, leading to the appearance of the electric dipole moment:

$$\mathbf{d} = -\bar{e}\mathbf{r}. \tag{3.11}$$

The truncated Hamiltonian is usually expressed in the Göppert-Mayer gauge [Göp31]:

$$\mathbf{A}' = \mathbf{A} + \nabla\chi, \qquad \chi = -\mathbf{r}\cdot\mathbf{A}_{\mathbf{r}=\mathbf{0}} \tag{3.12}$$

resulting in the dipolar interaction Hamiltonian:

$$\boxed{H_{\mathrm{opt}} = -\mathbf{d}\cdot\mathbf{E}.} \tag{3.13}$$

This expression of the Hamiltonian is valid for small field intensities and has the advantage of being linear with respect to the electric field. The detail of this derivation and some considerations on the validity of this approximation are detailed in [CDG87, chap. VI.B.]. For the rest of this manuscript, we will only consider *dipole-allowed* transitions in semiconductors.

A large variety of such optical transitions are possible, as excitation of valence electron to higher conduction bands, or transitions from core electrons, but we are here only interested in transition energies of the order of the material bandgap, in order to engineer the exciton properties through nanostructuration of the matter, as we will discuss in the next section.

3.1.2 Confining the carriers

In the previous section, we have presented the case of bulk semiconductors. We are now interested in what happens when the physical dimensions of the semiconductor approach the exciton

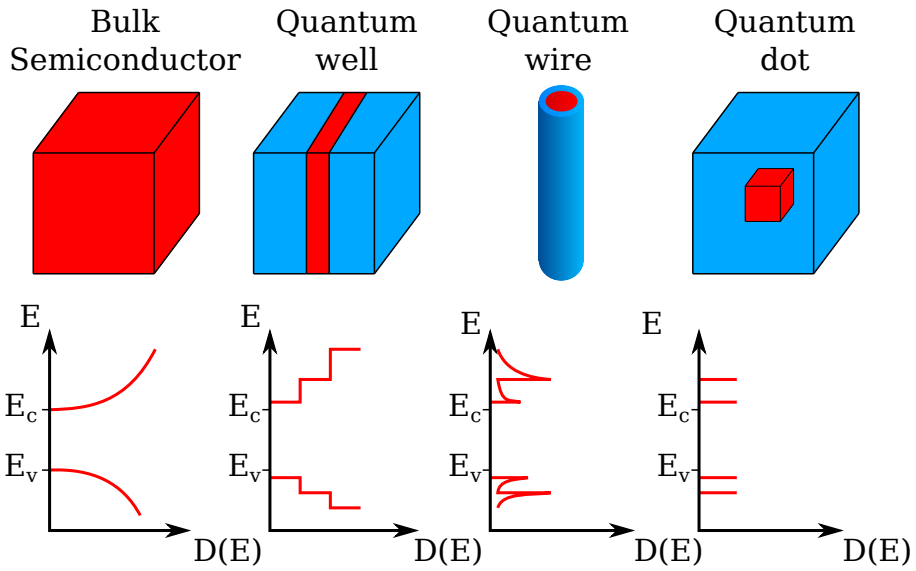

Figure 3.4 – Confinement of semiconducting materials.
Upper row: Schematic representation of the confinement of a low bandgap semiconductor (red) in a higher bandgap semiconductor (blue), from the unconfined bulk case (left) to the 3D confinement (right). Lower row: Corresponding density of states induced by the confinement, showing the $E^{p/2-1}$ dependence of the density of state as a function of the semiconductor dimensionality p.

Bohr radius, as is the case in NWs or QDs. As depicted in figure 3.4, such confinement can be achieved by physically limiting the size of the semiconductor, or by growing heterostructures, that is by embedding a low gap semiconductor in a higher gap semiconductor or an insulator.

Confining the semiconductor along a given direction quantises the electrons wave vector in this direction, changing the available electronic density of states. This is shown in the bottom row of figure 3.4. For a p-dimensional semiconductor, the corresponding electronic density of state $D(E)$ follows $D(E) \propto E^{p/2-1}$. In the case of a quantum dot the electron wave functions are confined along the 3 directions of space, resulting in Dirac-like density of state functions.

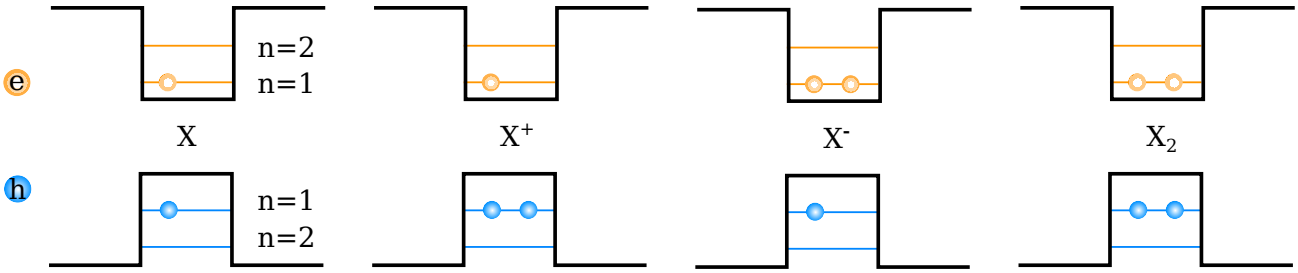

Figure 3.5 – Exciton complexes in a quantum dot.
Examples of confined carriers in a type-I quantum dot. Due to confinement, the electronic states are discrete inside the dot, while they are still forming a continuum outside the energy trap. From left to right: exciton, positively and negatively charged excitons, and biexciton.

Figure 3.5 provides a sketch of such discrete electronic energy levels inside a QD, where the energy bands are represented flat. They are disposed in a type-I alignment, meaning that the smaller gap material provides a lower (resp. higher) energy for the electron (resp. hole),

resulting in a confinement potential inside this material for both carriers. A type-II alignment indicates that only one type of carrier is confined. The quantum dot possesses a ground state, and possibly several excited levels, indicated by the number n.

The detailed calculation of the carriers energy levels requires to consider both the confinement potential shown in figure 3.5 and the Hamiltonian of equation (3.7). By analogy with the previous section a single electron-hole pair in the QD is designated as an exciton. Several carriers can be trapped in the dot as long as Pauli's principle is fulfilled, which limits the number of occupancy in each level. A single electron-hole pair is designated as an exciton (X), while an exciton associated with a hole (an electron) is called positively (negatively) charged exciton (resp. X^+ and X^-). Two excitons inside the QD form a biexciton X_2, so forth and so on. Because of the discrete energy levels, the emission originating from an exciton recombination inside a QD is expected to occur at a very well defined energy, giving rise to a sharp transition line. When the dot contains more carriers than a single exciton, the Coulomb interaction shifts the energy of the emitted photons upon recombinations of the excitonic cascade.

Selection rules govern the optical transitions. With a limited number or available electronic states, it is easier to grasp the implications of the Fermi golden rule. As an example, total momentum conservation imposes that the excitation of an electron from the HH band ($J = -3/2$) results in a spin $-1/2$ electron in the conduction band and a spin $+3/2$ hole in the valence band. Recombination between a $J = -3/2$ HH and a spin $-1/2$ electron is forbidden. Thus as a consequence, an eventual spin-flip process after excitation can lead to so-called *dark excitons* that can not recombine radiatively. This plays a great role in the optical properties of the emitting structures, and is detailed later in section 3.3.2 and chapter 4.

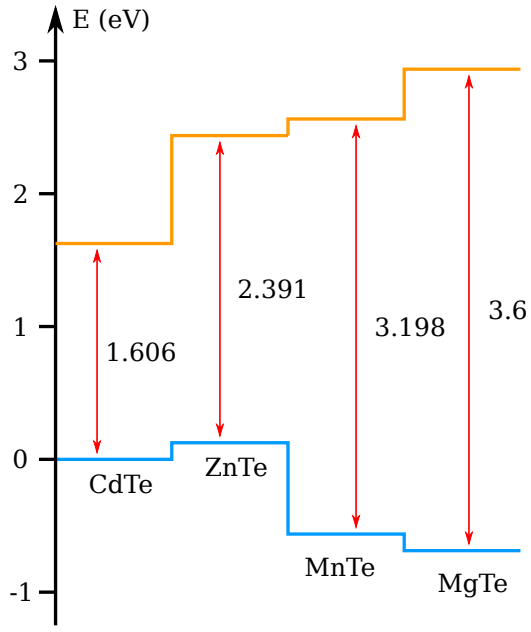

Figure 3.6 – Te-based compound band alignments.
Band alignment of different Te-based binary compounds used in this thesis. Note the relative alignment of the CdTe and ZnTe bands. Adapted from [VN03].

Alignment of the valence and conduction bands play an important role in carrier confinement, as is illustrated in figure 3.6 for some Te-based semiconductors. An unstrained CdTe-ZnTe

heterojuction would present a type-II band alignment for the hole: if arranged in a ZnTe-CdTe-ZnTe QD-like structure, the electron confinement inside the CdTe would be ensured because the conduction band of CdTe has a lower energy than the one of ZnTe, but holes would not be confined in the CdTe region because it has a lower valence band energy than ZnTe. However, alloying semiconductors allows to tune their bandgap within the limits of the non-alloyed semiconductors bandgaps. Finally, the effect of strain inside the heterostructure has to be taken into account for the calculation of the energy levels. It can change the band structure inside the QD, and break the symmetry of the system, favouring some excitonic states with defined optical properties. This will be detailed later during the study of a single NWQD in chapter 4.

3.1.3 Tailoring photonic nanostructures with semiconductors

Up to this point, we only discussed the *electronic* properties of semiconducting QDs, i.e. what happens to the electrons wave function when confined in a potential trap. But as we are interested in the *optical* properties of such structures, we also need to consider the effect of the semiconducting material on light itself. This is particularly crucial as most semiconductor have a high refractive index (n between 2 and 3).

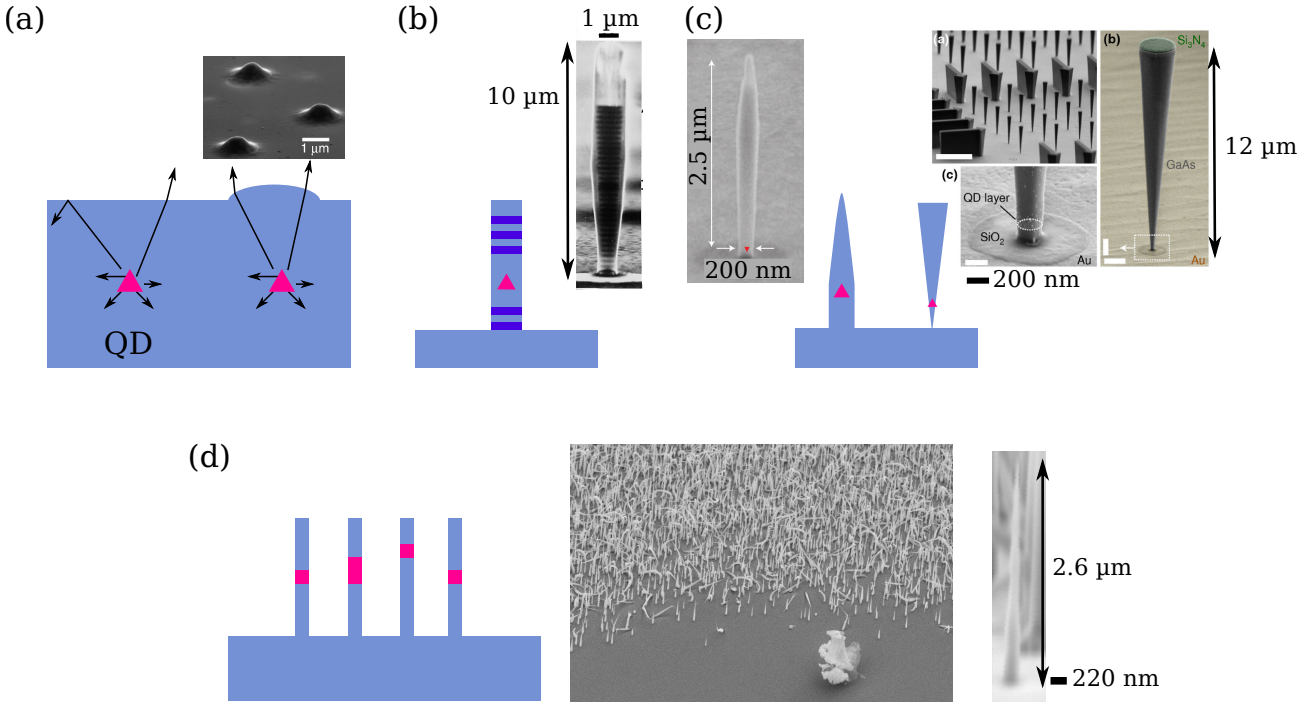

Figure 3.7 – Structuring matter around QDs.
Sketches and SEM images of various QD structures. (a) Self-assembled QDs buried in a bulk semiconductor, or with deterministically positioned microlenses to improve light extraction [Gsc+15]. (b) The micropillar strategy with Bragg reflectors, illustrating the 1D cavity strategy [Gér+98]. (c) The nano needle [Cla+10] and photonic trumpets [Mun+13] as 1D waveguiding strategies. (d) Semiconducting nanowires with embedded QDs. Note the difference in length scales and the high variety of NW morphologies.

Figure 3.7 shows various structures that can contain one (or several) QDs. The main problem associated with self-assembled QDs inside a bulk semiconductor is their very poor extraction efficiency. Because the photons emitted by the QD are in a high refractive index material (e.g. $n = 3$ gives an angle of total internal reflection of around 20°), most of them experience total internal reflection when reaching the sample boundary [see panel (a)]. Furthermore, as we usually collect photons emitted only on one side of the sample, all the photons emitted towards the other sides are lost.

Several strategies are employed to tackle this problem, like etching lenses on top of the dots (figure 3.7 (a) [Gsc+15]), or placing them inside cavities that can be two- or one-dimensional (figure 3.7 (b) [Gér+98]). Waveguiding methods are also used, as in the photonic "needle" [Cla+10] and "trumpet" [Mun+13] strategies [figure 3.7 (c)]. Nevertheless, all these strategies rely on a top-down approach, meaning that the physical engineering of the material takes place *after* the QD growth. Such processes steps can create surface defects that are detrimental to the optical quality of the structure.

Another approach is to fabricate semiconducting nanostructures in the form of wires in a bottom-up manner, as represented in panel (d). This allows to grow different kind of heterostructure, both in the radial (horizontal) and longitudinal (vertical) direction, with a very good crystalline quality. It also gives more control on the physical dimensions of the structure. Different growth processes can be used to fabricate nanowires, such as metalorganic chemical vapour deposition, or MBE as is the case of all the NWs we used in this work. MBE-grown NWs have a typical height of a few microns, and a relatively small diameters in the order of a few tens to a few hundreds of nanometres. MBE thus allows to fabricate smaller structures than the top-down approaches.

The presence of a tailored and very high refractive index material breaks the symmetry of the system, inducing photonic polarisation. As an example, it is easy to understand that vertical structures tend to favour photon guiding along the vertical direction. The transverse nature of light waves thus imposes a polarisation of the emitted photons preferentially in the horizontal plane. Further symmetry breaking can be used to favour a well defined polarisation state, as illustrated for example in the study of the oval photonic micropillar [Mun+12].

When studying structured single nano-objects like NWs, it is thus important to take into account the effects of the nano-structuration on both the electronic and the photonic properties of the system.

3.1.4 Semiconducting nanowire growth

In order to control the optical properties of semiconducting emitters it is necessary to tailor both the emitter shape and dimensions and its surrounding environment. Semiconducting nanowires hence appear as extremely promising structures as they allow such electronic and photonic design. Their fabrication constitutes a key challenge in our research team, where several approaches and materials are investigated. The NWs used in this thesis were grown by MBE.

The growth process is sketched in figure 3.8 for the case of CdTe insertions inside ZnTe NWs. The same principle applies to more complicated Te-based or Se-based structures. In the case of the Te-based NWs, all the details can be found in Pamela Rueda-Fonseca PhD thesis and subsequent publications [Rue15; Rue+14].

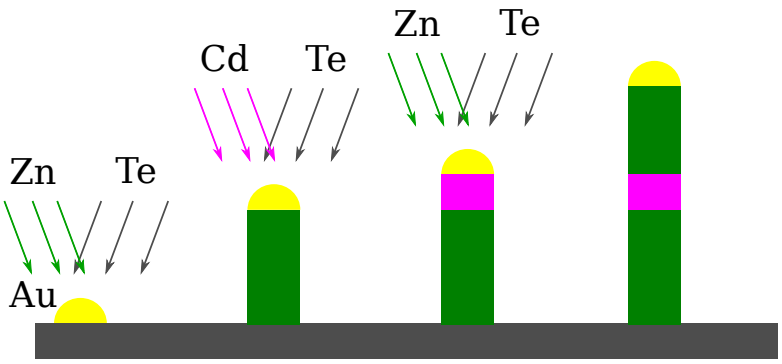

Figure 3.8 – Schematic of the MBE growth process.
NWs are grown by Au-catalysed MBE. After the growth of a buffer, a small amount of Au is evaporated on the sample and annealed to form Au droplets. II-VIs atom fluxes are then sent towards the substrate. Crystallisation occurs at the Au interface with the substrate, thus the growth mainly happens below the droplet. Varying the atom fluxes allows to grow different kind of structures.

The sample is placed inside a ultra-high vacuum chamber, a buffer layer of suitable material is grown (ZnTe or ZnSe), and a thin layer of gold is evaporated on top of the buffer. The gold is then annealed to form small droplets on the surface of the substrate. Atom fluxes are sent towards the substrate with adjustable proportions, where they diffuse and adsorb on the sample surface. The Au droplet acts as a catalyst for the crystallisation that occurs at its interface with the substrate surface. Hence, the crystal growth happens preferentially below the droplet even though some 2D growth occurs on the whole surface, at a much slower speed.

Heterostructures are created by changing the atom fluxes. Longitudinal (i.e. along the NW axis) and radial growth are competing during the process, but compounds ratios and temperature variations allow to favour one or the other [Rue+14; Rue15]. Therefore it is possible to grow cone-shaped structures, or radial heterostructures, etc. We will come back more precisely to each NW morphological properties when discussing their optical response.

However, it must be noted that this growth process can result in samples with large morphological variability between NWs from the same substrate. As briefly shown previously, slight changes in the NW morphology can have an impact on its optical properties. Therefore, we will show in the next sections that it is of crucial importance to extract statistically significant characteristics of NWs before characterising their optical properties in depth. As an example, this implies measuring the excitonic emission wavelength for a large amount of single NWs on a given substrate before studying one NW in depth, in order to bound the excitonic energy scales that we can use to model its emission properties.

3.2 Nanowire quantum dot spectroscopy: experimental details

This section introduces the experimental methods used in this thesis in order to perform NW spectroscopy.

3.2.1 Optical spectroscopy

Linear spectroscopy setup

Let us first introduce the microphotoluminescence (µPL) setup, sketched in figure 3.9.

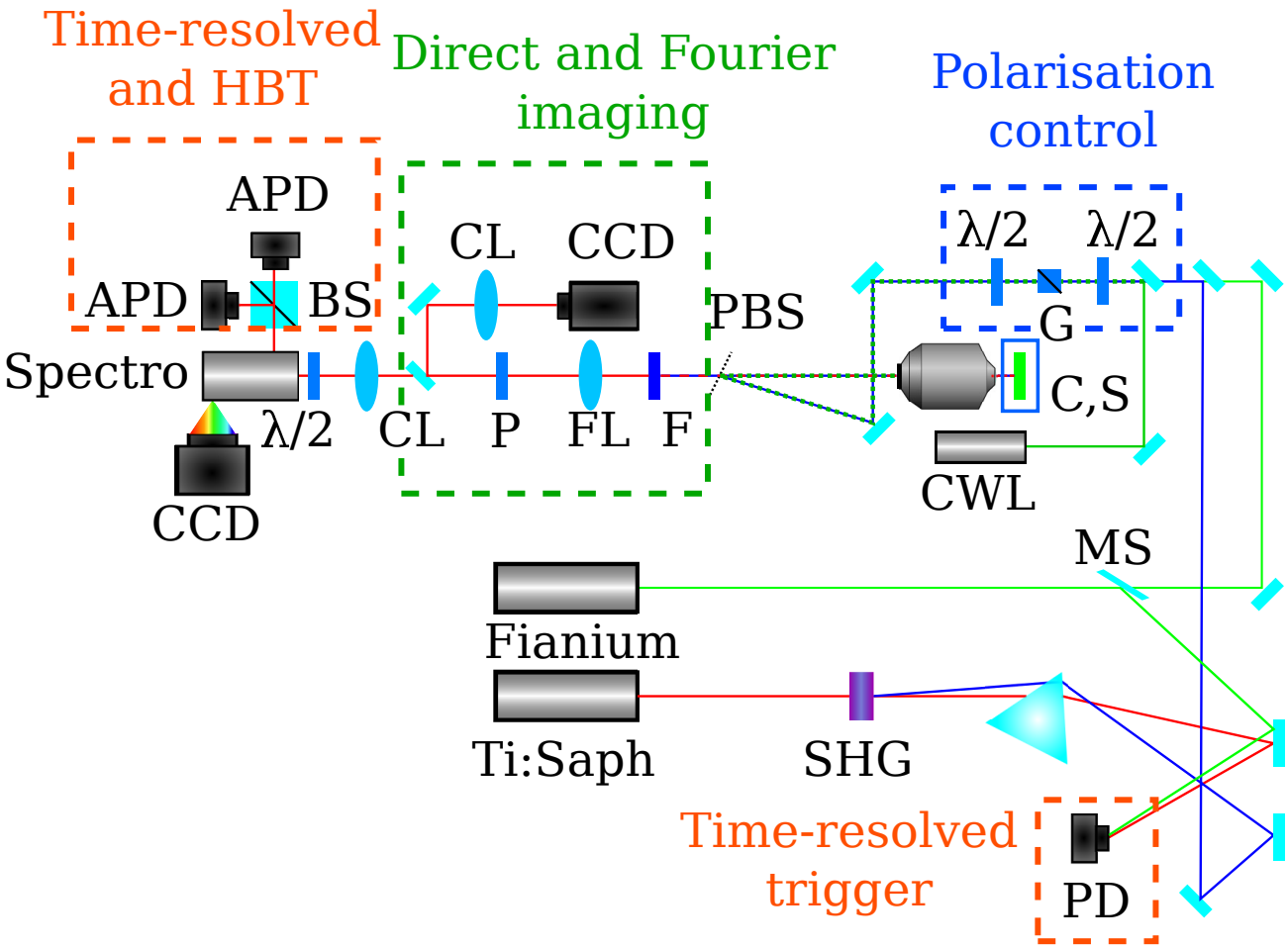

Figure 3.9 – Optical spectroscopy setup.
Schematic of the spectroscopy setup with the different optical stages. $\lambda/2$: Half-wavelength retardation plate, APD: Avalance Photodiode; BS: Beam Splitter; C,S: Cryostat and sample; CCD: Charged-coupled device camera; CL: Collection lens; CWL: Continuous wave laser; F: Longpass filter; FL: Fourier Lens; G: Glan-Taylor polariser; Fianium: ps-pulsed supercontinuum laser; MS: Microscope cover slip; P: Polariser; PBS: Pellicle Beam Splitter; PD: Photodiode; SHG: frequency doubling crystal for the Ti:Saph; Spetro: iHR550 Spectrometer; Ti:Saph: frequency doubled Nd:YAG pumped Titanium:Sapphire laser (ps-pulsed)

Three different lasers have been used. The first one is a continuous wave (cw) solid-state laser with an emission wavelength at 488 nm (LBX-488 from oxxius [Oxx]). The second one is a ps-pulsed Titanium:Sapphire (Ti:Saph) laser at 894 nm pumped by a frequency doubled Nd:YAG laser at 532 nm (Tsunami and Millenia respectively, from Spectra Physics [Phy]). It is then frequency doubled to produce ∼6 ps pulses at 447 nm with a sharp spectral bandwidth. The 447 nm pulses have a maximum power of 3 mW and a repetition rate of 80 MHz. The

last laser is a tunable spectrally filtered ps-pulsed supercontinuum laser (WhiteLase SC and Superchrome from Fianium [Fia]) that produces ∼15 ps pulses with a 10 nm minimum spectral bandwidth (also tunable). These pulses have a maximum power density of 1 mW/nm and a repetition rate of 76 MHz.

Each laser beam is spatially filtered and controlled in polarisation via a set of halfwave plates and Glan-Taylor prism. It can then be injected into a microscope objective using a pellicle beam splitter (6% reflection). We use a 40× objective with a high NA of 0.75 (Zeiss EC Plan-Neofluar 40×/0.75, 2mm working distance). It focuses the excitation laser on the sample surface, which is inside a cryostat for Helium-temperature cooling (Oxford Instruments [Oxf]). Fluorescence is collected in a confocal geometry and filtered by a longpass filter to block the light originating from the laser, before being sent to a spectrometer for spectral analysis. The spectrometer is a Horiba Jobin-Yvon iHR550 equipped with a 600gr/mm grating [Job] that disperses the light on a Princeton Instruments Pixxis1000 CCD camera [Pri]. A polariser can be used to analyse the polarisation state of the fluorescent light. Other optical elements will be introduced later. This setup thus enables the characterisation of the NWQD fluorescence properties by spectral analysis, i.e. by determining the energy of the excitonic emission and its power.

Time-resolved µPL

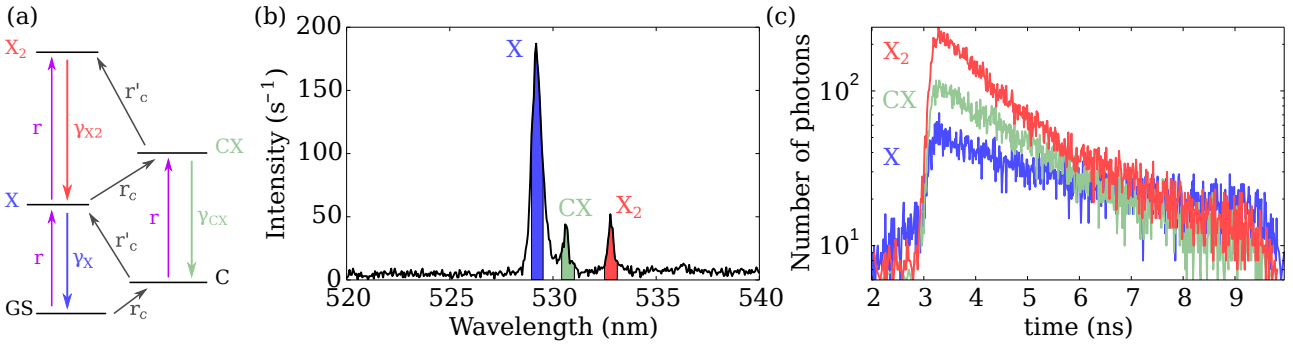

Figure 3.10 – Principle of time-resolved spectroscopy.
Application to CdSe QDs inside ZnSe NWs. (a) Sketch of the excitonic cascade inside the QD as proposed in [Suf+06]. Excitations are denoted in purple or gray upwards arrows with their corresponding power-dependent pumping rates. The downward arrows indicate excitonic transitions, associated to the fluorescence spectrum (b) at liquid helium temperature and low excitation power. They have a characteristic rate γ_i. (c) Corresponding time traces (obtained for different pumping powers). The shaded area in (b) indicate the integrated spectral bandwidth for the measurement.

In order to determine the dynamics of the excitonic emission, it is necessary to investigate the time scale over which the fluorescence process occurs in the QD. This is done using either one of the pulsed laser in a time-resolved photoluminescence (TRPL) experiment. Part of the laser pulse (the IR fundamental beam in the case of the Ti:Saph, or a small amount of the Fianium beam reflected by a microscope cover slip) is sent to a fast photodiode. The fluorescence signal is spectrally filtered using the spectrometer and sent to the transmission APD in the setup (the BS is removed). When detected, the fluorescence photon triggers a time counting module which records the time between the photon arrival time and the next excitation pulse.

This allows to recreate the temporal histogram of the fluorescence signal. The APD response time is of the order of 50 ps (ID100 from ID Quantique [Qua]), while the typical lifetimes of our emitters range from a few hundreds of picoseconds to a few nanoseconds.

Such measurements are exemplified in figure 3.10 for a CdSe QD inserted inside a ZnSe/ZnMgSe core-shell NW, considering the various types of excitons present in the system (neutral, charged and biexciton). The QD spectrum at liquid He temperature and under pulsed excitation at low pumping power is represented, with the spectral integrated bandwidth used in the transient measurement on the last panel for each spectral line. The energy diagram on the left illustrates the excitonic population as discussed in section 3.1.2. The quantum dot can be empty (ground state GS), trap a single charge (C), be in its first excited state (X), or in a charged (CX) or doubly excited (X_2) state.

The upward arrows in the energy diagram represent an excitation event which depends on the laser power. As proposed in refs. [Suf+06] and [Sal+09], the creation of an electron-hole pair occurs with a rate r identical for all transitions, while the single charge excitation events occurs at different rates according to the charging state of the trap (rates r_c and r'_c). The downward vertical arrows represent transitions associated with the measured spectral lines. These transitions can be radiative, or non-radiative. Each of these transition is associated with a lifetime τ_i, and conversely a decay rate $\gamma_i = 1/\tau_i$. They can be further decomposed in $\tau_{i,\mathrm{r}}$ (resp. $\gamma_{i,\mathrm{r}}$) and $\tau_{i,\mathrm{nr}}$ (resp. $\gamma_{i,\mathrm{nr}}$) for the radiative and non-radiative parts of the total decay time. Decay time measurements lead to the determination of the total decay rates γ_i for each transition. A more complete modelling is then necessary to separate radiative and non-radiative terms.

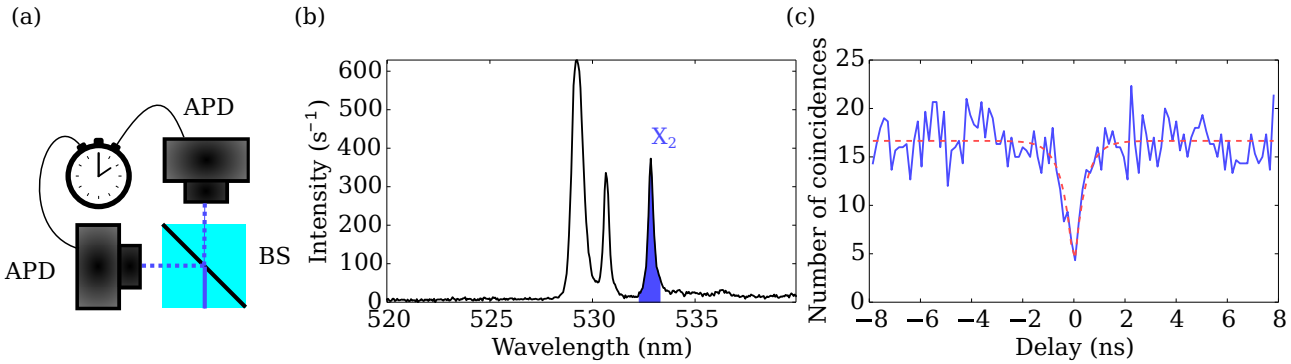

Figure 3.11 – Principle and example of a $g^{(2)}$ measurement.
CdSe QDs inside ZnSe NWs. (a) Schematic of the HBT setup. A 50/50 beam splitter sends the incoming photons to either one of the APDs, while the delay between two consecutive counts is measured. (b) Spectrum of the same NWQD as in figure 3.10 for a higher excitation power. The measurement is performed on the biexciton, the shaded area indicates the integrated spectral bandwidth. (c) $g^{(2)}$ measurement of the biexciton (blue), with a simple fit (red dashes). The dip at zero delay is a signature of photon antibunching.

The use of a Hanbury Brown and Twiss (HBT) setup also allows us to perform correlation measurements on the NWQD fluorescence [HT56b; HT56a]. To do so, either pulsed or cw excitation can be used. The florescence signal is spectrally filter and sent to two APDs through

a 50-50 beam splitter. In opposition to lifetime measurements, here one APD serves as the start trigger and the other one as the stop. The histogram of delays τ between two consecutive photons is thus retrieved. If $p(t)$ represents the probability to detect a photon at a given time t and $p(t'|t)$ the conditional probability to detect a photon at a time t', having detected one at the time t, the HBT setup allows to determine the function:

$$g^{(2)}(\tau) = \frac{p(t+\tau|t)}{p(t+\tau)} = \frac{p(\tau|0)}{p(\tau)}. \tag{3.14}$$

This function is the second order correlation function of the emitted light, and gives informations about its statistical nature [Man79]. As in atomic physics, the fluorescence from a single quantum dot can be thought of as de-excitation from a two-level system, and is thus expected to lead to sub-poissonian photon statistic [SM83; Ima+00]. An example of second order correlation measurement is presented in figure 3.11 for the same NWQD as before, under cw excitation. The $g^{(2)}$ measurement is performed at He temperature on the X_2 line (blue shaded area). It exhibits a dip around zero delay, known as the *antibunching* effect. This means that the QD cannot emit two photons at the same energy and at the same time, and is therefore used as a characterisation of single-photon emission from our QD.

All these results will be presented and discussed more in details in section 3.3

Spatial characterisation: Fourier imaging

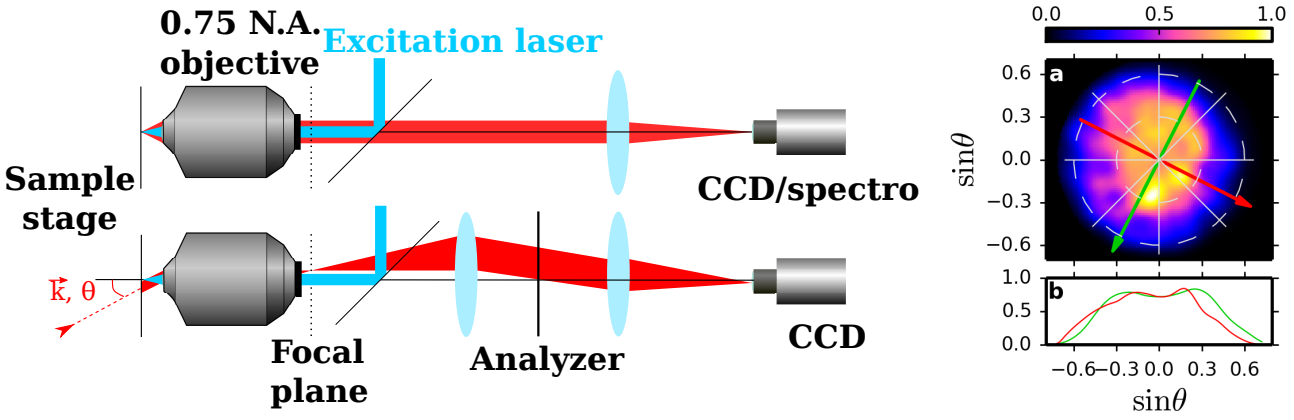

Figure 3.12 – Fourier plane imaging.
Principle of the Fourier imaging technique. As opposed to the confocal microscopy technique, the aim is to image the back focal plane of the objective on the CCD camera. An additional lens and an analyser are thus added in the setup. We can thus analyse the light polarisation as a function of its direction of emission θ. An example is shown on the right, from a CdTe QD inside a ZnTe NW. The intensity is mapped in units of $\sin\theta$. Cross-sections are also plotted for easier analysis. It represents a direct mapping of the radiation diagram of a single NWQD.

Finally, after having characterised the spectral and temporal properties of the fluorescence signal, we can characterise its spatial properties using Fourier imaging (also called back focal plane imaging). This is done by adding a lens to the confocal microscopy setup (denoted as the Fourier lens), which images the back focal plane of the microscope objective onto a CCD

camera using the flip mirror. The principle of the measurement is sketched in figure 3.12. The addition of the Fourier lens transforms plane waves originating at a given angle from the sample into points on the CCD camera. Hence, it allows direct imaging of the direction at which the photons are emitted, up to an angle from the sample normal equal to $\arcsin(\mathrm{NA}) = 48.5^{\circ}$ in our setup. In other terms, we are able to project the radiation diagram of the emitted photons onto the CCD plane. Polarisation analysis in the Fourier plane is also possible, as sketched on figure 3.12. This technique is extensively used and discussed in chapter 4.

3.2.2 Sample preparation for single NWQD spectroscopy

Two kinds of methods have been employed to perform spectroscopy on single NWQDs. In the first case, one directly uses the as-grown sample, ensuring that NWs are studied in their fabrication state. In this case, NWs are commonly *pointing along the optical axis* of the setup. However, this configuration presents several drawbacks because of the high density of NWs and their random position on the sample:

- it can be difficult to isolate the emission coming from a single given NW from the one coming from a neighbouring wire or a substrate defect
- it is difficult to precisely locate a given NW to perform successive experiments on it.

The second method is to mechanically disperse the NWs on a pre-patterned substrate. This ensures us that we can find NWs well-isolated from one another, and that we can precisely locate them to perform different experiments on them. However, they can be damaged during the deposition process. In this configuration we can only study NWs that are *lying on the substrate*, in the plane perpendicular to the optical axis, and the interaction between their fluorescence and the substrate has to be taken into account. As will be demonstrated later, these two configuration play a great role in NWQDs studies as they provide different informations on the QD according to its radiation diagram properties. We will detail here the fabrication of the patterned substrate.

As the NWQD fluorescence is possibly emitted in every directions, the fact that the NW lies on the substrate means that a significant fraction might be lost inside the substrate. To prevent this from happening, the patterned substrate is covered with a metallic mirror in order to reflect the light towards the microscope objective. To prevent luminescence quenching coming from the close-by metallic surface, a dielectric Al_2O_3 spacer is added using ALD [Dre74; CPS78], [NH12, Ch. 10]. Its thickness is chosen to ensure constructive interference between the light reflected from the mirror and the direct emission from the NW. It can be calculated using the theory of dipole radiation near planar substrates or within multi-layer systems, relying again on matrix formalism [CCM96; BW99; PHM00]. In order to take into account the fact that the QD (modelled as a dipole) is inside the NW, the theory developed in [PHM00] has been preferred as it extends the theory presented in [CCM96] to dipoles placed inside the stratified medium, at the expense of not encompassing the modification of the temporal dynamics of the radiation (e.g. decay time reduction).

The geometry used to derive the radiation emitted by the dipole is presented in figure 3.13. The multilayer system is orthogonal to the z' (optical) axis. A rotation of angle φ of the

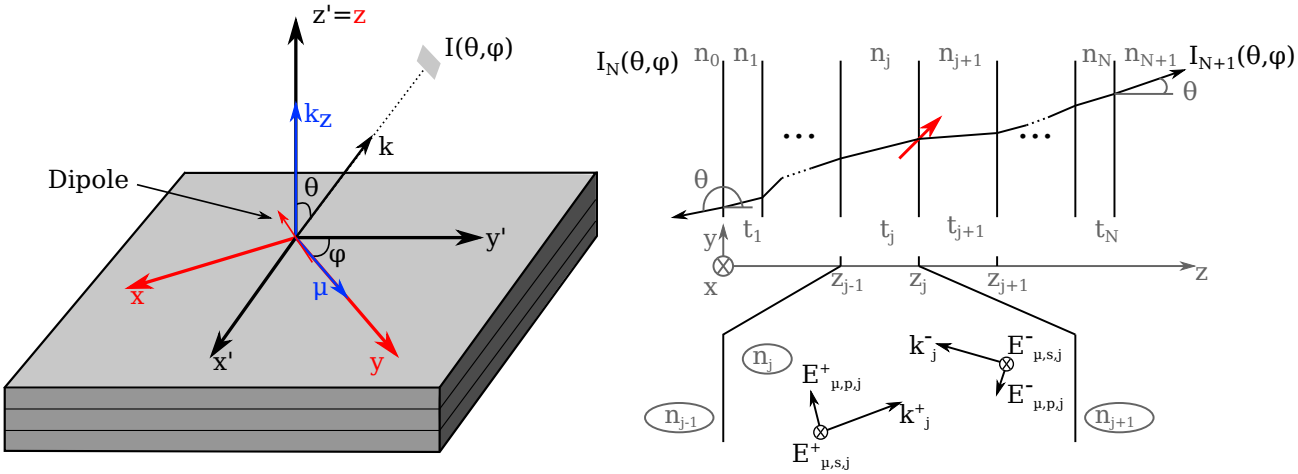

Figure 3.13 – Radiating dipole inside a multilayer system.
Geometry for the derivation of the radiation properties of a dipole within an arbitrary multilayer system. The left panel shows the coordinate systems (x', y', z') (laboratory) and (x, y, z) (dipole), as well as the (y, z) in-plane geometry and the conventions for the electric fields inside a single layer. The rotation to the (x, y, z) frame is convenient because the dipole lies in the (y, z) plane, as shown on the upper right panel.

laboratory frame (x', y', z') around the z' direction is performed to obtain a $(x, y, z = z')$ system aligned with the main dipole axis, so that the dipole lies in the (y, z) plane. The field radiated by the dipole can thus be expressed as:

$$\mathbf{E}_{\text{tot}}(\mathbf{r}) = \mathbf{E}_{\text{tot}}(\boldsymbol{\rho}, z) = \frac{1}{k_0^2}\int \boldsymbol{E}_{\boldsymbol{\mu}} \exp\{i\boldsymbol{\mu} \cdot \boldsymbol{\rho}\} \mathrm{d}^2\boldsymbol{\mu} \tag{3.15a}$$

$$\boldsymbol{E}_{\boldsymbol{\mu}} = \frac{1}{k_0}\int \boldsymbol{E}_{[\boldsymbol{\mu}, \boldsymbol{k_z}]} \exp\{ik_z z\} \mathrm{d}k_z \tag{3.15b}$$

where we have decomposed the total wave vector $\mathbf{k}$ into the in-plane wave vector $\boldsymbol{\mu}$ and the k_z component in the (x, y, z) coordinate system, where $\boldsymbol{\rho}$ is the in-plane position vector. In this coordinate system we thus have:

$$k = [k_x, k_y, k_z] = [\boldsymbol{\mu}, k_z], \quad \boldsymbol{\mu} = [0, \mu]. \tag{3.16}$$

The system is composed of N stacked layers, isotropic in the x direction, characterised by the index j with thickness t_j and (possibly complex) refractive index n_j. The wave vector in the j-th layer is thus $k_j = n_j k_0$. It is further assumed without loss of generality that the dipole is placed at the j-the boundary, and that layers j and $j+1$ have the same refractive index. The field in each layer is decomposed into s and p polarised components, where the s polarisation vector lies always parallel to the interfaces. The field in the j-th layer is thus given by:

$$\begin{aligned}\mathbf{E}_j(\mathbf{r}) = \frac{1}{k_0^2}\sum_{\nu=s,p}\int \Big[&\mathbf{E}^{+}_{\boldsymbol{\mu},\nu,j} \exp\{i\boldsymbol{\mu} \cdot \boldsymbol{\rho}\} \exp\{ik_{z,j}(z - z_{j-1})\} + \\ &\mathbf{E}^{-}_{\boldsymbol{\mu},\nu,j} \exp\{i\boldsymbol{\mu} \cdot \boldsymbol{\rho}\} \exp\{-ik_{z,j}(z - z_{j-1})\}\Big] \mathrm{d}^2\boldsymbol{\mu}\end{aligned} \tag{3.17}$$

which is just the sum of positively and negatively z-propagating fields of each polarisation state. The polarisation states can thus be represented as:

$$\mathbf{E}^{\pm}_{\boldsymbol{\mu},\nu,j} = E^{\pm}_{\boldsymbol{\mu},\nu,j}\boldsymbol{\kappa}^{\pm}_{\boldsymbol{\mu},\nu,j} \tag{3.18}$$

where

$$\boldsymbol{\kappa}^{\pm}_{\boldsymbol{\mu},s,j} = [1,0,0] \qquad \boldsymbol{\kappa}^{\pm}_{\boldsymbol{\mu},p,j} = \frac{1}{k_j}\left[0, \pm k_{z,j}, -\mu\right]. \tag{3.19}$$

We can define the field amplitude vector as:

$$\mathbf{A}_{\boldsymbol{\mu},\nu,j} = \begin{pmatrix} E^{+}_{\boldsymbol{\mu},\nu,j} \\ E^{-}_{\boldsymbol{\mu},\nu,j} \end{pmatrix} \tag{3.20}$$

Again, $\mathbf{A}_{\boldsymbol{\mu},\nu,j}$ can be propagated using the transfer matrix formalism:

$$\mathbf{A}_{\boldsymbol{\mu},\nu,j} = \mathbf{P}_j^{-1}\mathbf{T}^{-1}_{\nu,j}\mathbf{T}_{\nu,j+1} \cdot \mathbf{A}_{\boldsymbol{\mu},\nu,j+1}, \qquad j = 0,1,\ldots,N \tag{3.21}$$

where the transmission matrices $\mathbf{T}_{\nu,j}$ and the propagation matrix $\mathbf{P}_j$ are given by:

$$\mathbf{T}_{s,j} = \begin{pmatrix} 1 & 1 \\ \frac{k_{zj}}{k_0} & -\frac{k_{zj}}{k_0} \end{pmatrix} \qquad \mathbf{T}_{p,j} = \begin{pmatrix} \frac{k_{zj}}{k_j} & -\frac{k_{zj}}{k_j} \\ -\frac{k_j}{k_0} & -\frac{k_j}{k_0} \end{pmatrix} \tag{3.22a}$$

$$\mathbf{P}_j = \begin{pmatrix} \exp\{ik_{z,j}t_j\} & 0 \\ 0 & \exp\{-ik_{z,j}t_j\} \end{pmatrix}. \tag{3.22b}$$

Recursively applying equation (3.21) allows to express the field amplitude in the 0-th medium as a function of the field in the j-th medium:

$$\begin{aligned} \mathbf{A}_{\boldsymbol{\mu},\nu,0} &= \mathbf{T}^{-1}_{\nu,0}\mathbf{T}_{\nu,1}\prod_{\sigma=1}^{j}\mathbf{P}_\sigma^{-1}\mathbf{T}^{-1}_{\nu,\sigma}\mathbf{T}_{\nu,\sigma+1} \cdot \mathbf{A}_{\boldsymbol{\mu},\nu,j+1} \\ &= \mathbf{L}_{\nu,j} \cdot \mathbf{A}_{\boldsymbol{\mu},\nu,j+1} \end{aligned} \tag{3.23}$$

where we have introduced the matrix:

$$\mathbf{L}_{\nu,j} = \begin{pmatrix} \alpha^{+}_{\nu,j} & \alpha^{-}_{\nu,j} \\ \beta^{+}_{\nu,j} & \beta^{-}_{\nu,j} \end{pmatrix}. \tag{3.24}$$

We thus only need to derive the field radiated by the dipole in the j-th layer, and we will be able to propagate it towards the semi-infinite half spaces. Assuming an oscillating dipole $\tilde{\mathbf{d}}\exp\{-i\omega t\}$, which acts as a current source:

$$\mathbf{j}(\mathbf{r},t) = -i\omega\tilde{\mathbf{d}}\exp\{-i\omega t\}\delta(\mathbf{r}) \tag{3.25}$$

the dipolar field $\mathbf{E}^d(\mathbf{r},t) = \mathbf{E}^d(\mathbf{r})\exp\{-i\omega t\}$ can be found after a slightly lengthy derivation and decomposed into $\nu = s,p$ polarisations:

$$\mathbf{E}^{d\pm}_{\boldsymbol{\mu},\nu,j} = E^{d\pm}_{\boldsymbol{\mu},\nu,j}\boldsymbol{\kappa}^{\pm}_{\boldsymbol{\mu},\nu,j} \tag{3.26a}$$

$$E^{d\pm}_{\boldsymbol{\mu},\nu,j} = \frac{i}{8\pi^2\varepsilon_0}\frac{k_0}{k_{z,j}}\left(\tilde{\mathbf{d}} \cdot \boldsymbol{\kappa}^{\pm}_{\boldsymbol{\mu},\nu,j}\right) \tag{3.26b}$$

If the dipole is the only source of radiation in the system, the amplitude vectors in both semi-infinite half-spaces are:

$$\mathbf{A}_{\boldsymbol{\mu},\nu,0} = \begin{pmatrix} 0 \\ E^{-}_{\boldsymbol{\mu},\nu,0} \end{pmatrix} \qquad \mathbf{A}_{\boldsymbol{\mu},\nu,N+1} = \begin{pmatrix} E^{+}_{\boldsymbol{\mu},\nu,N+1} \\ 0 \end{pmatrix} \tag{3.27}$$

Adding the dipole field at the j-th boundary into equation (3.23) gives the relation between the fields in the two half-spaces:

$$\mathbf{A}_{\boldsymbol{\mu},\nu,0} = \mathbf{L}_{\nu,N} \cdot \mathbf{A}_{\boldsymbol{\mu},\nu,N+1} + \mathbf{L}_{\nu,j-1}\mathbf{P}_{j}^{-1} \cdot \begin{pmatrix} -E^{d+}_{\boldsymbol{\mu},\nu,j} \\ E^{d-}_{\boldsymbol{\mu},\nu,j} \end{pmatrix} \tag{3.28}$$

As detailed in [PHM00], equation (3.28) differs from the well-known matrix relation between the fields in the two half-spaces by the second term of the right-hand side, which contains three separate physical quantities: the dipole radiation term, the distance between the dipole and the first lower interface, and the response of the whole structure below the dipole location. Equation (3.28) can be solved to find an explicit formulation for the fields, giving:

$$E^{+}_{\boldsymbol{\mu},\nu,N+1} = U^{+}_{\nu,j-1}\exp\{-ik_{z,j}t_j\}E^{d+}_{\boldsymbol{\mu},\nu,j} + U^{-}_{\nu,j-1}\exp\{ik_{z,j}t_j\}E^{d-}_{\boldsymbol{\mu},\nu,j} \tag{3.29a}$$

$$E^{-}_{\boldsymbol{\mu},\nu,0} = V^{+}_{\nu,j-1}\exp\{-ik_{z,j}t_j\}E^{d+}_{\boldsymbol{\mu},\nu,j} + V^{-}_{\nu,j-1}\exp\{ik_{z,j}t_j\}E^{d-}_{\boldsymbol{\mu},\nu,j} \tag{3.29b}$$

where:

$$U^{\pm}_{\nu,j} = \pm\frac{\alpha^{\pm}_{\nu,j}}{\alpha^{+}_{\nu,N}} \qquad V^{\pm}_{\nu,j} = \pm\left(\beta^{+}_{\nu,N}\frac{\alpha^{\pm}_{\nu,j}}{\alpha^{+}_{\nu,N}} - \beta^{\pm}_{\nu,j}\right) \tag{3.30}$$

Finally, we can find the radiated field in the direction $\mathbf{k}$:

$$E^{\pm}_{\mathbf{k},\nu,j} = \frac{k_{z,j}}{k_j}E^{\pm}_{\boldsymbol{\mu},\nu,j} \tag{3.31}$$

or the corresponding intensity.

We can now apply these calculation to optimise the fabrication of the mirror for dispersed NWs. As an example, the case of CdTe-ZnTe NWQDs is illustrated in figure 3.14. The investigated geometry is presented in panel (a), and consists in an optically thick Au mirror with an Al_2O_3 spacer of varying thickness. The QD is modelled as a radiating dipole in the horizontal (x or y) or vertical (z) direction centered in an 100 nm thick homogeneous ZnTe layer, corresponding roughly to the NW diameter around the QD. The NW is thus modelled as an infinite layer here. The luminescence is collected in the upper half-space in a numerical aperture of 0.45. For comparison, we also compute the radiated intensity with no ZnTe layer for a dipole just above the Al_2O_3-Air interface, i.e. neglecting the presence of the NW core and shell. Panel (a) further contains the radiation diagram of the different dipoles radiating at a wavelength of 620 nm for a spacer thickness of 250 nm. This value is chosen from panel (b), which represents the collected intensity as a function of the spacer thickness. It corresponds to a maximum of collected intensity for the in-plane dipole in ZnTe. The dramatic difference between the computation without and with the ZnTe layer shows that its inclusion is of significance importance, as the QD is embedded in a thick semiconducting shell. In order to avoid evanescent coupling between the

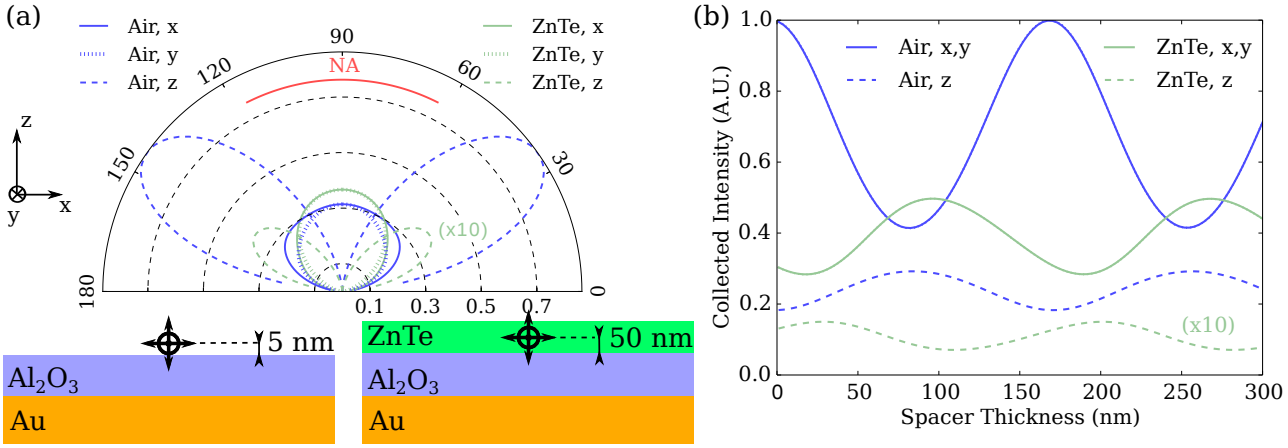

Figure 3.14 – Effect of the Al_2O_3 spacer thickness on the properties of a radiating dipole. (a) Stacked Al_2O_3-Au and ZnTe-Al_2O_3-Au systems with the radiating x, y and z dipoles, and corresponding radiation patterns for a 250 nm thick spacer at a wavelength of 620 nm. The experimental numerical aperture NA=0.45 is indicated in red, and the legend indicates the surrounding material of the dipole and its orientation. The x and y-oriented dipoles have very similar radiation patterns in the $x-z$ plane, with a well-centred emission lobe towards the z axis. (b) Integrated intensity in the experimental NA for each configuration as a function of the Al_2O_3 thickness. The lines corresponding to the y dipole are superimposed with the x dipole ones. For both panels, note that the (ZnTe, z) curve has been multiplied by 10 for visibility. From these simulations, we can deduce that the optimum spacer thickness for a CdTe QD in a ZnTe NW is around 250 nm.

QD radiation and the metallic substrate via local SPP lauching, we further restricted the choice of the spacer thickness to values greater than 100 nm, explaining the retained value. We can also see that the dipole orientation bears great importance for the choice of the spacer thickness. We favoured the horizontal dipole (i.e. in the (x, y) plane) as preliminary observations reported that the QD luminescence is predominantly aligned with the NW axis, hence in the plane of the substrate [Ste13, Ch. 3],[Art+13].

The patterned substrate is fabricated from a standard silicon (Si/SiO_2) substrate. A positive photoresist (Shipley S1805) is spin-coated on the substrate and soft baked on a hot plate at 115 °C for 1 minute. Labelled square arrays of alternated horizontal and vertical marks are patterned on the resist using optical lithography. The resist is then developed, and a dry etching step is performed using reactive ion etching (RIE) with a CHF_3 plasma. Finally, the resist mask is removed using acetone, leaving the patterned array as deep holes in the top SiO_2 layer.

This pre-pattered substrate is then covered with an optically thick (≈100 nm) Au layer using electron beam (e-beam) evaporation. The final Al_2O_3 layer is deposited using ALD, which ensures a good precision on the deposited thickness as well as really smooth and conformal deposition.

As an example, figure 3.15 shows part of such a substrate for optical studies of single NWs. Isolated NWs can be localised with respect to the large marks to be studied in multiple setups and/or processed.

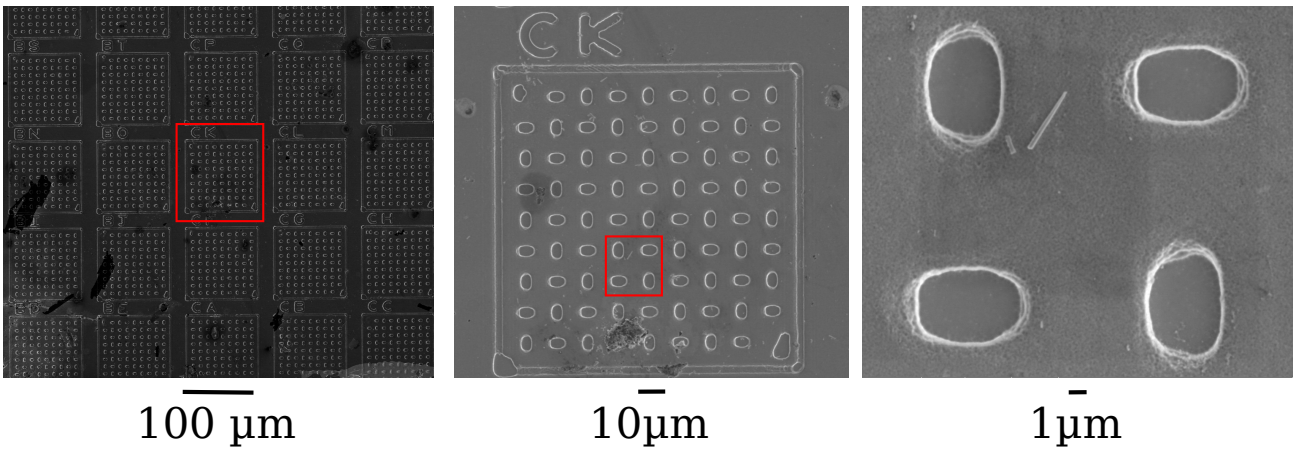

Figure 3.15 – Patterned substrate for optical study of single NWQDs.
Progressive zooms of SEM images on a single NW on a patterned substrate. The difference labelled regions are visible, as well as the marks allowing location of the NW.

3.3 The importance of statistics in single NWQD spectroscopy: NWQD zoology

In the previous sections, we have introduced the basics of semiconductor optics related to the study of NWQD. The theoretical description of light emission has been restricted to electric dipole allowed transitions. Thus, the determination of the intrinsic emitting dipole (orientation, amplitude, etc.) inside a nanowire quantum dot arises as a fundamental question. It is at the heart of this work, as it will govern the coupling possibilities with external antennas. It is also a very complicated question to address because of the high number of factors at play, from the intrinsic electronic properties of the emitting structures to the photonic effects created by the nanowires and their interaction with the surrounding medium, e.g. a reflecting substrate.

In the next two sections, we will show statistical measurements on Te-based and Se-based NWQDs respectively. They evidence the general properties of these emitters, but also demonstrate their large variability from NW to NW. A first description taking into account the photonic effects created by the structure and its interaction with the substrate will be tested in order to determine the influence on these photonic effects on the NWQDs properties.

3.3.1 Te-based nanowire quantum dots

NW presentation

The Te-based NWs used in this thesis were fabricated in order to study the effect of magnetic doping in NWQDs in the context of DMS, within the frame of Pamela Rueda-Fonseca's and Alberto Artioli's PhD thesis [Rue15] [Art16]. They originate from a single sample grown by MBE as sketched in section 3.1.4. More details on their growth process can be found in Pamela Rueda-Fonseca's work [Rue+14], [Rue15, Ch. 4] [Rue+16].

The typical structure of the NWs is presented in figure 3.16. The NWs crystallise in a ZB phase, with a tapered shape. The ZnTe core is around 200 nm thick at the base, and surrounded by a 20 nm shell made of ZnMgTe. ZnMgTe has a higher bandgap than ZnTe,

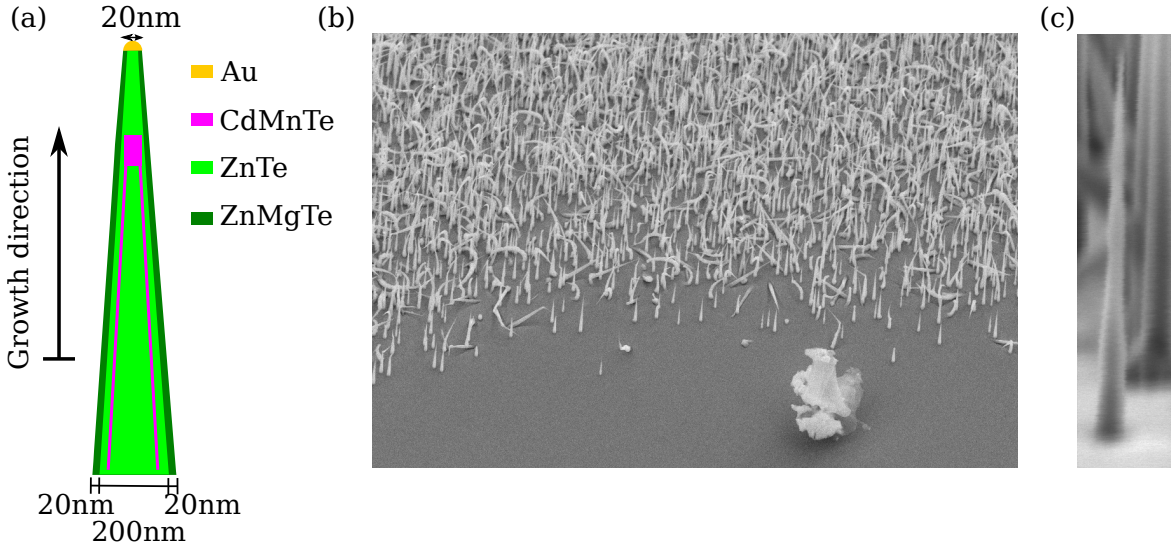

Figure 3.16 – M3082: NWs structure.
(a) Schematic of the NWs from sample M3082. The ZnTe NWs have a cone shape and are surrounded by a ZnMgTe shell. The CdTe QD is doped with Mn atoms, and is located around the two-third of the NW height. The Au catalyst droplet is still present. (b) A large field tilted SEM image reveals that some NWs are kinked. (c) A close zoom on one straight NW reveals thickness variations along the growth axis.

so this shell prevents surface induced losses or recombinations due to trapped charges. The CdTe QD is doped with Mn atoms, which possess a non-zero nuclear spin, making the QD a DMS. The Mn content fraction inside the dot is around 10%. The presence of these magnetic dopants highly increases the magnetic interaction between the carriers confined inside the QD and an externally applied magnetic field, which will be of crucial importance in chapter 4. During the QD growth, CdMnTe can also adsorb on the facets of the NW resulting in very thin CdMnTe stripes around the NW. However, these segments are often too damaged to emit any photoluminescence, and are not present on all the NWs. As can be seen on the SEM images in figure 3.16, the NWs morphology varies strongly from wire to wire, and the NW diameter can exhibit variations along the growth axis.

Localising NWQDs

NWs are mechanically dispersed from their growth substrate onto a pre-patterned substrate for optical studies, whose fabrication has been detailed in the previous section. The sample is then studied by CL at cryogenic temperatures (∼5 K). In order to minimise the damage caused to the NWs by the e-beam, we chose to use a 30 keV acceleration voltage at the expense of reducing the excitation efficiency of the setup, as a lot of electrons simply pass through the NW. The current was kept as low as possible, around 880 pA. We then scan the sample at a low magnification (2000×), collecting CL emission around the QD expected luminescence wavelength (620 nm, [Ste13]) with a 80 nm large bandwidth. This allows us to directly locate potentially efficient NWQDs.

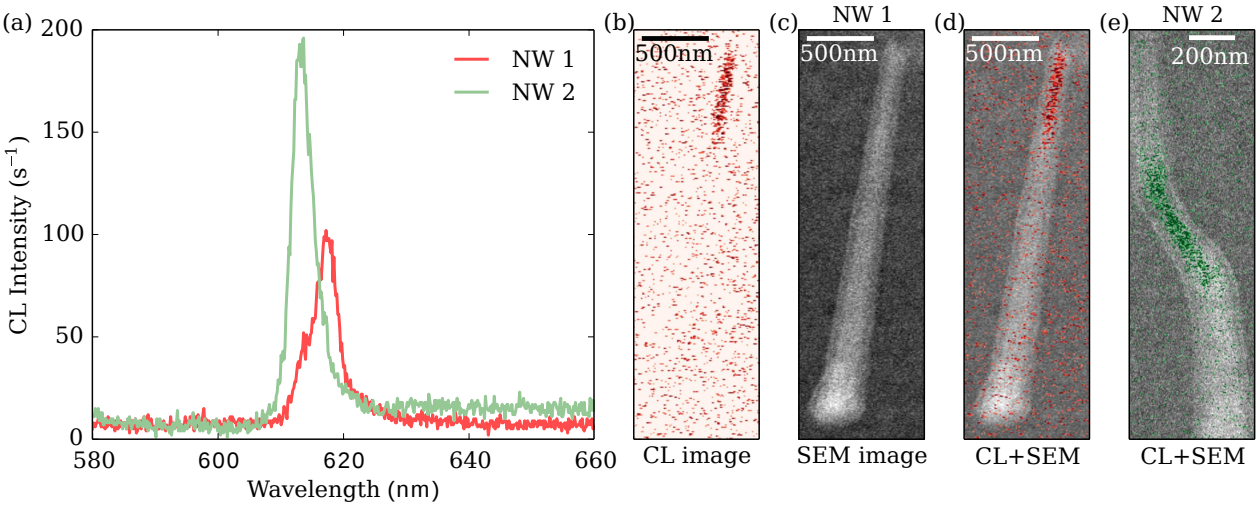

Figure 3.17 – CL of two NWQDs.
(a) Liquid helium temperature CL spectra of two different NWQDs. (b) Monochromatic CL image at 618 nm. (c) Corresponding SEM image. (d) Superimposition of the monochromatic CL image and the SEM image, allowing to probe the localisation of the luminescence inside the NW. A well localised emission arising from the tip of the NW is attributed to the QD luminescence. (e) Same process revealing the presence of a QD at the kink of a kinked NW.

A selection procedure is then established. We reject small pieces of buffer layer that are detached from the growth substrate during the mechanical dispersion. Figure 3.17 then shows the successive steps of the process for two NWs. First, a spectrum is recorded to extract the wavelength of the main emission line. Emitters deviating too much from the typical central wavelength and spectral lineshape of figure 3.17 (a) are discarded, as they might turn out to be defects in the NW. Then, a monochromatic CL image is recorded at the main emission line energy, as well as a SEM image [figure 3.17 (b) and (c)]. Again, we use a low resolution and a short dwell time of the e-beam scan to avoid damaging the NW. The combined CL+SEM images [figure 3.17 (d) and (e)] allows to precisely locate the QD position inside the NW. We further reject NWs if the luminescence comes from their base as it is only due to excitons trapped on defects, or if it is spread over a very long distance along the NW axis as this indicates a non-localised emission, in opposition with the localisation of charges normally provided by the dot. Such delocalised emission can originate from the CdTe segments around the NW. Note that the length over which a CL signal is detected does not correspond directly to the size of the QD, but rather to a combination of the size of the dot and of the carriers diffusion lengths inside the NW. The QD size has been determined from energy dispersive X ray spectroscopy [Rue+16] combined with transmission electron microscope measurements on other NWs from the same sample. It is around 10 nm. While further modelling including the carriers diffusion lengths in the NW to fit the CL profile can be implemented, as presented in refs [Nog+14; Art16], we simply determined the QD position inside the NW by considering that it lies at the center of the CL signal, fitting it by a 2D Gaussian function.

A more thorough spectral study will be subsequently made using µPL. We can however extract several primary informations. First, the luminescence from the QDs is located in a

rather large spectral region ranging from 600 to 635 nm, probably indicating a dispersion in QD shape and internal strain. Second, the QD position can sometimes be correlated with a kink, i.e. a change in growth direction along the NW axis, even though we found no systematic link between the presence of a kink and of a QD (see figure 3.17 (e) or [Ste13][Art16]).

Spectral and temporal properties

The selected NWs are then studied in the µPL setup, using pulsed excitation from the frequency doubled Ti:Saph laser at 447 nm. A typical spectrum at cryogenic temperature and low pumping power is presented in figure 3.18 (a). The main exciton line is measured here at 615 nm with a full width at half maximum (FWHM) of around 4 nm and an asymmetric lineshape. The corresponding time-resolved measurement is shown in panel (b) and can be fitted with the sum of a mono-exponential decay function and a constant background, giving access to the exciton total decay time $\tau = 1.03$ ns. We have studied the effect of rotating the polarisation direction of the exciting laser beam with respect to the NW axis. Because of the large NW diameter, even at the QD position, a very small dependence with the exciting polarisation is observed, on the order of 5% on the collected intensity. The maximum of PL intensity is always measured when the polarisation direction of the laser beam matches the NW axis. Hence, for the rest of the manuscript, all the measurements are presented with an exciting field polarised along the NW axis.

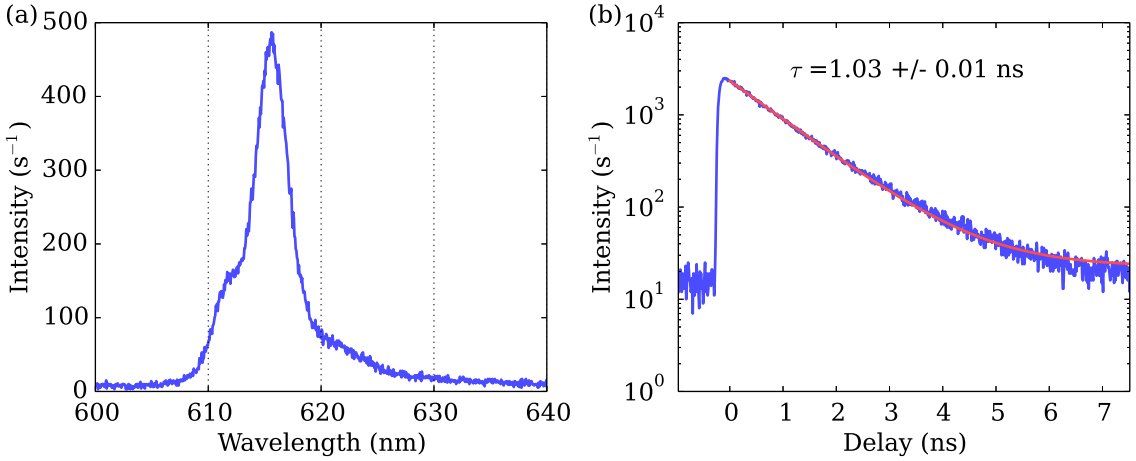

Figure 3.18 – PL spectrum and TRPL of a single NWQD.
(a) µPL spectrum of a single CdMnTe/ZnTe/ZnMgTe NWQD at 4 K excited by a ps-pulsed frequency doubled Ti:Saph laser at 447 nm and low power (∼5 µW). (b) Corresponding decay transient and monoexponential fit, yielding an exciton lifetime $\tau = 1.03$ ns. The zero delay indicates the arrival of the excitation pulse.

The results of such low pumping power µPL-TRPL combined experiments on a larger set of NWs from the same sample are gathered in figure 3.19. The central wavelength values are quite uniformly distributed within the 600-635 nm spectral region, while a slight majority of QD exhibit an exciton lifetime of around 0.5 ns with a large spread towards longer decay time.

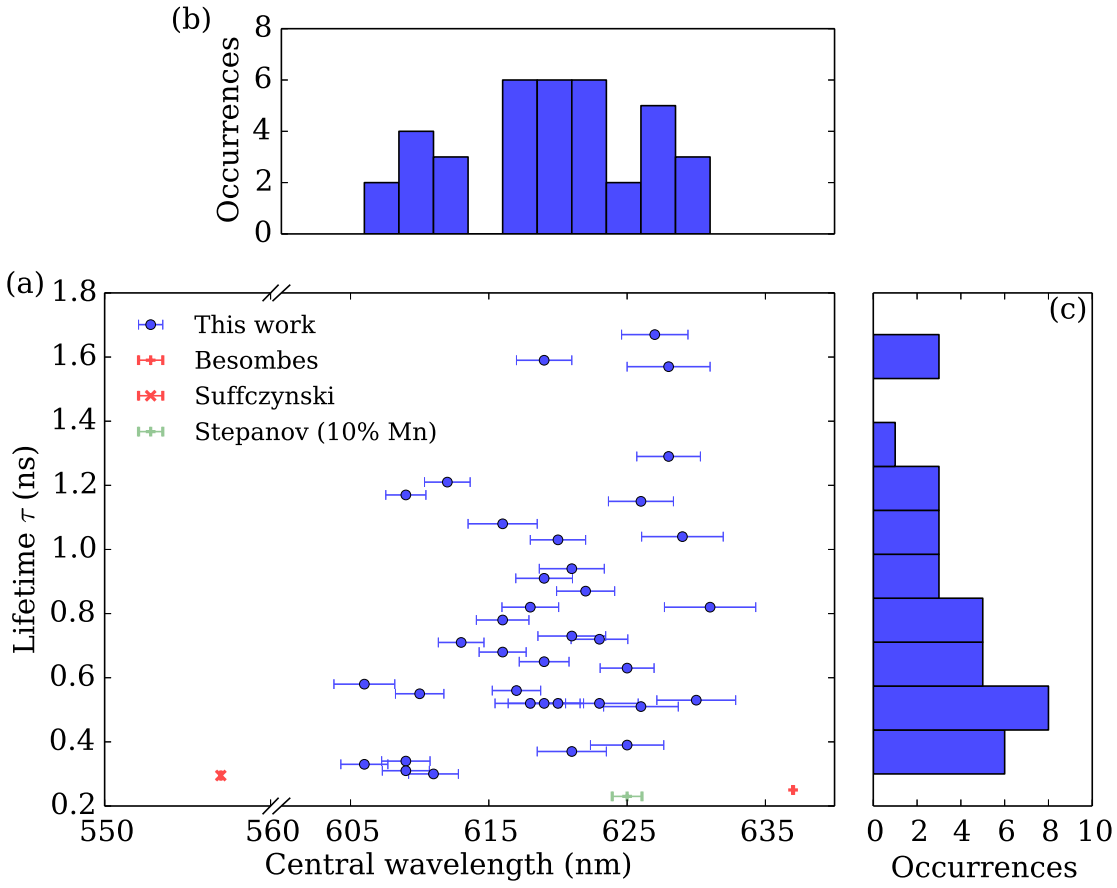

Figure 3.19 – PL-TRPL statistics of single NWQDs.
(a) Scatter plot of the measured central wavelength and exciton lifetime from the sample M3082. Horizontal bars indicate the FWHM of the PL line. For comparison, typical values for CdTe/ZnTe self-assembled QDs from the literature are reported ([Bes01; Suf+06]), as well as Mn-doped CdTe/ZnTe self-assembled QDs [Ste13]. Note the broken horizontal axis. (b) and (c) Histogram of the respective occurrences.

For comparison, we have also reported the exciton wavelength, FWHM and decay time of *self-assembled* CdTe/ZnTe quantum dots from the works of Besombes [Bes01] and Suffczyński et al. [Suf+06] as well as Mn-doped CdTe/ZnTe *self-assembled* QDs from the work of Stepanov [Ste13] (Mn fraction of 10%, as assumed in our NWQDs). The typical exciton wavelength lies between 550 and 630 nm, which is compatible with our findings, although they are likely to be very different in shape and size than our QD embedded inside NWs. A large variety of factors can contribute to the exciton energy distribution, such as a the dispersion in QD sizes from NW to NW, the strain induced by the NW core and shell on the QD and its effect on confinement and energy levels inside the dot [FC14]. Fluctuations in the concentration of the Mn atoms from one QD to the other could also play a role in this energy variation. As an example, the energy gap of bulk $Cd_{1-x}Mn_xTe$ (expressed in eV) varies according to [Fur88]:

$$E_G = 1.606 + 1.592x. \tag{3.32}$$

However, this would require a 20% Mn fraction variation within the sample, which is way above the experimental variations as confirmed by structural analysis [Rue15], so this latter factor can be safely assumed to play a much minor role.

In addition, both the exciton lifetime and spectral linewidth are found to be much smaller in the case of self-assembled QDs. For non-magnetic QDs, the linewidth is of the order of 0.07 nm, while it is an order of magnitude larger (≈0.1 nm) for Mn-doped self-assembled QDs. In the case of our magnetic NWQD, we find an average linewidth of 4.4 ± 0.9 nm. This large increase in exciton linewidth is partially attributed to the presence of the Mn atoms. In absence of external magnetic field, they create a fluctuating internal magnetic field inside the QD leading to inhomogeneous broadening of the exciton line by Zeeman effect [Fur88]. Other effects can also contribute to the line broadening in NWQDs, such as influence of surface states due to the proximity of the NW surfaces or exciton-phonon coupling which is increased by the reduced dimensionality of the system [Bou+12c].

The large increase in our observed decay times is attributed to the small valence band offset between CdTe and ZnTe associated with the effect of strain from the core-shell NW structure, which differs from the self-assembled QD case and is studied in depth in chapter 4. This results in a poorly confined hole, a small electron-hole wavefunction overlap and thus a long radiative decay rate. We also note that the total decay rate might be dominated by its non-radiative component, resulting also in a small quantum yield. These assertions on the temporal excitonic properties will be discussed in more details in chapters 4 and 5

Far-field and polarisation properties

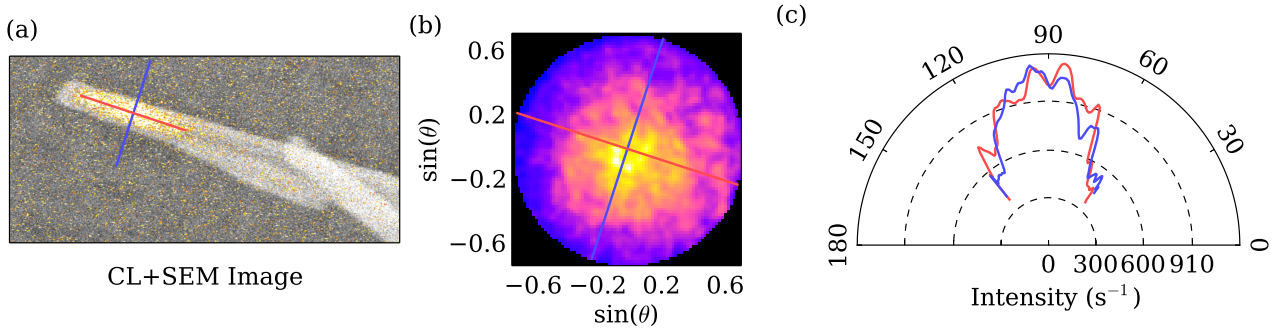

Figure 3.20 – Spatial properties of a single NWQD luminescence.
(a) Combined monochromatic CL and SEM images of a single NWQD at the exciton luminescence energy. The blue and red lines define the spatial directions for the radiation pattern measurement. The NWs next to our emitter of interest showed no luminescence around the QD emission energy. (b) Fourier microscopy image of the exciton luminescence, mapping the radiation diagram of the NWQD on a 2D plane, in units of $\sin\theta$. The directions in (a) are reported in the figure. (c) Cuts of (b) along and orthogonal to the NW axis (red and blue respectively).

Along with the spectral and temporal properties of the NWQDs light emission, we can analyse its spatial distribution and polarisation state. As mentioned in section 3.2.1, this is done in a Fourier microscopy configuration. A typical result is presented in figure 3.20. The pattern on the sample allows us to correlate SEM images and µPL results in the same geometrical frame defined

by the NW growth axis, as shown in figure 3.20 (a). The emission from a single NWQD exciton is spectrally filtered using long- and low-pass filters, and its direction of emission is imaged using the Fourier setup, resulting in the unpolarised 2D radiation diagram of figure 3.20 (b). Figure 3.20 (c) presents two line cuts of this radiation diagram. They correspond to the total intensity radiated in the plane formed by the vertical axis, i.e. perpendicular to the substrate, and the lines projected on figures 3.20 (a) and (b). A qualitative comparison with the simulated radiation patterns from figure 3.14 (a) shows that these patterns resemble the emission from a dipole parallel to the plane of the substrate. Furthermore, the 2D pattern reveals an isotropic emission diagram, indicating that the NW shape does not create a strong dielectric antenna effect. This examples shows what could typically be expected for the radiation pattern from such a NWQD, with a centred emission lobe in the $k = 0$ direction, favoured by the design of the sample mirror.

However, gathering radiation patterns for a larger number of NWQDs shows a more complex reality. The results for this set of NWs is presented in figure 3.21 (a), where we have reproduced figure 3.19 (a) and colour-coded the first Stokes parameter of the emission, i.e. the degree of linear polarisation along the NW axis of the emitted light. It is classically defined by [McM61]:

$$S_1 = \frac{I_0 - I_{90}}{I_0 + I_{90}} \tag{3.33}$$

where I_0 and I_{90} represent the intensity of the light polarised along or orthogonal to the NW axis, respectively. The direction of polarisation is encoded in the sign of S_1, as a positive value (red) indicates light polarised along the NW axis and a negative value (blue) indicates light polarised orthogonal to the NW axis. The magnitude of this degree of polarisation then scales from 0 to 1. As can easily be seen from figure 3.21 (a), most of the NWs emit light polarised along their growth axis. The average degree of linear polarisation is 0.4 with a standard deviation of 0.17.

In addition to this polarisation inhomogeneities, radiation patterns can strikingly differ from one dot to another. Several examples are shown in panels (b)-(e), where the green solid line indicates the NW growth axis. The symbols in figure 3.21 (a) correspond to each type of emission pattern, marked by the symbol in the upper left corner of the corresponding panels. The first type (panel (b), squares) corresponds to the NW presented in figure 3.20 for reference, and is the most commonly observed radiation pattern. The second one, in panel (c) (triangles), shows the emission coming from a NW which emits light polarised orthogonal to its growth axis. Interestingly, the pattern is divided in two lobes, with a pronounced dip in intensity near the center. The NW from panel (d) (circles) exhibits a "doughnut" shaped pattern slightly off-centred, and emits with a polarisation oriented along its axis. Finally, the last NWQD (panel (e), diamonds) also emits with a longitudinal polarisation, but the pattern displays clearly visible fringes orthogonal to the NW axis. This is a well-known feature arising from guiding of coherent light inside the NW, as detailed in several angle-resolved microscopy experiments dealing with nanowires [Sun+14], surface plasmons [She+11; Har+13] or even epsilon-near-zero waveguides [Ves+13]. These fringes arise from the interferences between the light scattered at each end of the NW end and are similar to the ones observed in the Young's slits experiments. The angle separation θ between consecutive fringes is of the order of $\sin\theta = 0.2$, which indicates a separation between the two sources of approximately 3 µm, in agreement with the growth parameters and the size of the NWs [Rue15].

Figure 3.21 shows that the majority of the QDs emit linearly polarised light along their NW

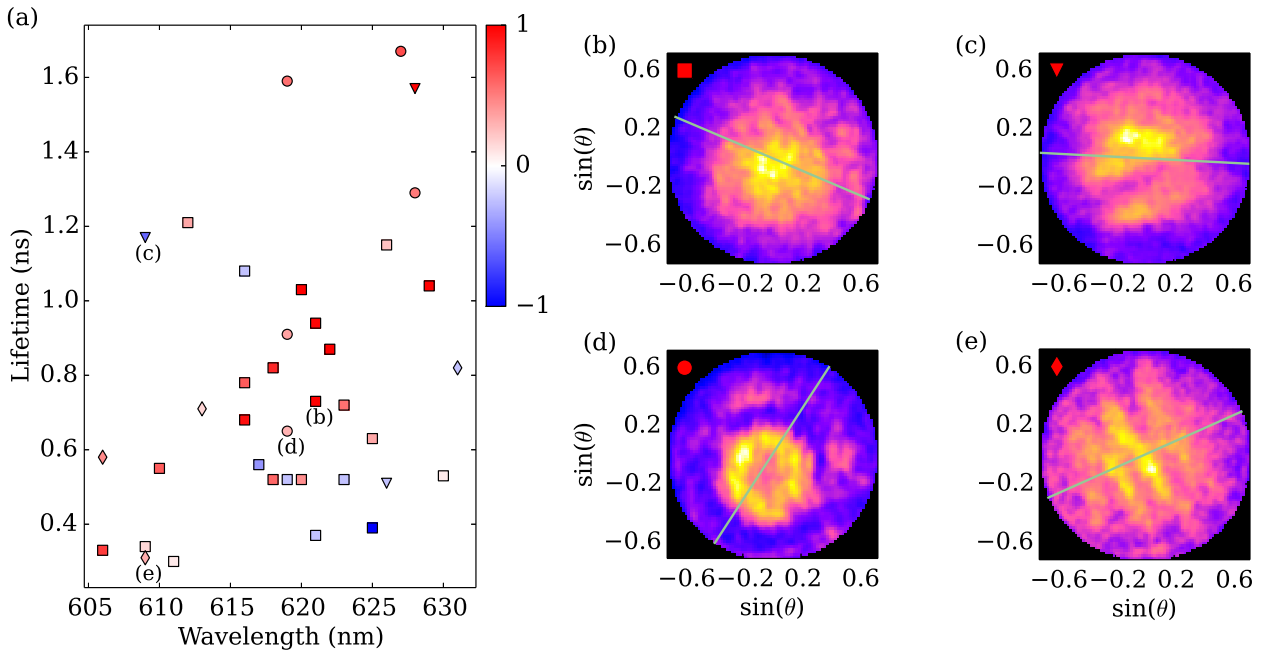

Figure 3.21 – Statistics on the spatial properties of the NWQDs luminescence. (a) Colour-coded statistical distribution of the S_1 Stokes parameter for the different NWQDs exciton emission as a function of emission wavelength and exciton lifetime. The symbols indicate the type of radiation pattern, as reported in panels (b)-(e). (b)-(e) Different radiation patterns measured for different NWQDs, reported in (a). The green line indicates the NW axis.

axis, with an isotropic, centred radiation pattern. The dispersion in energy with respect to exciton lifetime follows a trend roughly centred in the graph. The QDs exhibiting a deviation from this trend tend to exhibit a lower degree of polarisation, or even a negative value of S_1, i.e. a radial polarisation, and are gathered on the lower right part of the chart. We are thus tempted to affirm that the "regular" emission behaviour is related to the red square patterns, and that guiding (red diamonds) can occur for thicker NWs. The QDs not following this trend display a somewhat abnormal behaviour that is discussed in section 4.5.

We first attempted to find a generalised description of the NWQD emission using these statistical measurements. We used a commercial finite-element method software (Comsol multiphysics v.4.1 [Com]) to simulate the emission from a localised emitter inside the NW, taking into account a realistic geometry including the substrate and the experimental setup collection efficiency.

The initial assumption of this study was to attribute all the observed phenomena to a photonic effect arising from the NW shape and very high refractive index ($n \approx 3$). The QD was modelled as an emitting dipole for which we considered all the possible orientations and a unitary amplitude. The NWs geometrical properties were determined by SEM images, and the emitter location inside the wire by the CL experiments. While this provides us with the position of the QD along the axis, it does not give any information on possible off-centring of the QD with respect to the NW axis, so we also investigated this possibility. We started by a centred dipole

and computed the radiated far-field inside the experimental NA. We then introduced off-centring of the QD. It allowed us to extract radiation patterns for each dipole orientation and position, as well as the values of S_1. These simulations confirm that in a majority of cases, the expected emission polarisation is along the NW axis because of the dielectric screening experienced by the three orthogonal dipoles. When centred on the NW axis, the longitudinal (x) dipole experiences no or little screening, while the in-plane radial dipole (y) experiences screening from the NW/air boundary, and the vertically oriented dipole (z) experiences screening from both the NW/air and NW/substrate boundary. As an example, the table below shows the relative intensity radiated by a linearly polarised electric dipole centred inside a NW of 120 nm diameter and oriented along one of the three directions of space, normalised to the strongest contribution in both 4π integration, or inside the experimental NA, taking into account the metallic mirror and the dielectric spacer. We can see that the dipole oriented along the NW axis (x axis) is always the strongest. In addition, while the vertical dipole is slightly favoured over the in-plane orthogonal dipole, its detrimental radiation pattern makes it very poorly collected inside the experimental NA.

Dipole orientation	**NA=4π**	**NA=0.72**
x (NW)	1	1
y	0.43	0.36
z	0.63	0.07

The simulated radiation patterns mainly resemble the one from figure 3.21 (b). This corresponds to the red squares in panel 3.21 (a). Increasing the NW diameter or changing the taper angle lead to guiding features such as the ones presented in panel 3.21 (e) and with a positive S_1 [red diamonds in figure 3.21 (a)]. However, small off-centring of the emitting dipoles inside the NW can lead to radiations patterns resembling the ones of figure 3.21 (c) and (d)

However, polarisation results were less convincing. As mentioned above, the emission from dipoles aligned with the NW axis are favoured by the structure, as often reported in the literature [Wee+09]. This means that screening effects always tend to induce positive S_1 parameters, evaluated to $S_1 \approx 0.47$ for the table above, in contradiction with the dispersion we observe in our measurements. We thus have to relax the initial assumption that we can simply model the QD by a linear dipole and find a detailed description of all the separate dipole contributions from the QD. As explained in sections 3.1.1 and 3.1.2, this requires the determination of the carriers quantum states to derive the optically allowed transitions inside the QD using the Fermi golden rule.

Considering the high dispersion in spectral, temporal and spatial properties of the Te-based NWQDs emission, a large ensemble of measurements has to be performed to fully understand the exciton properties inside a given structure. In both self-assembled and nanowire QD communities, several sets of measurements have been proposed, whether they are based on correlation measurements [Suf+06; Sal+09; Poe+10], Zeeman effect [Huo+13] or, as we intend to show, polarisation measurements [Ton+12; Spi+12]. We leave here the case of Te-based NWQDs for the rest of this section, but we will come back to this problem in chapter 4 where we show how the quantum states of the carriers inside a single QD can be retrieved by polarisation-resolved Fourier microscopy.

3.3.2 Se-based nanowire quantum dots

As mentioned in the introduction, Se-based NWQDs are promising candidates in the purpose of creating optimal on-demand single photon sources operating at room temperature, as previously demonstrated by Bounouar et al. [Bou+12a] in our group. The NW growth and initial optical characterisation work was done by Thibault Cremel during his PhD thesis. We especially focused on the temporal properties of these NWQDs emission. We performed TRPL as a function of temperature in order to understand the internal dynamics of the QDs, and confirmed their single photon source character up to 200 K. We then took advantage of the very high aspect ratios of the NWs to explore a photonic approach to control their emission properties, by embedding them in an optical fibre-like structure, and studied the evolution of their dynamics with respect to the coupling to the NW guided mode.

Samples presentation

The NWs were grown by MBE as described in section 3.1.4 on Gallium-Arsenide (GaAs) substrates, after the growth of a ZnSe buffer layer and using dewetted Au droplets as catalysts. More details on the growth process can be found in Thibault Cremel's PhD thesis, or in ref. [Zan+15].

A very small quantity of Au was used to create the catalysts droplet, resulting in a very low density of NWs on the growth substrate, as can be seen in figure 3.22 (a) and (b). The average distance between neighbouring NWs is of the order of 1 µm, making them easily accessible for single NW optical characterisation on the growth sample. Three samples were investigated, their structure is sketched in figure 3.22 (c). Contrary to the Te-based NWs, the Se-based NWs are not tapered. The core is a WZ phase ZnSe NW, around 10 nm in diameter. The QD is a CdSe insertion of variable height h, controlled by the growth time. The NW is embedded in a ZnMgSe shell, typically 5 to 10 nm thick, which has a higher bandgap than ZnSe and thus isolates the surface of the active region of the NW from air, resulting in improved optical properties. The total NW length is of the order of 500 to 700 nm depending on the sample. The first sample is designated as M3226, in which the QDs are expected to be around 10 nm in height, and the NWs are 500 nm long. NWs were characterised directly from the as-grown sample, i.e. standing vertically on the substrate. We will present more results on this sample in the next section. NWs from samples M3258 and M3260 were mechanically dispersed on pre-patterned substrates to perform multiple characterisations on the same NWs. The NWs are 700 nm long. QDs from M3258 are expected to be 5 nm in height, while NWs from M3260 contain two QDs, which are expected to be respectively 5 and 10 nm in height. However, we could only clearly identify only one exciton line for these NWQDs. The expected sizes of the QDs are determined from the atom fluxes during the MBE growth process, and have not yet been confirmed by structural measurements.

A characteristic single NWQD µPL spectrum is shown in figure 3.23 (a) for a relatively high pumping power. Three lines are visible, corresponding to the exciton X, the charged exciton CX and the biexciton X_2. The identification of each line was performed by power-dependent measurement under cw excitation (not shown in this work). The precise nature (positively or negatively charged exciton) of the CX line is still unknown, but the strong difficulty in obtaining residual p-doping of ZnSe and CdSe materials hints towards a negatively charged exciton. We used the Fianium supercontinuum laser to excite the structures, using a pulsed pump beam

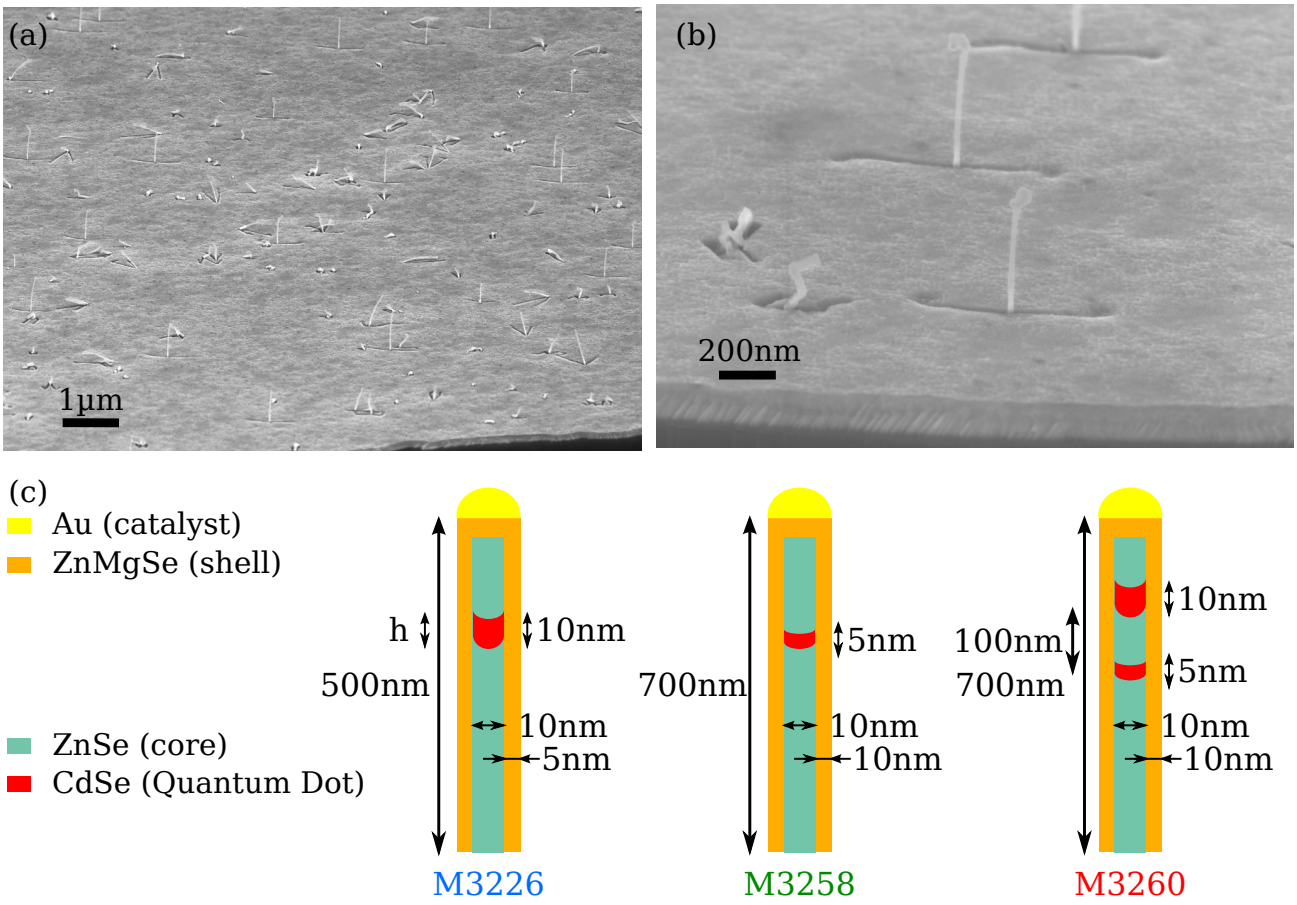

Figure 3.22 – Presentation of the Se-based NWQDs.
(a) Large field SEM image of a growth substrate, showing thin, vertical ZnSe NWs with a low density. (b) Zoom on one NW, and (c) sketch of the core-shell NWQD geometries. Typical height are 500 to 700 nm. The shadow features in (b) are caused by rotation problems of the sample holder while growing the NWs.

centred at a wavelength of 485 nm with a 10 nm spectral full width at half maximum, and a 10 ps pulse duration. This excitation wavelength is below the ZnSe bandgap ($\sim$ 440 nm) and was chosen because it allows us to induce so-called 0D-1D transitions above the QD gap energy but below the barrier gap energy. This ensures us that we do not excite the substrate layers when performing characterisation on the as-grown sample. Each emission line was characterised using TRPL, as exemplified in figure 3.23 (b), and the typical spectral integration bandwidth used is shaded in panel (a). For a low pumping power, the time transient reveals a monoexponential decay, fitted here in red with a time constant of 1.2 ns.

Similarly to what we presented in the previous section, it is interesting to consider the dispersion in energy and decay rate over all the QDs we studied, as it gives an information on the possible variations in QD size, or internal strain in the NWs. It is represented on the scatter plot in figure 3.23 (c) for the exciton line, where the horizontal size of the markers represents the full width at half maximum of the PL line, and their vertical size the uncertainty on the transient fit.

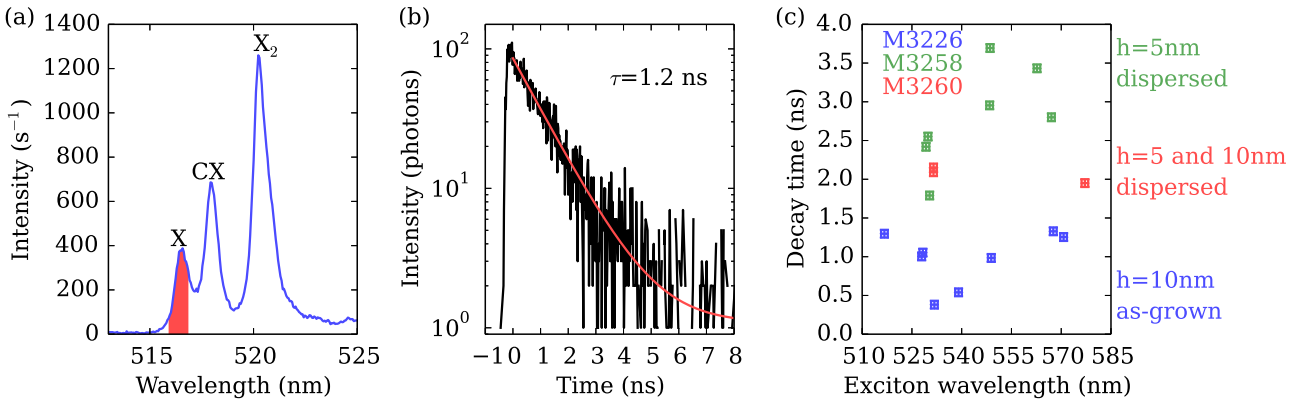

Figure 3.23 – TRPL Statistics of the Se-based NWQDs.
(a) Typical CdSe QD spectrum for a high pumping power, revealing the exciton (X), charged exciton (CX) and biexciton (X_2) lines. (b) Lifetime measurement of the exciton lifetime at low pumping power. The typically integrated spectral bandwidth is shaded in panel (a). A monoexponential fit gives a lifetime of $\tau = 1.2$ ns. (c) Summary plot of the central exciton emission wavelength versus exciton lifetime at liquid helium temperature for all the studied NWQDs, coming from three different samples. Error bars indicate the full width at half maximum of the exciton line (horizontal), and fitting errors on the lifetime (vertical).

We can see that the luminescence from the QDs is quite dispersed in central wavelength, with luminescence ranging from 512 to 580 nm. The exciton lifetimes are also distributed, with measured time constants ranging from 0.39 to 3.7 ns. No clear correlation is observed between central wavelength and decay time, which could have otherwise given us some insight on the confinement of the carriers inside the QDs and their dynamics [SGB99; Dri+05; MBM06; Bou+12b; Gon+15].

The large variation in emission wavelength could be attributed to size variations of the QDs. However, we note that we do not find any direct correlation between the *expected* QD size and resulting central emission wavelength, and especially between M3226 and M3258 which are supposed to contain QDs with a factor two in height between the two samples. We further note that we expect the diameters of the QDs to be equivalent between all samples, ruling out diameter variations as an explanation for this change in energy. Structural analysis on several NWs are still pending, and should clarify the possible height distribution from one QD to an other.

The variability in decay rate has several possible origins: a strong variation in non-radiative decay rates due to e.g. shell thickness variations, crystalline defects or crystal phase changes, or different coupling to dark states. A careful and statistical analysis of the temperature dependence of the exciton and bi-exciton recombination rate has been performed on the last two samples (M3258 and M3260) to determine the cause of such a variability, and is presented in the next section.

Temperature dependence of the temporal dynamics

Selected NWQDs from samples M3258 and M3260 were thus studied by TRPL as a function of temperature. The results are reported in figure 3.24 (a) and (b) respectively. The solid

line represents the exciton lifetime, and the dashed line represents the biexciton lifetime. One example QD is highlighted for each sample, while the shaded lines represent measurements on other QDs.

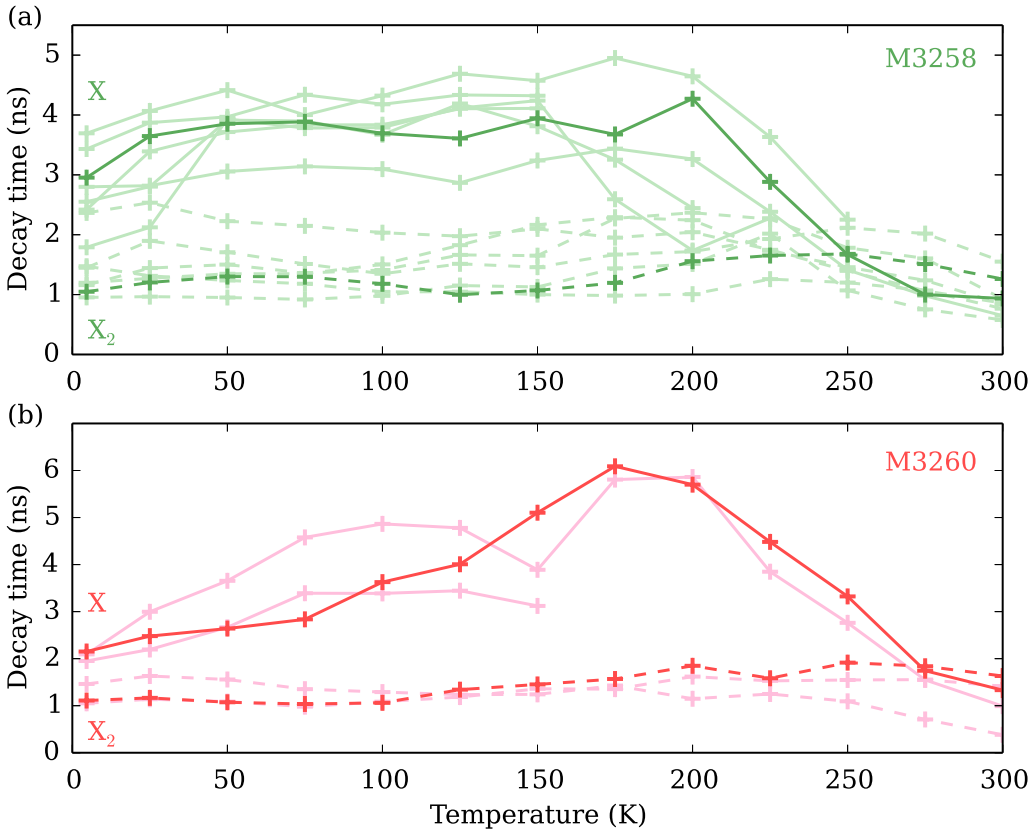

Figure 3.24 – Exciton and biexciton lifetimes as a function of temperature.
(a) Exciton and biexciton lifetimes for several NWQDs as a function of temperature, respectively in solid and dashed lines, for the M3258 sample. The highlighted curves for X and X_2 correspond to measurements on the same NWQD. (b) Same experiment for the M3260 sample. The M3258 presents very long exciton lifetimes, rapidly increasing with temperature and reaching a plateau around 4 ns for a temperature of 50 K. It then drastically decreases after 200 K. The same phenomenon is observed for the M3260 sample with a much slower increase as a function of temperature. In both cases the biexciton lifetime remains quite constant.

In both samples we found a biexciton lifetime close to half of the exciton lifetime at liquid helium temperature, which is expected for an almost radiatively limited exciton recombination [Bac+99] i.e. a strong carrier confinement [WNS06]. The ratio τ_X/τ_{X_2} is 2.1±0.4 for the M3258 sample, and 2.0±0.5 for the M3260 sample. In addition, we note that QDs from M3258 show a larger decay time than the ones from M3260, already indicating different QD characteristics.

Increasing the temperature yields strikingly different results. Starting with sample M3258, we see that the exciton decay transient rapidly increases with the temperature, reaching $\sim$ 4 ns at 50 K. It remains quite constant up to 200 K, after which it decreases rapidly towards 1 ns at room temperature. On the contrary, the biexciton lifetime remains quite constant throughout the temperature variation range, but is distributed from 1 to 2.5 ns within the measured QDs.

Things differ for the M3260 sample where the exciton and biexciton lifetimes are measured at liquid helium temperature close to 2 and 1 ns respectively. Increasing the temperature also leads to an increase in exciton lifetime, however much slower than in the M3258 sample. Here the saturation plateau appears at higher temperature, around 175 K, and the exciton lifetime reaches 5.5 ns. The biexciton lifetime remains stable around 1-1.5 ns.

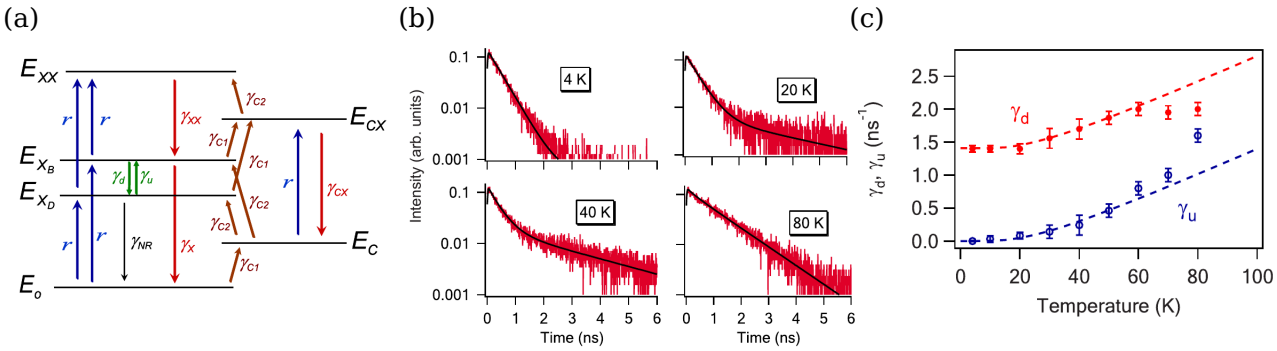

Figure 3.25 – Previously reported behaviour of CdSe NWQDs as a function of temperature.
(a) Energy diagram of the considered transitions: the excitonic state is split between the dark and the bright excitons, with the dark exciton having a lower energy than the bright exciton. The charged exciton and biexcitons were also included. (b) Decay transients at different temperature for the exciton transition. (c) Spin-flip rate between the bright and dark exciton as a function of temperature. Adapted from [Sal+09].

Extensive characterisation had already been done on CdSe insertions in ZnSe NWs in our group, using photon correlation techniques to investigate the internal dynamics of the light emission from the QDs [Sal+09; Bou+12b] and reporting a strong influence of the dark exciton state X_D, as shown in figure 3.25. This dark state is created by a spin flip from one of the carriers after the exciton creation. As the the carriers have a parallel spin they cannot recombine radiatively according to the Fermi golden rule. However, this dark exciton state has a lower energy than the bright exciton state, and should thus be populated *before* the bright state, resulting in the characteristic dynamics represented in 3.25 including bi-exponential time transients at intermediate temperatures (20 to 100 K). The fact that we observe mono-exponential time traces throughout the whole temperature range, with an increase, a plateau and a finally rapid decrease in measured lifetime as a function of temperature for all the QDs tends to favour the explanation of a thermally activated dark state formed by the ground electron level and the first excited hole level, as mentioned in [Har+09; Poe+10]. The proposed energy diagram is presented in figure 3.26. The pumping rates r, r_c and r'_c are power dependent, and three excitonic transitions can be optically probed, with a decay rate γ_X, γ_{CX} and γ_{X_2} respectively. The flipping rate between the bright and dark state γ_u and γ_d are governed by the temperature. A verification of this model is pending Thibault Cremel's PhD thesis, and will be discussed in greater details in his work. The difference we observe in the behaviour of the M3258 and the M3260 samples can be explained by a different energy splitting between the bright and dark states in the two samples. We note that in ref [Poe+10], the excitation of this dark state is the result of the recombination of a biexciton triplet state, which we did not observe in the µPL

spectrum.

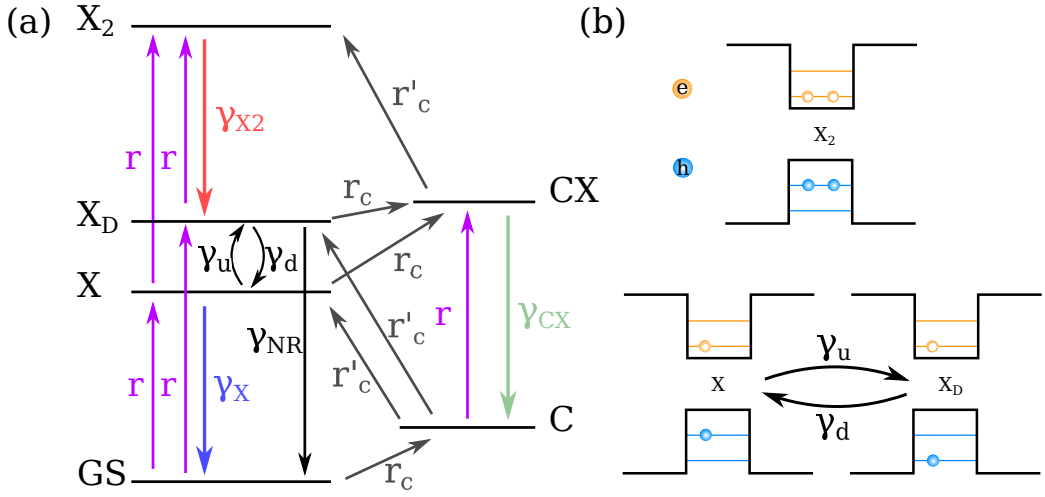

Figure 3.26 – Proposed energy diagram for the current CdSe NWQDs.
(a) Energy diagram of the considered transitions: the excitonic state is split between the dark and the bright excitons, with the dark exciton having a higher energy than the bright exciton. Note that here the dark exciton is composed of an electron in the first energy level of the QD, and a hole in the second energy level, as reported in [Har+09; Poe+10]. (b) Schematic of the relevant excitonic complexes X_2, X_D and X.

Finally, we performed g^2 measurements as a function of temperature to confirm the single photon emitter behaviour from the NWQDs. The results are presented in figure 3.27 for 10, 100 and 200 K. We used a continuous wave excitation at 488 nm because it provided a stronger photoluminescence signal than the pulsed excitation. We obtained around 10^4 photons/s, and integrated over typically 4 hours. Several measurements are averaged for each plot, with a binning of 2 time steps to decrease the noise amplitude. We performed the measurement on the brightest emission line at each temperature, i.e. the biexciton line at 10 K and the exciton line at higher temperature.

The degradation of the emission can be seen when increasing the temperature, but the dip at zero delay is still visible up to 200 K, confirming the QD-like behaviour of the emitter and the robustness of the single photon emission against temperature. A simple fit allows to retrieve the radiative lifetime of the transition. The comparison with the measured lifetime is presented in the table below.

Temperature, Complex	Radiative lifetime	Lifetime
10 K, X_2	0.35 ns	1.2 ns
100 K, X	0.5 ns	3.1 ns
200 K, X	0.36 ns	3.26 ns

These results indicate an increase of the role of non-radiative states when the temperature increases, which degrades the luminescence properties of the QDs and hence the autocorrelation measurements.

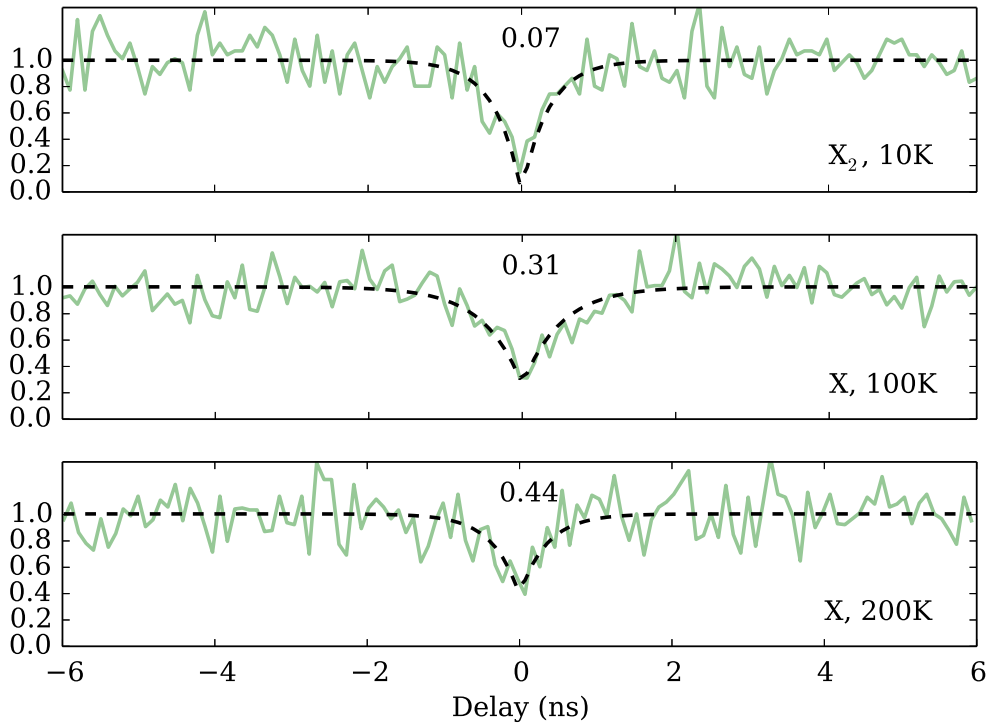

Figure 3.27 – $g^{(2)}$ measurement as a function of temperature
$g^{(2)}$ measurement as a function of temperature for quantum dots from the M3258 sample. A clear antibunching is observed at 10 K which is deteriorated when increasing the temperature up to 200 K. The numbers represent the minimum value of the fitting function.

Indirect determination of the dipole orientation: a photonic approach

After characterisation of the exciton and biexciton dynamics in these Se-based NWs, we made use of the fact that they are fabricated with a low density on the growth sample to study them in their as-grown configuration. The aim of this experiment was to determine the intrinsic orientation of the emitting dipole inside the NWQD, and try to use a photonic approach to modify its coupling to free space radiation following the work presented in ref. [Cre+14].

Several NWQDs from the M3226 sample were studied directly on their growth substrate. We used atomic layer deposition to add an Al_2O3 shell to the NW. Alumina deposited using ALD results in a very conformal shell with a precisely controllable size, owing to the slow deposition rate of the ALD process, as can be seen in figure 3.28 (a) and (b). We systematically investigated the effect of this oxide shell thickness, starting from uncapped NWs and growing a shell of different radii, up to 120 nm. Because of the lack of singular features on the sample, it was not possible to locate each studied NW, we thus only present statistical results and can not follow the effect of the oxide shell growth on a defined NW. For each NW we identified the X, CX and X_2 line and performed TRPL at low pumping power to avoid repopulation of the X level by the biexciton. The time traces were fitted by a monoexponential decay, and the fitting time constants are reported in figure 3.28 (c).

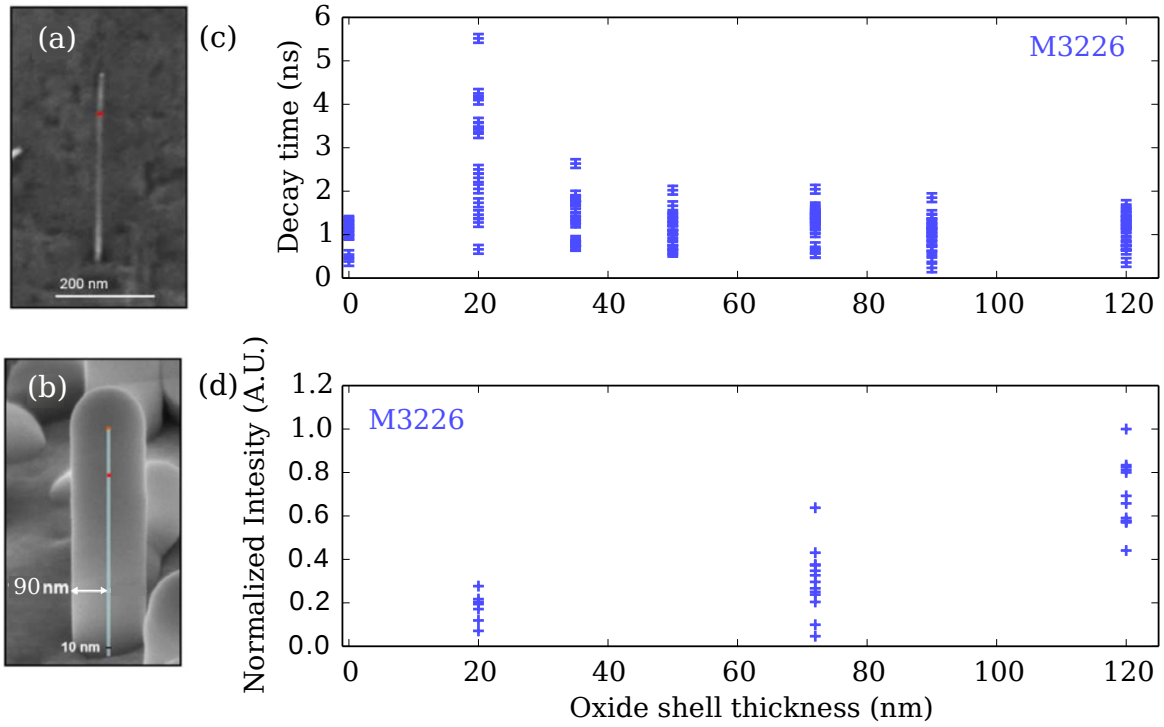

Figure 3.28 – Exciton decay time as a function of the oxide shell thickness.
(a) and (b) SEM images of a bare ZnSe NW, with the QD indicated in red, and of the NW embedded in a 170 nm thick oxide shell. (c) Statistical measurements of the exciton lifetime on several NWQDs as a function of the oxide shell thickness. (d) Statistical measurements of the exciton emission intensity integrated over the entire PL exciton line at saturation pumping power. The measured lifetimes reveal a highly varying lifetime from dot to dot. It also evidences a strong trend of increase in lifetime for small oxide shell thicknesses, and then reduction of the lifetime as the oxide shell is larger. The total fluorescence from the exciton follows the opposite trend, revealing an increase in light emission from structures with thick oxide shells.

The decay times with no additional oxide shell are the same as the one presented in figure 3.22 (c) (blue symbols), and are ranging from 0.39 to 1.4 ns. Looking at the envelope of the entire resulting scattered plot, we observe a strong increase in the maximum decay constant for a 20 nm shell thickness. The exciton lifetime then decreases and seems to slightly oscillate up to our maximum shell thickness of 120 nm. However, for a given shell thickness, we measured a distribution of lifetimes ranging from a few hundreds of picoseconds to around 2 ns.

The strong variation of the envelope indicates that, at least for some NWs, the emission is strongly coupled to the presence of the shell. This can be understood if one considers the possible dipole orientations upon exciton recombination inside the QD. The emission can be thought of as the one of a linearly polarised dipole, either along or orthogonal to the NW axis. The dipole oriented along the NW axis is weakly influenced by the presence of the shell, and does not suffer from a strong dielectric screening. Conversely, the one oriented orthogonal to the NW axis is both screened by the difference in electric permittivity between the NW and the surrounding material, and can couple efficiently to guided modes along the NW axis.

This interpretation is confirmed by a measurement of the maximum emitted photolumi-

nescence from the NWQDs exciton, presented in figure 3.28 (d) (normalised). We show the integrated µPL intensity of the exciton line at saturation pumping power as a function of the shell thickness for several NWQDs. This measurement has been done separately from the time-resolved study, so there is no one-to-one correlation with the measured decay times. However, we can see that the envelope varies in opposition with the lifetime envelope, indicating that the maximum emitted intensity increases as the exciton lifetime decreases. This can be attributed to several factors: a reduction in dielectric screening of the radial dipole because of the presence of the oxide shell, a dielectric antenna effect redirecting the emitted light towards the collection objective, and an increased coupling between the emitter and a guided mode supported by the coated NW structure.

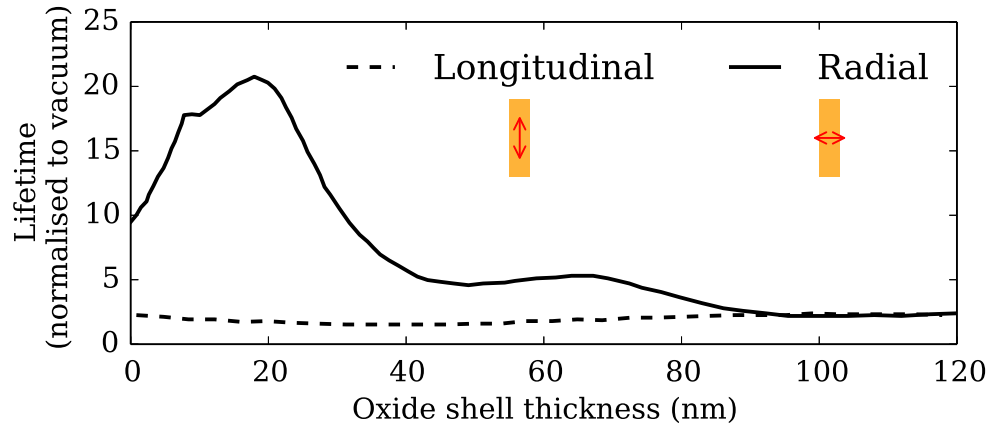

Figure 3.29 – Simulated lifetimes for the capped NWQDs.
Simulated lifetimes of longitudinal (dashed lines) and radial (solid lines) dipoles as a function of oxide shell thickness (normalised to vacuum) integrated over the experimental numerical aperture.

Numerical simulations of the corresponding structures were carried out by Niels Gregersen for Thibault Cremel's PhD thesis, simulating the QD as a dipole emitter either in the longitudinal or radial direction. The coupling to guided modes supported by the structure was calculated to extract the radiative lifetime of the emitter. While the final results are not available yet, preliminary results are shown in figure 3.29. A qualitative comparison with the envelope of figure 3.28 (c) reveals that at least some emitters are of radial type. As the simulation do not include any non-radiative processes, the distribution observed in the experimental results can have two origins: the QD can emit with a linear combination of the longitudinal and radial dipole, with different contribution of each dipole from dot to dot, or non-radiative processes can play a role, as pointed out in the previous section, explaining the deviation from the case of a perfectly radiative QD. A final conclusion still has to be found for the case of these Se-based NWQDs, and will be presented in Thibault Cremel's PhD thesis.

3.4 Conclusion on the statistical measurements of the luminescence properties of NWQDs

In this chapter we have presented the optical properties of II-VI semiconducting nanowires quantum dots. After a brief reminder on semiconductor optics, we have detailed the experimental setups used in this thesis, and their operation. We have applied µPL, TRPL and Fourier imaging to Te-based and Se-based NWQDs. By extracting the optical properties of a large number of single emitters, we aimed at providing a description of their behaviour using optical methods. In the case of Te-based NWQDs, we have combined TRPL, polarisation measurements and Fourier imaging. We have evidenced a large dispersion in exciton lifetimes and emission wavelengths, as well as different polarisation behaviours and radiation patterns. While our model based on the description of the QDs by a linear dipole could explain part of the results, such as the case of positive S_1 parameters or radiation patterns, it failed to reproduce the polarisation results.

In the case of Se-based NWQDs, we have used temperature-dependent TRPL and used an external shell deposition to study the dots. We have shown that explaining the QD emission dynamics requires the knowledge of the QD electronic levels, as the temperature dependence of the exciton lifetime does not corresponds to the expected properties of a simple, well confined exciton isolated inside the QD. By studying the effect of the shell deposition, we have shown that the dispersion in the results requires a more precise QD modelling that a simple linear dipole model, which only describes the envelope of our measurements.

It thus appear of crucial importance to perform more combined measurements on a single structure, and to refine our description of the QD. Indeed, simply modelling the exciton emission as a linear dipole and ascribing all the optical properties of the NWQDs to the dielectric antenna effects provided by the NW is not sufficient. In the next chapter, we detail a complete study of a single NWQD that allows us to fully determine the QD electronic states and model the NWQD radiation properties accordingly.

Chapter 4

A Light Hole Exciton in a Nanowire Quantum Dot

Résumé en Français

Le chapitre précédent nous a permi de démontrer qu'il n'est pas suffisant de considérer que les propriétés d'émission des boîtes quantiques insérées dans des nanofils sont uniquement dûes à des effets photoniques. En effet, des calculs basés simplement sur les propriétés optiques de ces structures sont incapables de reproduire correctement les mesures de polarisation effectuées sur différents nanofils. Il faut donc invalider l'hypothèse que les boîtes peuvent être simplement décrites par des dipoles linéaires, et obtenir une description des propriétés électroniques de ces boîtes pour tenir compte des propriétés excitoniques intrinsèques aux émetteurs.

On propose ici une caractérisation multi-instrumentale basée sur la cathodoluminescence, l'imagerie de Fourier résolue en polarisation et la spectroscopie magnéto-optique pour déterminer les propriétés électroniques et optiques d'une boîte de CdMnTe dans un fil cœur/coquille de ZnTe/ZnMgTe. Un modèle analytique de la contrainte mécanique subie par le cœur de ZnTe et par la boîte est proposé dans des cas limites, et partiellement validé par l'expérience. Un modèle paramétrique est alors proposé pour décrire l'effet de la contrainte et du confinement sur la bande de valence. Couplé à des simulations numériques du diagramme de rayonnement du cœur et de la boîte (méthode des éléments finis), il mène à un excellent accord avec nos expériences (figure 4.9). On trouve alors que l'état fondamental de trou est de type lourd dans le cœur, et léger dans la boîte, mais également les paramètres de mélange entre les états de trous dans ces deux systèmes. Une étape de spectroscopie magnéto-optique utilisant l'effet Zeeman géant dû à l'interaction d'échange entre le trou et les atomes de Mn confinés dans la boîte confirme l'exceptionnel caractère léger du trou dans la boîte, et permet une détermination de la séparation entre les états de trou dans la boîte $\Delta_{LH} = -22$ meV.

A la lumière de ces résultats, on peut conclure sur la dispersion des premières mesures sur les boîtes de CdMnTe. Il est proposé que le faible décalage de bande de valence entre CdTe et ZnTe mène à une configuration critique de l'alignement des bandes dans la structure (figure 4.11), expliquant les grandes variations observées.

Introduction

As we demonstrated in section 3.3, simply ascribing the µPL properties of NWQDs to a photonic antenna effect induced by the NW geometry and its interaction with the substrate is a dead-end, as it does not accurately describe the measured polarisation properties nor encompasses the dispersion in the results. The main assumption to relax is thus that the QD can be modelled as a linear dipole with an arbitrary orientation to be determined by the polarisation measurements. Instead, we have to account for the excitonic properties of the NW, i.e. find the available transitions inside the QD and their corresponding probabilities, as sketched in sections 3.1.1 and 3.1.2, in order to see if some can be intrinsically favoured. We thus performed a much more refined analysis on a Te-based NWQD. They present two main advantages with respect to the Se-based NWs: they grow in a ZB crystal phase with cubic symmetry which simplifies the calculations, and the QDs are doped with magnetic atoms allowing their study by magneto-optical spectroscopy, offering an independent characterisation to compare with our results.

Here we apply a multi-instrumental approach to a single Te-based NWQD to provide a complete model of both the NW core and dot properties. We show in an original combination of Fourier imaging and magneto-optical spectroscopy that we can fully characterise the electron and hole quantum states inside the core and the dot. We first recall the effect of strain on the optical properties of semiconductors, and present two analytical limiting models. Then we develop a full valence band mixing calculation to describe the effects of strain and confinement on the optical properties of both the core and the dot. We compare the experimental results to numerical simulations based on this model, and retrieve the electronic states of the electrons and the holes inside the NW core and quantum dot.

In light of these results, we turn back to propose a final conclusion on the electronic and optical properties of the Te-based NWQDs studied in this work.

4.1 NW presentation and model

To simplify the interpretation of the results and lower the number of available degrees of freedom in the model, we chose to lead this experiment on a standing NW. This dramatically reduces its interaction with the substrate, allowing us to access more easily to its intrinsic radiation properties. The usual CL-based selection process was carried out on a piece of the growth sample in a region of low NW density to select a NW with a well isolated emission line at the expected QD exciton wavelength. The area is close to a sample edge, allowing side-imaging of the NW in the CL setup. As shown in figure 4.1 (a) the NW is isolated from its neighbours by around 2 µm.

Its CL spectrum is presented in panel 4.1 (b), with the corresponding SEM [fig. 4.1 (c)] and monochromatic CL+SEM [fig. 4.1 (d)] images. We separated 2 different contributions. The blue shaded area in the spectrum clearly corresponds to the QD emission, and is well localised along the NW axis. The blue contribution come from the ZnTe core emission. Intensity profiles along the NW axis are reported in figure 4.1 (e) for each contribution. We will thus study the emission properties of both the ZnTe core and the CdMnTe QD from the same NW, evidencing the effect of the shell on the core, and of the shell and core on the dot.

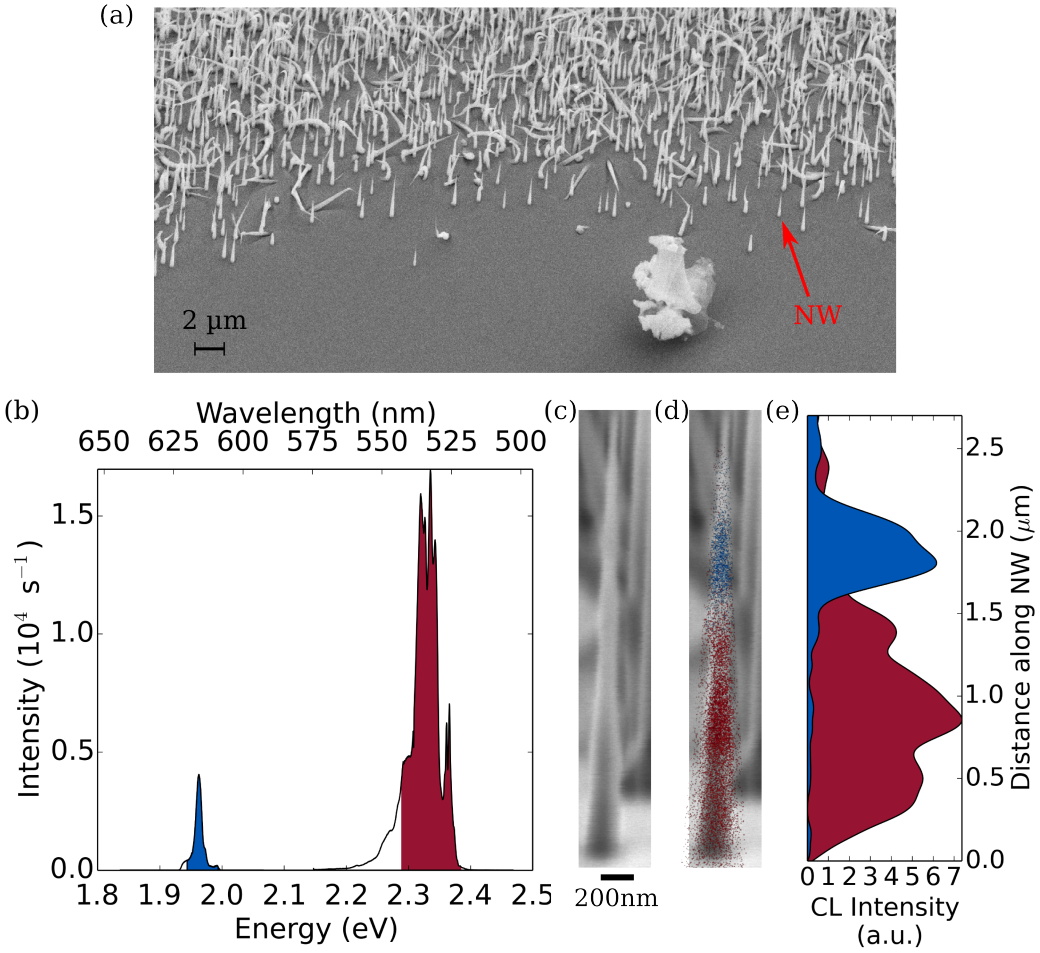

Figure 4.1 – Presentation of the NW.
(a) Large field tilted SEM image of the NW. It is located on a side of the sample in a region of low NW density, and the presence of the dust conveniently allows for its localisation. (b) CL spectrum of the NW. The peak at 2.35 eV comes from the ZnTe core luminescence, and the one at 1.96 eV from the QD luminescence. (c) SEM image of the NW, revealing its morphology. (d) Coloured CL images superimposed on the SEM image [colours corresponding to the shaded areas in (b)] revealing the spatial localisation of the luminescence. (e) Cut profile of the CL images along the NW axis for a better localisation of the luminescence. The ZnTe profile will be further used in the simulation of the emission from the core.

As reminded in section 3.1.1, the intrinsic properties of the light emitted by a semiconductor are governed by the Fermi golden rule, and we know that the relevant electronic states are the conduction band Γ_6 and the light and heavy hole valence bands of Γ_8 symmetry (fig. 3.2 and 3.3). We can thus define the conduction and valence wave functions as:

$$\Psi^c_{\pm 1/2} = \epsilon_e(\mathbf{r})\, u^c_{\pm 1/2}(\mathbf{r}) \tag{4.1a}$$
$$\Psi^v_{\pm 1/2} = \epsilon_{LH}(\mathbf{r})\, u^v_{\pm 1/2}(\mathbf{r}) \tag{4.1b}$$
$$\Psi^v_{\pm 3/2} = \epsilon_{HH}(\mathbf{r})\, u^v_{\pm 3/2}(\mathbf{r}) \tag{4.1c}$$

where ϵ_e, ϵ_{LH} and ϵ_{HH} are the electron, light hole and heavy hole envelope functions, and the

$u^{j=\{c,v\}}_{i=\{\pm1/2,\pm3/2\}}$ are the Bloch functions of the Γ_6 and Γ_8 bands [Fis10, p.53-54]:

$$u^c_{1/2} = |S,\uparrow\rangle \tag{4.2a}$$
$$u^c_{-1/2} = |S,\downarrow\rangle \tag{4.2b}$$
$$u^v_{+3/2} = \frac{-i}{\sqrt{2}}|p_x + ip_y,\Uparrow\rangle \tag{4.2c}$$
$$u^v_{+1/2} = \frac{-i}{\sqrt{6}}|p_x + ip_y,\Downarrow\rangle + i\sqrt{\frac{2}{3}}|p_z,\Uparrow\rangle \tag{4.2d}$$
$$u^v_{-1/2} = \frac{i}{\sqrt{6}}|p_x - ip_y,\Uparrow\rangle + i\sqrt{\frac{2}{3}}|p_z,\Downarrow\rangle \tag{4.2e}$$
$$u^v_{-3/2} = \frac{i}{\sqrt{2}}|p_x - ip_y,\Downarrow\rangle \tag{4.2f}$$

where S, p_x, p_y and p_z are the s and cubic orbitals functions, and $|\uparrow\downarrow\rangle$, $|\Uparrow\Downarrow\rangle$ are the electron and hole spin components respectively, projected along the quantisation axis. Due to the symmetry of the problem, this quantisation axis is both the optical axis and the NW growth axis.

For simplicity, we now replace the functions $\left|u^j_i\right\rangle$ by the spin projection $|i\rangle_j$ where $j = h, e$ stand for holes or electrons. The optically active transitions are given by the non-zero matrix elements of the form ${}_h\langle\pm3/2|H_{opt}|\pm1/2\rangle_e$ and ${}_h\langle\pm1/2|H_{opt}|\pm1/2\rangle_e$ where H_{opt} has been defined in equation (3.13) as $H_{opt} = -\mathbf{d}\cdot\mathbf{E}$. If we assume first for simplicity a same overlap between the electron-light hole and electron-heavy hole wavefunctions so that $\langle\epsilon_{HH}|\epsilon_e\rangle / \langle\epsilon_{LH}|\epsilon_e\rangle = 1$, we find:

$${}_h\langle-3/2|H_{opt}|+1/2\rangle_e = \frac{-1}{\sqrt{2}}(\mathbf{p_x} - i\mathbf{p_y}) = -\sigma^- \tag{4.3a}$$
$${}_h\langle-1/2|H_{opt}|+1/2\rangle_e = \sqrt{\frac{2}{3}}\mathbf{p_z} = \sqrt{\frac{2}{3}}\,\pi \tag{4.3b}$$
$${}_h\langle+1/2|H_{opt}|+1/2\rangle_e = \frac{1}{\sqrt{6}}(\mathbf{p_x} + i\mathbf{p_y}) = \frac{1}{\sqrt{3}}\,\sigma^+ \tag{4.3c}$$
$${}_h\langle+3/2|H_{opt}|-1/2\rangle_e = \frac{1}{\sqrt{2}}(\mathbf{p_x} + i\mathbf{p_y}) = \sigma^+ \tag{4.3d}$$
$${}_h\langle+1/2|H_{opt}|-1/2\rangle_e = \sqrt{\frac{2}{3}}\mathbf{p_z} = \sqrt{\frac{2}{3}}\,\pi \tag{4.3e}$$
$${}_h\langle-1/2|H_{opt}|-1/2\rangle_e = \frac{-1}{\sqrt{6}}(\mathbf{p_x} - i\mathbf{p_y}) = \frac{-1}{\sqrt{3}}\,\sigma^- \tag{4.3f}$$

where $\sigma^\pm$ designates the emission of a circularly polarised photon, and π the emission of a photon linearly polarised along the z axis.

These optical transitions are summarised in figure 4.2 (a) for a degenerate Γ_8 band, where the states are designated by their spin projection along the z axis. The key element is to realise that the nature of the hole state is encoded in the emitted photon properties. While the spin degeneracy in the case of bulk materials cannot be lifted without an additional external excitation, like a magnetic field [Fur88], the difference between light hole and heavy hole excitons resides in the π contribution from the light hole exciton emission.

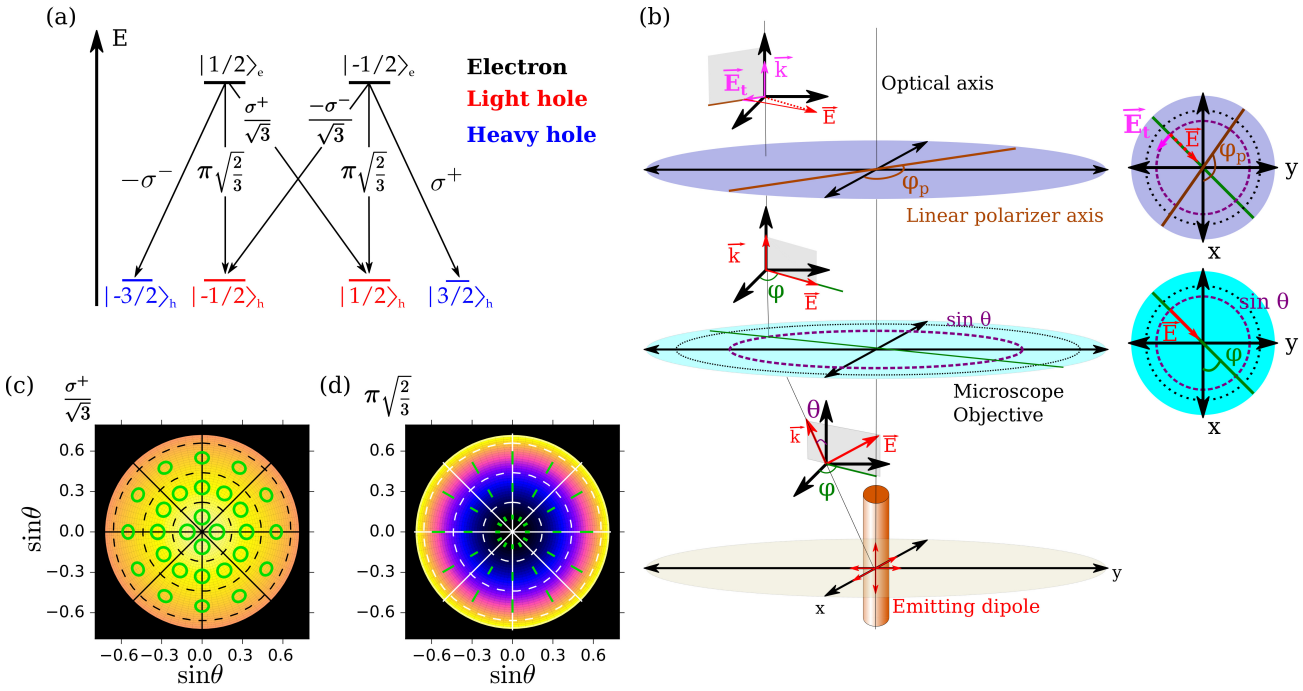

Figure 4.2 – Principle of the polarisation-resolved Fourier microscopy method. (a) Dipole-allowed transitions in a semiconductor representing the conduction band and the valence band in a fully degenerate case. (b) Definition of the coordinate system and demonstration of the projection of the electric field vector in the Fourier plane with respect to the polariser direction. A photon emitted in a direction (θ,φ) is projected in the (x,y) Fourier plane with the polar coordinates $(\rho = \sin\theta,\, \varphi)$ after the microscope objective. The linear polariser projects the electric field $\mathbf{E}$ on its orientation φ_p, resulting in the transmitted electric field $\mathbf{E_t}$. (c) and (d) Unpolarised intensity maps corresponding to the σ and π components of the light hole exciton recombinations in an homogeneous medium. We can see that the $\sigma^{\pm}$ emission is maximum at the center ($k = 0$) of the diagram, while the π emission is zero at the center and favours light emission at large θ angles. The polarisation state of the electric field is represented in green ellipses and lines (see text).

In order to clearly evidence the difference between π and $\sigma^{\pm}$ emission, we represent in figure 4.2 (c) and (d) the simulated radiation patterns expected for pure σ and π emitters respectively, in a homogeneous medium. It corresponds e.g. to a Fourier imaging experiment as sketched in figure 4.2 (b) where the NW is replaced by vacuum. In the radiation diagrams, we further indicate the polarisation state of the emitted photons as a function of their emission direction in green lines and ellipses, which represent the trajectory of the electric field vector in the $x-y$ plane during one optical period: a straight line designates a linearly polarised photon along the line direction, while a circle represents a circularly polarised photon. It is clear that both radiation patterns strikingly differ from one another. However, direct comparison of the intensity patterns with measurements is limited by several factors. First, while heavy hole excitons only radiate with $\sigma^{\pm}$ transitions, light hole excitons emit a combination of π and $\sigma^{\pm}$ transitions, making a direct identification difficult. Furthermore, the photonic effect and dielectric screening of the NW applies differently to each kind of transition ($\sigma^{\pm}$ or π) an can thus change the radiation pattern and relative weight of each excitonic emission. Finally, imperfections in the collection optics affects the measured total radiations diagrams. However, combining the

spatially resolved polarisation analysis with the intensity measurement appears to be a much more sensitive criterion to discriminate between light and heavy hole excitons, as it consists in differentiating circularly polarised light from linearly radially polarised light.

Our approach is thus to perform Fourier plane imaging of the NW core and QD luminescence to extract the unpolarised and polarisation-resolved radiation patterns, and the degree of linear polarisation (or Stokes parameters) for a large collection of angles. Each kind of *dipole transition* ($\sigma^{\pm}$ or π) is then simulated using a a finite-element method software (Comsol multiphysics v.4.1 [Com]), taking into account a realistic geometry, i.e. the whole NW structure determined from the SEM and CL images 4.1 (c)-(e), the presence of the substrate and imperfections in the collection from the objective. The field radiated by the structure is modelled as an electric dipole, and the full electric field vector is propagated to the far-field through a readily implemented algorithm, from which we obtain the 3 complex field components in the upper half-space. We have checked that this field is transverse, with only two components in spherical coordinates (E_θ, E_φ). The latter are transformed by the objective lens into an electric field in the (x, y) plane as:

$$E_x = E_\theta \cos\varphi - E_\varphi \sin\varphi \tag{4.4a}$$

$$E_y = E_\theta \sin\varphi + E_\varphi \cos\varphi \tag{4.4b}$$

as depicted in figure 4.2. The resulting complex functions $E_{x,y}(\mathbf{u}, \theta, \varphi)$, where $\mathbf{u} = \mathbf{x}, \mathbf{y}, \mathbf{z}$ is the direction of the oscillating dipole, are calculated and developed in a numerical post-treatment step into spherical harmonics Y_{lm} with l ranging from 0 to 4. The far field patterns resulting from any electronic transition matrix element established in equations (4.3) can thus be reconstructed by the linear combination $\mathbf{d} = d_x\mathbf{x} + d_y\mathbf{y} + d_z\mathbf{z}$.

We want to stress here that this simulation step thus encompasses *all the photonic properties of the emitter and its surrounding.* We can thus compute the radiation patterns produced by pure heavy hole or pure light hole exciton recombinations, as the dipole elements $d_{i=x,y,z}$ are given by the selection rules, and compare them to the experimental results. The lacking ingredient in this procedure is thus a description of the valence bands of the NW core and QD, which is the object of the following section. Ultimately, this description should lead to the determination of three new dipole elements d_x, d_y, d_z governing the QD emission, which may differ from the ones given by the selection rules in the bulk material.

4.2 The effect of strain in a semiconductor

It must be noted that the hole states in figure 4.2 (a) were sketched in a fully degenerate case, which does not represent the reality of our NWs. Because of Mn incorporation in the QD, lateral growth of the core and the presence of the shell, all the sections constituting our NW can be subject to strain, leading to a modification of the energy levels. We thus need to find a correct description of the effect of strain on the band structure of our structure before entering into a detailed analysis of its emission properties.

As thoroughly detailed in [Fis10], this is commonly described in the frame of Luttinger-Kohn and Bir-Pikus theory. The original article describing the Hamiltonian around the Γ_8 level using

group theory is the work of Luttinger and Kohn [LK55], and has been then systematically used in the work of Bir and Pikus to describe the effect of strain [BP62].

The Hamiltonian derived in [LK55] describing the Γ_8 band reads [Fis10, sec.4.1.2]:

$$\begin{aligned} H_{LK} = &\left(\gamma_1 + \frac{5}{2}\gamma_2\right)\tilde{q}^2\mathbf{I}_4 - 2\gamma_2\left(\tilde{q}_x^2 J_x^2 + \tilde{q}_y^2 J_y^2 + \tilde{q}_z^2 J_z^2\right) \\ &- 4\gamma_3\left(\{\tilde{q}_x\tilde{q}_y\}\{J_x J_y\} + \{\tilde{q}_y\tilde{q}_z\}\{J_y J_z\} + \{\tilde{q}_z\tilde{q}_x\}\{J_z J_x\}\right) \\ &+ \frac{\bar{e}\hbar}{m_0}\left[\kappa_{LK}\mathbf{J}\cdot\mathbf{B} + q_{LK}\left(J_x^3 B_x + J_y^3 B_y + J_z^3 B_z\right)\right]. \end{aligned} \tag{4.5}$$

$\gamma_{1,2,3}$ are the Luttinger parameters, κ_{LK} and q_{LK} are related to respectively isotropic and anisotropic terms in the Zeeman effect, $\tilde{q}^2 = q^2\hbar^2/(2m_0)$, and $\mathbf{I}_4$ is the 4×4 identity matrix. $J_{x,y,z}$ are the components of the orbital momentum $\mathbf{J}$ so as $J = 3/2$, with the usual commutation relations $[J_x J_y] = iJ_z$ etc., and so $\mathbf{J}^2 = (15/4)\mathbf{I}_4$. $\{ab\} = (ab+ba)/2$. In absence of magnetic field q_x and q_y commute, so that $\{q_x q_y\} = q_x q_y$ and:

$$H_{LK} = \frac{\hbar^2}{m_0}\left[\frac{1}{2}\gamma_1 q^2\mathbf{I}_4 - \gamma_2\sum_w q_w^2\left(J_w^2 - \frac{1}{3}\mathbf{J}^2\right) - \gamma_3\left(q_x q_y\left(J_x J_y + J_y J_x\right) + c.p.\right)\right] \tag{4.6}$$

where *c.p.* stand for circular permutation. This Hamiltonian is the starting point to describe energy variations caused by a deformation of the semiconductor, considering the following:

- $\mathbf{u} = u_x\mathbf{x} + u_y\mathbf{y} + u_z\mathbf{z}$ is the displacement field

- $\tilde{\varepsilon} = [\tilde{\varepsilon}_{ij}]$ is the strain tensor where $\tilde{\varepsilon}_{ij} = \frac{1}{2}\left(\frac{\partial u_i}{\partial x_j} + \frac{\partial u_j}{\partial x_i}\right)$, $x_i = x, y, z$

- $\tilde{\sigma}$ is the stress tensor, related to the strain tensor by the stiffness tensor $\tilde{c}$ through Hooke's law $\tilde{\sigma}_{ij} = \sum_{kl}\tilde{c}_{ijkl}\tilde{\varepsilon}_{kl}$

- In the case of cubic semiconductors, e.g. for our ZB Te-based NWs, the stiffness tensor can be written in the Voigt notation as [FC14]:

$$\tilde{c} = \begin{pmatrix} c_{11} & c_{12} & c_{12} & 0 & 0 & 0 \\ c_{12} & c_{11} & c_{12} & 0 & 0 & 0 \\ c_{12} & c_{12} & c_{11} & 0 & 0 & 0 \\ 0 & 0 & 0 & c_{44} & 0 & 0 \\ 0 & 0 & 0 & 0 & c_{44} & 0 \\ 0 & 0 & 0 & 0 & 0 & c_{44} \end{pmatrix} \tag{4.7}$$

The local deformation of the semiconductor heterostructure is due to the lattice mismatch between the different compounds. The equilibrium condition is presence of a force per unit volume $\mathbf{F}$ is known as the Lamé-Clapeyron-Navier equation, and reads for each coordinate i:

$$\sum_{jkl} c_{ijkl}\frac{\partial}{\partial x_j}\left(\frac{\partial u_k}{\partial x_l} + \frac{\partial u_l}{\partial x_k}\right) + F_i = 0. \tag{4.8}$$

Solving this equations allows to relate the lattice mismatch to the strain and stress experienced by the material as a function of its stiffness coefficients. As detailed in [Fis10, sec.4.6.4], the components of the strain tensor $\tilde{\varepsilon}_{ij}$ have the same xy symmetry than the $q_x q_y$ terms, so the strain Hamiltonian can be identified to the quadratic terms in (4.6). In their article, Bir and Pikus introduced the parameters $a_v, b_v, d_v/\sqrt{3}$ so that:

$$\tilde{H}_{BP} = a_v \tilde{\varepsilon}_{\text{hyd}} \mathbf{I}_4 + b_v \sum_i \tilde{\varepsilon}_{ii} \left(J_i^2 - \frac{1}{3} J^2 \right) + \frac{d_v}{\sqrt{3}} \left[\tilde{\varepsilon}_{xy} \left(J_x J_y + J_y J_x \right) + c.p. \right] \tag{4.9}$$

where $\tilde{\varepsilon}_{\text{hyd}} = \tilde{\varepsilon}_{xx} + \tilde{\varepsilon}_{yy} + \tilde{\varepsilon}_{zz}$ is the hydrostatic strain. $\tilde{\varepsilon}_{\text{hyd}}$ is an isotropic strain, and we define the shear strain as $\tilde{\varepsilon}_{\text{shear}} = 2\tilde{\varepsilon}_{zz} - \tilde{\varepsilon}_{yy} - \tilde{\varepsilon}_{xx}$. This leads to the final form of the Bir-Pikus Hamiltonian. Using the notation of [FC14] for cubic semiconductors along the [111] axis, i.e. as in the case of our ZnTe NWs, it is commonly written in matrix form in the $(|3/2\rangle_h ; |1/2\rangle_h ; |-1/2\rangle_h ; |-3/2\rangle_h)$ basis as: in matrix form as:

$$H_{BP} = \begin{pmatrix} P+Q & -S & R & 0 \\ -S^* & P-Q & 0 & R \\ R^* & 0 & P-Q & S \\ 0 & R^* & S^* & P+Q \end{pmatrix} \tag{4.10}$$

where:

$$P = a_v \sum_w \tilde{\varepsilon}_{ww} = a_v \tilde{\varepsilon}_{\text{hyd}} \tag{4.11a}$$

$$Q = \frac{d_v}{2\sqrt{3}} (\tilde{\varepsilon}_{xx} + \tilde{\varepsilon}_{yy} - 2\tilde{\varepsilon}_{zz}) = -\frac{d_v}{2\sqrt{3}} \tilde{\varepsilon}_{\text{shear}} \tag{4.11b}$$

$$R = -\frac{\sqrt{3}}{6} (b_v + \frac{2d_v}{\sqrt{3}}) (\tilde{\varepsilon}_{xx} - \tilde{\varepsilon}_{yy} - 2i\tilde{\varepsilon}_{xy}) + \frac{2}{\sqrt{6}} (b_v - \frac{d}{\sqrt{3}}) (\tilde{\varepsilon}_{xz} + i\tilde{\varepsilon}_{yz}) \tag{4.11c}$$

$$S = \frac{\sqrt{3}}{3} (2b_v + \frac{d_v}{\sqrt{3}}) (\tilde{\varepsilon}_{xz} - i\tilde{\varepsilon}_{yz}) - \frac{1}{\sqrt{6}} (b_v - \frac{d}{\sqrt{3}}) (\tilde{\varepsilon}_{xx} - \tilde{\varepsilon}_{yy} + 2i\tilde{\varepsilon}_{xy}) \tag{4.11d}$$

Fortunately, this expression will not be used as is in the rest of this section, as a number of simplifications can be applied to make it more friendly.

4.2.1 ZnTe core luminescence: a simple approach

We start by studying the ZnTe core emission, as it first appears to be an extremely convenient test-bed for both the theoretical approach and the experimental analysis. As the case of infinitely long cylindrical core-shell NWs has been extensively discussed in the work [FC14], we will consider that the NW is infinite and has a circular symmetry, as shown in figure 4.3.

The mismatch between the core material and the shell material is written as $f = \Delta a/a$ where a is the lattice constant of the core material. Assuming that the materials have the same values of stiffness constants, the Lamé-Clapeyron-Navier equation (4.8) can be solved in the

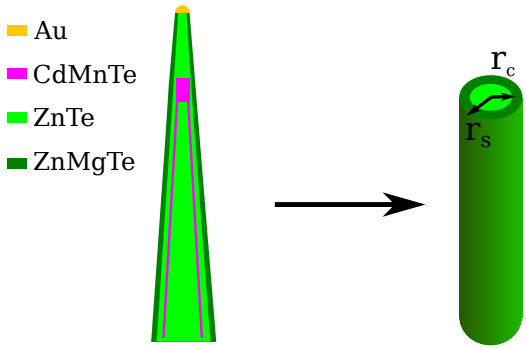

Figure 4.3 – Considered geometry for the study of the ZnTe core luminescence. Sketch of the considered geometry for the derivation of the effect of the strain from the shell on the luminescence of the ZnTe core of the NW. We assume an infinite nanowire with a circular symmetry. The core and shell radii r_c and r_s are both defined from the NW revolution axis.

cylindrical coordinates system, leading to:

$$\tilde{\varepsilon}^c_{zz} = (1-\eta)f \tag{4.12a}$$
$$\tilde{\varepsilon}^c_{\theta\theta} = \tilde{\varepsilon}^c_{rr} = (1-\eta)(f+B_s) \tag{4.12b}$$
$$\tilde{\varepsilon}^s_{zz} = -\eta f \tag{4.12c}$$
$$\frac{\tilde{\varepsilon}^s_{\theta\theta} - \tilde{\varepsilon}^s_{rr}}{2} = B_s \frac{r_c^2}{r^2} \tag{4.12d}$$
$$\frac{\tilde{\varepsilon}^s_{\theta\theta} + \tilde{\varepsilon}^s_{rr}}{2} = -\eta(f+B_s) \tag{4.12e}$$
$$B_s = -f\frac{c_{11}+2c_{12}}{c_{11}+c_{12}+2c_{44}} \tag{4.12f}$$
$$f + B_s = f\frac{-c_{11}+2c_{44}}{c_{11}+c_{12}+2c_{44}} \tag{4.12g}$$

where superscripts c and s refer to the core and the shell, respectively, and $\eta = r_c^2/r_s^2$ is the ratio of the core and shell cross-sections. Reintroducing these results in the Hamiltonian (4.10), we find that for the core only the P and Q terms are left. The resulting exciton energy is then:

$$\boxed{E_X = E_X^0 - (a_c + a_v)\tilde{\varepsilon}_{\text{hyd}} \pm \frac{d_v}{2\sqrt{3}}\tilde{\varepsilon}_{\text{shear}}} \tag{4.13}$$

where the + sign should be used for a light hole and the − sign for a heavy hole, a_c describes the effect of strain on the conduction electron, and a_v and d_v its effect on the holes. E_X^0 is the bulk exciton energy. *Thus, the strain from the shell introduces a global shift of the valence band energy through the P term, which is proportional to the isotropic (or hydrostatic) strain, and lifts the light and heavy hole degeneracy through the anisotropic Q term which is proportional to the shear strain.*

In its explicit form, equation (4.13) reads:

$$E_X = E_X^0 - (a_c+a_v)\frac{c_{11}-c_{12}+6c_{44}}{c_{11}+c_{12}+2c_{44}}(1-\eta)f \pm \frac{d_v}{\sqrt{3}}\frac{c_{11}+2c_{12}}{c_{11}+c_{12}+2c_{44}}(1-\eta)f. \tag{4.14}$$

The value of the deformation potentials $a = 5.3$ eV and $d/\sqrt{3} = 2.5$ eV can be found in [War+72; Dan+89], and the values of stiffness constants $c_{11} = 73.7$ GPa, $c_{12} = 42.3$ GPa and $c_{44} = 32.1$ GPa in [Lee70]. They result in respective shifts of the light and heavy hole excitons of (in meV, with f in %):

$$E_{HH} = 2381 - 88(1-\eta)f \tag{4.15a}$$
$$E_{LH} = 2381 - 44(1-\eta)f \tag{4.15b}$$

or more importantly a light-heavy hole splitting Δ_{LH} of:

$$\Delta_{LH} = -44(1-\eta)f. \tag{4.16}$$

We can then insert our numbers in, that is a core and shell radii as visible in the SEM image 4.1 (d) and a lattice mismatch $f = 1.04\%$ corresponding to the lattice mismatch between the ZnTe core and the $Zn_{0.8}Mg_{0.2}Te$ shell.

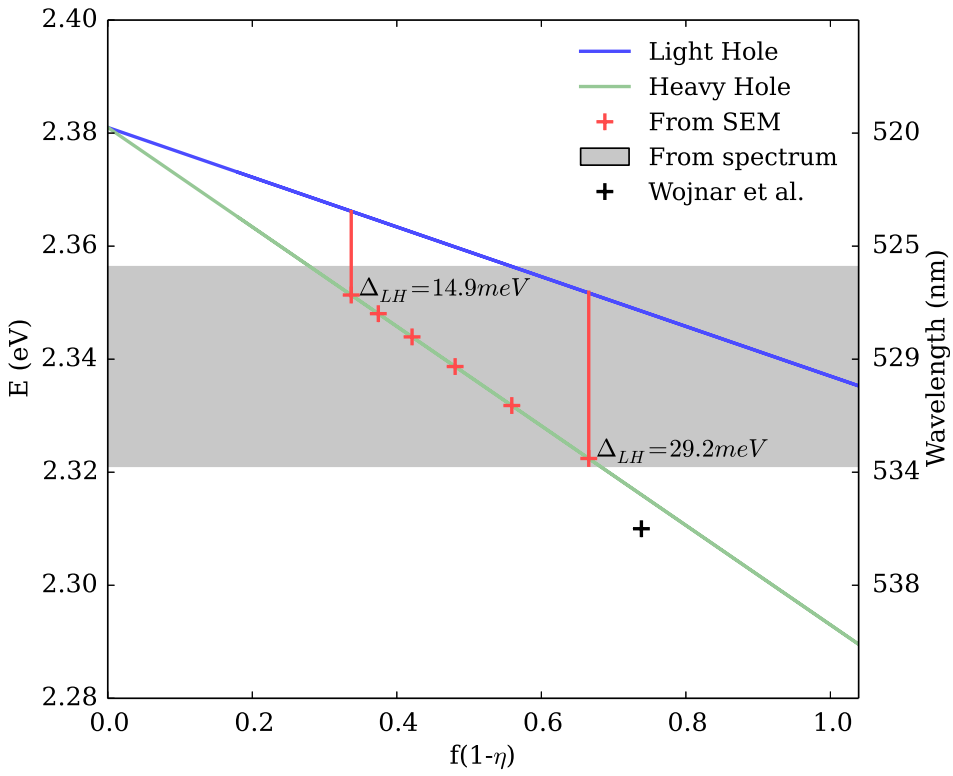

Figure 4.4 – Effect of strain on the ZnTe core hole states.
Light and heavy hole exciton energies (blue and green lines respectively) as a function of the lattice mismatch f between the core and the shell materials and the ratio of their radii η. The red dots represent the values of varying η along the NW axis due to its tapered shape, while the grey shaded area represents the width of the core luminescence spectrum. The black cross corresponds to the value reported in [Woj+12] for comparison. From these energy values, we can conclude that the hole ground state in the NW core is expected to be a heavy hole.

For illustration purpose we report values of radii corresponding to several points along the cone-shaped NW axis, as the core shrinks down in size while the shell thickness remains constant (20 nm). As represented in figure 4.4, the heavy hole (green) is then the ground state and is split by 15 to 29 meV from the light hole (blue). The red line with crosses shows the expected position of the exciton energy as a function of the NW radius. The grey dashed region corresponds to the dispersion in energy observed in the spectrum from figure 4.1 (b), and a quite good agreement is found. We have also reported the experimental value from Wojnar et al. [Woj+12], as they reported heavy hole emission from the NW core around 2.31 eV. In such cases, previous studies assumed that only the heavy hole will play a role in the NW core transitions, simplifying the analysis as we only consider degenerate $\sigma^{\pm}$ transitions [Woj+12].

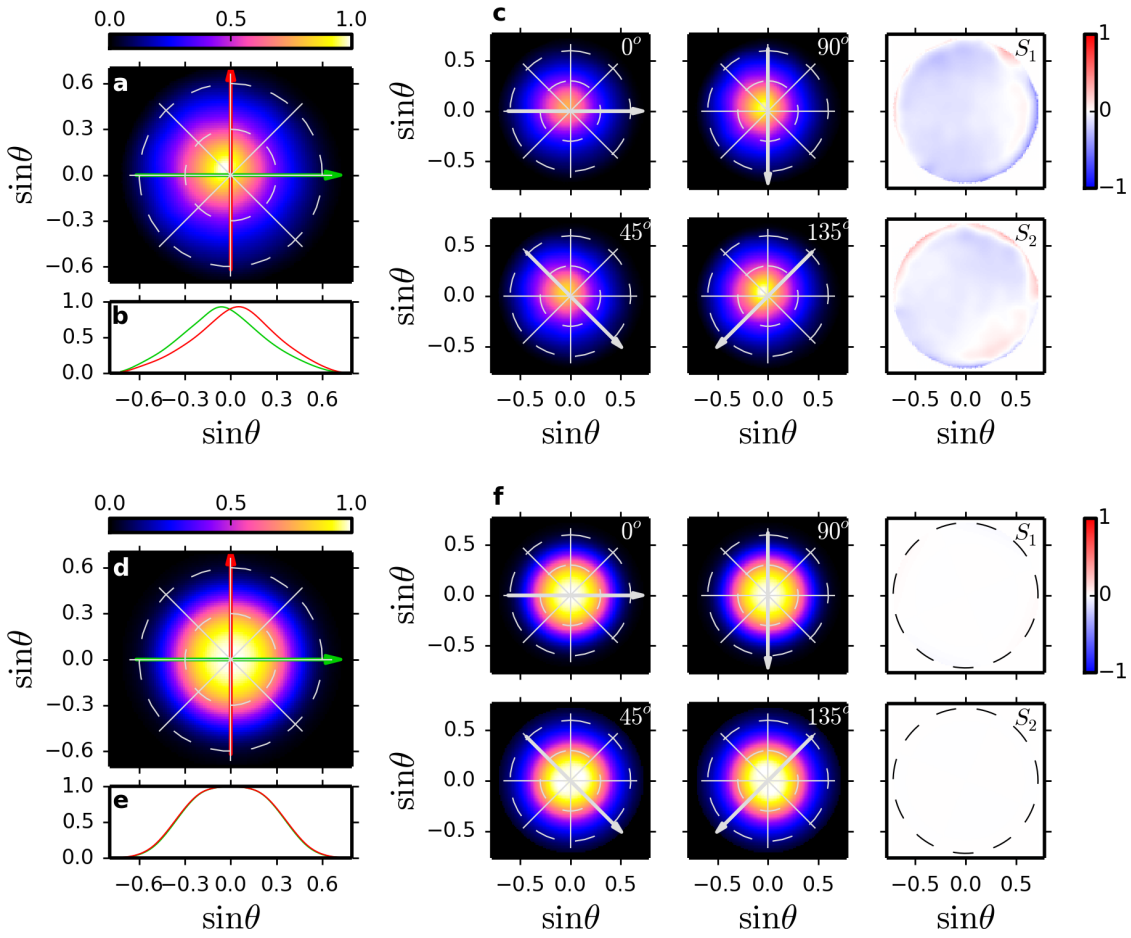

Figure 4.5 – Fourier plane microscopy: experiments and simulations.
Comparison between the Fourier microscopy measurements on the ZnTe luminescence (a)-(c) and the simulated maps (d)-(f) assuming only heavy-hole excitonic transitions (i.e. $\sigma^{\pm}$ dipoles). (a) and (d) Unpolarised intensity maps, with their respective cross-sections along the red and green lines in (b) and (e). (c) and (f) Polarisation-resolved intensity and Stokes parameters maps.

We performed the radiation diagram measurement in the µPL setup. As no straightforward geometrical basis can be defined, we use two set of arbitrary orthogonal directions ($0^o, 90^o$ and

$(45^o, 135^o)$ to construct the two Stokes parameters S_1 and S_2 in each basis respectively:

$$S_1 = \frac{I_0 - I_{90}}{I_0 + I_{90}} \qquad S_2 = \frac{I_{45} - I_{135}}{I_{45} + I_{135}} \tag{4.17}$$

The measurement results are presented in figure 4.5 (a-c). The emission of the NW is then modelled using COMSOL as an incoherent superposition of circularly polarised emitters distributed along the NW axis, and with relative weights corresponding to the CL intensity measured in figure 4.1 (e). The results are presented in figure 4.5 (d-f).

The agreement between the experiments and the simulation is quite good. The experimental unpolarised radiation pattern measurement reveals a single peak, slightly off-centred, with rotational symmetry which is well reproduced by the simulation, although perfectly centred. The polarisation-resolved diagrams shows the exact same structure and are also in good agreement with the simulations. A qualitative comparison with the theoretical pattern in a homogeneous medium of figure 4.2 (c) is still possible. For degenerate $\sigma^{\pm}$ emitters, the unpolarised and all the polarised radiation patterns are expected to be of circular symmetry, with a zero degree of linear polarisation. We note a small difference between the measured and simulated Stokes parameters, as the experimentally determined S_1 and S_2 show a slightly negative value of both parameters while the simulation results give a zero degree of linear polarisation, as expected from $\sigma^{\pm}$ radiation. The average degree of linear polarisation, integrated over the whole diagram, is $\sim 2\%$. This discrepancy can not be described by considering only $\sigma^{\pm}$ transitions. Therefore, a more refined approach has to be used to properly describe the emission from the core. The main approximation responsible for these observed differences could be that the cone shape of the NW makes the calculation of the strain inside the core not valid any more. The P and Q terms in equation (4.10) would then be non-zero, and the off-diagonal elements introduce mixing between the light and heavy hole states.

4.2.2 The QD case: a limiting model

In the case of the QD, no analytical calculation has been presented yet to solve the problem of a spheroidal inclusion inside a cylindrical core-shell structure with rotational symmetry. However, we can present the interesting limiting case of an ellipsoidal quantum dot embedded inside an elastically isotropic matrix, corresponding to the limiting case of a QD much smaller than the core radius and a core radius much larger than the shell radius, i.e. a situation where the dot is small enough and the core large enough so that the QD only "feels" the effect of the core, but no effect from the shell or the outer surface.

The strain components inside and outside the QD have been calculated analytically ([Esh57], [Esh59]). The QD is assumed to be an ellipsoid with a diameter D in the (x, y) plane and a height L along the z axis. Hence the case $L/D \gg 0$ represents an infinitely long cylinder, and the case $L = D$ the spherical case. The assumption of an elastically isotropic material further simplifies the stiffness tensor $\tilde{c}$, leaving only two terms $\lambda = c_{iijj}$ and $\mu = c_{ijij} = c_{ijji}$ for $i \neq j$,

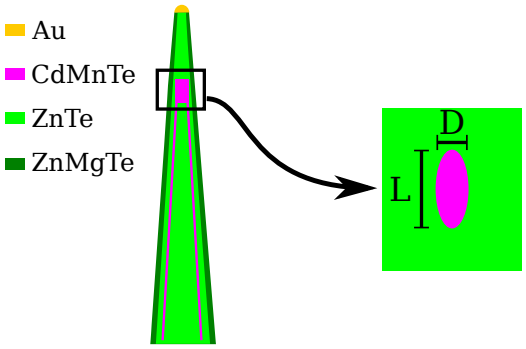

Figure 4.6 – Considered geometry for the study of the QD luminescence.
Sketch of the considered geometry for the derivation of the effect of the strain from the core on the luminescence of the NWQD. We assume an infinite matrix made of the core material, and an ellipsoidal QD with height L and diameter D.

and $c_{iiii} = \lambda + 2\mu$, or in its full form:

$$\tilde{c} = \begin{pmatrix} \lambda+2\mu & \lambda & \lambda & 0 & 0 & 0 \\ \lambda & \lambda+2\mu & \lambda & 0 & 0 & 0 \\ \lambda & \lambda & \lambda+2\mu & 0 & 0 & 0 \\ 0 & 0 & 0 & \mu & 0 & 0 \\ 0 & 0 & 0 & 0 & \mu & 0 \\ 0 & 0 & 0 & 0 & 0 & \mu \end{pmatrix}. \tag{4.18}$$

The strain components inside the QD are then:

$$\tilde{\varepsilon}_{rr}^{QD} = \tilde{\varepsilon}_{\theta\theta}^{QD} = f - f_{shear}\zeta\left(L/D\right) \tag{4.19a}$$
$$\tilde{\varepsilon}_{zz}^{QD} = f + 2f_{shear}\left(\zeta\left(L/D\right) - 1\right) \tag{4.19b}$$

where

$$f_{shear} = \frac{f}{2}\frac{3\lambda+2\mu}{\lambda+2\mu} \tag{4.20}$$

is the shear strain and the relevant shape factor $\zeta\left(L/D\right)$ is defined as:

$$\zeta\left(x\right) = \begin{cases} 1 - \dfrac{1 - x/\sqrt{1-x^2}\cos^{-1}x}{1-x^2}, & x < 1 \\ 1 + \dfrac{1 - x/\sqrt{x^2-1}\cosh^{-1}x}{x^2-1}, & x > 1 \end{cases} \tag{4.21}$$

Using again equation (4.11b) $\Delta_{LH} = 2Q^{QD} = -\frac{d_v}{\sqrt{3}}\tilde{\varepsilon}_{shear}$ with $\tilde{\varepsilon}_{shear} = \tilde{\varepsilon}_{rr} + \tilde{\varepsilon}_{\theta\theta} - 2\tilde{\varepsilon}_{zz}$ we can report the effect of the uniform strain on the QD in figure 4.7.

In the case of spherical QDs ($L/D = 1$), we find a zero splitting between the light and heavy hole states, meaning that they would be fully degenerate as sketched in figure 4.2 (a). We can also see that a "flat" QD ($L/D < 1$) favours a heavy hole ground state ($\Delta_{LH} > 0$) while an elongated QD ($L/D > 1$) favours a light hole ground state ($\Delta_{LH} < 0$). This finding appears in qualitative agreements with atomistic calculations in the case of indium arsenide QDs inserted inside indium phosphide NWs [Zie13].

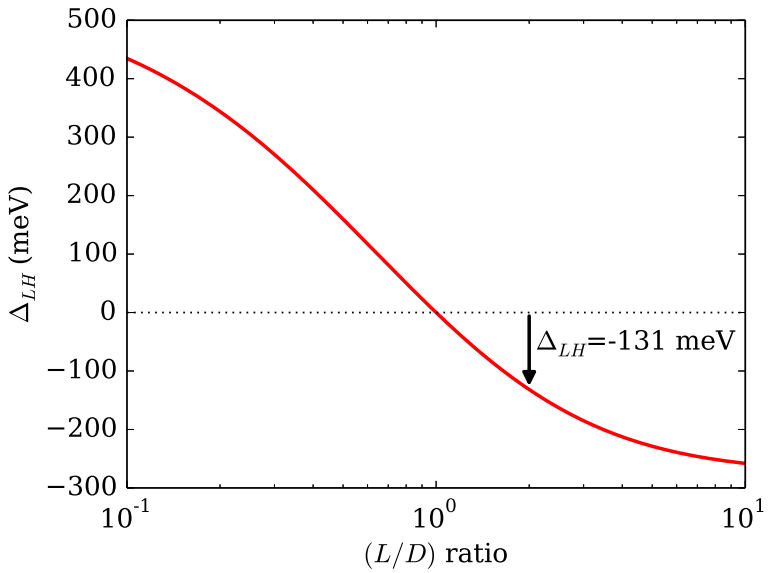

Figure 4.7 – Light hole-heavy hole splitting in the ellipsoidal QD.
Calculated light hole-heavy hole splitting Δ_{LH} for an ellipsoidal CdTe QD inserted in an infinite ZnTe matrix, assuming an isotropic elasticity of the materials.

According to EDX measurements on NWs from the same sample, the typical value of $L/D = 2$ can be used to model our QDs. Here, it yields a value of $\Delta_{LH} = -130$ meV, indicating that the hole ground state of the QD is a light hole. This splitting is larger in magnitude than the values of $\Delta_{LH} \in [15, 30]$ meV found for the ZnTe core inside the ZnMgTe shell. Hence, as for the ZnTe core case we assume pure transitions to the ground hole state, i.e. pure light hole transitions here.

As for ZnTe, the comparison between the Fourier microscopy experiments and simulations including only light-hole states is presented in figure 4.8. The relevant dipole elements are thus $\sigma^{\pm}/\sqrt{3} + \pi\sqrt{2/3}$. The experimental unpolarised pattern presents a rough rotational symmetry around the z axis, with a slight power imbalance and a central dip, revealed by the red and green cross-sections. The presence of the dip in the center is characteristic of the π transition, which is the signature of the light-hole exciton recombination. The polarisation-resolved patterns reveal two asymmetric lobes aligned with the polarised axis. Note the non-monotonic position of the maximum intensity lobe as a function of the polariser angle. Finally, the Stokes parameters maps reveal a distinct four-quadrant shape, characteristic of a strong π transition along the z axis due to the azimuthal, linearly polarised electric field [see figure 4.2 (d)]. The degree of linear polarisation integrated over the whole numerical aperture is $\sim 40\%$. The simulated patterns reproduce the rotational symmetry, the presence of the dip in the unpolarised pattern and of the two lobes aligned with the polarised axis, as well as the four-quadrant shapes of the Stokes parameters diagrams. However, no power imbalance is observed in the unpolarised diagram nor in the polarisation-resolved measurements. As the model consists in degenerate $\sigma^{\pm}$ and π transitions, it can only result in rotationally symmetric patterns. Therefore, the integrated simulated degree of linear polarisation is zero, in contradiction with our measurements. As for the ZnTe, this is a clear indication that the simplified strain model is not enough to describe the electronic properties of the QD inside the NW. However, it confirms that the dominant hole

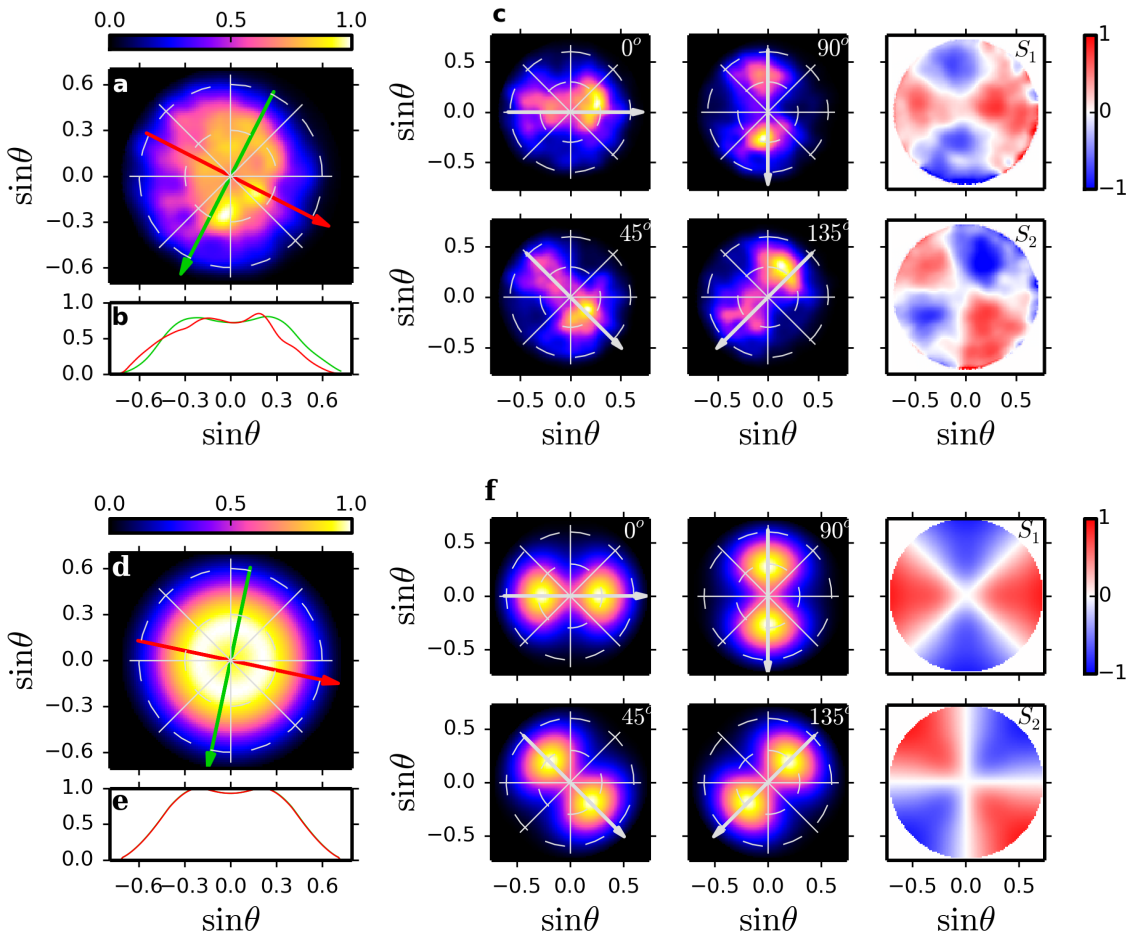

Figure 4.8 – Fourier plane microscopy: experiments and simulations.
Comparison between the Fourier microscopy measurements on the CdTe luminescence (a)-(c) and the simulated maps (d)-(f) assuming only light-hole excitonic transitions with dipole elements $\sigma^{\pm}/\sqrt{3} + \pi\sqrt{2/3}$. (a) and (d) Unpolarised intensity maps, with their respective cross-sections along the red and green lines in (b) and (e). (c) and (f) Polarisation-resolved intensity and Stokes parameters maps.

state inside the QD is of light hole character.

4.3 A more refined approach: full valence band mixing calculations

No analytical calculation or simulations provides us yet with a correct description of the strain Hamiltonian for the core in a tapered core/shell NW, nor for a QD in a core/shell NW problem. It is customary to treat this problem by considering that the light and heavy hole bands are mixed, resulting in new hole functions [Kou+04; Lég+07; Ton+12; Huo+13]. In its general

form, the Hamiltonian (4.10) can be written as:

$$\mathcal{H} = \begin{pmatrix} -\frac{1}{2}\Delta_{LH} & -\sigma e^{i\chi} & \rho e^{-2i\psi} & 0 \\ -\sigma e^{-i\chi} & \frac{1}{2}\Delta_{LH} & 0 & \rho e^{-2i\psi} \\ \rho e^{2i\psi} & 0 & \frac{1}{2}\Delta_{LH} & \sigma e^{i\chi} \\ 0 & \rho e^{2i\psi} & \sigma e^{-i\chi} & -\frac{1}{2}\Delta_{LH} \end{pmatrix} \tag{4.22}$$

where Δ_{LH} is the light and heavy hole splitting, $\tilde{\rho} = \rho e^{-2i\psi}$ is the in-plane mixing term and $\tilde{\sigma} = \sigma e^{i\chi}$ is the out-of-plane mixing term. The Δ_{LH} terms on the diagonal with opposite signs for light and heavy holes lead to a splitting between the two states. It is measured in hole energy, so $\Delta_{LH} > 0$ represents a heavy hole ground state, and $\Delta_{LH} < 0$ a light hole ground state. The off-diagonal mixing terms reveal that the pure hole states are no longer the relevant ones describing the electronic transitions. New hole states corresponding to a linear combination of the pure states have to be calculated, diagonalising the Hamiltonian (4.22). This description of the valence band is implemented to parametrise our numerical post-treatment step for the simulation method. We apply $\mathcal{H}$ to the simulated elementary electric fields to fit the measured Fourier images and retrieve the mixing parameters.

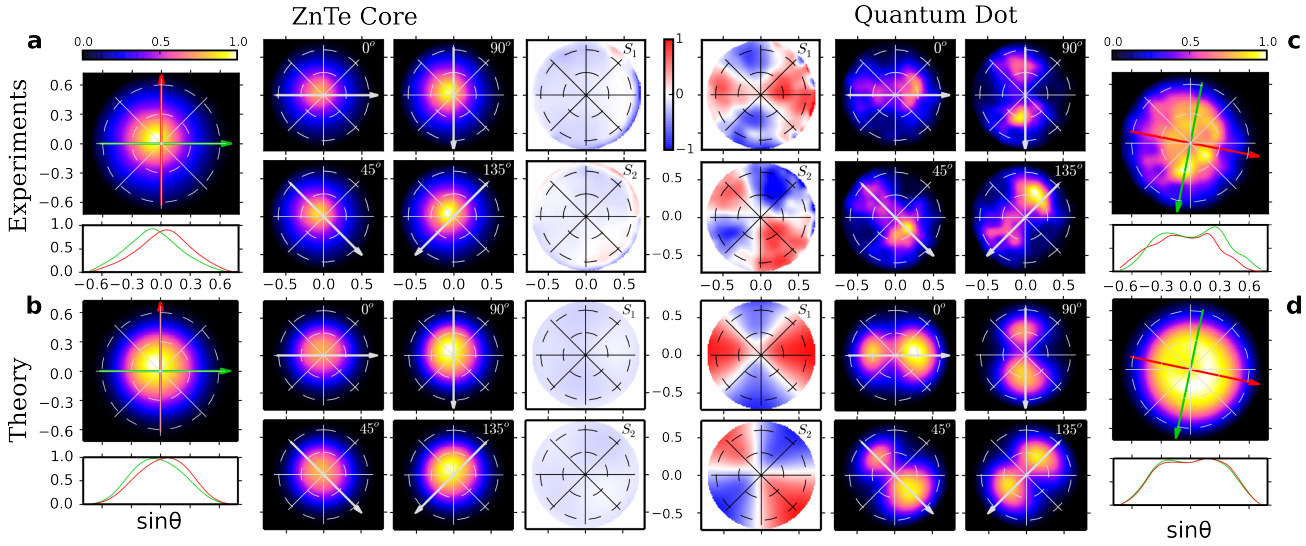

Figure 4.9 – Fourier plane microscopy: experiments and simulations for both the core and the QD luminescence.
In each panel we present the normalized unpolarised far field radiation diagram with two cross sections along the direction of the red and green arrows, the linearly polarised radiation diagrams at $\{0^o, 90^o\}$ and $\{45^o, 135^o\}$ sharing the same normalization factor (the direction of polariser is indicated by the white arrow), and the S1 and S2 stokes parameter maps. (a) Experimental results for the ZnTe emission line. (b) Corresponding simulation results ($\rho/\Delta_{LH} = 0.14$, $\sigma/\Delta_{LH} = 0.24$, $\psi = 112°$, $\chi = 186°$). (c) Experimental results for the QD emission line. (d) Corresponding simulations ($\rho/\Delta_{LH} = -0.23$, $\sigma/\Delta_{LH} = -0.06$, $\psi = 170°$, $\chi = 137°$).

The measurements and corresponding simulations are gathered in figure 4.9. First, we note that no realistic mixing parameters allowed us to reproduce the off-centring of the ZnTe radiation, which is hence attributed to a small tilt of the NW with respect to the z axis. We

subsequently modified the simulation geometry to account for this tilt, determined from the unpolarised radiation pattern to be of 5° in the $\{z;\varphi = 135°\}$-plane. The following distinct features with precise physical origins can be used to fit the experimental maps:

- Further off-centering of each map and azimuthal variation along the φ direction are due to the out-of-plane mixing strength and its phase $\tilde{\sigma} = \sigma e^{-i\chi}$.

- The overall degree of polarisation, and the subsequent non-zero degree of linear polarisation along the $k = 0$ direction are governed by the in-plane mixing strength and its phase $\tilde{\rho} = \rho e^{-2i\psi}$.

However, as no feature allows us to retrieve the value of Δ_{LH}, the diagonal term of $\mathcal{H}$ has to be factored out, and we can only compute mixing strengths *relatively to the light hole-heavy hole splitting*.

Concerning the ZnTe core luminescence, we have found that the off-centring is strongly dominated by the tilt of the NW, because it consists mainly in $\sigma^{\pm}$ emission which appears to be guided by the NW structure in the COMSOL simulations (not shown). The hole states appear to be of strong heavy hole character. The NW tilt can induce a residual degree of linear polarisation. However, non-zero in- and out-of-plane mixing terms with amplitudes $\rho/\Delta_{LH} = 0.14$ and $\sigma/\Delta_{LH} = 0.24$ have to be introduced to reproduce all the features from the experimental measurements:

- The overall degree of linear polarisation, of the order or $\sim 2\%$, unambiguously comes from an in-plane mixing owing to the $\tilde{\rho}$ term and not only from the NW tilt.

- An additional out-of-plane mixing component $\tilde{\sigma}$ in the same direction than the physical tilt angle has to be added to reproduce the small white contribution on the right half of the S_1 diagrams and the reddish contribution in the bottom right quarter of the S_2 diagram.

The QD luminescence can be fairly well reproduced as well. It consists in a strong light hole excitonic transition, with mixing amplitudes $\rho/\Delta_{LH} = -0.23$ and $\sigma/\Delta_{LH} = 0.06$.

- The unpolarised radiation pattern presents the same azimuthal asymmetry than the experimental one, and the unbalanced two lobes patterns and Stokes parameters maps are reproduced.

- The remaining degree of polarisation in the Stokes parameters maps are due to the $\tilde{\rho}$ term.

- As for the core luminescence a non-zero additional out-of-plane term $\tilde{\sigma}$ has to be added to reproduce the "opening" of the four-quadrant Stokes maps in the $k = 0$ direction, and the intensity balance between the lobes in the polarisation-resolved intensity maps.

4.4 Magneto-optical spectroscopy

The QD contains a large fraction of Mn atoms ($\sim 10\%$). When an external magnetic field is applied on the QD, the presence of these localised additional spins $S = 5/2$ strongly increases

the coupling of the electrons and holes to the applied field via the exchange interaction, resulting in the so-called giant Zeeman effect. This coupling can be expressed by the Hamiltonian [GK11]:

$$H = -\alpha \sum_{\mathbf{r}_i} \delta\left(\mathbf{r} - \mathbf{r}_i\right) \mathbf{S}_i \cdot \boldsymbol{\sigma}_e - \beta \sum_{\mathbf{r}_i} \delta\left(\mathbf{r} - \mathbf{r}_i\right) \mathbf{S}_i \cdot \mathbf{J}_h \tag{4.23}$$

where α and $\beta/3$ are the exchange integrals for the electron and hole, $\mathbf{r}_i$ is the position of the magnetic atoms with spin operator $\mathbf{S}_i$, and $\boldsymbol{\sigma}_e$ and $\mathbf{J}_h$ are the electron spin operator and hole kinetic momentum operator. Using the mean field approximation and the virtual crystal approximation, the splitting inside each electronic (electron, light and heavy hole) level can be expressed easily as a function of the magnetisation $\langle M \rangle$. Assuming that it is applied along the quantisation axis, we get [GK11]:

$$\Delta_e = \alpha \frac{\langle M \rangle}{g_{Mn}\mu_B} \tag{4.24a}$$

$$\Delta_{HH} = -\beta \frac{\langle M \rangle}{g_{Mn}\mu_B} = 3\Delta_{LH} \tag{4.24b}$$

where μ_B is the Bohr magneton. Δ_e splits the electron levels $|+1/2\rangle_e$ and $|-1/2\rangle_e$ while Δ_{HH} (resp. Δ_{LH}) splits the heavy (light) hole levels $|+3/2\rangle_h$ and $|-3/2\rangle_h$ ($|+1/2\rangle_h$ and $|-1/2\rangle_h$). The consecutive energy shift is much larger than in the case of non-doped semiconductors, and can reach values as large as the light hole-heavy hole splitting, allowing an independent characterisation of the hole states via magneto-optical spectroscopy. The interaction between the confined carriers inside a QD and the Mn spins in the presence of an external magnetic field is usually further simplified by considering that the Mn atoms are uniformly spread inside the QD. The applied magnetic field induces a magnetisation which is averaged over the QD volume, giving rise to a global magnetic moment M inside the dot.

Treating the magneto-optical properties of such structure is beyond the scope of this work, and the magneto-optical spectroscopy of nanowire quantum dots was the research topic of Alberto Artioli during the time of this thesis [Art16]. He performed the analysis of this isolated nanowire with Dr. David Ferrand, and a summary of the findings are presented in this section. The sample was mounted on a liquid helium cryostat equipped with a solenoid magnet producing a magnetic field from 0 to 11 T oriented *along the NW axis*. A confocal microscopy setup with an objective of NA=0.4 was used. Excitation was performed using a cw laser emitting at 488 nm, and the µPL signal was separated into right and left handed circular polarisation using a $\lambda/4$ and a linear polarisation divider. Both polarisations were spectrally analysed in a spectrometer and detected on a CCD camera. They were always recorded at the same time. In the presence of the magnetic field B, the magnetic moment M inside the dot follows a modified Brillouin function $B_{5/2}$:

$$M = M_{sat} B_{5/2}\left(\frac{5\mu_b B}{k_B(T + T_{AF})}\right) \tag{4.25}$$

where T is the temperature and k_B is the Boltzmann constant. Two empirical parameters appear, M_{sat} and T_{AF}, which both take into account an effective Mn concentration x_{eff} [Fur88] [Gaj+94]. T_{AF} and x_{eff} take into account the antiferromagnetic interaction, which represents the tendency for some atoms to favour antiparallel spin alignment. What is important to

remember here is that with around 10% of Mn concentration inside the dot, the effective concentration is $x_{eff} = 4.4\%$ and results in $T_{AF} = 2.7$ K, providing a nearly maximal coupling between the magnetic dopants and the carriers, and thus between the applied field and the carriers. Using the values from [GPF79] gives *the maximum expected energy shift for light and heavy hole excitons inside our structure, respectively* $E_{sat}^{LH} = 25$ meV *and* $E_{sat}^{HH} = 55$ meV. At low temperature the energy shift of the excitonic lines is expected to vary linearly as a function of M/M_{sat}, which provides a convenient representation.

The results of the magneto-optical spectroscopy experiments are gathered in figure 4.10. Panel (a) shows the µPL spectrum at the QD energy for zero field and at 11 T, resolved in σ^+ and σ^- polarisations. For zero field the same broad line than presented in figure 4.1 is visible with the same intensity for the two polarisations. At 11 T, two lines are visible. The lowest energy one shows a very moderate imbalance between the two circular polarisations, while the highest energy line is only present in the σ^+ polarisation. The Zeeman energy diagram of the electrons and holes inside the QD is shown in panel (b) assuming a light-hole ground state. At low temperature photo-carriers relax to their respective lowest energy level ($|-1/2\rangle_e$ and $|+1/2\rangle_h$). Because of this relaxation, we expect both a red shift of the light-hole exciton line [dashed black arrow in Fig. 4.10 (b)], and a strong linear polarisation along z (π polarisation) according to the optical selection rules recalled in figure 4.2 (a). Note that with the opposite assumption of a heavy-hole ground state, we would expect a σ^+ polarisation. The second expected transition occurs between the $|-1/2\rangle_e$ electron level and the $|+3/2\rangle_h$ heavy hole level, resulting in σ^+ polarised emission according to the optical selection rules. The Zeeman shift of the two lines visible on the spectrum (a) is reported in panel (c). A 25 meV red shift is observed for the first line presenting no circular dichroism, and a 37 meV shift is observed for the highest energy line which only appears at magnetic fields larger than 6 T. As detailed in the previous paragraph, a red shift of 25 meV corresponds to the maximum expected shift for a light hole exciton. Both the measured giant Zeeman shift and the polarisation properties of the first line are in agreement with a light hole character. Additionally, the second line presents a shift larger than the maximum accessible Zeeman shift for a light hole and hence has to be attributed to a heavy hole, again in agreement with the theoretical Zeeman energy diagram presented in figure 4.10 (b). As the Zeeman shift of the heavy hole level is lower than the maximum expected value, it can be further postulated that the heavy hole is not fully confined inside the QD. Extrapolating this shift to zero field gives the light hole-heavy hole splitting Δ_{LH} in absence of external magnetic field $\Delta_{LH} = -22$ meV, much smaller than the calculated value of -131 meV assuming an infinite matrix.

Finally, measuring the circular degree of polarisation, or Stokes parameter S_3:

$$S_3 = \frac{I_{\sigma^+} - I_{\sigma^-}}{I_{\sigma^+} + I_{\sigma^-}} \tag{4.26}$$

as a function of the applied magnetic field can give information on the hole states mixing. It is represented in figure 4.10 (d). The strong σ^+ polarisation of the heavy hole line is a direct consequence of the optical selection rules. However, the light hole exciton line appears slightly σ^+ polarised at large magnetic field, as can be seen in the spectrum in figure 4.10 (a). This partial circular polarisation results from the out-of-plane mixing term $\tilde{\sigma}$ and provides an

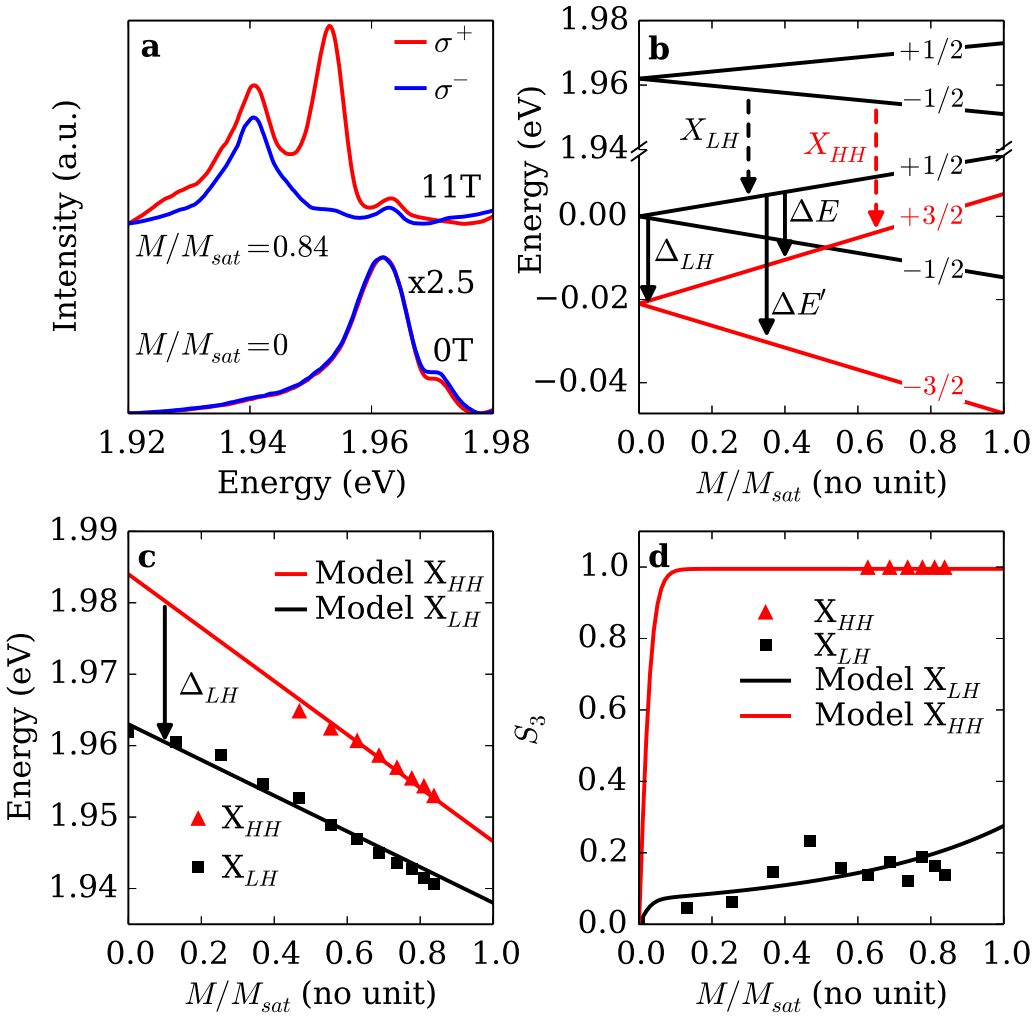

Figure 4.10 – Magneto-optical spectroscopy of the NWQD.
(a) Photoluminescence spectra of the QD emission line recorded at B=0 T and B=11 T (corresponding to a magnetic moment $M/M_{sat} = 0.84$). The magnetic field is applied along the NW axis, also oriented along the optical axis. σ^+ (solid red) and σ^- (dashed blue) polarisations are recorded simultaneously. The intensity at zero field has been multiplied by 2.5. (b) Theoretical Zeeman diagram for the electrons, light and heavy hole levels (indicated by their spin projection along the z axis) split by the exchange interaction with the Mn atoms. The X_{LH} (resp. X_{HH}) corresponds to the light (resp. heavy) hole exciton transition. (c) Measured Zeeman shift of the LH (black squares) and HH (red triangles) exciton lines as a function of the QD magnetic moment. The solid lines correspond to the expected shift for a CdMnTe QD with a 10% Mn concentration. (d) Circular degree of polarisation S_3 of the LH and HH exciton lines as a function of the QD magnetic moment. The solid lines correspond to the expected values of S_3 taking into account the valence band mixing induced by a perturbation term $|\sigma| = 2.2$ meV.

evaluation of the mixing strength. To first order, the mixed light hole state can be written:

$$|X_{LH}\rangle = |+1/2\rangle_h |-1/2\rangle_e + \beta |-3/2\rangle_h |-1/2\rangle_e + \gamma |+3/2\rangle_h |-1/2\rangle_e \tag{4.27}$$

with $|\gamma| = \left|\frac{\sigma}{\Delta E}\right|$ and $|\beta| = \left|\frac{\rho}{\Delta E'}\right|$ where ΔE (resp. $\Delta E'$) is the energy difference between the $|+1/2\rangle_h$ and $|+3/2\rangle_h$ levels (resp. $|+1/2\rangle_h$ and $|-3/2\rangle_h$), also shown in figure 4.10 (b). Taking into account the ratio of collection efficiency between $\sigma^{\pm}$ and π transitions in the small 0.4 N.A. given by $f_{\sigma\pi} = 1.88$, we find that the Stokes parameter takes the form:

$$S_3 = \frac{3 f_{\sigma\pi} \gamma^2}{2 + 3 f_{\sigma\pi} \gamma^2} \tag{4.28}$$

Using the experimental value of $S_3 = 0.18$ at large magnetic field, we find that the ratio of out-of-plane mixing is $\left(\frac{\sigma}{\Delta E}\right)^2 \approx 3\%$ in relative agreement with the value determined using the Fourier microscopy technique. Using the hole energy level deduced from the Zeeman diagram, we find an out-of-plane mixing perturbation term of $|\sigma| = 2.2$ meV. The theoretical S_3 parameters are reported in solid lines in figure 4.10 (d).

4.5 Discussion and conclusions on Te-based nanowire quantum dots

Using the combination of CL, magneto-optical spectroscopy and Fourier plane imaging, we have been able to propose a complete model for one CdMnTe QD inserted inside a ZnTe/(Zn,Mg)Te core-shell NW. We found a predominant light hole character, with a small residual mixing from the heavy hole band. The ZnTe core luminescence was attributed to heavy-hole excitons with a small mixing component from the light-hole band. Other NWQDs have been subject to magneto-optical spectroscopy only, from Alberto Artioli's PhD work. Several points are important to mention:

- Some QDs were found to have a heavy hole ground state, deduced from the larger Zeeman shift observed at high magnetic field,
- The electron appears well confined inside the QD (again from magneto-optical measurements, not presented here), as can be expected by the large conduction band offset between ZnTe and CdTe (see figure 3.6),
- Considering that the electron is well confined inside the dot, the fact that we observe long exciton lifetimes suggests a different confinement for the electron and the hole, e.g. a poorly confined hole or a different spatial localisation of electrons and holes,
- The fact that we observe a maximum Zeeman shift for the light hole, but not for the heavy hole (see figure 4.10) indicates that the light hole is better confined than the heavy hole.

In short, the aforementioned points and the dispersion in the results from section 3.3.1 in the statistical analysis of Te-based NWQDs properties fall down to the complete knowledge of the QD electronic states, e.g. the spatial confinement profiles, the electrons and holes wavefunctions

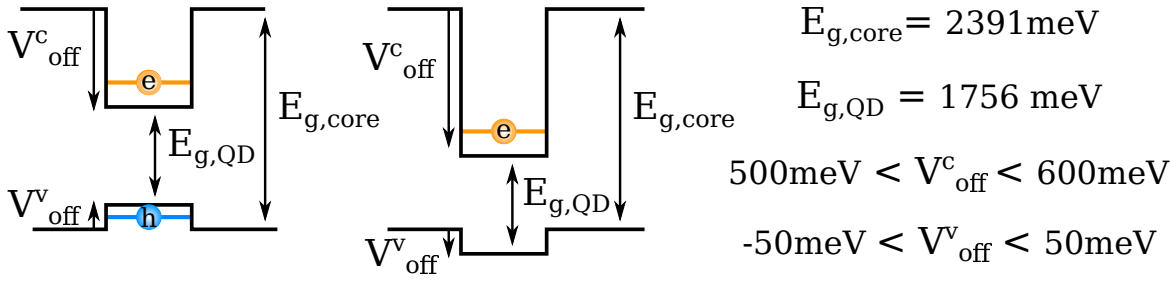

Figure 4.11 – Unstrained QD band profiles.
Possible band profiles of the CdMnTe QD inside a ZnTe NW core, in the absence of strain. The QD gap energy $E_{g,QD}$ accounts for the Mn content as expressed in equation (3.32). A positive band offset energy V^i_{off} indicates a confined carrier. Adapted from [Art16].

envelopes etc. We made significant progress in the understanding of these properties, but some questions remain.

The exact valence band offset between the QD and the core is unknown in our structure. Considering the values reported in figure 3.6, we expect it to be small, between -50 meV (not confined hole, type II alignment) and 50 meV (confined hole, type I alignment) [Art16]. The possible band alignments are presented in figure 4.11 in unstrained configuration. The band offset is affected by strain through a complex interplay between different strain terms, and we think that strain and shape inhomogeneity from one dot to an other are sufficient to infer drastically different QD behaviours, e.g. promoting either a light or heavy hole ground state. This small valence band offset has to be compared to the value of $\Delta_{LH} = -22$ meV we extracted from the magneto-optical spectroscopy. It is possible that in the absence of magnetic field, the heavy hole level is below the barrier level, leading to the unconfined heavy hole which would explain the absence of this transition in the zero field spectrum in figure 4.10 (a). As discussed in ref. [Art16], the presence of the magnetic field could improve the heavy hole confinement inside the dot, explaining the appearance of this line only at high magnetic field.

Atomistic calculations on III-V NWQDs revealed that strain localises the light and heavy hole in different spatial regions of the QD [NM08], [Zie13]. The results of ref. [Zie13] are summarised in figure 4.12. It demonstrates that for an elongated NWQD, the ground state is a light hole state in the center of the QD, but a heavy hole state is more favoured in energy at the poles. Especially, in the case of an elongated dot figure 4.12 (b) (top left) shows a light hole-heavy hole splitting of ~ -100 meV at the QD center, but additional calculations in the article reveal an actual splitting of ~ -20 meV, to be compared with our predicted value of $\Delta_L H = -130$ meV from section 4.2.2 and our experimental finding of $\Delta_{LH} = -22$ meV. Furthermore, both refs. [NM08] and [Zie13] reveal that even if the first electron and hole wavefunctions are confined and have a good overlap inside the QD, the higher energy states reveal more complicated spatial profiles, with a smaller overlap between the electrons and holes wavefunctions: see e.g. the heavy hole wavefunction **h3** in figure 4.12 (b) (right) which shows a heavy hole confined at the poles of the dot. Transition from light to heavy hole ground state can very well explain the difference in polarisation measurements we observed in the large ensemble of NWQDs presented in section 3.3.1, as a light hole ground state induces a strong, positive S_1 parameter, while a heavy hole ground state leads to a negative S_1 value.

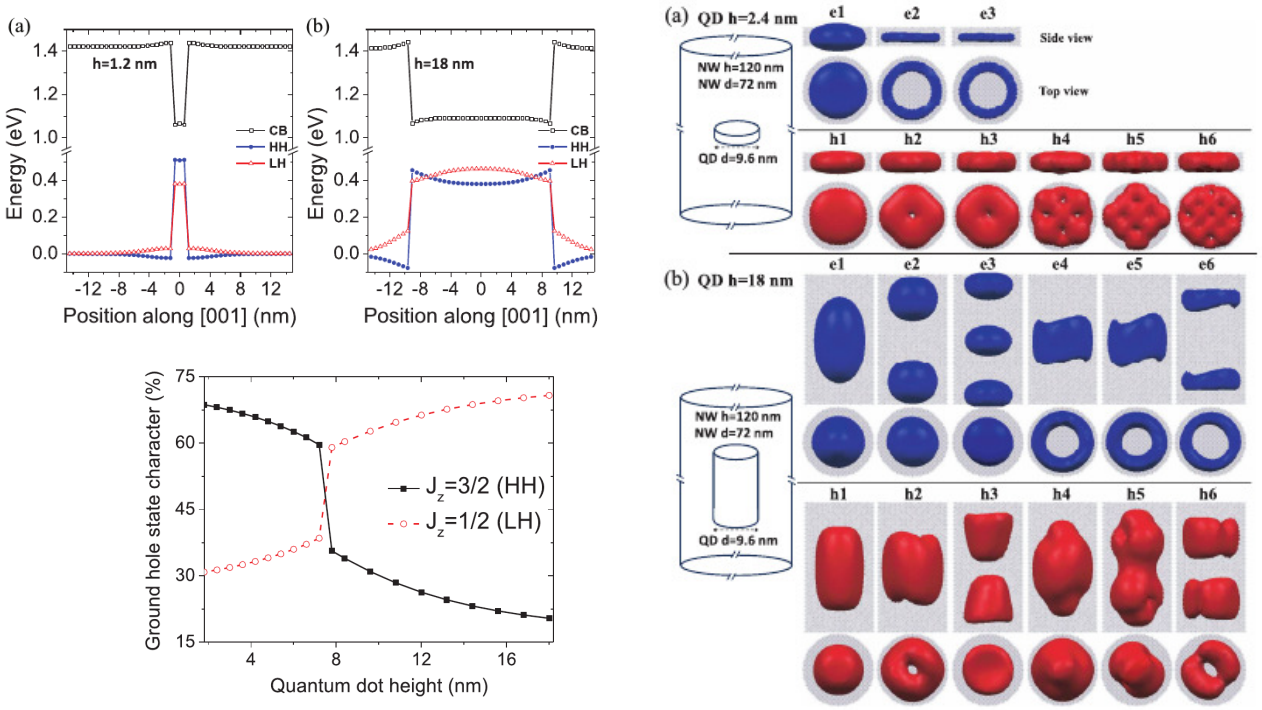

Figure 4.12 – Band structure and electronic states in III-V NWQDs.
Results of atomistic calculations considering InAs insertions in InP NWs. All the figures are adapted from [Zie13]. Upper-left (a) and (b): energy of the conduction (black), light (red) and heavy (blue) hole bands for a thin insertion (a) or an elongated QD (b) along the NW axis [001]. Lower left: Light (red) and heavy (black) hole character of the ground hole state as a function of QD height. Right (a) and (b): Electron and hole wavefunctions in the flat (a) or elongated (b) insertions. In the case of an elongated QD, note that the third excited state **h3** corresponds to the heavy hole and presents a hole confined at the QD poles.

In addition, the presence of a strain-induced piezoelectric field inside the QD is possible, leading to charge separation at each pole of the QD, which decreases the electron-hole overlap and therefore increases the exciton lifetime. As a consequence, increasing the QD aspect ratio results in:

- Stronger light hole character and thus higher, positive S_1 value,
- Lower QD exciton energy,
- Longer exciton lifetime.

This tendency is shown in black solid line in figure 4.13, which is a reminder of figure 3.21. The "expected", normal behaviour of the NWQDs thus corresponds to the red squares (or, to some extent, diamonds which represent larger NWs), which tend to align along the black line simply serving as a guide for the eye. We think that the deviating points correspond to different QD configurations, probably with a heavy hole ground state owing to e.g. a different QD shape or strain configuration. A more precise modelling of the system would require more complex

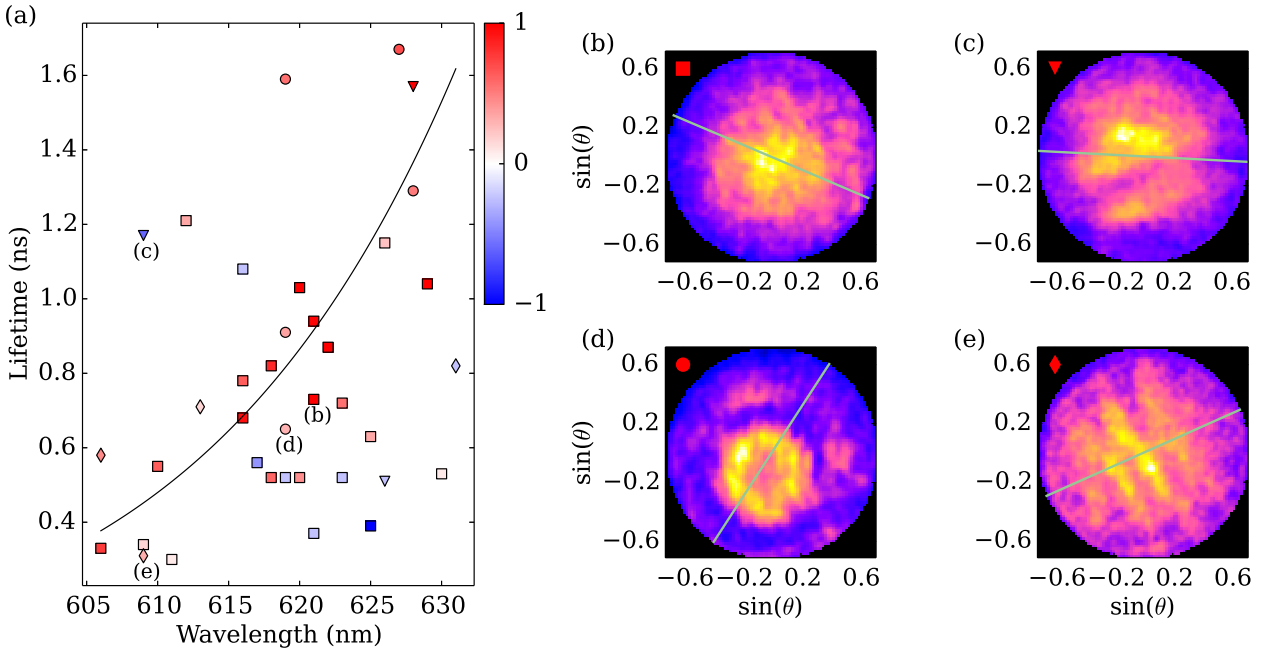

Figure 4.13 – Statistical polarisation properties of Te-based NWQDs.
Reminder of figure 3.21. A guide for the eye has been added in black line in panel (a) to illustrate the tendency of light hole excitons to present a longer lifetime and a lower energy with increasing QD length.

calculations, such as atomistic simulations, which are not easily implemented especially with II-VI semiconducting materials, and are the object of a current project in our laboratory.

In the past two chapters, we have extensively characterised the emission properties of Te-based NWQDs. We have proposed combined characterisation methods allowing for the determination of the spectral properties of their emission, the temporal dynamics of the exciton recombination and a polarisation-resolved determination of their radiation pattern. Gathering these information with the CL spectroscopy and LDOS imaging of plasmonic nanoantennas discussed in chapter 2 gives us all the keys to try and fabricate coupled NW-antenna systems. The fabrication of these devices is the object of the next chapter, in which we propose a fabrication method allowing for the deterministic fabrication of plasmonic antennas in the vicinity of NWQDs.

Chapter 5

Nanowire Quantum Dot-Plasmonic Antenna Hybrid Structures

Résumé en Français

Ce dernier chapitre traite de l'utilisation des résultats rassemblés au cours de ce travail de thèse pour réaliser des systèmes hybrides couplant une boîte quantique insérée dans un nanofil à semiconducteur avec des antennes plasmoniques.

Le système proposé est présenté en figure 5.3, il s'agit d'une antenne rectangulaire dont l'axe long est aligné avec la direction de polarisation de la lumière émise par la boîte. Le couplage au mode dipolaire longitudinal de l'antenne est privilégié, et la géométrie de l'antenne est déterminé par cathodoluminescence (CL) (voir figure 5.4). Une étape de caractérisation en microphotoluminescence (μPL) permet de déterminer l'orientation de la polarisation de l'émission spontanée de la boîte.

On propose alors un procédé de lithographie en deux étapes, basé sur le repérage en cathodoluminescence à température cryogénique de la position de la boîte dans le fil par rapport à un repère de marques pré-lithographiées. La procédure est détaillée en figure 5.5, et permet de lithographier les antennes à volonté avec la géométrie souhaitée. On détermine une précision dans le positionnement de l'antenne d'environ 50 nm.

On étudie alors l'effet du couplage entre la boîte et l'antenne en comparant les propriétés de μPL d'une même boîte avant et après fabrication de l'antenne, en fonction de la longueur de l'antenne. On observe une exaltation de l'intensité émise par la boîte. Les mesures de diagramme de rayonnement montrent que cet effet n'est pas dû à une redirection de l'émission de la boîte vers l'objectif. Etonnament, les mesures de temps de déclin ne montrent pas de diminution significative du temps de vie de l'exciton après la fabrication de l'antenne. En analysant les propriétés de μPL des boîtes à faible et forte puissance d'excitation impulsionnelle, on peut remonter au mécanisme d'exaltation de l'émission spontanée de la boîte. Dans la meilleure configuration (antenne la plus courte), on établit le couplage radiatif entre la boîte et l'antenne, résultant en une exaltation d'un facteur 2 de la fluorescence. L'exaltation restante est attribuée à une augmentation de l'absorption du faisceau d'excitation dans le nanofil.

Introduction

As discussed in the introduction chapter, controlling the spontaneous emission of an emitter requires controlling the optical density of states in its vincinity. We have demonstrated in chapters 1 and 2 how this can be achieved using plasmonic nanoantennas. In parallel, the careful characterisation of II-VI nanowire quantum dots allowed us to determine their spectral, spatial and temporal properties. We are now in position of trying to fabricate hybrid nanowire-nanoantenna systems in order to modify the intrinsic optical properties of the embedded quantum dot.

The fabrication of the coupled device requires a precise alignment of the antenna with the QD. Several experiments in the fields of self-assembled [Cur+10; Pfe+10; Coe+11; Kuk+14; Pfe+14] or colloidal [Cur+13; Bel+13; HAM16] quantum dots already demonstrated coupling between these solid-state emitters and plasmonic antennas. The first results involving coupling to nanowires were shown within the time frame of this work, with III-V nanowires ([Cas+14; Cas+15; Ram+15]). However, some of these works rely on probabilistic coupling, i.e. by dispersion of a large amount of plasmonic particles and emitters (e.g. [HAM16]) of by fabrication of antennas on a layer of self-assembled QDs before etching of the non-coupled structures ([Kuk+14]), while other make use of morphological criteria to locate the emitter ([Cur+10; Pfe+10; Coe+11; Pfe+14; Cas+14; Cas+15; Ram+15] and then deterministically place or fabricate the antenna in its near-field. None of these techniques can be applied in our case, as we target deterministic positioning of the antenna and the QD is fully embedded inside the NW, thus producing no recognisable morphological feature allowing for its localisation.

We first present the design of such hybrid system with Te-based nanowire quantum dots, before entering into the challenges of its experimental realisation. Finally, we show that we managed to enhance the radiative properties of the nanowire quantum dot through radiative coupling with the plasmonic antenna.

5.1 Design of the hybrid system

In figure 5.1, we recall the main characteristics of the Te-based NWQDs. The NWs grow in a ZB phase, and they present a tapered shape. They have a ZnMgTe shell of ∼20 nm thickness, a large ZnTe core and a CdMnTe QD. The exciton emission spans a range of wavelengths for different wires, and is around 620 nm. They have a rather long exciton lifetime, as exemplified in figure 5.1 (c). As detailed during the statistical study of the Te-based NWQDs in section 3.3.1, the emission from the CdMnTe QD is mainly linearly polarised along the NW axis, hence in the plane of the substrate. This has been investigated in details in section 4 and attributed to the light-hole character of the exciton in these NWQDs. Coupling to the nanoantennas requires the polarisation of the emitted light to be matched to the the one of the antenna mode. As this polarisation is in the plane of the substrate, the use of patch antennas is inappropriate for the Te-based NWQDs. Furthermore, the large NW radius would impose a thick spacing layer, reducing the coupling between the antenna and the ground plane.

Instead, previous cathodoluminescence characterisation on rectangular Au antennas on a Si/SiO_2 substrate gave us the necessary initial information in order to design a relevant and simple test system. The nanoantennas were fabricated with the same process used in the fabrication of the patch antennas (see section 2.3.2) on a Si substrate with a 100 nm thick thermal

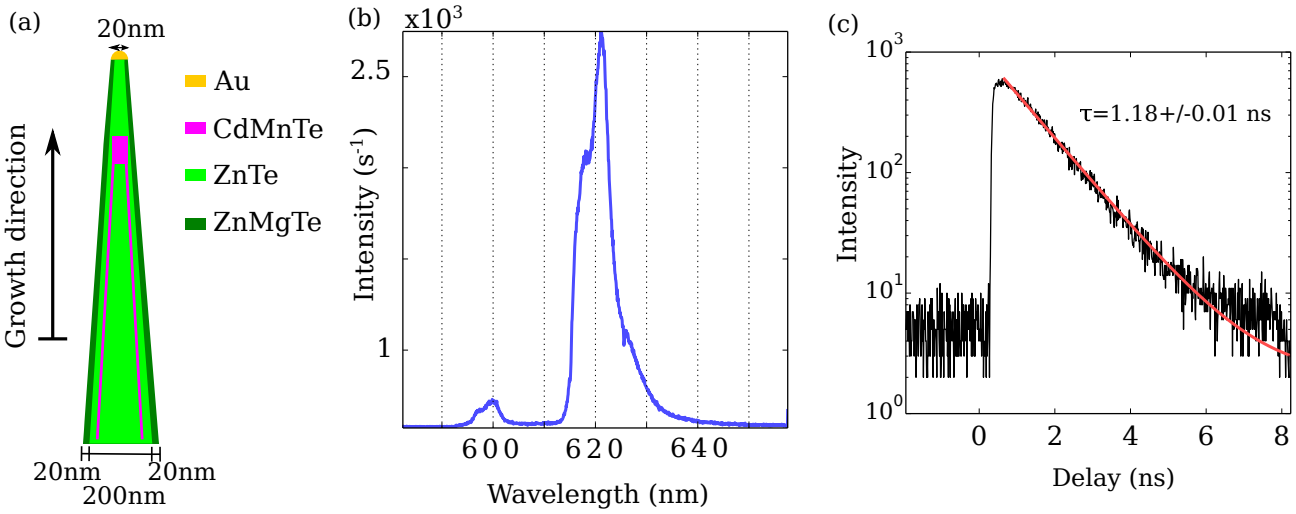

Figure 5.1 – Presentation of the emitting system.
(a) Structure of the Te-based NWQDs. The NWs are ZnTe/ZnMgTe core/shell structures with a tapered shape, and the QD is a CdMnTe insertion. (b) Typical µPL spectrum of the NWQD emission. As seen in section 3.3.1, the exciton emission wavelength varies from dot to dot, but is around 620 nm. (c) Typical TRPL experiment at low pumping power from the NWQD, showing a long decay time.

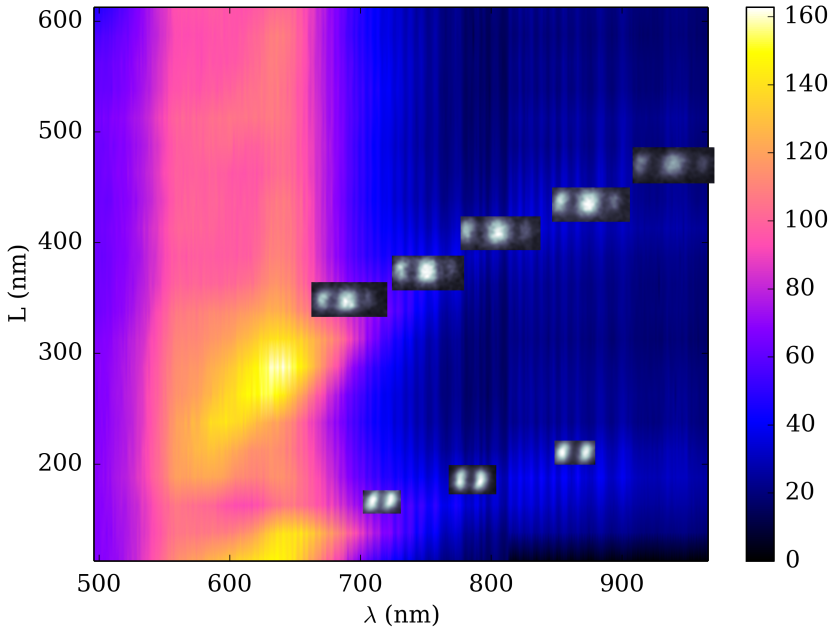

Figure 5.2 – CL spectra of rectangular antennas.
Colour-coded intensity map of the CL spectra of Au rectangular antennas on a Si/SiO_2 substrate. The antenna width is 100 nm and the length L is reported in ordinates. The intensity is expressed in photons/s. Inset: LDOS images of the corresponding antenna modes, integrated over a 100 nm bandwidth. Note that we do not represent the transverse mode.

oxide layer. They consists in single Au rectangles of 100 nm width and a variable length L. While this does not strictly correspond to the dispersed NW substrate, and hence prevents a direct comparison of the antennas properties, it provides us with a good estimation of relevant parameters. The length of the antennas was varied from 100 to 600 nm. We performed CL spectroscopy on the antennas, and obtained the spectral map presented in figure 5.2. The dispersion of the successive modes is clearly visible, and the LDOS imaging of the relevant resonances (in inset, at their corresponding length and wavelength position) confirms that we fabricated antennas supporting the fundamental dipolar mode and its first higher order (quadrupolar) mode. We find that on such high refractive index substrates ($n_{SiO_2} \sim 1.46$ with respect to $n_{Al_2O_3} \sim 1.77$ at 620 nm), the relevant length for an antenna to support a dipole-like mode at the QD emission wavelength of 620 nm is around L=100 nm. As we want to enhance the emission from our NWQDs, we favoured coupling to the dipolar mode with respect to the quadrupolar mode [MKP07].

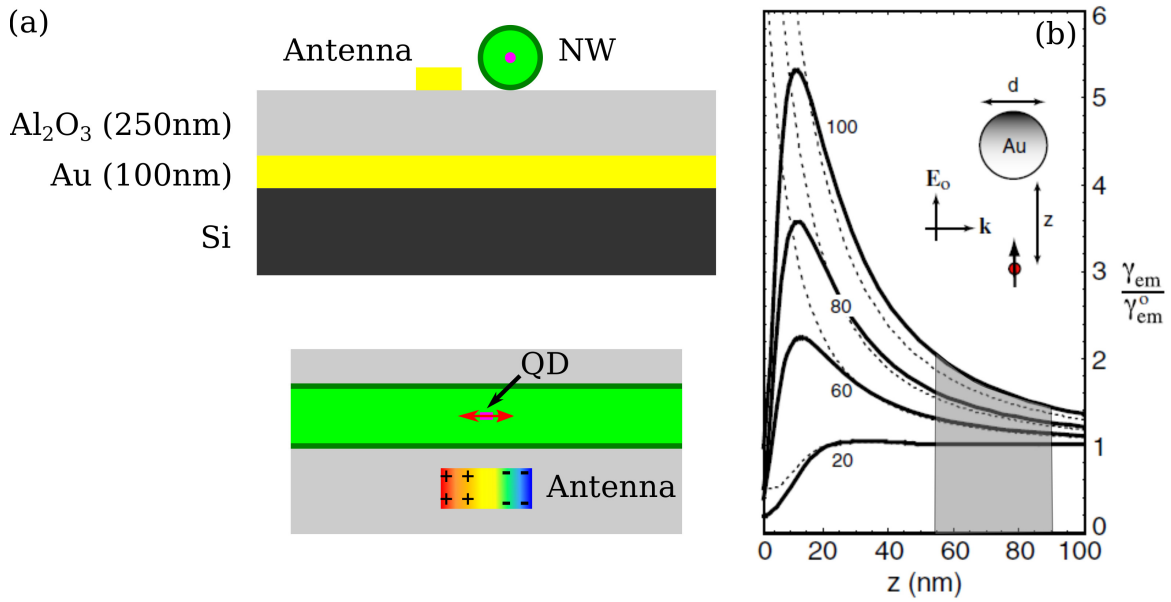

Figure 5.3 – Schematic of the hybrid NW-antenna structure.
(a) Schematic of the target geometry of the nanowire-antenna hybrid structure, side view (top) and top view (bottom), to scale. The red arrow represents the polarisation direction of the light emitted by the QD. We aim to align the antenna long axis with this direction, to couple to the dipolar mode, represented here by the surface charge density of the mode. (b) Expected radiative rate enhancement of a dipole brought near a spherical Au nanoparticle in vacuum (from [ABN06], solid lines are multiple multipole method calculations and dashed lines correspond to the dipole limit) with the range of our experimental parameters shaded in grey. The numbers next to the lines correspond to the sphere diameter.

The antenna modes are polarised along the antenna long axis. This means that for an efficient coupling, we need to align the antenna long axis with the polarisation direction of the emitted light. The retained geometry is depicted in figure 5.3 (a) in the case of a QD emitting with a linear polarisation along the NW axis. The Al_2O_3 spacer thickness is kept at 250 nm to improve the light collection from the NWQDs (see section 3.2.2). The main drawback of this

geometry is that even if the antenna axis is aligned with the light polarisation, it consists in a largely non-optimal coupling geometry, as detailed for example in refs. [Tho+04; MKP07; Cho+08]. Luminescence quenching by non-radiative energy transfer is prevented automatically by the presence of lateral core growth and by the shell of the NW, which also puts a lower bound on the distance between the QD and the antenna. Due to the conical shape of the NW, this distance is at least 50 nm. This is a serious limitation on the increase in LDOS that the antenna will provide around the NW, and thus puts an upper bound on the spontaneous emission enhancement we might observe.

As a rule of thumb, this can be illustrated using the work of Anger, Bharadwaj, and Novotny [ABN06], adapted in figure 5.3 (b). The radiative rate enhancement of a dipole placed near a gold spherical nanoparticle in vacuum is computed for several particles sizes as a function of the particle-dipole distance. The range of parameters corresponding to our experimental configuration is shaded in grey, considering the *optical distance* between our QDs and antennas, i.e accounting for the refractive index of the core and shell materials. In such configuration, a modest radiative rate enhancement of a factor 2 can still be expected. This estimation has to be balanced with the fact that our system presents a non-optimal coupling geometry, but that our antennas are elongated, which results in a larger particle polarisability as demonstrated in section 1.3, and thus a larger scattering cross section than for a sphere of the same dimension.

The relevant antenna parameters are then determined experimentally. A set of rectangular nanoantennas of width 70 nm and variable length L from 85 to 140 nm is fabricated on the same substrate hosting the dispersed NWs, in a region free of NWs. As a reminder, the substrate consists in a metallic (Au) mirror and a dielectric spacer (Al_2O_3) of thickness 250 nm. We can thus characterise the nanoantennas using CL on the exact same substrate that will host the hybrid nanowire-nanoantenna structures.

The result of this CL characterisation is presented in figure 5.4 (a) in the form of a waterfall plot, as a function of the antenna length. The antenna spectra consist in two separate peaks: a broad and intense resonance that does not shift with antenna length, and a satellite resonance that shifts towards the longer wavelengths as the antenna length increases. The spectra can be fitted by two Gaussian functions (represented respectively by red dashes and blue dashed-dotted lines). The dispersion of the second resonance as a function of antenna length is marked by the blue line with squares.

LDOS imaging is performed with a $\sim$ 100 nm spectral integration bandwidth over each resonance, as shown by the shaded areas. It allows us to attribute unambiguously the red-shifting resonance to the dipolar mode of the antennas [figure 5.4 (b)]. The origin of the fixed resonance is more complex. As seen in figure 2.25 (b), previous studies on rectangular antennas have revealed the contribution of the transverse antenna mode, i.e. the dipolar resonance along the short antenna axis. However, this mode is quite weak and does not correspond to the main CL process. Contrary to the case of figure 2.25 (b), the LDOS image integrated over the whole fixed resonance showed no precise spatial structure at any antenna length [figure 5.4 (c)]. Moreover, similarly to the case of patch antennas as discussed in section 2.3.5, we observed this resonance at the same energy for any antenna shape (disks, squares and rectangles of various dimensions). Its energy is only determined by the Al_2O_3 spacer thickness, and we mainly attribute it to the scattering by the nanoantenna of the continuum of SPPs modes sustained by the Air/Al_2O_3/Au multilayer system, as in section 2.3.5. As discussed in section 2.3.6, the excitation of this continuum of SPPs represents a loss channel which is detrimental to our

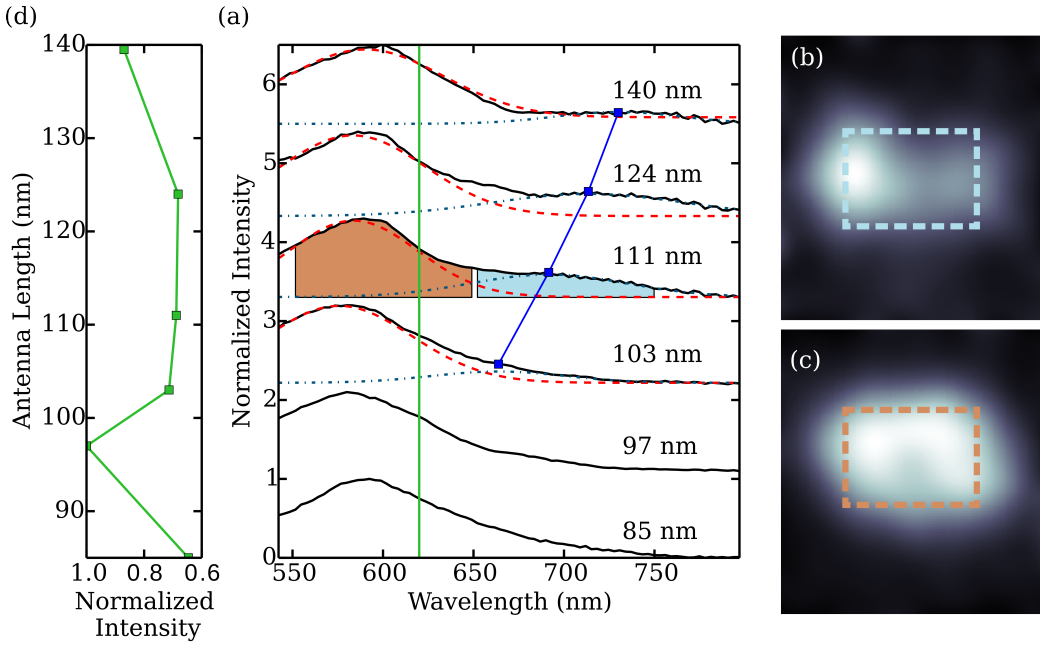

Figure 5.4 – Experimental determination of the antenna parameters using cathodoluminescence.
(a) Cathodoluminescence spectra of the rectangular Au antenna (width 70 nm and varying length L) on the dispersed NW substrate. The spectrum consists in two Gaussian resonance, fitted in dashed red and dashed-dotted blue lines. The antenna lengths are indicated on the right. The two resonances are analysed by LDOS imaging and attributed to the antenna dipolar mode (b) and to diffraction of SPP modes (c). The spectral integration bandwidth for the LDOS imaging is reported in shaded areas. (d) Cut profile at the QD wavelength of (a) showing an antenna resonant length around 97 nm.

fluorescence enhancement experiment. The fraction of the QD emission that couples to these SPP modes is not funnelled into the antenna dipolar mode and contributes mainly to Joule heating in the antenna, increasing the non-radiative part of the fluorescence process.

An intensity profile of the CL signal around the QD emission wavelength is presented in green solid line in figure 5.4 (a) and reported in panel (d). It shows an increase in CL intensity for antenna lengths around 97 nm. As can be seen in panel (a) by prolongation of the dispersion of the dipolar mode, this increase occurs at the length for which this modes appears on the side of the fixed resonance. This intensity profile also predicts an increase in the antenna scattering efficiency for longer antenna length (140 nm), which corresponds to the onset of the second antenna longitudinal mode (the quadrupolar mode), as shown e.g. in figure 5.2.

While designing the hybrid system, it is crucial to keep in mind that the antenna has to be placed in the near field of the NW, which has a very high refractive index ($n_{\mathrm{ZnTe}} \sim 3$). The increase in local refractive index is likely to cause a red-shift of the antenna LSPR wavelength as demonstrated in section 1.3, or conversely will require the fabrication of shorter antennas to compensate for this effect.

5.2 Fabrication of the coupled NW-nanoantenna system

As mentioned in the introduction, deterministic fabrication of nanoantennas in the vicinity of NWQDs requires a precise knowledge of the position of the QD inside the NW. As no morphological feature allow us to directly retrieve the dot position, none of the techniques previously reported in the literature allows for this localisation. Following previous work in our group ([DD10; Nog+13]) based on electron-beam lithography assisted with cathodoluminescence detection, we developed a two-step lithography process allowing us to align the electron beam lithography setup with selected NWs buried under the electro-sensitive resist. After dispersion and a full optical characterisation as detailed in section 3.3.1, we fabricate precise alignment marks around the NWs of interest on the pre-patterned substrate using electron beam lithography. The SEM is coarsely aligned with respect to the already present ovoid marks. The precise marks consists in two shifted squares as shown in black dashed lines in figure 5.5 (a). The sample is then mounted inside the CL setup and cooled down at cryogenic temperature. A precise SEM image and a monochromatic CL image at the QD emission wavelength are acquired after alignment of the electron beam onto the precise alignment marks, resulting in figure 5.5 (b)-(c). The CL signal is then fitted by a 2D Gaussian profile from which we extract the QD position, shown by the red cross in panel (b). This provides us with the absolute QD position within the frame defined by the precise alignment marks. The antennas are then fabricated using the same lithography process. Before exposure of the resist to define the antenna structures, a final alignment step onto the fine alignment marks is performed, exposing them as well - this explains the fact that they are covered with gold in frame (a) after the whole fabrication process. Examples of our realisations are presented in figure 5.5 (d)-(e). The fabrication process and the alignment method is detailed further in appendix B, where we also show the evolution of the process for the new Nanobeam nB5 [Nan] lithography system.

The antennas have a fixed width of 70 nm and a length L ranging from 50 to 140 nm. This length range is based on the previous CL results for isolated antennas, and accounts for the expected shift of the LSPR due to the presence of the high refractive index NW in the antenna near field. This red shift requires to fabricate shorter antennas than the ones characterised in section 5.1. The antenna side of length L is fabricated parallel to the measured polarisation direction of the QD emission. Despite careful previous calibration of our lithography process, small deviations in antenna dimensions are measured, owing to the irregular profile of the resist around the NW. We targeted a point contact between the antenna and the NW. Our SEM measurement revealed an average gap of 12 ± 50 nm, which means that some antennas are slightly far from the NW side [as in figure 5.5 (d)], while other lie on top of the NW, and hence directly above the QD. In term of direct QD-antenna distance, this means that the antennas are located 50 to 110 nm away from the QD. As the NW radius is at least 25 nm at the QD position, and the QD radius is around 10 nm, the minimum optical distance between the QD and the antenna is $\sim$50 nm. Hence, a significant fraction of the optical distance between the QD and the antenna is due to the core and shell thicknesses. The remaining air gap between the antenna and the QD is thus expected to play a smaller role in the coupling between the two structures. This positioning error has several origins. First, the final alignment procedure has a typical error of 20 nm, further degraded in our case by the poor contrast in the SEM images of the alignment marks under the resist. Electrostatic, thermal and mechanical drifts in the

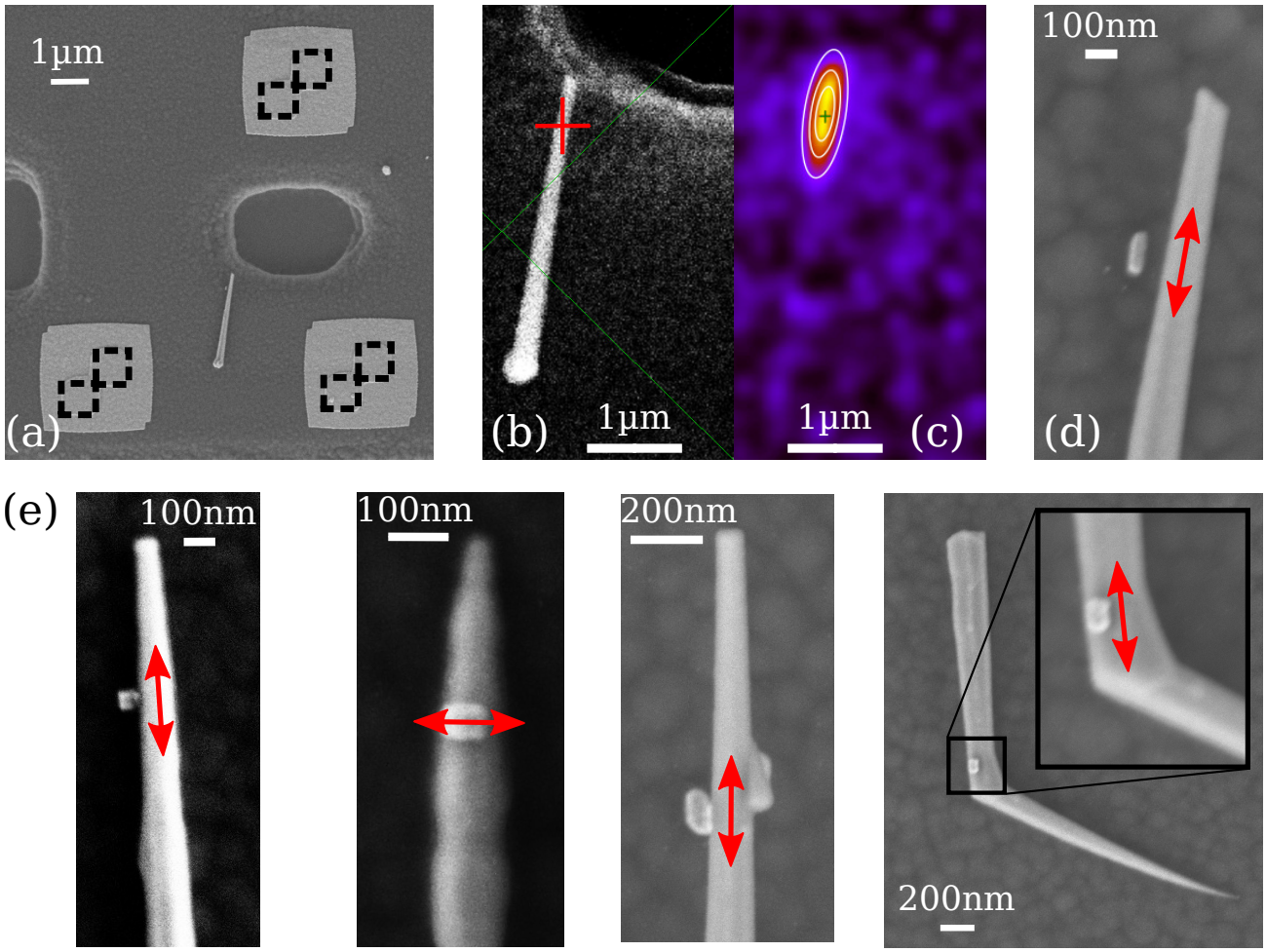

Figure 5.5 – Deterministic antenna fabrication.
(a) Large field SEM image of an isolated NW with the coarse alignment marks (ovoid hole), and the fine alignment marks, emphasised by black dashed lines as they have been exposed in the final alignment step and are hardly visible under the final Au layer. (b) Higher magnification SEM image of the NW after alignment with respect to the fine alignment marks. (c) Corresponding monochromatic CL image at the QD emission wavelength. The red cross in (b) corresponds to the green cross in (c) and indicates the center of the 2D Gaussian fit of the CL profile. White lines are contour lines of the fit. (d) Resulting coupled NW-antenna system. The resulting NW-antenna gap is 60 nm. (e) Several examples of hybrid systems, where the antenna is in close contact or on top of the NWQD. Note that in the third panel, the antenna is the rectangle on the left side of the NW, the one on the right side being a small excrescence. The red arrows indicate the measured polarisation direction of the emitted light.

successive low temperature CL and SEM images acquisition lead to an error of around 30 nm.

5.3 Photoluminescence of the NW-antenna system

5.3.1 Experimental results

The coupled NW-antenna systems are characterised using the same procedure as the statistical study of Te-based NWs (section 3.3.1): we perform µPL, TRPL and Fourier imaging at the QD emission wavelength using the frequency doubled, ps-pulsed excitation at 447 nm from the Ti:Saph laser.

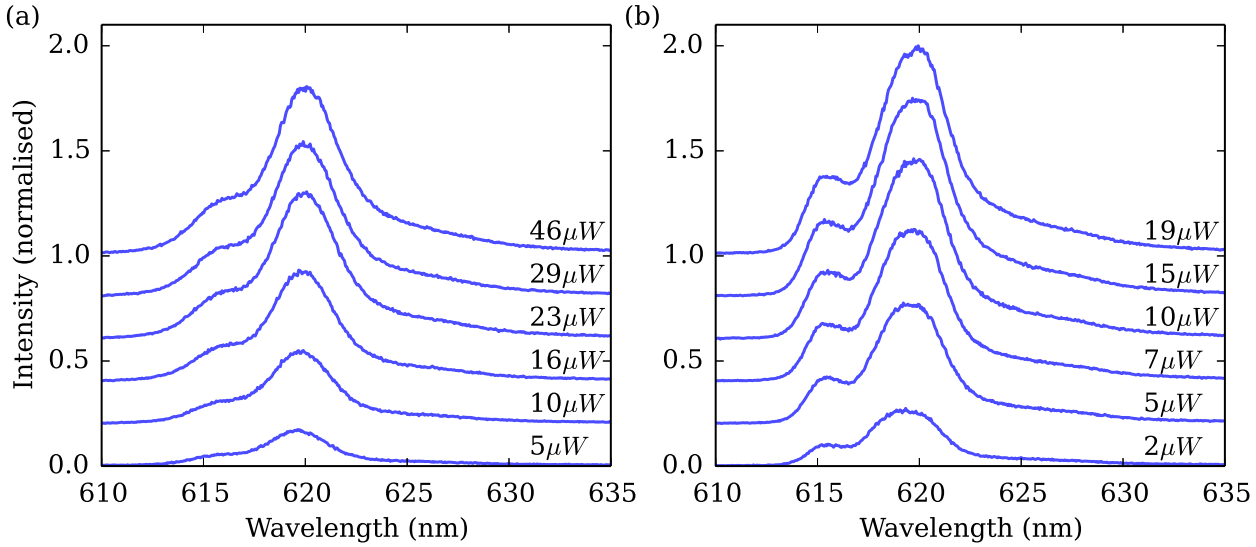

Figure 5.6 – Comparison of µPL before and after antenna fabrication.
Comparison of the µPL properties of the same NWQD before (a) and after (b) antenna fabrication. We can see that the process does not degrade the spectrum from the QD, as the same features are found at the same energy in both panels. The excitation power is indicated on each curve. All the spectra are normalised to the same value, allowing relative amplitude comparison.

Figure 5.6 shows the measurement of the QD signal as a function of the excitation power P_{exc} before (a) and after (b) antenna fabrication. We can see that the process does not change the µPL properties of the emitters. All the spectra are normalised to the same intensity value. The same spectral features are found before and after antenna fabrication: the exciton emission is still present at the same energy, and so is the small (yet unattributed) second peak at 615 nm. We can see from the pumping power used (indicated above each curve) that a stronger excitation power was necessary to saturate the transition without the antenna.

The QD emission spectrum is fitted by a Gaussian function which is integrated over the whole excitonic transition linewidth to determine the total intensity emitted by the structure. The result is shown in figure 5.7 (a) where we compare the data before and after antenna fabrication on the same QD. The total PL intensity first increases with P_{exc}, and then saturates because of

the complete occupation of the discrete excitonic states inside the QD. At any given excitation power, one clearly sees an increase in the collected signal in presence of the antenna. Reference measurements on other NWQDs present on the same substrate, which have experienced the same process but do not have an antenna in their vicinity, show no change in their emission properties. The integrated intensity emitted by the QD at saturation is denoted I_s, and the ratio I_s/I_{s0} is reported in figure 5.7 (b), where the subscript 0 refers to before antenna fabrication. In order to analyse the µPL efficiency at very low pumping power, we also extract the slope at the origin g of the saturation curves as in 5.7 (a). The ratio g/g_0 before and after antenna fabrication is plotted as a function of antenna length in figure 5.7 (c). The arrow in both panels refers to the antenna whose saturation curve is presented in (a). These curves are to be compared with the CL intensity profile at the QD emission wavelength of 620 nm in 5.4 (d). Both ratios evidence an increased efficiency of the system after antenna fabrication for small antenna lengths (i.e. below 80 nm), and the onset of a second increase in efficiency for lengths above 120 nm. The fact that the enhancements occur for smaller antenna lengths than in figure 5.4 (d) is due to the red shift of the SPR because of the presence of the high refractive index NW, as detailed in section 5.1.

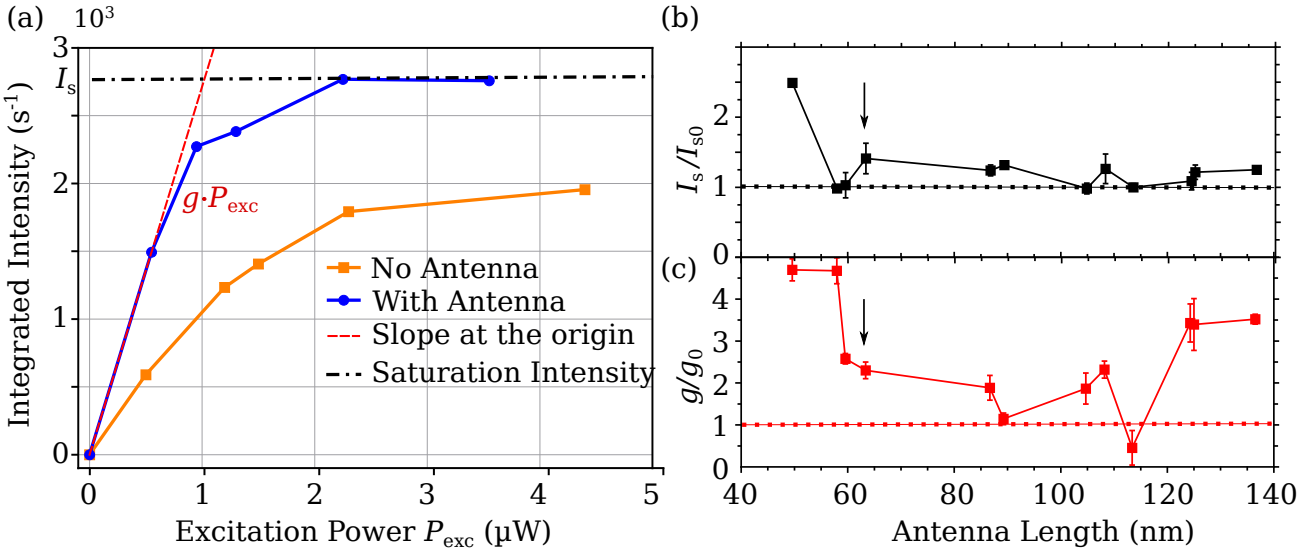

Figure 5.7 – µPL of the coupled NW-antenna structures.
(a) Power-dependent µPL of a same NWQD before and after antenna fabrication, evidencing the parameters I_s and g and their change due to coupling to the antenna. (b) Ratio I_s/I_{s0} as a function of antenna length. Error bars are calculated from the signal to noise ratio of the intensity measurement. (c) Ratio g/g_0 as a function of antenna length. Error bars are calculated by comparing the slope at the origin with a linear fit of the first two data points and the origin. The arrow in (b) and (c) refers to the NWQD shown in (a). Dashed lines indicate the position of a unity ratio.

5.3.2 Discussion on the fluorescence enhancement of the NWQDs

Previous studies have revealed a modification of the luminescence collection because of redirection of the light by the nanoantennas [Cur+10; Nog+13; Ram+15]. This is not the case in our experiment, as demonstrated in figure 5.8 (b)-(c) which shows a typical Fourier image of

the QD luminescence before and after antenna fabrication respectively, evidencing no change in radiation diagram. This is not surprising considering the selected design of our system. Usually, directive emission of light relies on interference phenomena and requires substantially out-of-phase signals, or high order plasmonic modes. In Yagi-Uda antennas, this is achieved by placing scattering elements with comparable scattering efficiencies and out-of-phase emission to achieve selective interference [Cur+10; Ram+15] in a given direction. Here, our antenna consists in a single element with a small scattering efficiency, supporting a dipolar mode that radiates orthogonally to the surface. As the NW-antenna distance is small, there is no significant accumulated phase shift between the light emitted from the NW and the one scattered by the antenna. We also engineered the substrate to increase the light redirection normal to the sample surface, so the reflected light has to be in phase with the direct emission from the NW at the sample surface. In addition, the antenna scattering efficiency is smaller than the emission from the QD, so a possible interference effect between the scattered and the emitted light would be very weak, resulting in no additional directional scattering.

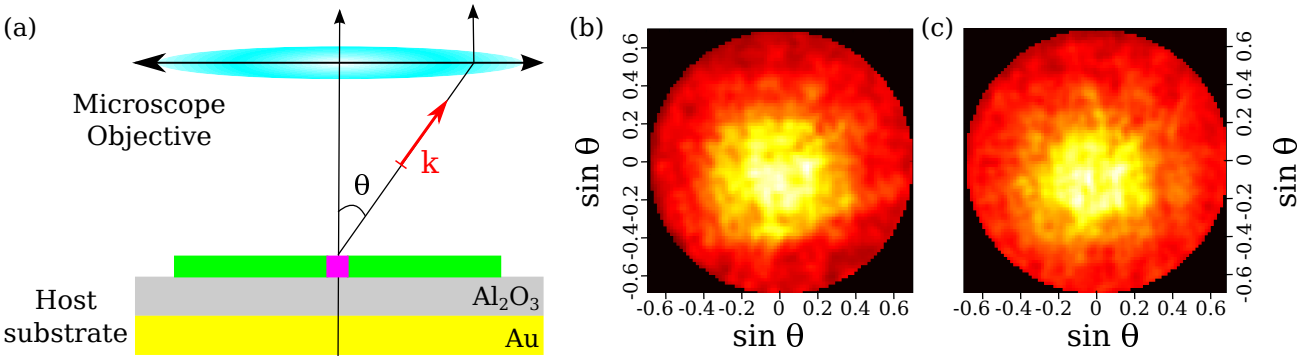

Figure 5.8 – Fourier measurements before and after antenna fabrication.
(a) Reminder of the Fourier imaging setup. The NW lies on the mirror substrate. A photon emitted in a direction (θ, φ) is projected on a position $(\sin\theta, \varphi)$. (b) and (c) Radiation patterns of a NWQD before and after antenna fabrication, evidencing no change in the fraction of collected light α_{coll}.

Aside from a better collection of the emitted light, a higher µPL efficiency is the result of an increased radiative decay rate of the emitter. As already mentioned, it is known as the Purcell effect and results from the increased local density of optical states close to the emitter. It is classically demonstrated by measuring the lifetime of the emitter before and after antenna fabrication. In the case of a perfectly radiative emitter, this is traditionally translated into the well known relation:

$$\frac{\gamma}{\gamma_0} = \frac{P}{P_0} \tag{5.1}$$

where γ is the emitter decay rate, P the total radiated power (i.e. integrated in a closed surface around the emitter), and the subscript 0 denotes the quantity before antenna fabrication. The ratio of measured exciton decay rate before and after antenna fabrication γ/γ_0 is plotted as a function of antenna length in figure 5.9. For equation (5.1) to hold means that this curve should be exactly the same as in figure 5.7 (b). This is clearly not the case, as we observe an average ratio of γ/γ_0 of 0.94 with a standard deviation of ± 0.2, which does not appear to be correlated

with the ratio I_s/I_{s0}. One of the reasons for this is that our emitters are far from being perfectly radiative structures. As already mentioned in section 3.3.1, we expect non-radiative recombinations to play a major role in the exciton dynamics of these NWQDs. Furthermore, the high dispersion in decay rates and the fact that we observe some ratios of $\gamma/\gamma_0 \leq 1$ lead us to believe that the small band offset between CdMnTe and ZnTe results in a poor hole confinement that can change dramatically from one NW to another. All this added makes equation (5.1) not valid any more.

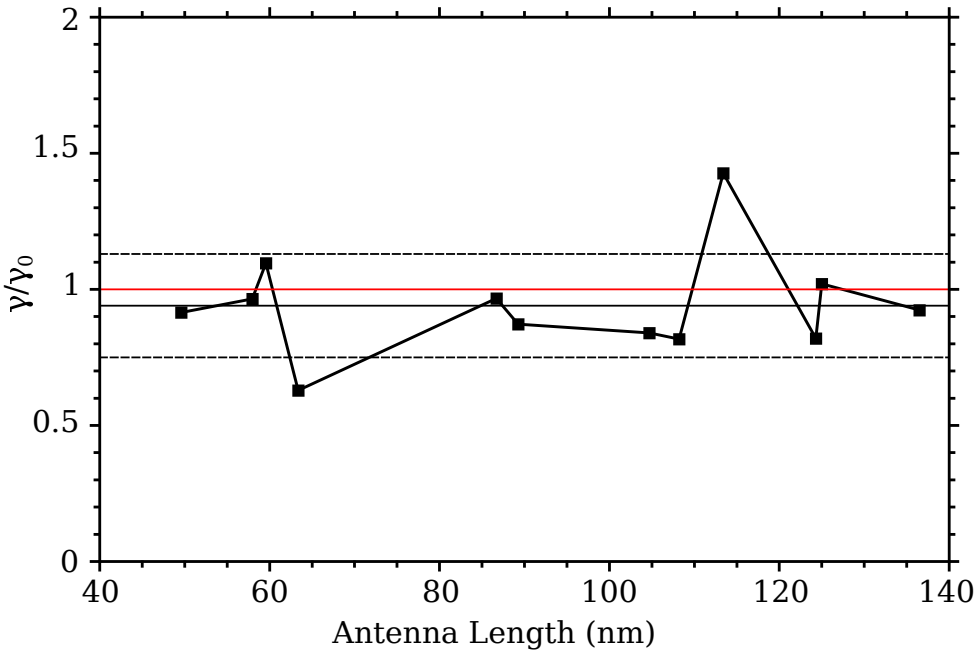

Figure 5.9 – TRPL measurements as a function of antenna length.
Ratio of decay rates γ/γ_0 as a function of antenna length. The mean value is 0.94 (black solid lines) with a standard deviation of ±0.2 (black dashed lines). The red solid line indicates the position of the unity ratio.

A better description comes from the parameters I_s and g that were introduced previously. We start by considering I_s. Assuming that we only detect the excitonic transition, and considering that the experiment is carried out under pulsed excitation, we have:

$$I_s = f\frac{\gamma_r}{\gamma_r + \gamma_{nr}}\alpha_{coll} = f\eta_Q\alpha_{coll} \tag{5.2}$$

where f is the laser repetition rate (80 MHz), α_{coll} is the fraction of emitted light collected by the microscope objective, and we recall from section 3.2.1 that the exciton lifetime is given by $\tau = 1/\gamma = 1/(\gamma_r + \gamma_{nr})$, where γ_r is the radiative decay rate and γ_{nr} the non-radiative decay rate. η_Q is the emitter's quantum yield. Under pulsed excitation with a high enough pumping power, i.e. at saturation, we can assume that each pump pulse creates one exciton inside the QD, saturating the transition. The value of I_s is thus directly proportional to the probability for this exciton to recombine radiatively, which is given by η_Q. We have shown that the light collection is not significantly enhanced by coupling with the antenna, α_{coll} is the same before

and after antenna fabrication (see figure 5.8), and f is kept constant. Consequently, *a change in I_s directly reflects a change in the emitter's quantum yield*. This change is attributed to the resonant coupling with the nanoantenna. As predicted in section 5.1 the value for this resonant length is lower than for the isolated antennas in figure 5.4 (d). This is thus a direct evidence of radiative coupling between the antenna and the nanowire quantum dot. The quantum yield enhancement is modest as the coupling geometry is far from optimal, and the QD emission wavelength lies very close to the main absorption peak of the antenna structure.

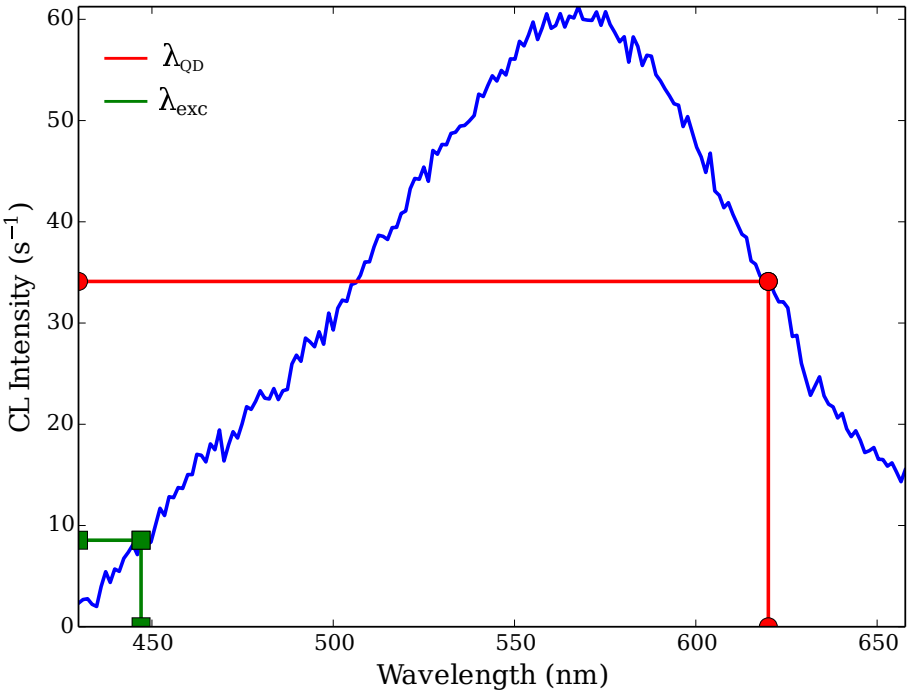

Figure 5.10 – CL spectrum of a single antenna.
CL spectrum of a single antenna around the fixed resonance evidenced in figure 5.4 (a), comparing the LDOS at the excitation wavelength λ_{exc} (green) and at the emission wavelength λ_{QD} (red). It evidences a non-zero LDOS at the excitation wavelength, inducing an increased absorption inside the NW.

This radiative coupling is not the only mechanism leading to the increased µPL observed from the hybrid structure. Figure 5.10 shows the CL spectrum of one of the antennas, with both the excitation (green) and the emission (red) wavelength reported on the graph. It shows even if the CL intensity is smaller at the excitation wavelength, there is still a remaining increase in LDOS due to the presence of the antenna at this wavelength. It means that the exciting field produced by the focused laser beam is also locally enhanced by the presence of the antenna. The main contribution to this LDOS comes from the fixed resonance in figure 5.4 (a) and does not vary with antenna length. The effect of the enhancement of the exciting field can be retrieved by analysing the slope at the origin g. In the limit of very low excitation:

$$g = \eta_Q \alpha_{abs} \alpha_{coll} \tag{5.3}$$

where α_{abs} is the fraction of exciting power absorbed in the NW. A direct evaluation of α_{abs} is challenging, but combining equations (5.2) and (5.3) shows that the ratio $(g/g_0)/(I_{\mathrm{s}}/I_{\mathrm{s0}})$ directly gives the change in absorption. The comparison of figures 5.7 (b) and (c) shows that the absorption inside the NW is enhanced by a factor 2.2 ± 1.1 over the whole antenna length range. As an example, this means that the fourfold enhancement of g/g_0 observed in figure 5.7 (c) for low power µPL experiments on the NW-antenna system with the smallest antenna length comes in equal parts from a twofold enhancement of the absorption of the exciting field and a twofold quantum yield enhancement.

Finally, the change in I_{s} revealed an increased quantum yield of the hybrid structure, but the time-resolved measurements showed no change in total decay rate (figure 5.9, implying that:

$$\frac{\tau}{\tau_0} = \frac{\gamma_{\mathrm{r0}} + \gamma_{\mathrm{nr0}}}{\gamma_{\mathrm{r}} + \gamma_{\mathrm{nr}}} \approx 1 \tag{5.4}$$

Rewriting equation (5.2) as $I_{\mathrm{s}} = f\gamma_{\mathrm{r}}\tau\alpha_{\mathrm{coll}}$ yields:

$$\frac{I_{\mathrm{s}}}{I_{\mathrm{s0}}} = \frac{f\gamma_{\mathrm{r}}\tau\alpha_{\mathrm{coll}}}{f\gamma_{\mathrm{r0}}\tau_0\alpha_{\mathrm{coll0}}} \tag{5.5}$$

As mentioned previously, f and α_{coll} remain unchanged, leading to:

$$\frac{I_{\mathrm{s}}}{I_{\mathrm{s0}}} = \frac{\gamma_{\mathrm{r}}\tau}{\gamma_{\mathrm{r0}}\tau_0} \approx \frac{\gamma_{\mathrm{r}}}{\gamma_{\mathrm{r0}}} > 1 \tag{5.6}$$

The fact that the measured decay rate is the same before and after antenna fabrication confirms that the total decay rate is dominated by the non-radiative term γ_{nr}, and that the increase in quantum yield is essentially due to an increase of the radiative term γ_{r}.

5.4 Conclusion

In this chapter we have demonstrated deterministic coupling between single semiconducting nanowire quantum dots and plasmonic nanoantennas. It relies on a newly developed method combining CL imaging and a two-steps electron beam lithography process. We achieved a precision of 50 nm, but it can be improved. This experiment has been done using the Zeiss SEM (LEO, [Zei]) lithography setup. The newly acquired Nanobeam nB5 setup [Nan] allows for a much more precise and fully automated realignment as well as more precision in the lithography process itself, which will lead to a better final precision and opens up the possibility of fabrication of a larger number of structures, improving both our success rate and statistical analysis.

Our method has the advantage of relying only on the luminescence of the emitters for their precise localization. It also grants full characterization of individual nanoemitters and antennas. CL spectroscopy and LDOS imaging of individual nanoantennas is demonstrated as a powerful technique to experimentally determine antennas parameters for the fabrication of coupled plasmonic-semiconductor emitters. Furthermore, we demonstrate two effects of the nanoantennas on the QD: an absorption enhancement of a factor 2, and a light emission enhancement due to radiative coupling to the antenna up to a factor 2.5, in a spectral region where plasmonic

losses are an important non-radiative recombination channel, extending the control of light emission from semiconducting nanostructures towards the visible spectral region. The effect could be greatly increased for a smaller QD-antenna distance, i.e. using a thinner NW shell. The implementation of this method is a crucial step towards fabricating more complex and versatile coupled structures. It can be applied to all kind of nanoemitters, aiming at controlling their optical properties like their polarization response [Kuk+14; Cas+15] or emission diagram [Cur+10; Bel+13].

Conclusions and perspectives

Conclusions

We have demonstrated the deterministic radiative coupling between plasmonic nanoantennas and semiconducting nanowire quantum dots. With a balanced effect of both absorption and fluorescence rate enhancement, the coupling results in an improved light emission from the QD. An efficient coupling between the two elements requires spectral, spatial and polarisation matching of the antenna mode and of the QD emission. To achieve this, we developed an original combination of techniques to fully characterise NWQDs and plasmonic nanoantennas. We have also shown the efficiency of our novel CL-based two step lithography technique to fabricate at will nanoantennas in the near-field of nano objects.

We used cathodoluminescence to investigate the linear optical properties of plasmonic nanoantennas. We have shown that in realistic configurations including a bulk substrate, especially in the case of Insulator-Metal substrates, the interaction between the antenna and the substrate leads to a complicated interpretation of the results. We extensively discussed the CL properties of plasmonic patch antennas, showing that their CL response is due not only to the discrete spectrum of local surface plasmon modes they support, but also to the continuum of surface plasmon polaritons supported by the layered structure, and finally to the interband transitions inside the metallic materials.

While we still lack of a comprehensive theory or simulation procedure for the CL response of such systems, we experimentally showed that several degrees of freedom can be used to tune the properties of these patch antennas. The role of the antenna size, spacing layer thickness and materials have been investigated, demonstrating that we can independently tune the dispersion relation of the patch modes and their position by changing respectively the spacer thickness and the antenna size. We have also shown that replacing Au layers with Al layers allows one to create patch antennas operating in the blue spectral region, which is inaccessible to Au antennas. We have shown that we can image the radiative part of the LDOS along the electron beam trajectory, allowing a spatial characterisation of the antenna modes. This work shows the potential of CL for plasmonic antenna characterisation beyond the diffraction limit.

We have also performed extensive optical characterisation work on semiconducting nanowire quantum dots, which represent a promising but emerging alternative to their self-assembled counterparts. We have shown that the determination of their optical properties necessarily requires the knowledge of their electronic properties as well.

We provided a microphotoluminescence study on a statistical set of Se-based NWQDs, re-

vealing an exciton behaviour unconventional with respect to the previous studies of Gregory Sallen and Samir Bounouar in our group [Sal+09; Bou+12c; Bou+12a; Bou+12b]. While the final explanation of this behaviour is still pending, we think it strongly hints towards the interaction of the carriers with an excited hole state. We have also shown single photon emission up to 200 K, and used the convenient nanowire geometry to demonstrate a photonic approach of probing the dipole orientation inside the dot and enhancing the extraction efficiency of the QD fluorescence by fabricating a waveguide structure in the form of a shell around the wire.

We also studied Te-based NWQDs doped with Mn atoms. The results on a statistical set of these emitters were clarified by the study of a single nanowire standing on the growth substrate. We evidenced the effect of the strain produced by the shell on the core and dot luminescence, and provided a complete model of the valence band structure of this emitter. We used polarisation-resolved Fourier microscopy to unambiguously reveal the hole character of the exciton in both the NW core and QD and study its mixing with the other holes states. Furthermore, we evidenced for the first time a light hole ground state character of the exciton inside the QD. These findings were supported by additional magneto-optical spectroscopy performed by Alberto Artioli [Art16]. All these effects combined with the measurement of the exciton lifetime, emission polarisation and radiation pattern allowed us to give a qualitative physical insight on the origin of the apparent dispersion in the results. A new set of study is now under way for these Te-based systems, and will from now on benefit from a stronger numerical support including atomistic simulations with the aim of demonstrating the use of strain engineering inside nanowire structures to control the properties of the embedded QD.

Perspectives

Despite our experimental effort, the demonstrated coupling between the Te-based NWQDs and the antennas remains modest for several reasons:

- The exciton emission wavelength is close to the Au interband absorption band, strongly degrading the ability of the antenna to promote the radiative recombination rate over Joule induced losses,

- The coupling geometry is far from optimal, as we would rather find a geometry in which the "effective" exciton dipole is aligned with the antenna and orthogonal to its end facet,

- The distance between the antenna and the QD is too large, owing mainly to the thickness of the NW core and shell, but also to our imprecision in fabrication.

Nevertheless, this provides a proof-of-principle experiment on the fabrication of such hybrid structures. In the light of the conclusions of chapter 4 for Te-based NWQDs, we can turn back to the Se-based NWQDs. In the case of Se-based NWQDs, the band configuration is a bit more favourable than for the Te-based ones, as ref. [Hin+14] reports values of the conduction and valence band offsets of $V^{c}_{off} = 900$ meV and $V^{v}_{off} = 110$ meV respectively. Contrary to the Te-based QDs, this larger band offset allows for higher energy levels of the trap to be confined inside the dot, as we expect from the thermal behaviour of the exciton emission presented in section 3.3.2.

In terms of QD shape we expect to have a QD length over diameter ratio L/D between 0.5 and 1. As in the case of the Te-based NWQDs, the QD experiences a compressive strain from the core due to the lattice mismatch of the core and QD. Therefore, a qualitative comparison with figure 4.7 shows that in the Se-based QDs the hole ground state is expected to be of heavy hole character. This is coherent with polarisation measurements made by Thibault Cremel (not presented here), showing an exciton luminescence polarised in the direction orthogonal to the NW axis.

Keeping in mind all the aforementioned points, the natural extension of this work would be to try and couple Se-based NWQDs to Al patch plamonic antennas:

- With an exciton emission wavelength around 550 nm, the Se-based NWQDs could efficiently be coupled to Al antennas which do not feature any interband losses in this spectral region,
- The thin shell around these NWs make them better suited to couple to plasmonic antennas as the near-field of the dot is more easily accessible, and they can easily be inserted in the spacing layer of a patch antenna,
- As reported in chapter 3 we expect a strong heavy hole character from these QDs, whose emission is polarised orthogonal to the NW axis. This is optimal for a coupling to the patch antenna modes, which require a vertically polarised emission. Additionally, we expect the coupling to the patch antenna mode to be stronger than in a simple sideways coupling as done for the Te-based QDs.

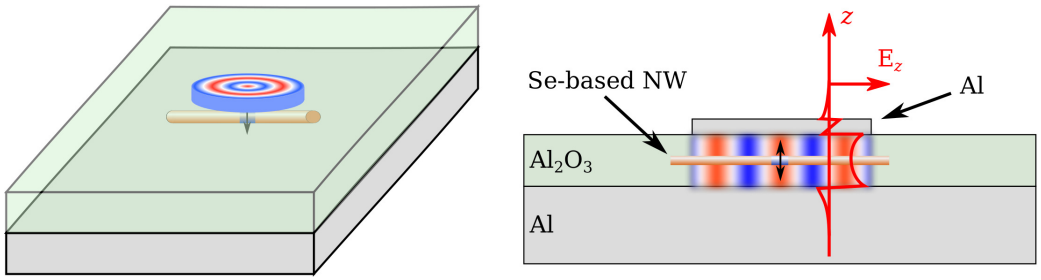

Figure 5.11 – Al circular patch antennas for Se-based NWQDs.
Sketch of the possible configuration of a circular patch antenna for fluorescence enhancement of CdSe QDs inserted in ZnSe NWs. As these NWs are thin ($\approx$ 20 nm diameter), they can be inserted in the spacing layer of a patch antenna. The heavy-hole character of the exciton favours polarisations orthogonal to the NW, in and out of the plane of the substrate. Usually, the out of plane contribution is screened by the substrate, but in this configuration it can efficiently excite a patch mode and couple to free space radiation.

Room temperature single photon emission has already been demonstrated using Se-based NWQDs, and we have shown that the ones we studied provided single photon emission up to 200 K. Therefore, the coupled Se-based NWQD - Al patch antenna system has the potential to be a fast single photon emitter at room temperature.

Finally, our lithography process allows for the deterministic fabrication of structures around arbitrary objects and is not limited to NWQDs. As we can rely on SEM or CL images, it can be applied to any kind of nano-object, whether they emit fluorescence or not. In this context, and with the improved accuracy of the new lithography system, we started to fabricate hybrid non-linear nano-structures based on aluminium antennas an non-linear nanocrystals such as potassium titanyl phosphate (KTP).

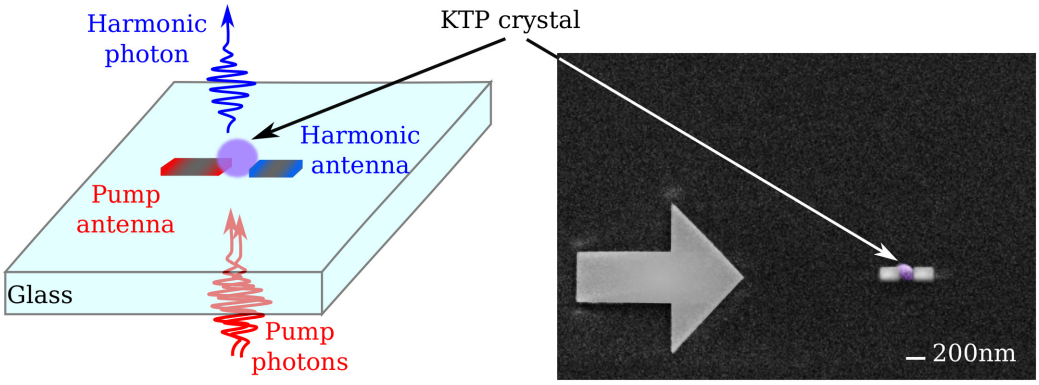

Figure 5.12 – Hybrid structures for non-linear nano-optics.
Left: sketch of a hybrid non-linear nanodevice composed of a KTP crystal and two Al antennas on a glass substrate for second harmonic generation. The antennas can be designed to be resonant at both pump and harmonic wavelengths, or we can use an asymmetric configuration with e.g. one antenna enhancing the pump signal, and the second antenna enhancing the harmonic signal. Right: False colour SEM image of a test realisation of a KTP crystal coupled with two rectangular Al antennas. The same procedure as in chapter 5 has been used, with a simple SEM image for alignment instead of the superimposed CL+SEM image.

These hybrid structures belong in the much larger field of non-linear nano-optics. In a collaboration with Guillaume Bachelier, we fabricate nanostructures to observe non-linear phenomena such as second harmonic generation at the single nanoparticle level. A first step towards these structures has been taken with our recent demonstration of the double enhancement of second harmonic generation in aluminium nanoantennas by fabricating antennas resonant at both the fundamental and harmonic frequency. Non-linear spectroscopy of single nanocrystals is under way thanks to Guillaume Bachelier and his students, and we are starting test fabrication steps, as demonstrated in figure 5.12. At this moment the crystals are $\sim$ 200 nm large, and the fabrication of perfectly positioned antennas in their vicinity is possible thanks to the new lithography setup. However the process has to be performed on glass substrates, which is insulating, and will potentially prove more challenging on smaller objects. This last perspective is by far the most exciting as it opens up towards the new domain of non-linear nano-plasmonics and nano-optics, which is yet largely unexplored.

Conclusion en Français

Durant ce travail de thèse, nous avons démontré la fabrication déterministe d'antennes plasmoniques couplées radiativement à des boîtes quantiques insérées dans des nanofils à semiconducteur. Une augmentation de l'absorption du faisceau excitateur et une accélération du taux de désexcitation radiative ont été établies comme responsable de l'exaltation des propriétés optiques de la boîte. L'efficacité du couplage dépend du recouvrement spectral et spatial entre l'émission spontanée de la boîte et le mode de plasmon supporté par l'antenne, ainsi que de l'orientation de la polarisation des deux champs. Nous avons donc mis au point une combinaison de techniques permettant de caractériser les propriétés spectrales et spatiales des résonances supportées par les antennes plasmoniques, et les propriétés spectrales, spatiales et temporelles de l'émission spontanée de boîtes quantiques insérées dans des nanofils. Pour atteindre un tel couplage, nous avons mis au point une technique de fabrication originale basée sur le repérage de la boîte grâce à la cathodoluminescence.

La caractérisation des antennes est faite par cathodoluminescence. On a montré que, dans une configuration expérimentale réaliste incluant un substrat métallique, l'interaction entre l'antenne et le substrat complique l'interprétation des résultats de cathodoluminescence. Les propriétés de cathodoluminescence d'antennes patchs plasmoniques ont été exposées, en on a montré qu'elles ne sont pas seulement reliées au nombre discret de modes de plasmons qu'elles supportent. Bien qu'une interprétation complète des résultats ne soit pas encore achevée, nous avons démontré l'existence de plusieurs degrés de liberté pour modifier les propriétés de ces antennes, en changeant notamment leur taille et l'épaisseur de la couche d'isolant les séparant du plan de masse. Nous avons également également démontré la fabrication d'antennes patchs opérant sur tout le spectre visible. Enfin, nous avons montré l'utilisation de la cathodoluminescence pour imager la partie radiative de la densité locale d'états électromagnétiques au voisinage des antennes, ce qui démontre l'intérêt de la cathodoluminescence comme technique de caractérisation optique permettant de descendre sous la limite de diffraction.

Nous avons également effectué un travail de caractérisation de plusieurs boîtes quantiques insérées dans des nanofils à semiconducteurs. Dans le cas de fils basés Se, nous avons révélé un comportement de l'émission spontanée en fonction de la température inattendu au vu des études portant sur des échantillons précédents. Bien que l'explication définitive soit encore en cours d'élaboration, un modèle se basant sur l'existence d'un exciton noir formé par le premier état excité de trou dans la boîte est proposé. Nous avons également démontré une émission de photons uniques jusqu'à une température de 200 K*. De plus, nous avons montré une stratégie diélectrique de modification d'émission de la boîte en déposant une coquille d'oxyde autour du fil. L'accélération du déclin de l'exciton est accompagnée d'une augmentation de la fluorescence mesurée, confirmant une exaltation des propriétés radiatives de la boîte. Dans le cas des fils basés*

Te, une modélisation des effets de confinement et de contrainte sur la bande de valence dans de cœur et la boîte accompagnée de mesures de microscopie de Fourier résolue en température et de spectroscopie magnéto-optique nous a permis de déterminer les propriétés électroniques dans ces parties du système. De façon remarquable, on a montré que la contrainte induit la promotion d'un trou léger dans la boîte. A la lumière de ces résultats, nous avons proposé une interprétation sur la dispersion de l'ensemble des mesures effectuées sur un grand nombre de fils du même échantillon.

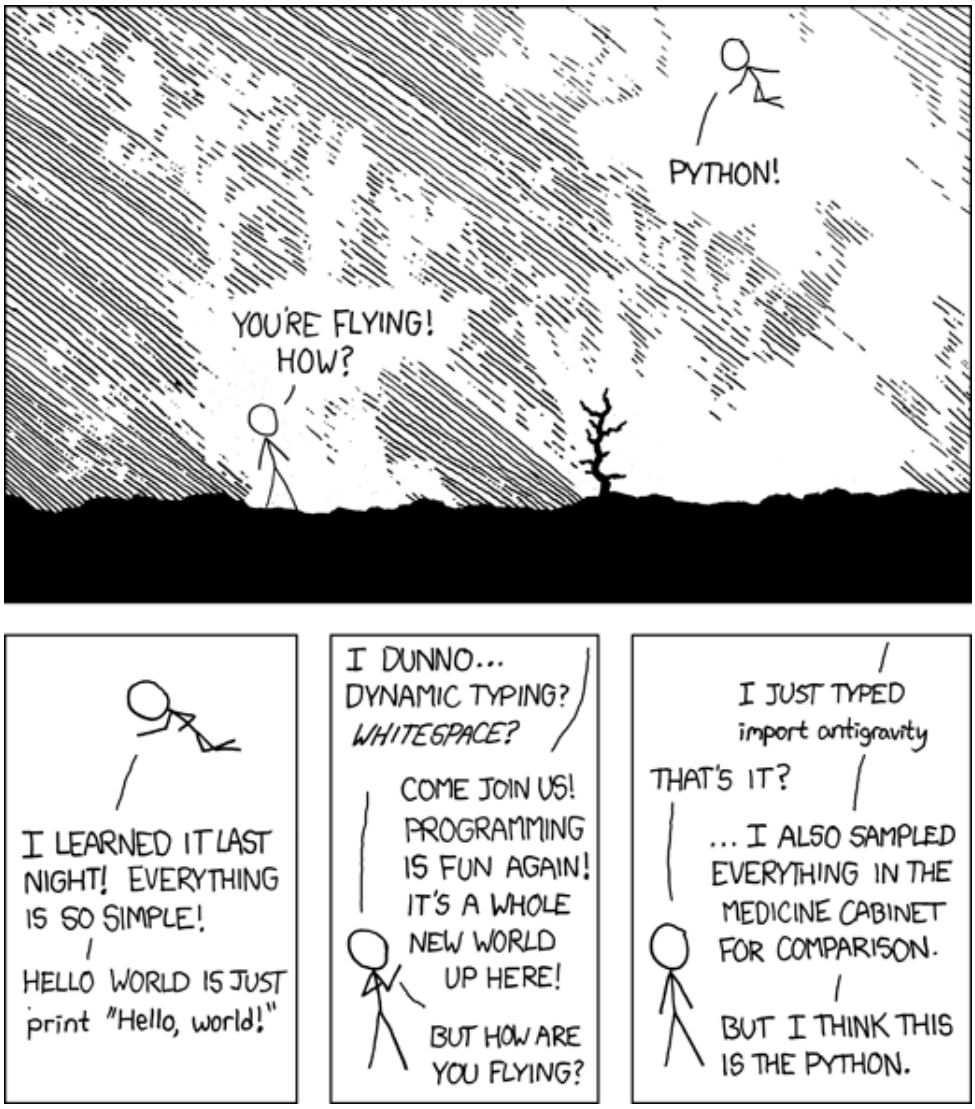

Credits to [XKC]

Appendix A

Cathodoluminescence LDOS imaging: numerical treatment

In this appendix, we detail the numerical procedure we used to process the energy-selective CL images for LDOS imaging, which was briefly discussed in section 2.3.4.

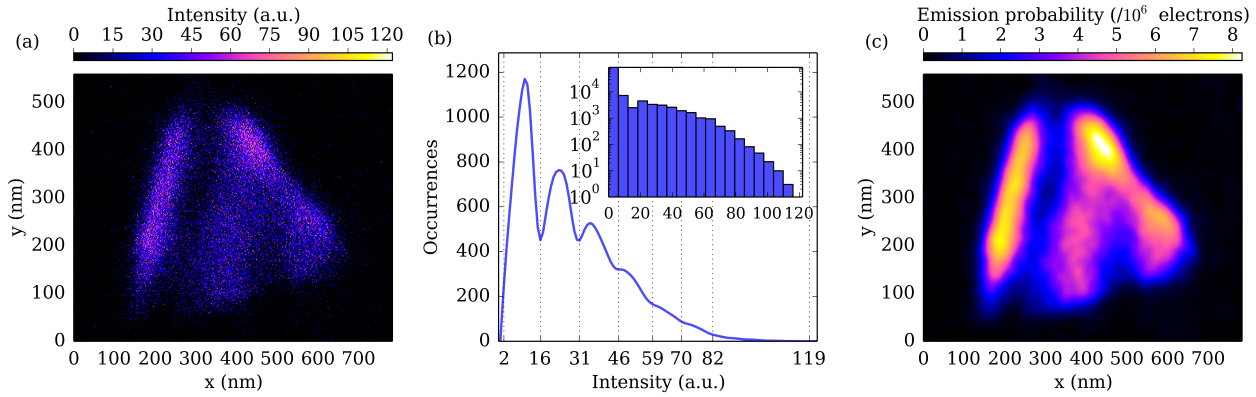

Figure A.1 – Numerical treatment of the LDOS images.
(a) Raw CL image of an triangular Au antenna on Si/SiO_2, as directly obtained from the CL setup. (b) Digitisation of the CL signal after smoothing by a Hanning window. Inset: raw histogram from (a) showing the peak for zero signal which is one order of magnitude larger than the non-zero ones. (c) Filtered CL image using a bi-dimensional Gaussian filter of 10 nm. The emission probability in photon per incident electron is deduced from the beam current, dwell time and pixel size.

The antenna CL signal is filtered in energy using the exit slit of the spectrometer, which can be up to 7 mm wide, corresponding to a ∼80 nm spectral bandwidth using the 150gr/mm grating. It is sent to an avalanche photodiode connected to an electronic pulse generator. The output of this pulse generator is connected to the external input of the SEM. Hence, instead of visualising the usual scattered electron signal from the SEM, each electron beam position displays the signal from the pulse generator. We set the pulse duration to be smaller than the electron dwell time on a given pixel, so that several pulse can be detected on a given position, enabling photon counting. A typical result image is presented in figure A.1 (a) in the case of a triangular antenna on a Si/SiO_2 substrate. The image is treated using a home made python

script based on the `scikit-image` module [Sci]. We first compute the histogram of the image intensity values, and remove the first contribution which corresponds to a zero signal. The rest of the histogram thus corresponds to non-zero intensity values. It is smoothed using a Hanning window of $\sim$10 bins, and digitised as shown in figure A.1 (b). Each peak corresponds to an increasing number of photon counting event. The inset shows the full image histogram, evidencing that the first peak corresponding to a null signal is much larger than the rest of the occurrences. This procedure allows us to convert the intensity values of panel (a) into a number of detected photons. We then apply a bi-dimensional Gaussian filter on the digitised image to account for the spatial extension of the electron beam excitation. Finally, as we know the pixel size, the electron beam current and the dwell time, we can evaluate a photon emission probability per incident electron. The resulting image is presented in figure A.1 (c). Throughout the manuscript we only showed normalised filtered CL images, as the intensity values can be deduced from the spectra. As can be seen in figure A.1 (c), the typical emission probability is of the order of a few photons/10^6 electrons. It goes up to $\gtrsim$ 100 photons/10^6 electrons for dipolar-type modes.

Appendix B

Alignment of the lithography setup

In this appendix, we present the evolution of the fabrication technique used during this thesis. The first step corresponds to the method used throughout this work, and especially for the fabrication of coupled nanowire-nanoantenna systems in chapter 5, using the commercial software Elphy [Rai] and the Zeiss LEO SEM [Zei] for the lithography. It has then been adapted and improved to be used on the new Nanobeam nB5 setup [Nan]. As for the CL images treatment, it is based on home made python code, and uses the `scikit-image` module [Sci].

Elphy-based method

The first method is based on the commercial lithography software Elphy [Rai], which is installed on both the lithography SEM and the CL SEM. We perform CL at cryogenic temperature to locate the NWQD. As in the LDOS imaging described in chapter 2 and appendix A, the energy-filtered image is acquired using an avalanche photodiode.

We use the *manual field alignment procedure* of the software, which consists in acquiring images of patterns on the substrate and pointing their center to define a coordinate frame for each image with respect to the SEM stage. As mentioned in chapter 5, we first scan the coarse alignment marks and then the precise alignment marks previously fabricated around the antenna, defining the coordinate frame around the QD (see figure B.1). Note that for this low-temperature CL experiment, no resist is present on the sample, providing us with a good contrast on the SEM image for the manual alignment. We then acquire two subsequent images *directly using the Elphy image acquisition tool*, recording first the CL signal and then the SEM signal. Typical resulting images are presented in figure B.2 (a),(b). For each image, the software records an image file and a metadata file containing the coordinates of the image scan. Hence, the CL and SEM images can be directly imported in the software at their absolute position with respect to our marks matrix.

To allow a precise antenna design, we further need to superimpose the information of the QD location on the SEM image. We use the CL images processing procedure detailed in appendix A. We then define the region of interest in the filtered CL image [presented in figure B.2 (b)] where the QD is located to avoid parasitic contributions from other artefacts from the image (e.g. the scale bar and green cross automatically added by the software). The intensity profile in this region is then fitted using a bi-dimensional Gaussian profile. The position of the center

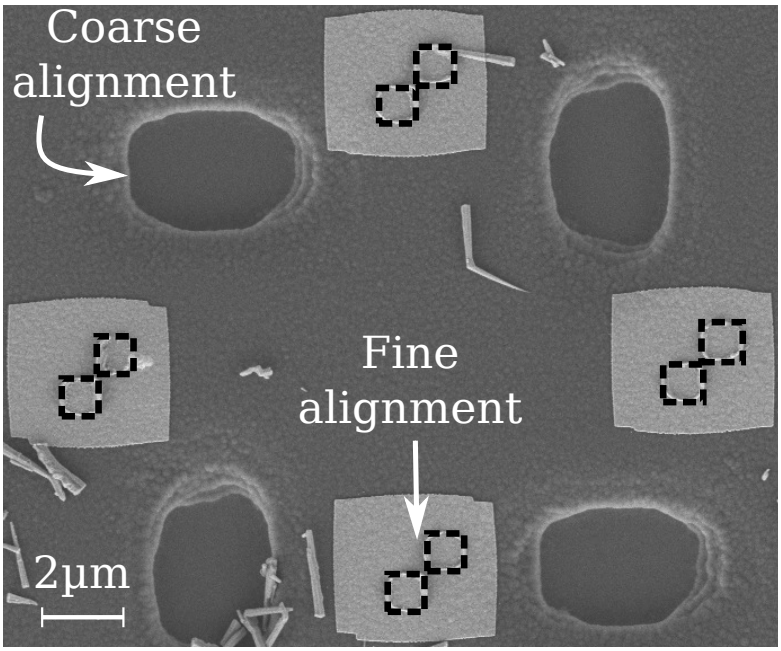

Figure B.1 – Wide field view of the alignment mark system.
Wide field SEM image of a NW with the two mark systems used for realignment using Elphy. As mentioned in section 3.2.2 and shown in figure 3.15, the coarse alignment marks are made using optical lithography and are used to find the NWs for multiple characterisations. They are also used to fabricate the fine alignment marks. The latter are used for the CL localisation of the NWQDs (figure B.2) and the fabrication of the antenna as described in chapter 5.

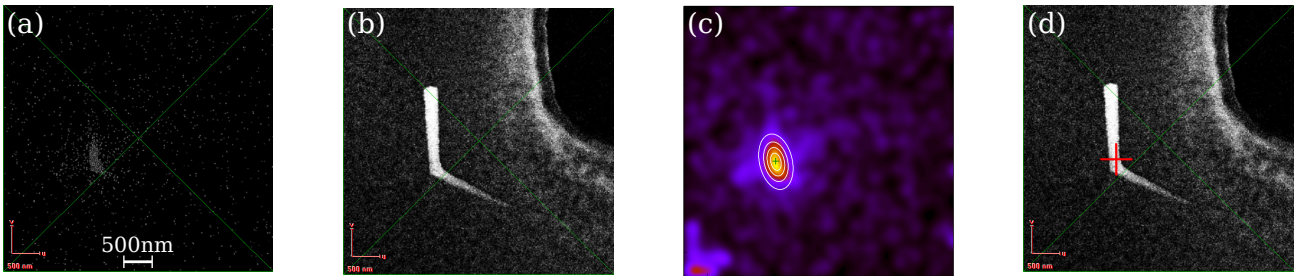

Figure B.2 – Elphy-based procedure to locate the NWQD.
(a) Raw CL image at 5 K acquired using the Elphy image acquisition tool. (b) Subsequent SEM image acquired using the image acquisition tool at the same position. (c) Filtered CL image following the same procedure as in appendix A. The white lines are contour lines of a bi-dimensional Gaussian fit. The green cross is the center of the fit. (d) Corresponding SEM image with the QD position indicated by a red cross, allowing for the fabrication of the nearby NA.

of this profile is considered to be the QD location, and reported on the SEM image as in figure B.2 (d). We generate an additional metadata file, allowing the direct import of this image in the software.

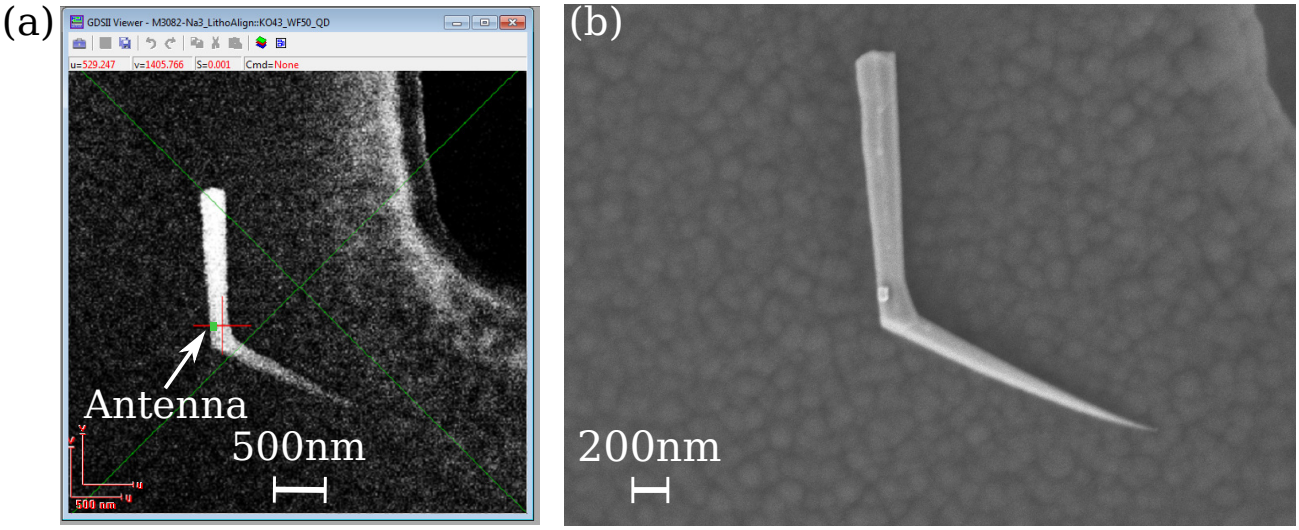

Figure B.3 – Deterministic fabrication of the antenna.
(a) SEM image as imported in Elphy, with the red cross indicating the QD position. The green rectangle represents the target antenna to be fabricated. (b) High definition SEM image of the resulting system after antenna fabrication.

The resulting image import in Elphy is presented in figure B.3 (a), where the green rectangle represents the target antenna to be fabricated on top of the QD. For antenna fabrication, the same procedure is repeated in the lithography setup. In this case, the presence of the resist on the substrate surface degrades the SEM image quality. We use *the same coarse and fine alignment marks* that we used for the CL experiment to manually align the electron beam above the NWQDs. Figure B.3 (b) shows a high resolution SEM image of the resulting system, confirming the good precision of the process.

Beyond Elphy

The method has then been fully implemented in a python-based code to allow for the use of any kind of images (optical microscope, SEM image etc.) encompassing the alignment marks matrix. It can thus be extended to deterministically lithography structures next to any kind of nano-object. As an example, we now detail the fabrication of Al antennas around a KTP nanocrystal on a glass substrate. It is based on the new patterned substrates fabricated using the nB5 system, where we define square arrays of precise alignment marks, some of which are visible in figure B.4 (a). The position of these marks is known with respect to a coordinate frame set by larger marks outside the region of interest in which we disperse the nano-structures.

Using a SEM image displaying at least two marks, we can then determine the absolute position of any point on the sample. The SEM image is imported in python, and we select a region of interest encompassing a mark [red shaded rectangle in figure B.4 (a)]. We use the Sobel transform to detect vertical and horizontal edges in the region of interest, as respectively

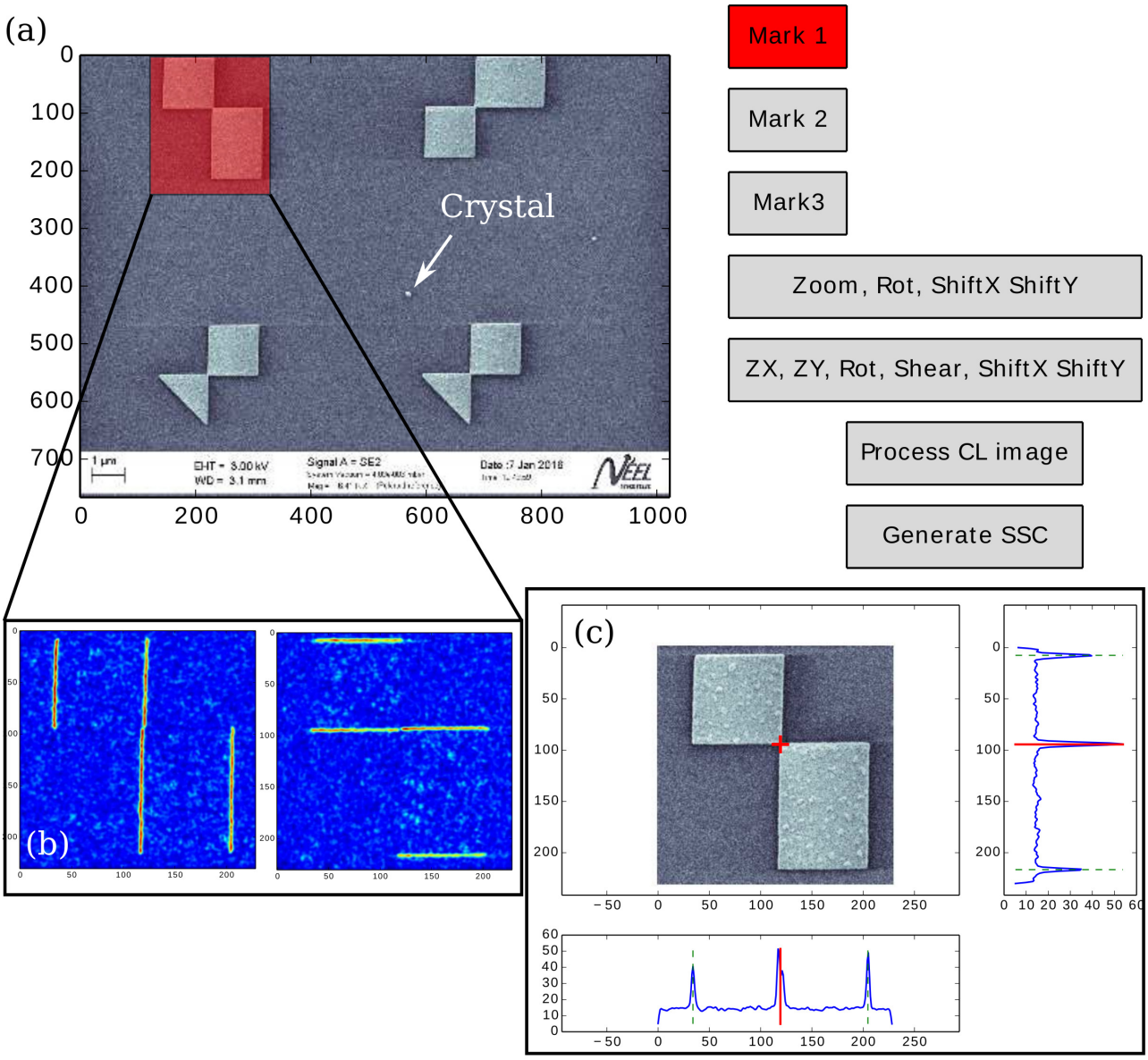

Figure B.4 – Locating a nano-object.
(a) Mark fitting software developed to accommodate any kind of image for deterministic lithography. Up to three marks can be fitted, allowing for the correction of various aberrations. It can be combined to the corresponding CL image in the case of emitting structures, and generates metadata files compatible with our two patterning software. (b) Vertical (left) and horizontal (right) Sobel transforms of the mark selected in (a), showing the vertical and horizontal edges of the mark. (c) Resulting mark center fitting based on the binning of the Sobel-transformed images.

represented in figure B.4 (b). The filtered images are binned along the vertical and horizontal direction respectively, and we compare the positions of the edges to the different marks designs, to fit the position of the center of the mark as demonstrated by the red cross in figure B.4 (c). We then set the expected coordinates for the mark with respect to the sample frame.

Repeating the operation for a second mark allows to define a transformation from the pixel coordinates of the image to the physical coordinates. Using a similarity transform, we can correct for a scaling factor, rotation and shift aberrations in the image. We can then save the corrected image along with a metadata file indicating its position in the frame of the substrate. Using three marks instead of two allows to define an affine transform to correct for a non uniform zoom (i.e. different in the horizontal and vertical directions) and an additional shear. The aberration correction has to be implemented as it can be very convenient to use rotated SEM or CL image acquisitions. Furthermore, in the case of insulating substrates such as the one presented here, it allows to compensate for the electrostatic drift accumulating during the scan. The image can then be imported into Elphy or KLayout [KLa], which is another (free) lithography software that we use for the nB5 system.

The corrected image as imported in KLayout is shown in figure B.5 (a), where the thin pink shapes represented the lithography mask for the patterned substrate. The green structures are the target fabrication structures, serving as a test for the precision of the process. We can see e.g. on the lower left corner that a small correction has been applied to the SEM image (circled in red).

During the lithography procedure, the nB5 system can align automatically on the coarse marks outside of the region of deposition of the crystals (5 mm apart on the substrate). With this coarse alignment, we have experimentally checked that a 25 nm precision in realignment can be achieved, which corresponds to the theoretical precision limit for the Elphy-based system according to its technical specifications. Using an automatic alignment on finer, closer marks fabricated every 500 µm on the sample, a 5 nm is achieved. The final system is shown in figure B.5 (b).

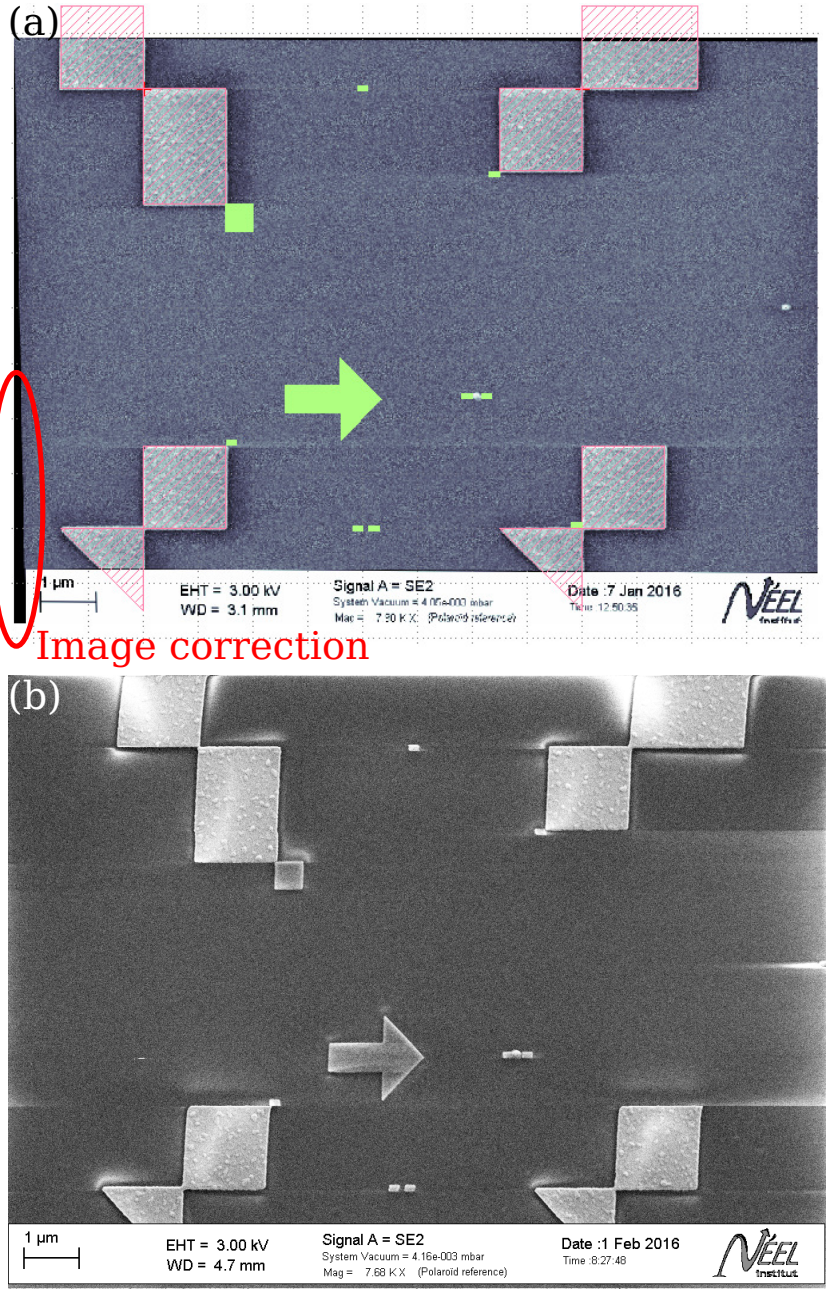

Figure B.5 – Fitmark Antenna.
(a) Corrected SEM images from figure B.4 imported in KLayout. The pink pattern is the lithography mask used to fabricate the patterned substrate. We can see the perfect fit of the mark positions with the mask after the transformation of the SEM image. The green structures are to be fabricated to test the precision of the re-alignment procedure. The image correction (a small rotation and a shear) is visible in the lower left corner, and circled in red. (b) Resulting SEM image after fabrication. The precision in re-alignment is very good. Note the position of the upper left square in contact with the mark, as well as the rectangles in the diagonal. The dimer antenna well surrounds the nanocrystal. The drift in the image comes from the fact that the substrate is insulating.

Appendix C

Glossary

List of Symbols

B Magnetic induction vector.

C_{abs} Absorption cross-section.

C_{ext} Extinction cross-section.

C_{sca} Scattering cross-section.

D Electric displacement vector.

E Electric field vector.

$\bar{e}$ Elementary electronic charge.

E_f Fermi energy.

ε Complex electric permittivity.

H Magnetic field vector.

k Electromagnetic wave vector.

k_0 Free-space wave vector.

κ Imaginary part of the refractive index.

k_{spp} Surface plasmon in-plane wave vector.

λ_{lsp} Localised surface plasmon resonance wavelength.

n Real part of the refractive index.

$\tilde{n}$ Complex refractive index.

ω Electromagnetic angular frequency.

ω_p Plasma pulsation.

$\tilde{\mathbf{q}}$ Wave vector transferred from the electron.

q Electron wave vector.

List of Acronyms

µPL microphotoluminescence.

ALD atomic layer deposition.

APD avalanche photodiode.

CCD charge-coupled device.

CL cathodoluminescence.

cw continuous wave.

DMS diluted magnetic semiconductors.

DOS density of states.

EELS electron energy loss spectroscopy.

HBT Hanbury Brown and Twiss.

HH heavy hole.

IMIM Insulator-Metal-Insulator-Metal.

IR infra-red.

KTP potassium titanyl phosphate.

LDOS local density of states.

LH light hole.

LSP localized surface plasmon.

LSPR localized surface plasmon resonance.

MBE molecular beam epitaxy.

MIBK:IPA methy-isobutyl ketone:isopropanol.

NA numerical aperture.

NMP N-methyl-2-pyrrolidone.

NW nanowire.

NWQD nanowire quantum dot.

PMMA poly(methyl methacrylate).

QD quantum dot.

RIE reactive ion etching.

SEM scanning electron microscope.

SPP surface plasmon polariton.

SPR surface plasmon resonance.

Ti:Saph Titanium:Sapphire.

TR transition radiation.

TRPL time-resolved photoluminescence.

UV ultra-violet.

WZ wurtzite.

ZB zinc blende.

Bibliography

[Aar+05] Jaan Aarik, Aarne Kasikov, Marco Kirm, Sven Lange, Teet Uustare, and Hugo Mändar. "Optical properties of crystalline Al_2O_3 thin films grown by atomic layer deposition". In: *Proc. SPIE 5946, Optical Materials and Applications*. 2005. DOI: 10.1117/12.639047.

[ABN06] Pascal Anger, Palash Bharadwaj, and Lukas Novotny. "Enhancement and Quenching of Single-Molecule Fluorescence". In: *Physical Review Letters* 96.11 (Mar. 2006), p. 113002. DOI: 10.1103/physrevlett.96.113002.

[Ako+06] N. Akopian, N. H. Lindner, E. Poem, Y. Berlatzky, J. Avron, D. Gershoni, B. D. Gerardot, and P. M. Petroff. "Entangled Photon Pairs from Semiconductor Quantum Dots". In: *Physical Review Letters* 96.13 (Apr. 2006). DOI: 10.1103/physrevlett.96.130501.

[Arb+14] Arnaud Arbouet, Adnen Mlayah, Christian Girard, and Gérard Colas des Francs. "Electron energy losses and cathodoluminescence from complex plasmonic nanostructures: spectra, maps and radiation patterns from a generalized field propagator". In: *New J. Phys.* 16.11 (Nov. 2014), p. 113012. DOI: 10.1088/1367-2630/16/11/113012.

[Art+13] A. Artioli, P. Rueda-Fonseca, P. Stepanov, E. Bellet-Amalric, M. Den Hertog, C. Bougerol, Y. Genuist, F. Donatini, R. André, G. Nogues, and et al. "Optical properties of single ZnTe nanowires grown at low temperature". In: *Applied Physics Letters* 103.22 (2013), p. 222106. DOI: 10.1063/1.4832055.

[Art16] Alberto Artioli. "Magnetic Polaron in (Cd,Mn)Te quantum dot inserted in ZnTe nanowire". PhD thesis. Université Grenoble Alpes, 2016.

[Att] Attolight. URL: http://www.attolight.com/.

[AZ84] K. Arya and R. Zeyher. *Light Scattering in Solids*. Springer-Verlag, Berlin, 1984.

[Bac+99] G. Bacher, R. Weigand, J. Seufert, V. D. Kulakovskii, N. A. Gippius, A. Forchel, K. Leonardi, and D. Hommel. "Biexciton versus Exciton Lifetime in a Single Semiconductor Quantum Dot". In: *Physical Review Letters* 83.21 (Nov. 1999), p. 4417. DOI: 10.1103/physrevlett.83.4417.

[Bar+11] Edward S. Barnard, Toon Coenen, Ernst Jan R. Vesseur, Albert Polman, and Mark L. Brongersma. "Imaging the Hidden Modes of Ultrathin Plasmonic Strip Antennas by Cathodoluminescence". In: *Nano Lett.* 11.10 (Oct. 2011), p. 4265. DOI: 10.1021/nl202256k.

[Bau+11] Björn Baumeier, Felix Huerkamp, Tamara A. Leskova, and Alexei A. Maradudin. "Scattering of surface-plasmon polaritons by a localized dielectric surface defect studied using an effective boundary condition". In: *Physical Review A* 84.1 (July 2011). DOI: 10.1103/physreva.84.013810.

[BBN03] Michael R. Beversluis, Alexandre Bouhelier, and Lukas Novotny. "Continuum generation from single gold nanostructures through near-field mediated intraband transitions". In: *Physical Review B* 68.11 (Sept. 2003), p. 115433. DOI: 10.1103/physrevb.68.115433.

[BDN09] Palash Bharadwaj, Bradley Deutsch, and Lukas Novotny. "Optical Antennas". In: *Adv. Opt. Photon.* 1.3 (Aug. 2009), p. 438. DOI: 10.1364/aop.1.000438.

[Bel+13] C. Belacel, B. Habert, F. Bigourdan, F. Marquier, J.-P. Hugonin, S. Michaelis de Vasconcellos, X. Lafosse, L. Coolen, C. Schwob, C. Javaux, and et al. "Controlling Spontaneous Emission with Plasmonic Optical Patch Antennas". In: *Nano Lett.* 13.4 (Apr. 2013), p. 1516. DOI: 10.1021/nl3046602.

[Bes+04] L. Besombes, Y. Léger, L. Maingault, D. Ferrand, H. Mariette, and J. Cibert. "Probing the Spin State of a Single Magnetic Ion in an Individual Quantum Dot". In: *Physical Review Letters* 93.20 (Nov. 2004). DOI: 10.1103/physrevlett.93.207403.

[Bes+15] L. Besombes, H. Boukari, C. Le Gall, A. Brunetti, C.L. Cao, S. Jamet, and B. Varghese. "Optical control of the spin of a magnetic atom in a semiconductor quantum dot". In: *Nanophotonics* 4.1 (Jan. 2015). DOI: 10.1515/nanoph-2015-0003.

[Bes01] Lucien Besombes. "Optical spectroscopy of individual II-VI semiconductor quantum dots". PhD thesis. Université de Grenoble, 2001.

[BH83] Craig F. Bohren and Donald R. Huffman. *Absorption and Scattering of light by Small Particles*. Wiley-VCH, 1983.

[Big+14] F. Bigourdan, F. Marquier, J.-P. Hugonin, and J.-J. Greffet. "Design of highly efficient metallo-dielectric patch antennas for single-photon emission". In: *Optics Express* 22.3 (2014), p. 2337. DOI: 10.1364/oe.22.002337.

[Bou+12a] S. Bounouar, M. Elouneg-Jamroz, M. den Hertog, C. Morchutt, E. Bellet-Amalric, R. André, C. Bougerol, Y. Genuist, J.-Ph. Poizat, S. Tatarenko, and et al. "Ultrafast Room Temperature Single-Photon Source from Nanowire-Quantum Dots". In: *Nano Lett.* 12.6 (June 2012), p. 2977. DOI: 10.1021/nl300733f.

[Bou+12b] S. Bounouar, C. Morchutt, M. Elouneg-Jamroz, L. Besombes, R. André, E. Bellet-Amalric, C. Bougerol, M. Den Hertog, K. Kheng, S. Tatarenko, and et al. "Exciton-phonon coupling efficiency in CdSe quantum dots embedded in ZnSe nanowires". In: *Physical Review B* 85.3 (Jan. 2012). DOI: 10.1103/physrevb.85.035428.

[Bou+12c] S. Bounouar, A. Trichet, M. Elouneg-Jamroz, R. André, E. Bellet-Amalric, C. Bougerol, M. Den Hertog, K. Kheng, S. Tatarenko, and J.-Ph. Poizat. "Extraction of the homogeneous linewidth of the spectrally diffusing line of a CdSe/ZnSe quantum dot embedded in a nanowire". In: *Physical Review B* 86.8 (Aug. 2012). DOI: 10.1103/physrevb.86.085325.

[BP62] G. L. Bir and G. E. Pikus. In: *Soviet Pysics, Solid State* 3 (1962), p. 2221.

[BP66] James R. Biard and Gary E. Pittman. "Semiconductor Radiant Diode". English. US3293513. 1966.

[BST86] J. J. Burke, G. I. Stegeman, and T. Tamir. "Surface-polariton-like waves guided by thin, lossy metal films". In: *Physical Review B* 33.8 (Apr. 1986), p. 5186. DOI: 10.1103/physrevb.33.5186.

[But+10] J. Butet, G. Bachelier, I. Russier-Antoine, C. Jonin, E. Benichou, and P.-F. Brevet. "Interference between Selected Dipoles and Octupoles in the Optical Second-Harmonic Generation from Spherical Gold Nanoparticles". In: *Physical Review Letters* 105.7 (Aug. 2010). DOI: 10.1103/physrevlett.105.077401.

[BW99] Max Born and Emil Wolf. *Principles of Optics*. 7th. Cambridge, 1999.

[BYS86] G. T. Boyd, Z. H. Yu, and Y. R. Shen. "Photoinduced luminescence from the noble metals and its enhancement on roughened surfaces". In: *Physical Review B* 33 (1986), p. 7923. DOI: 10.1103/PhysRevB.33.7923.

[Cas+14] Alberto Casadei, Emanuele F. Pecora, Jacob Trevino, Carlo Forestiere, Daniel Rüffer, Eleonora Russo-Averchi, Federico Matteini, Gozde Tutuncuoglu, Martin Heiss, Anna Fontcuberta i Morral, and et al. "Photonic-Plasmonic Coupling of GaAs Single Nanowires to Optical Nanoantennas". In: *Nano Lett.* 14.5 (May 2014), p. 2271. DOI: 10.1021/nl404253x.

[Cas+15] Alberto Casadei, Esther Alarcon Llado, Francesca Amaduzzi, Eleonora Russo-Averchi, Daniel Rüffer, Martin Heiss, Luca Dal Negro, and Anna Fontcuberta i Morral. "Polarization response of nanowires à la carte". In: *Scientific Reports* 5 (Jan. 2015), p. 7651. DOI: 10.1038/srep07651.

[CCM96] J.-Y. Courtois, J.-M. Courty, and J. C. Mertz. "Internal Dynamics of Multilevel Atoms near a Vacuum-Dielectric Interface". In: *Physical Review A* 53.3 (1996), p. 1862. DOI: 10.1103/PhysRevA.53.1862.

[CDG87] Claude Cohen-Tannoudji, Jacques Dupont-Roc, and Gilbert Grynberg. *Photons et atomes. Introduction à l'électrodynamique quantique.* Editions du CNRS, 1987.

[Cho+08] Mustafa H. Chowdhury, James Pond, Stephen K. Gray, and Joseph R. Lakowicz. "Systematic Computational Study of the Effect of Silver Nanoparticle Dimers on the Coupled Emission from Nearby Fluorophores". In: *The Journal of Physical Chemistry C* 112.30 (July 2008), p. 11236. DOI: 10.1021/jp802414k.

[Chr+15] Sotirios Christodoulou, Fernando Rajadell, Alberto Casu, Gianfranco Vaccaro, Joel Q. Grim, Alessandro Genovese, Liberato Manna, Juan I. Climente, Francesco Meinardi, Gabriele Rainò, and et al. "Band structure engineering via piezoelectric fields in strained anisotropic CdSe/CdS nanocrystals". In: *Nat Comms* 6 (July 2015), p. 7905. DOI: 10.1038/ncomms8905.

[Cla+10] Julien Claudon, Joël Bleuse, Nitin Singh Malik, Maela Bazin, Périne Jaffrennou, Niels Gregersen, Christophe Sauvan, Philippe Lalanne, and Jean-Michel Gérard. "A highly efficient single-photon source based on a quantum dot in a photonic nanowire". In: *Nature Photonics* 4 (Jan. 2010), p. 174. DOI: 10.1038/nphoton.2009.287.

[Coe+11] Toon Coenen, Ernst Jan R. Vesseur, Albert Polman, and A. Femius Koenderink. "Directional Emission from Plasmonic Yagi–Uda Antennas Probed by Angle-Resolved Cathodoluminescence Spectroscopy". In: *Nano Lett.* 11.9 (Sept. 2011), pp. 3779–3784. DOI: 10.1021/nl201839g.

[Com] Comsol. URL: https://www.comsol.com/.

[CPS78] R. R. Chance, A. Prock, and R. Silbey. "Molecular Fluorescence and Energy Transfer Near Interfaces". In: *Advances in Chemical Physics* (1978). DOI: 10.1002/9780470142561.ch1.

[Cre+14] T. Cremel, M. Elouneg-Jamroz, E. Bellet-Amalric, L. Cagnon, S. Tatarenko, and K. Kheng. "Bottom-up approach to control the photon outcoupling of a II-VI quantum dot with a photonic wire". In: *Phys. Status Solidi C* 11.7-8 (Apr. 2014), p. 1263. DOI: 10.1002/pssc.201300737.

[Cur+10] A. G. Curto, G. Volpe, T. H. Taminiau, M. P. Kreuzer, R. Quidant, and N. F. van Hulst. "Unidirectional Emission of a Quantum Dot Coupled to a Nanoantenna". In: *Science* 329.5994 (Aug. 2010), pp. 930–933. DOI: 10.1126/science.1191922.

[Cur+13] Alberto G. Curto, Tim H. Taminiau, Giorgio Volpe, Mark P. Kreuzer, Romain Quidant, and Niek F. van Hulst. "Multipolar radiation of quantum emitters with nanowire optical antennas". In: *Nat Comms* 4 (Apr. 2013), p. 1750. DOI: 10.1038/ncomms2769.

[Dan+89] Le Si Dang, J. Cibert, Y. Gobil, K. Saminadayar, and S. Tatarenko. "Optical study of residual strains in CdTe and ZnTe layers grown by molecular beam epitaxy on GaAs". In: *Applied Physics Letters* 55.3 (1989), p. 235. DOI: 10.1063/1.101917.

[Dav09] T.J. Davis. "Surface plasmon modes in multi-layer thin-films". In: *Optics Communications* 282.1 (Jan. 2009), p. 135. DOI: 10.1016/j.optcom.2008.09.043.

[DD10] Fabrice Donatini and Le Si Dang. "A single-step electron beam lithography of buried nanostructures using cathodoluminescence imaging and low temperature". In: *Nanotechnology* 21.37 (Aug. 2010), p. 375303. DOI: 10.1088/0957-4484/21/37/375303.

[Des+13] Saniya Deshpande, Junseok Heo, Ayan Das, and Pallab Bhattacharya. "Electrically driven polarized single-photon emission from an InGaN quantum dot in a GaN nanowire". In: *Nat Comms* 4 (Apr. 2013), p. 1675. DOI: 10.1038/ncomms2691.

[Dev+03] Eloise Devaux, Thomas W. Ebbesen, Jean-Claude Weeber, and Alain Dereux. "Launching and decoupling surface plasmons via micro-gratings". In: *Applied Physics Letters* 83.24 (2003), p. 4936. DOI: 10.1063/1.1634379.

[Dod86] M.J. Dodge. *Refractive index in Handbook of Laser Science and Technology.* Vol. IV. Optical Materials: Part 2. CRC Press, 1986.

[Dor+09] Jens Dorfmüller, Ralf Vogelgesang, R. Thomas Weitz, Carsten Rockstuhl, Christoph Etrich, Thomas Pertsch, Falk Lederer, and Klaus Kern. "Fabry-Pérot Resonances in One-Dimensional Plasmonic Nanostructures". In: *Nano Lett.* 9.6 (June 2009), pp. 2372–2377. DOI: 10.1021/nl900900r.

[Dou+10] Adrien Dousse, Jan Suffczyński, Alexios Beveratos, Olivier Krebs, Aristide Lemaître, Isabelle Sagnes, Jacqueline Bloch, Paul Voisin, and Pascale Senellart. "Ultrabright source of entangled photon pairs". In: *Nature* 466.7303 (July 2010), pp. 217–220. DOI: 10.1038/nature09148.

[Dre74] Karl H. Drexhage. "IV Interaction of Light with Monomolecular Dye Layers". In: *Progress in Optics* 12 (1974), p. 163. DOI: 10.1016/s0079-6638(08)70266-x.

[Dri+05] A. F. van Driel, G. Allan, C. Delerue, P. Lodahl, W. L. Vos, and D. Vanmaekelbergh. "Frequency-Dependent Spontaneous Emission Rate from CdSe and CdTe Nanocrystals: Influence of Dark States". In: *Physical Review Letters* 95.23 (Dec. 2005). DOI: 10.1103/physrevlett.95.236804.

[Dua+01] Xiangfeng Duan, Yu Huang, Yi Cui, Jianfang Wang, and Charles M. Lieber. "Indium phosphide nanowires as building blocks for nanoscale electronic and optoelectronic devices". In: *Nature* 409.6816 (Jan. 2001), pp. 66–69. DOI: 10.1038/35051047.

[EPS63] H. Ehrenreich, H.R. Philipp, and B. Segall. "Optical Properties of Aluminum". In: *Physical Review* 132.5 (1963), p. 1918. DOI: 10.1103/PhysRev.132.1918.

[Esh57] J. D. Eshelby. "The Determination of the Elastic Field of an Ellipsoidal Inclusion, and Related Problems". In: *Proceedings of the Royal Society A: Mathematical, Physical and Engineering Sciences* 241.1226 (Aug. 1957), pp. 376–396. DOI: 10.1098/rspa.1957.0133.

[Esh59] J. D. Eshelby. "The Elastic Field Outside an Ellipsoidal Inclusion". In: *Proceedings of the Royal Society A: Mathematical, Physical and Engineering Sciences* 252.1271 (Oct. 1959), pp. 561–569. DOI: 10.1098/rspa.1959.0173.

[Est+08] R. Esteban, R. Vogelgesang, J. Dorfmüller, A. Dmitriev, C. Rockstuhl, C. Etrich, and K. Kern. "Direct Near-Field Optical Imaging of Higher Order Plasmonic Resonances". In: *Nano Lett.* 8.10 (Oct. 2008), pp. 3155–3159. DOI: 10.1021/nl801396r.

[ETG10] R. Esteban, T. V. Teperik, and J. J. Greffet. "Optical Patch Antennas for Single Photon Emission Using Surface Plasmon Resonances". In: *Physical Review Letters* 104.2 (Jan. 2010), p. 026802. DOI: 10.1103/physrevlett.104.026802.

[Eth+16] Maeliss Ethis de Corny, Nicolas Chauvet, Guillaume Laurent, Mathieu Jeannin, Logi Olgeirsson, Aurélien Drezet, Serge Huant, Géraldine Dantelle, Gilles Nogues, and Guillaume Bachelier. "Optimized wave-mixing in single and compact aluminum nanoantennas". In: *Submitted to ACS Photonics* (2016).

[FC14] David Ferrand and Joël Cibert. "Strain in crystalline core-shell nanowires". In: *The European Physical Journal Applied Physics* 67.3 (Aug. 2014), p. 30403. DOI: 10.1051/epjap/2014140156.

[FEI] FEI. URL: http://www.fei.com.

[Fia] Fianium. URL: http://www.fianium.com/.

[Fil+12] Robert Filter, Jing Qi, Carsten Rockstuhl, and Falk Lederer. "Circular optical nanoantennas: an analytical theory". In: *Physical Review B* 85.12 (Mar. 2012), p. 125429. DOI: 10.1103/physrevb.85.125429.

[Fis10] Guy Fishman. *Semi-Conducteurs: les bases de la théorie k.p.* Ecole Polytechnique, 2010.

[Fis88] Guy Fishman. *Energie et fonction d'onde des semi-conducteurs.* Editions de Physique, 1988.

[FQ33] G. I. Finch and A. G. Quarrell. "The Structure of Magnesium, Zinc and Aluminium Films". In: *Proceedings of the Royal Society A: Mathematical, Physical and Engineering Sciences* 141.844 (Aug. 1933), p. 398. DOI: 10.1098/rspa.1933.0126.

[Fur88] J. K. Furdyna. "Diluted magnetic semiconductors". In: *Journal of Applied Physics* 64.4 (1988), R29. DOI: 10.1063/1.341700.

[Gaj+94] J. A. Gaj, W. Grieshaber, C. Bodin-Deshayes, J. Cibert, G. Feuillet, Y. Merle d'Aubigné, and A. Wasiela. "Magneto-optical study of interface mixing in the CdTe-(Cd,Mn)Te system". In: *Physical Review B* 50.8 (Aug. 1994), pp. 5512–5527. DOI: 10.1103/physrevb.50.5512.

[Gar] F. J. García de Abajo. URL: http://nanophotonics.csic.es/widgets/TR/index.html.

[Gar10] F. J. Garcìa de Abajo. "Optical excitations in electron microscopy". In: *Rev. Mod. Phys.* 82.1 (Feb. 2010), p. 209. DOI: 10.1103/revmodphys.82.209.

[Gér+98] J.M. Gérard, B. Sermage, B. Gayral, B. Legrand, E. Costard, and V. Thierry-Mieg. "Enhanced Spontaneous Emission by Quantum Boxes in a Monolithic Optical Microcavity". In: *Physical Review Letters* 81.5 (1998), p. 1110. DOI: 10.1103/PhysRevLett.81.1110.

[GG14] Davy Gérard and Stephen K Gray. "Aluminium plasmonics". In: *J. Phys. D: Appl. Phys.* 48.18 (Dec. 2014), p. 184001. DOI: 10.1088/0022-3727/48/18/184001.

[GK08] F. J. Garcìa de Abajo F. J.a de Abajo and M. Kociak. "Probing the Photonic Local Density of States with Electron Energy Loss Spectroscopy". In: *Physical Review Letters* 100.10 (Mar. 2008), p. 106804. DOI: 10.1103/physrevlett.100.106804.

[GK11] Jan A. Gaj and Jacek Kossut. *Introduction to the Physics of Diluted Magnetic Semiconductors.* Ed. by Springer Science and Business Media. 2011.

[Gon+15] Ke Gong, James E. Martin, Lauren E. Shea-Rohwer, Ping Lu, and David F. Kelley. "Radiative Lifetimes of Zincblende CdSe/CdS Quantum Dots". In: *The Journal of Physical Chemistry C* 119.4 (Jan. 2015), p. 2231. DOI: 10.1021/jp5118932.

[Göp31] Maria Göppert-Mayer. "Über Elementarakte mit zwei Quantensprüngen". In: *Annalen der Physik* 401 (1931), p. 273. DOI: 10.1002/andp.19314010303.

[GPF79] J.A. Gaj, R. Planel, and G. Fishman. "Relation of magneto-optical properties of free excitons to spin alignment of Mn^{2+} ions in $Cd_{1-x}Mn_xTe$". In: *Solid State Communications* 29.5 (Feb. 1979), pp. 435–438. DOI: 10.1016/0038-1098(79)91211-0.

[Gsc+15] M. Gschrey, A. Thoma, P. Schnauber, M. Seifried, R. Schmidt, B. Wohlfeil, L. Krüger, J. -H. Schulze, T. Heindel, S. Burger, and et al. "Highly indistinguishable photons from deterministic quantum-dot microlenses utilizing three-dimensional in situ electron-beam lithography". In: *Nat Comms* 6 (July 2015), p. 7662. DOI: 10.1038/ncomms8662.

[Gu+11] Lin Gu, Wilfried Sigle, Christoph T. Koch, Burcu Ögüt, Peter A. van Aken, Nahid Talebi, Ralf Vogelgesang, Jianlin Mu, Xiaogang Wen, and Jian Mao. "Resonant wedge-plasmon modes in single-crystalline gold nanoplatelets". In: *Physical Review B* 83.19 (May 2011). DOI: 10.1103/physrevb.83.195433.

[Hal+62] R. N. Hall, G. E. Fenner, J. D. Kingsley, T. J. Soltys, and R. O. Carlson. "Coherent Light Emission From GaAs Junctions". In: *Physical Review Letters* 9.9 (Nov. 1962), pp. 366–368. DOI: 10.1103/physrevlett.9.366.

[HAM16] Thang B. Hoang, Gleb M. Akselrod, and Maiken H. Mikkelsen. "Ultrafast Room-Temperature Single Photon Emission from Quantum Dots Coupled to Plasmonic Nanocavities". In: *Nano Lett.* 16.1 (Jan. 2016), pp. 270–275. DOI: 10.1021/acs.nanolett.5b03724.

[Har+09] Edmund Harbord, Peter Spencer, Edmund Clarke, and Ray Murray. "Radiative lifetimes in undoped and p -doped InAs/GaAs quantum dots". In: *Physical Review B* 80.19 (Nov. 2009). DOI: 10.1103/physrevb.80.195312.

[Har+13] Nicolai Hartmann, Dawid Piatkowski, Richard Ciesielski, Sebastian Mackowski, and Achim Hartschuh. "Radiation Channels Close to a Plasmonic Nanowire Visualized by Back Focal Plane Imaging". In: *ACS Nano* 7.11 (Nov. 2013), p. 10257. DOI: 10.1021/nn404611q.

[Hec+96] B. Hecht, H. Bielefeldt, L. Novotny, Y. Inouye, and D. W. Pohl. "Local Excitation, Scattering, and Interference of Surface Plasmons". In: *Physical Review Letters* 77.9 (1996), p. 1889. DOI: 10.1103/PhysRevLett.77.1889.

[Hei+13] M. Heiss, Y. Fontana, A. Gustafsson, G. Wüst, C. Magen, D. D. O'Regan, J. W. Luo, B. Ketterer, S. Conesa-Boj, A. V. Kuhlmann, and et al. "Self-assembled quantum dots in a nanowire system for quantum photonics". In: *Nat Mater* 12.5 (Feb. 2013), pp. 439–444. DOI: 10.1038/nmat3557.

[HGK75] H.-J. Hagemann, W. Gudat, and C. Kunz. "Optical constants from the far infrared to the x-ray region: Mg, Al, Cu, Ag, Au, Bi, C, and Al_2O_3". In: *J. Opt. Soc. Am.* 65.6 (June 1975), p. 742. DOI: 10.1364/josa.65.000742.

[Hil+03] R. Hillenbrand, F. Keilmann, P. Hanarp, D. S. Sutherland, and J. Aizpurua. "Coherent imaging of nanoscale plasmon patterns with a carbon nanotube optical probe". In: *Applied Physics Letters* 83.2 (2003), p. 368. DOI: 10.1063/1.1592629.

[Hin+14] Yoyo Hinuma, Andreas Grüneis, Georg Kresse, and Fumiyasu Oba. "Band alignment of semiconductors from density-functional theory and many-body perturbation theory". In: *Physical Review B* 90.15 (Oct. 2014). DOI: 10.1103/physrevb.90.155405.

[HK01] R. Hillenbrand and F. Keilmann. "Optical oscillation modes of plasmon particles observed in direct space by phase-contrast near-field microscopy". In: *Appl Phys B* 73.3 (Sept. 2001), pp. 239–243. DOI: 10.1007/s003400100656.

[HT56a] R. Hanbury Brown and R. Q. Twiss. "A Test of a New Type of Stellar Interferometer on Sirius". In: *Nature* 178.4541 (Nov. 1956), p. 1046. DOI: 10.1038/1781046a0.

[HT56b] R. Hanbury Brown and R. Q. Twiss. "Correlation between Photons in two Coherent Beams of Light". In: *Nature* 177.4497 (Jan. 1956), p. 27. DOI: 10.1038/177027a0.

[Huo+13] Y. H. Huo, B. J. Witek, S. Kumar, J. R. Cardenas, J. X. Zhang, N. Akopian, R. Singh, E. Zallo, R. Grifone, D. Kriegner, and et al. "A light-hole exciton in a quantum dot". In: *Nature Physics* 10.1 (Nov. 2013), p. 46. DOI: 10.1038/nphys2799.

[Ima+00] A. Imamoğlu, P. Michler, M. D. Mason, P. J. Carson, G. F. Strouse, and S. K. Buratto. "Quantum correlation among photons from a single quantum dot at room temperature". In: *Nature* 406.6799 (Aug. 2000), pp. 968–970. DOI: 10.1038/35023100.

[Jac75] J.D. Jackson. *Classical Electrodynamics*. Wiley, 1975.

[JC72] P. B. Johnson and R. W. Christy. "Optical Constants of the Noble Metals". In: *Physical Review B* 6.12 (Dec. 1972), p. 4370. DOI: 10.1103/physrevb.6.4370.

[JGM81] O. Jepsen, D. Glötzel, and A. R. Mackintosh. "Potentials, band structures, and Fermi surfaces in the noble metals". In: *Physical Review B* 23.6 (Mar. 1981), p. 2684. DOI: 10.1103/physrevb.23.2684.

[Job] Horiba Jobin-Yvon. URL: http://www.horiba.com.

[Kas+10] J. Kasprzak, B. Patton, V. Savona, and W. Langbein. "Coherent coupling between distant excitons revealed by two-dimensional nonlinear hyperspectral imaging". In: *Nature Photon* 5.1 (Dec. 2010), pp. 57–63. DOI: 10.1038/nphoton.2010.284.

[KF11] Paul M. Koenraad and Michael E. Flatté. "Single dopants in semiconductors". In: *Nat Mater* 10.2 (Feb. 2011), pp. 91–100. DOI: 10.1038/nmat2940.

[KGP10] Martin Kuttge, F. Javier García de Abajo, and Albert Polman. "Ultrasmall Mode Volume Plasmonic Nanodisk Resonators". In: *Nano Lett.* 10.5 (May 2010), p. 1537. DOI: 10.1021/nl902546r.

[KLa] KLayout. URL: http://www.klayout.de/.

[Kli12] Claus F. Klingshirn. *Semiconductor Optics*. 4th. Springer-Verlag Berlin Heidelberg, 2012.

[Kni+12] Mark W. Knight, Lifei Liu, Yumin Wang, Lisa Brown, Shaunak Mukherjee, Nicholas S. King, Henry O. Everitt, Peter Nordlander, and Naomi J. Halas. "Aluminum Plasmonic Nanoantennas". In: *Nano Lett.* 12.11 (Nov. 2012), p. 6000. DOI: 10.1021/nl303517v.

[Koc+06] S. W. Koch, M. Kira, G. Khitrova, and H. M. Gibbs. "Semiconductor excitons in new light". In: *Nat Mater* 5.7 (July 2006), pp. 523–531. DOI: 10.1038/nmat1658.

[Koc+14] Mathieu Kociak, Odile Stéphan, Alexandre Gloter, Luiz F. Zagonel, Luiz H.G. Tizei, Marcel Tencé, Katia March, Jean Denis Blazit, Zackaria Mahfoud, Arthur Losquin, and et al. "Seeing and measuring in colours: Electron microscopy and spectroscopies applied to nano-optics". In: *Comptes Rendus Physique* 15.2-3 (Feb. 2014), pp. 158–175. DOI: 10.1016/j.crhy.2013.10.003.

[Kou+04] A. V. Koudinov, I. A. Akimov, Yu. G. Kusrayev, and F. Henneberger. "Optical and magnetic anisotropies of the hole states in Stranski-Krastanov quantum dots". In: *Physical Review B* 70.24 (Dec. 2004). DOI: 10.1103/physrevb.70.241305.

[KR68] E. Kretschmann and H. Raether. "Notizen: Radiative Decay of Non Radiative Surface Plasmons Excited by Light". In: *Zeitschrift für Naturforschung A* 23.12 (Jan. 1968). DOI: 10.1515/zna-1968-1247.

[Kra+16] Vasily Kravtsov, Ronald Ulbricht, Joanna M. Atkin, and Markus B. Raschke. "Plasmonic nanofocused four-wave mixing for femtosecond near-field imaging". In: *Nature Nanotechnology* 11.5 (Feb. 2016), pp. 459–464. DOI: 10.1038/nnano.2015.336.

[KS14] Mathieu Kociak and Odile Stéphan. "Mapping plasmons at the nanometer scale in an electron microscope". In: *Chem. Soc. Rev.* 43.11 (2014), p. 3865. DOI: 10.1039/c3cs60478k.

[Kuk+14] V. I. Kukushkin, I. M. Mukhametzhanov, I. V. Kukushkin, V. D. Kulakovskii, I. V. Sedova, S. V. Sorokin, A. A. Toropov, S. V. Ivanov, and A. S. Sobolev. "Control of semiconductor quantum dot emission intensity and polarization by metal nanoantennas". In: *Physical Review B* 90.23 (Dec. 2014). DOI: 10.1103/physrevb.90.235313.

[Kut09] M. Kuttge. "Cathodoluminescence plasmon microscopy". PhD thesis. Utrecht University, 2009.

[Kuw+03] Hitoshi Kuwata, Hiroharu Tamaru, Kunio Esumi, and Kenjiro Miyano. "Resonant light scattering from metal nanoparticles: Practical analysis beyond Rayleigh approximation". In: *Applied Physics Letters* 83.22 (2003), p. 4625. DOI: 10.1063/1.1630351.

[Laf+16] A. Lafuente-Sampietro, H. Utsumi, H. Boukari, S. Kuroda, and L. Besombes. "Individual Cr atom in a semiconductor quantum dot: Optical addressability and spin-strain coupling". In: *Physical Review B* 93.16 (Apr. 2016). DOI: 10.1103/physrevb.93.161301.

[Lau+02] Lincoln J. Lauhon, Mark S. Gudiksen, Deli Wang, and Charles M. Lieber. "Epitaxial core–shell and core–multishell nanowire heterostructures". In: *Nature* 420.6911 (Nov. 2002), pp. 57–61. DOI: 10.1038/nature01141.

[Lee70] B. H. Lee. "Elastic Constants of ZnTe and ZnSe between 77–300K". In: *Journal of Applied Physics* 41.7 (1970), p. 2984. DOI: 10.1063/1.1659349.

[Lég+07] Y. Léger, L. Besombes, L. Maingault, and H. Mariette. "Valence-band mixing in neutral, charged, and Mn-doped self-assembled quantum dots". In: *Physical Review B* 76.4 (July 2007). DOI: 10.1103/physrevb.76.045331.

[LK15] Arthur Losquin and Mathieu Kociak. "Link between Cathodoluminescence and Electron Energy Loss Spectroscopy and the Radiative and Full Electromagnetic Local Density of States". In: *ACS Photonics* 2.11 (Nov. 2015), pp. 1619–1627. DOI: 10.1021/acsphotonics.5b00416.

[LK55] J. M. Luttinger and W. Kohn. "Motion of Electrons and Holes in Perturbed Periodic Fields". In: *Physical Review* 97.4 (Feb. 1955), p. 869. DOI: 10.1103/physrev.97.869.

[LMS15] Peter Lodahl, Sahand Mahmoodian, and Søren Stobbe. "Interfacing single photons and single quantum dots with photonic nanostructures". In: *Rev. Mod. Phys.* 87.2 (May 2015), pp. 347–400. DOI: 10.1103/revmodphys.87.347.

[Mad87] O. Madelung. *Numerical Data and Functional Relationships in Science and Technology, New Series, Group III*. Vol. 22. Springer-Verlag, Berlin, 1987.

[Mai07] Stefan A. Maier. *Plasmonics: Fundamentals and Applications*. Springer US, 2007.

[Maj+13] Todd A. Major, Mary Sajini Devadas, Shun Shang Lo, and Gregory V. Hartland. "Optical and Dynamical Properties of Chemically Synthesized Gold Nanoplates". In: *The Journal of Physical Chemistry C* 117.3 (Jan. 2013), pp. 1447–1452. DOI: 10.1021/jp311470t.

[Man79] L. Mandel. "Sub-Poissonian photon statistics in resonance fluorescence". In: *Opt. Lett.* 4.7 (July 1979), p. 205. DOI: 10.1364/ol.4.000205.

[MBM06] C. de Mello Donegà, M. Bode, and A. Meijerink. "Size- and temperature-dependence of exciton lifetimes in CdSe quantum dots". In: *Physical Review B* 74.8 (Aug. 2006). DOI: 10.1103/physrevb.74.085320.

[McM61] William H. McMaster. "Matrix Representation of Polarization". In: *Rev. Mod. Phys.* 33.1 (Jan. 1961), p. 8. DOI: 10.1103/revmodphys.33.8.

[McP+15] Kevin M. McPeak, Sriharsha V. Jayanti, Stephan J. P. Kress, Stefan Meyer, Stelio Iotti, Aurelio Rossinelli, and David J. Norris. "Plasmonic Films Can Easily Be Better: Rules and Recipes". In: *ACS Photonics* 2.3 (Mar. 2015), p. 326. DOI: 10.1021/ph5004237.

[Mic00] P. Michler. "A Quantum Dot Single-Photon Turnstile Device". In: *Science* 290.5500 (Dec. 2000), pp. 2282–2285. DOI: 10.1126/science.290.5500.2282.

[Mie08] Gustav Mie. "Beiträge zur Optik trüber Medien, speziell kolloidaler Metallösungen". In: *Annalen der Physik* 25 (1908), p. 377.

[MKP07] H. Mertens, A. F. Koenderink, and A. Polman. "Plasmon-enhanced luminescence near noble-metal nanospheres: Comparison of exact theory and an improved Gersten and Nitzan model". In: *Physical Review B* 76.11 (Sept. 2007). DOI: 10.1103/physrevb.76.115123.

[Moh+14] Abbas Mohtashami, Toon Coenen, Alessandro Antoncecchi, Albert Polman, and A. Femius Koenderink. "Nanoscale Excitation Mapping of Plasmonic Patch Antennas". In: *ACS Photonics* 1.11 (Nov. 2014), p. 1134. DOI: 10.1021/ph500225j.

[Muh05] P. Muhlschlegel. "Resonant Optical Antennas". In: *Science* 308.5728 (June 2005), pp. 1607–1609. DOI: 10.1126/science.1111886.

[Mun+12] Mathieu Munsch, Julien Claudon, Joël Bleuse, Nitin S. Malik, Emmanuel Dupuy, Jean-Michel Gérard, Yuntian Chen, Niels Gregersen, and Jesper Mørk. "Linearly Polarized, Single-Mode Spontaneous Emission in a Photonic Nanowire". In: *Physical Review Letters* 108.7 (Feb. 2012). DOI: 10.1103/physrevlett.108.077405.

[Mun+13] Mathieu Munsch, Nitin S. Malik, Emmanuel Dupuy, Adrien Delga, Joël Bleuse, Jean-Michel Gérard, Julien Claudon, Niels Gregersen, and Jesper Mørk. "Dielectric GaAs Antenna Ensuring an Efficient Broadband Coupling between an InAs Quantum Dot and a Gaussian Optical Beam". In: *Physical Review Letters* 110.17 (Apr. 2013). DOI: 10.1103/physrevlett.110.177402.

[Myr+08] Viktor Myroshnychenko, Jessica Rodríguez-Fernández, Isabel Pastoriza-Santos, Alison M. Funston, Carolina Novo, Paul Mulvaney, Luis M. Liz-Marzán, and F. Javier García de Abajo. "Modelling the optical response of gold nanoparticles". In: *Chem. Soc. Rev.* 37.9 (2008), p. 1792. DOI: 10.1039/b711486a.

[Nan] NanoBeam LTD. URL: http://www.nanobeam.co.uk/.

[Nel+07] Jaysen Nelayah, Mathieu Kociak, Odile Stéphan, F. Javier García de Abajo, Marcel Tencé, Luc Henrard, Dario Taverna, Isabel Pastoriza-Santos, Luis M. Liz-Marzán, and Christian Colliex. "Mapping surface plasmons on a single metallic nanoparticle". In: *Nature Physics* 3.5 (Apr. 2007), pp. 348–353. DOI: 10.1038/nphys575.

[New] Andor Newton. URL: http://www.andor.com.

[NH12] Lukas Novotny and Bert Hecht. *Principles of Nano-Optics*. 2nd Edition. Cambridge, 2012.

[NM08] Yann-Michel Niquet and Dulce Camacho Mojica. "Quantum dots and tunnel barriers in InAs/InP nanowire heterostructures: Electronic and optical properties". In: *Physical Review B* 77.11 (Mar. 2008). DOI: 10.1103/physrevb.77.115316.

[NM65] J. A. Nelder and R. Mead. "A Simplex Method for Function Minimization". In: *The Computer Journal* 7.4 (Jan. 1965), p. 308. DOI: 10.1093/comjnl/7.4.308.

[Nog+13] Gilles Nogues, Quentin Merotto, Guillaume Bachelier, Eun Hye Lee, and Jin Dong Song. "Fabrication and tuning of plasmonic optical nanoantennas around droplet epitaxy quantum dots by cathodoluminescence". In: *Applied Physics Letters* 102.23 (2013), p. 231112. DOI: 10.1063/1.4809831.

[Nog+14] Gilles Nogues, Thomas Auzelle, Martien Den Hertog, Bruno Gayral, and Bruno Daudin. "Cathodoluminescence of stacking fault bound excitons for local probing of the exciton diffusion length in single GaN nanowires". In: *Applied Physics Letters* 104.10 (Mar. 2014), p. 102102. DOI: 10.1063/1.4868131.

[Ort+99] A Ortiz, J.C Alonso, V Pankov, and D Albarran. "Violet-blue photoluminescence in aluminium oxide films prepared by ultrasonic spray pyrolysis". In: *Journal of Luminescence* 81.1 (Jan. 1999), p. 45. DOI: 10.1016/s0022-2313(98)00056-8.

[Ott68] Andreas Otto. "Excitation of nonradiative surface plasma waves in silver by the method of frustrated total reflection". In: *Z. Physik* 216.4 (Aug. 1968), p. 398. DOI: 10.1007/bf01391532.

[Oxf] Oxford Instruments. URL: http://www.oxford-instruments.com.

[Oxx] Oxxius. URL: http://www.oxxius.com/.

[Pfe+10] Markus Pfeiffer, Klas Lindfors, Christian Wolpert, Paola Atkinson, Mohamed Benyoucef, Armando Rastelli, Oliver G. Schmidt, Harald Giessen, and Markus Lippitz. "Enhancing the Optical Excitation Efficiency of a Single Self-Assembled Quantum Dot with a Plasmonic Nanoantenna". In: *Nano Lett.* 10.11 (Nov. 2010), p. 4555. DOI: 10.1021/nl102548t.

[Pfe+14] Markus Pfeiffer, Klas Lindfors, Hongyi Zhang, Bernhard Fenk, Fritz Phillipp, Paola Atkinson, Armando Rastelli, Oliver G. Schmidt, Harald Giessen, and Markus Lippitz. "Eleven Nanometer Alignment Precision of a Plasmonic Nanoantenna with a Self-Assembled GaAs Quantum Dot". In: *Nano Lett.* 14.1 (Jan. 2014), pp. 197–201. DOI: 10.1021/nl403730q.

[PHM00] L'ubos Polerecky, Jaroslav Hamrle, and Brian D. MacCraith. "Theory of the Radiation of Dipoles Placed within a Multilayer System". In: *Applied Optics* 39.22 (2000), p. 3968. DOI: 10.1364/A.O.39.003968.

[Phy] Spectra Physics. URL: http://www.spectra-physics.com.

[Poe+10] E. Poem, Y. Kodriano, C. Tradonsky, N. H. Lindner, B. D. Gerardot, P. M. Petroff, and D. Gershoni. "Accessing the dark exciton with light". In: *Nature Physics* 6.12 (Nov. 2010), p. 993. DOI: 10.1038/nphys1812.

[Pri] Princeton Instruments. URL: http://www.princetoninstruments.com/.

[PSL65] D. W. Pashley, M. J. Stowell, and T. J. Law. "The Crystal Structure of Evaporated Gold Films". In: *Phys. Stat. Sol. (b)* 10.1 (1965), p. 153. DOI: 10.1002/pssb.19650100115.

[Pur46] E.M. Purcell. "Spontaneous Emission Probabilities at Radio Frequencies". In: *Proceedings of the American Physical Society*. Vol. 69. B10. American Physical Society (APS), June 1946, p. 674. DOI: 10.1103/physrev.69.674.2.

[PVM91] B. Prade, J. Y. Vinet, and A. Mysyrowicz. "Guided optical waves in planar heterostructures with negative dielectric constant". In: *Physical Review B* 44.24 (Dec. 1991), pp. 13556–13572. DOI: 10.1103/physrevb.44.13556.

[Qua] ID Quantique. URL: http://www.idquantique.com/.

[Rai] Raith. URL: https://www.raith.com/.

[Rak95] Aleksandar D. Rakic. "Algorithm for the determination of intrinsic optical constants of metal films: application to aluminum". In: *Applied Optics* 34.22 (Aug. 1995), p. 4755. DOI: 10.1364/ao.34.004755.

[Ram+15] Mohammad Ramezani, Alberto Casadei, Grzegorz Grzela, Federico Matteini, Gözde Tütüncüoglu, Daniel Rüffer, Anna Fontcuberta i Morral, and Jaime Gómez Rivas. "Hybrid Semiconductor Nanowire–Metallic Yagi-Uda Antennas". In: *Nano Lett.* 15.8 (Aug. 2015), pp. 4889–4895. DOI: 10.1021/acs.nanolett.5b00565.

[Ros+11] D. Rossouw, M. Couillard, J. Vickery, E. Kumacheva, and G. A. Botton. "Multipolar Plasmonic Resonances in Silver Nanowire Antennas Imaged with a Subnanometer Electron Probe". In: *Nano Lett.* 11.4 (Apr. 2011), pp. 1499–1504. DOI: 10.1021/nl200634w.

[Rue+14] P. Rueda-Fonseca, E. Bellet-Amalric, R. Vigliaturo, M. den Hertog, Y. Genuist, R. André, E. Robin, A. Artioli, P. Stepanov, D. Ferrand, and et al. "Structure and Morphology in Diffusion-Driven Growth of Nanowires: The Case of ZnTe". In: *Nano Lett.* 14.4 (Apr. 2014), p. 1877. DOI: 10.1021/nl4046476.

[Rue+16] P. Rueda-Fonseca, E. Robin, E. Bellet-Amalric, M. Lopez-Haro, M. Den Hertog, Y. Genuist, R. André, A. Artioli, S. Tatarenko, D. Ferrand, and et al. "Quantitative Reconstructions of 3D Chemical Nanostructures in Nanowires". In: *Nano Lett.* 16.3 (Mar. 2016), pp. 1637–1642. DOI: 10.1021/acs.nanolett.5b04489.

[Rue15] Pamela Rueda-Fonseca. "Magnetic Quantum Dots in II-VI Semiconductor Nanowires". PhD thesis. Université Grenoble Alpes, 2015.

[Sal+09] G. Sallen, A. Tribu, T. Aichele, R. André, L. Besombes, C. Bougerol, S. Tatarenko, K. Kheng, and J. Ph. Poizat. "Exciton dynamics of a single quantum dot embedded in a nanowire". In: *Physical Review B* 80.8 (Aug. 2009). DOI: 10.1103/physrevb.80.085310.

[San+01] Charles Santori, Matthew Pelton, Glenn Solomon, Yseulte Dale, and Yoshihisa Yamamoto. "Triggered Single Photons from a Quantum Dot". In: *Physical Review Letters* 86.8 (Feb. 2001), pp. 1502–1505. DOI: 10.1103/physrevlett.86.1502.

[San+02] Charles Santori, David Fattal, Jelena Vučković, Glenn S. Solomon, and Yoshihisa Yamamoto. "Indistinguishable photons from a single-photon device". In: *Nature* 419.6907 (Oct. 2002), pp. 594–597. DOI: 10.1038/nature01086.

[Sar81] Dror Sarid. "Long-Range Surface-Plasma Waves on Very Thin Metal Films". In: *Physical Review Letters* 47.26 (Dec. 1981), p. 1927. DOI: 10.1103/physrevlett.47.1927.

[Sci] Scikit-image. URL: http://scikit-image.org/.

[Seu+01] J. Seufert, G. Bacher, M. Scheibner, A. Forchel, S. Lee, M. Dobrowolska, and J. K. Furdyna. "Dynamical Spin Response in Semimagnetic Quantum Dots". In: *Physical Review Letters* 88.2 (Dec. 2001). DOI: 10.1103/physrevlett.88.027402.

[SGB99] O. Stier, M. Grundmann, and D. Bimberg. "Electronic and optical properties of strained quantum dots modeled by 8-band $\mathbf{k} \cdot \mathbf{p}$ theory". In: *Physical Review B* 59.8 (Feb. 1999), p. 5688. DOI: 10.1103/physrevb.59.5688.

[She+11] Timur Shegai, Vladimir D. Miljković, Kui Bao, Hongxing Xu, Peter Nordlander, Peter Johansson, and Mikael Käll. "Unidirectional Broadband Light Emission from Supported Plasmonic Nanowires". In: *Nano Lett.* 11.2 (Feb. 2011), p. 706. DOI: 10.1021/nl103834y.

[Shi07] Andrew J. Shields. "Semiconductor quantum light sources". In: *Nature Photon* 1.4 (Apr. 2007), p. 215. DOI: 10.1038/nphoton.2007.46.

[SM83] R. Short and L. Mandel. "Observation of Sub-Poissonian Photon Statistics". In: *Physical Review Letters* 51.5 (Aug. 1983), p. 384. DOI: 10.1103/physrevlett.51.384.

[Spi+12] D. Spirkoska, Al. L. Efros, W. R. L. Lambrecht, T. Cheiwchanchamnangij, A. Fontcuberta i Morral, and G. Abstreiter. "Valence band structure of polytypic zinc-blende/wurtzite GaAs nanowires probed by polarization-dependent photoluminescence". In: *Physical Review B* 85.4 (Jan. 2012). DOI: 10.1103/physrevb.85.045309.

[Ste13] Petr Stepanov. "Magneto-Optical Spectroscopy of Magnetic Semiconductor Nanostructures". PhD thesis. Université Grenoble Alpes, 2013.

[Suf+06] J. Suffczyński, T. Kazimierczuk, M. Goryca, B. Piechal, A. Trajnerowicz, K. Kowalik, P. Kossacki, A. Golnik, K. P. Korona, M. Nawrocki, J. A. Gaj, and G. Karczewski. "Excitation mechanisms of individual Cd Te Zn Te quantum dots studied by photon correlation spectroscopy". In: *Physical Review B* 74.8 (Aug. 2006). DOI: 10.1103/physrevb.74.085319.

[Sun+07] Qingjiang Sun, Y. Andrew Wang, Lin Song Li, Daoyuan Wang, Ting Zhu, Jian Xu, Chunhe Yang, and Yongfang Li. "Bright, multicoloured light-emitting diodes based on quantum dots". In: *Nature Photon* 1.12 (Nov. 2007), pp. 717–722. DOI: 10.1038/nphoton.2007.226.

[Sun+14] Liaoxin Sun, Ming-Liang Ren, Wenjing Liu, and Ritesh Agarwal. "Resolving Parity and Order of Fabry–Pérot Modes in Semiconductor Nanostructure Waveguides and Lasers: Young's Interference Experiment Revisited". In: *Nano Lett.* 14.11 (Nov. 2014), p. 6564. DOI: 10.1021/nl503176w.

[Tar+04] A. I. Tartakovskii, M. N. Makhonin, I. R. Sellers, J. Cahill, A. D. Andreev, D. M. Whittaker, J-P. R. Wells, A. M. Fox, D. J. Mowbray, M. S. Skolnick, and et al. "Effect of thermal annealing and strain engineering on the fine structure of quantum dot excitons". In: *Physical Review B* 70.19 (Nov. 2004). DOI: 10.1103/physrevb.70.193303.

[Tho+04] M. Thomas, J.-J. Greffet, R. Carminati, and J. R. Arias-Gonzalez. "Single-molecule spontaneous emission close to absorbing nanostructures". In: *Applied Physics Letters* 85.17 (2004), p. 3863. DOI: 10.1063/1.1812592.

[Ton+12] Catherine Tonin, Richard Hostein, Valia Voliotis, Roger Grousson, Aristide Lemaitre, and Anthony Martinez. "Polarization properties of excitonic qubits in single self-assembled quantum dots". In: *Physical Review B* 85.15 (Apr. 2012), p. 155303. DOI: 10.1103/physrevb.85.155303.

[Tri+08] Adrien Tribu, Gregory Sallen, Thomas Aichele, Régis André, Jean-Philippe Poizat, Catherine Bougerol, Serge Tatarenko, and Kuntheak Kheng. "A High-Temperature Single-Photon Source from Nanowire Quantum Dots". In: *Nano Lett.* 8.12 (Dec. 2008), pp. 4326–4329. DOI: 10.1021/nl802160z.

[UA15] G. S. Unal and M. I. Aksun. "Bridging the Gap between RF and Optical Patch Antenna Analysis via the Cavity Model". In: *Scientific Reports* 5 (Nov. 2015), p. 15941. DOI: 10.1038/srep15941.

[Urb+13] Bernhard Urbaszek, Xavier Marie, Thierry Amand, Olivier Krebs, Paul Voisin, Patrick Maletinsky, Alexander Högele, and Atac Imamoglu. "Nuclear spin physics in quantum dots: An optical investigation". In: *Rev. Mod. Phys.* 85.1 (Jan. 2013), pp. 79–133. DOI: 10.1103/revmodphys.85.79.

[Ves+07] Ernst Jan R. Vesseur, René de Waele, Martin Kuttge, and Albert Polman. "Direct Observation of Plasmonic Modes in Au Nanowires Using High-Resolution Cathodoluminescence Spectroscopy". In: *Nano Lett.* 7.9 (Sept. 2007), pp. 2843–2846. DOI: 10.1021/nl071480w.

[Ves+13] Ernst Jan R. Vesseur, Toon Coenen, Humeyra Caglayan, Nader Engheta, and Albert Polman. "Experimental Verification of n = 0 Structures for Visible Light". In: *Physical Review Letters* 110.1 (Jan. 2013). DOI: 10.1103/physrevlett.110.013902.

[Via+05] Alexandre Vial, Anne-Sophie Grimault, Demetrio Macìas, Dominique Barchiesi, and Marc Lamy de la Chapelle. "Improved Analytical Fit of Gold Dispersion: Application to the Modeling of Extinction Spectra with a Finite-Difference Time-Domain Method". In: *Physical Review B* (2005). DOI: 10.1103/PhysRevB.71.085416.

[Via+13] Sviatlana Viarbitskaya, Alexandre Teulle, Renaud Marty, Jadab Sharma, Christian Girard, Arnaud Arbouet, and Erik Dujardin. "Tailoring and imaging the plasmonic local density of states in crystalline nanoprisms". In: *Nat Mater* 12.5 (Mar. 2013), pp. 426–432. DOI: 10.1038/nmat3581.

[Via07] Alexandre Vial. "Implementation of the critical points model in the recursive convolution method for modelling dispersive media with the finite-difference time domain method". In: *J. Opt. A: Pure Appl. Opt.* 9.7 (July 2007), p. 745. DOI: 10.1088/1464-4258/9/7/029.

[VN03] Chris G. Van de Walle and J. Neugebauer. "Universal alignment of hydrogen levels in semiconductors, insulators and solutions". In: *Nature* 423.6940 (June 2003), pp. 626–628. DOI: 10.1038/nature01665.

[Wan01] J. Wang. "Highly Polarized Photoluminescence and Photodetection from Single Indium Phosphide Nanowires". In: *Science* 293.5534 (Aug. 2001), pp. 1455–1457. DOI: 10.1126/science.1062340.

[War+72] W. Wardzyński, W. Giriat, H. Szymczak, and R. Kowalczyk. "Stress-induced splitting of excitons due to exchange interaction in zinc telluride". In: *physica status solidi (b)* 49.1 (1972), p. 71. DOI: 10.1002/pssb.2220490105.

[Wee+09] Maarten H. M. van Weert, Nika Akopian, Freek Kelkensberg, Umberto Perinetti, Maarten P. van Kouwen, Jaime Gómez Rivas, Magnus T. Borgström, Rienk E. Algra, Marcel A. Verheijen, Erik P. A. M. Bakkers, and et al. "Orientation-Dependent Optical-Polarization Properties of Single Quantum Dots in Nanowires". In: *Small* 5.19 (Oct. 2009), pp. 2134–2138. DOI: 10.1002/smll.200900423.

[Win+88] M.M. Wind, P.A. Bobbert, J. Vlieger, and D. Bedeaux. "The polarizability of truncated spheres and oblate spheroids on a substrate: Comparison with experimental results". In: *Thin Solid Films* 164 (Oct. 1988), pp. 57–62. DOI: 10.1016/0040-6090(88)90109-5.

[WNS06] Michael Wimmer, S. V. Nair, and J. Shumway. "Biexciton recombination rates in self-assembled quantum dots". In: *Physical Review B* 73.16 (Apr. 2006). DOI: 10.1103/physrevb.73.165305.

[Woj+12] Piotr Wojnar, Elżbieta Janik, Lech T. Baczewski, Sławomir Kret, Elżbieta Dynowska, Tomasz Wojciechowski, Jan Suffczyński, Joanna Papierska, Piotr Kossacki, Grzegorz Karczewski, Jacek Kossut, and Tomasz Wojtowicz. "Giant Spin Splitting in Optically Active ZnMnTe/ZnMgTe Core/Shell Nanowires". In: *Nano Lett.* 12.7 (July 2012), p. 3404. DOI: 10.1021/nl300254w.

[XKC] Randall Munroe XKCD. URL: https://xkcd.com/353/.

[YS08] Naoki Yamamoto and Takahiro Suzuki. "Conversion of surface plasmon polaritons to light by a surface step". In: *Applied Physics Letters* 93.9 (2008), p. 093114. DOI: 10.1063/1.2978248.

[Zan+15] V. Zannier, T. Cremel, A. Artioli, D. Ferrand, K. Kheng, V. Grillo, and S. Rubini. "Optical properties of single wurtzite/zinc-blende ZnSe nanowires grown at low temperature". In: *Journal of Applied Physics* 118.9 (Sept. 2015), p. 095702. DOI: 10.1063/1.4929821.

[Zei] Zeiss. URL: http://www.zeiss.com.

[Zie13] M. Zieliński. "Fine structure of light-hole excitons in nanowire quantum dots". In: *Physical Review B* 88.11 (Sept. 2013), p. 115424. DOI: 10.1103/physrevb.88.115424.

[Zre+02] A. Zrenner, E. Beham, S. Stufler, F. Findeis, M. Bichler, and G. Abstreiter. "Coherent properties of a two-level system based on a quantum-dot photodiode". In: *Nature* 418.6898 (Aug. 2002), pp. 612–614. DOI: 10.1038/nature00912.

[ZSM05] Anatoly V. Zayats, Igor I. Smolyaninov, and Alexei A. Maradudin. "Nano-optics of surface plasmon polaritons". In: *Physics Reports* 408.3-4 (Mar. 2005), pp. 131–314. DOI: 10.1016/j.physrep.2004.11.001.

Summary

In this work, we study the coupling between plasmonic nanoantennas and semiconducting nanowire quantum dots (NWQDs). This coupling requires spectral, spatial and polarisation matching of the antenna mode and of the NWQD emission. Hence, a full characterisation of both the antenna system and the NWQDs has to be performed to determine a relevant coupling geometry.

Using cathodoluminescence (CL) we investigate the relation between the CL signal of circular patch plasmonic antennas and the electromagnetic local density of states (LDOS). The successive resonances supported by these antennas are complex superimpositions of Bessel modes of different radial and azimuthal order. Applying an analytical LDOS model, we show that we can fabricate and characterise antennas down to single mode resonances. However, the antennas CL spectrum goes beyond the radiative part of the LDOS. By changing the spacing layer thickness and the antennas materials, we propose an explanation for the origin of the additional CL signal we observe that is not related to the radiative LDOS of the patch antennas. We also demonstrate the fabrication of Al patch antennas working in the blue spectral range and apply our method to other geometries.

We perform optical characterisation of different quantum dots (QDs) embedded inside semiconducting nanowires (NWs) made of II-VI materials. We use microphotoluminescence (µPL) to study the emission of single NWQDs. Time-resolved measurements and Fourier imaging allows us to extract their exciton lifetime and radiation patterns. The variability in the emission properties of the NWQDs due to inhomogeneity in the growth process are evidenced by studying a statistical set of nanowires. A complete model based on polarisation-resolved Fourier imaging and magneto-optical spectroscopy is detailed, allowing to fully determine the QD electronic and optical properties for an individual system.

Finally, we develop a cathodoluminescence-based two-step electron-beam lithography technique to deterministically fabricate plasmonic antennas coupled to NWQDs, enhancing their µPL properties. The coupling results in an enhanced absorption of the pump laser inside the NW and in an increase of the radiative rate of the QD, leading to up to a two-fold intensity enhancement factor for the coupled system.

Résumé

Ce travail de thèse porte sur l'étude du couplage entre des boîtes quantiques (BQs) insérées dans des nanofils à semiconducteurs et des antennes plasmoniques. Un couplage efficace requiert une caractérisation complète des leurs propriétés optiques respectives, pour assurer un recouvrement spectral et spatial de l'émission de la boîte et du mode de l'antenne et l'alignement de la polarisation du mode plasmonique avec l'émission de la BQ.

Les propriétés optiques d'antennes patchs plasmoniques circulaires ont été étudiées par cathodoluminescence (CL). Nous avons montré avec un modèle analytique de la densité locale d'états électromagnétiques (DLE) au voisinage des antennes que leurs résonances sont des superpositions de modes de Bessel d'ordre radiaux et azimutaux différents. Nous avons fabriqué et caractérisé des antennes mono et multimodes, et trouvé que la partie radiative de la DLE n'est pas la seule contribution au signal de CL. De plus, nous avons caractérisé des antennes de différentes épaisseur du plan diélectrique ou différents matériaux. L'analyse de ces résultats nous pousse à proposer une interprétation des contributions au signal de CL annexes à la partie radiative de la DLE supportée par l'antenne. Nous avons de plus démontré la fabrication d'antennes patchs en aluminium opérant dans la partie bleue du spectre électromagnétique, et appliqué la CL à d'autres géométries d'antennes.

Nous avons également étudié différentes boîtes quantiques insérées dans des nanofils à semiconducteurs faits d'alliages de matériaux II-VI. Des émetteurs uniques sont étudiés par microphotoluminescence (µPL). Des mesures résolues en temps ou par microscopie de Fourier permettent une caractérisation spectrale, temporelle et la détermination de leur diagramme de rayonnement. Nous avons de plus mis en évidence les variations de propriétés optiques des émetteurs dues aux inhomogénéité de fabrication en étudiant un large ensemble de BQs. La modélisation complète des propriétés électroniques et optiques d'une boîte unique est proposée en utilisant la microscopie de Fourier résolue en polarisation, et une étape de spectroscopie magnéto-optique.

Enfin, nous avons développé une méthode de lithographie électronique en deux étapes basée sur le repérage d'un émetteur unique par CL, permettant la fabrication d'antennes plasmoniques couplées de façon déterministe à des BQs insérées dans des nanofils. L'étude de ce couplage révèle un accroissement de l'absorption du faisceau d'excitation accompagné d'une accélération de l'émission de la boîte par couplage radiatif. Il en résulte une exaltation jusqu'à un facteur 2 de la µPL des boîtes.